Doctoral Thesis

Design of Nanocatalysts with High Thermal Stability and Durability for Methane Conversion

Euiseob Yang

School of Energy and Chemical Engineering

(Chemical Engineering)

Ulsan National Institute of Science and Technology

2021

Design of Nanocatalysts with High Thermal Stability and Durability for Methane Conversion

Euiseob Yang

School of Energy and Chemical Engineering

(Chemical Engineering)

Ulsan National Institute of Science and Technology

Design of Nanocatalysts with High Thermal Stability and Durability for Methane Conversion

A thesis/dissertation submitted to
Ulsan National Institute of Science and Technology
in partial fulfillment of the
requirements for the degree of
Doctor of Philosophy

Euiseob Yang

06.16.2021 of submission

Approved by

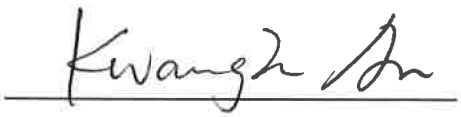

Advisor

Kwangjin An

Design of Nanocatalysts with High Thermal Stability and Durability for Methane Conversion

Euiseob Yang

This certifies that the dissertation of Euiseob Yang is approved.

June 16, 2021

Advisor: Kwangjin An

Sang Hoon Joo

Hyun You Kim

Ji-Wook Jang

Youngkook Kwon

Abstract

Methane is a substance with energetic, economic and environmental features of interest. It is the lightest hydrocarbon classified as a natural gas for heating, electricity generation and transportation. The shale gas technology revolutionizing energy trends has increased the availability of gas resources and made profound impacts on prices.

Despite the positive news of the increasing energy resources, methane is considered a second greenhouse gas dozens of times more potent than carbon dioxide. The applications of methane are limited because of its highly inert nature, with its symmetrical structures composed of only four C–H bonds. Methane is used in combustion to produce energy and exhaust emissions to produce carbon dioxide. It is not the solution to accomplish the carbon neutral to 2050, and many researchers have concentrated focus on CCUS—i.e., carbon capture, use and storage. Catalysis is the backbone of the industrial processes that have produced over 90% of chemicals and minimized environmental pollution. The catalytic methane conversion to value-added chemicals, such as oxygenates and hydrocarbons, is vital for sustainable development.

In this dissertation, we present the thermally stable catalysts composed of nanomaterials called nanocatalysts. Various types of high-performance catalysts have been designed to produce formaldehyde through the direct conversion of methane. We also designed a catalyst suitable for the dry reforming of methane to produce syngas using carbon dioxide as an oxidant. The chemical conversion of methane through heterogeneous catalysis is mainly accompanied by high-temperature reaction conditions, which leads to catalyst deactivation problems. In order to maintain long-term catalytic activity, it is necessary to prepare a catalyst with high thermal stability. The high-dispersion catalyst prepared by dispersing on a support with a large surface area can ensure high-temperature stability due to the strong metal-support interaction between the active site and the support. In addition, it is possible to increase the stability of the catalyst by encapsulating the surface of the existing high-activity catalyst with durable materials at high temperatures. Uniform coating of thermally stable metal oxides such as Al_2O_3 on the catalyst surface by atomic layer deposition can increase the stability of the catalyst structure, prevent carbon deposition, and even increase its activity.

As described in Chapter 2, we investigated the role of a vanadium oxide supported on mesoporous silica (VO_x/*m*-SiO_2) catalysts in methane oxidation to formaldehyde. The type of *m*-SiO_2 (SBA-15 and MCF-17), vanadium loading (1, 3, and 5%) and preparation method (wet impregnation; WI and dry impregnation; DI) were changed to produce VO_x/*m*-SiO_2 with different vanadium species. Because of the larger surface area and pore size, higher dispersion of vanadium loading, 1% VO_x/MCF-17 (DI),

showed the highest conversion (20.2%) in methane oxidation at 600 °C. Various characterizations revealed that DI was a better method to produce isolated tetrahedral monovanadate species in VO_x/*m*-SiO_2 catalysts than WI. As the vanadium loading was decreased from 5 to 1%, the methane conversion was further increased due to the higher degree of dispersion of monomeric VO_4 generated in the catalysts with low vanadium loading. The combined results demonstrate that the dispersion of vanadium and the isolated monomeric VO_4 phase increased when the vanadium catalyst was loaded on MCF-17 and prepared by the DI method.

In Chapter 3, we use hydrothermal synthesis followed by atomic layer deposition (ALD) to prepare an efficient and thermally stable catalyst based on novel SiO_2@V_2O_5@Al_2O_3 core@shell nanostructures to the selective oxidation of methane to formaldehyde, showing that the thickness of Al_2O_3 shells over SiO_2@V_2O_5 cores can be tuned by controlling the number of ALD cycles. Catalytic experiments performed in a flow reactor at 600 °C demonstrate that SiO_2@V_2O_5@Al_2O_3 nanostructures obtained after 50 ALD cycles exhibit the best catalytic activity (methane conversion = 22.2%; formaldehyde selectivity = 57.8%) and outperform all previously reported vanadium-based catalysts at 600 °C. The prepared catalysts are subjected to in-depth characterization, which reveals that their Al_2O_3 shell provides new surfaces for the generation of highly disperse T_d monomeric species with a V–O–Al bond by promoting interactions between Al_2O_3 and V_2O_5 nanoparticles during ALD. Moreover, the surface Al_2O_3 shell is found not only to protect V_2O_5 nanoparticles against sintering at 600 °C but also to anchor the produced T_d monomeric vanadium species responsible for the high catalytic performance.

In Chapter 4, we present coke-resistant catalysts for dry reforming of methane (DRM) composed of monodisperse Ni nanoparticles supported on CeO_2 nanorods are prepared and further coated with Al_2O_3 layers by ALD. Because the highly endothermic DRM requires a high reaction temperature to activate both CH_4 and CO_2, deactivation of the Ni catalyst may be induced by sintering and carbon coking. The performance of the catalyst in DRM and the amount of carbon deposited is correlated with the thickness of the Al_2O_3 layer in the Ni/CeO_2/Al_2O_3 catalysts. As the number of ALD cycles increases from 1 to 10, the conversion of CO_2 and CH_4 at 700 and 800 °C decreases, but the Ni/CeO_2/Al_2O_3 catalysts remain coke-free as thermogravimetric analysis shows no weight loss up to 800 °C. The Al_2O_3 layer generated by ALD curtails the coking substantially, but the weakly metallic character of Ni and blocking of Ni sites by the Al_2O_3 layer are major factors contributing to decreasing the catalytic conversion. The ALD technique provides an efficient way to fabricate atomically controlled oxide layers for improving the stability of catalysts against coke deposition and sintering.

Contents

List of Tables

List of Figures

Chapter 1

General Introduction

1.1. The State of Methane

The simplest alkane, methane is an important chemical compound in terms of energy and environmental issues. In the era of coal and oil, methane-based natural gas was primarily used as an energy source for electric power, industrial, residential and commercial sectors. However, with the successful commercialization of hydraulic fracturing that converts shale gas—the main component of methane—to resources, the supply has begun to accelerate. The energy transition from solid (coal) and liquid (oil) fuels to gas is thus underway, positioning methane as a cleaner energy source to sustainable energy generated from solar and water as a final goal.[1] However, methane is the second powerful greenhouse gas (GHG) after carbon dioxide (CO_2), which traps dozens of times more heat than CO_2. To accomplish carbon neutrality by 2050, a new paradigm of carbon use technologies must be developed.

Catalytic conversion of one-carbon (C_1) chemistry is crucial for the generation of value-added chemicals—e.g., syngas, oxygenates, and building blocks (ethylene and propylene)—from C_1 molecules of CH_4, CO_2, CO, and CH_3OH (Figure 1.1).[2–4] The resources of C_1 molecules are supplied from natural gas, shale gas, coal, biomass and organic waste.[5–7] To convert stable C_1 molecules (*e.g.*, CH_4 and CO_2), the role of catalysts is highly important in a heterogeneous system. Syngas production through steam reforming of methane (SRM, $CH_4 + H_2O \rightarrow CO + 3H_2$) is the typical process through which further reactions could be carried out to form C_{2+} hydrocarbons via the Fischer–Tropsch (FT) synthesis ($2nH_2 + nCO \rightarrow C_nH_{2n} + nH_2O$). To obtain the highly selective C_{5+} hydrocarbons, the role of metal active sites (Fe and Co) on catalysts is important. Through the reverse water-gas shift (RWGS) reaction (i.e., $H_2 + CO_2 \rightarrow CO + H_2O$) and FT synthesis, the olefin (C_nH_{2n}) and paraffin (C_nH_{2n+2}) are produced. However, the SRM is not only highly endothermic ($\Delta H°_{298\ K} = 206$ kJ mol^{-1}), but it requires multiple steps to obtain the products.[8] To simplify the process, the leading technology is, despite their difficulties, the direct conversion of CH_4 to desired chemicals including methanol,[9,10] formaldehyde,[11,12] ethane,[13,14] benzene,[15,16] and acetic acid[17,18] without undergoing syngas production. Its stable structure is responsible for the major problems associated with CH_4 activation. The symmetrical tetrahedral structure exhibits high C–H bond dissociation energy of 439 kJ mol^{-1}, low polarizability and a small electronegativity difference between C and H. The development of heterogeneous catalysis for methane conversion requires high temperature (> 550 °C); the thermal stability of catalysts is crucial to

preventing sintering, leaching, support dissolution and coke deposition.[19]

In this dissertation, we introduce the conversion of methane via various catalysts based on nanotechnology. Because the particles of the nanostructured catalyst are smaller and its surface area is more highly specified than conventional catalysts, higher catalytic activity can be expected. However, the stability of the catalytic structure of the nanoparticles is lower than that of the bulk structure and the melting point of the nanoparticles is lower than that of the bulk.[20] By focusing on improving the stability of the nanostructured catalyst, the activity and durability of the catalyst can be improved together. Metal oxide catalysts with high dispersion of active species could enhance the catalyst stability rather than metal species. Catalyst performance has been improved through surface modification of pristine catalysts with diverse methods—e.g., shell formation through strong metal-support interaction (SMSI),[21] core@shell methods,[22] and atomic layer deposition (ALD).[23–25]

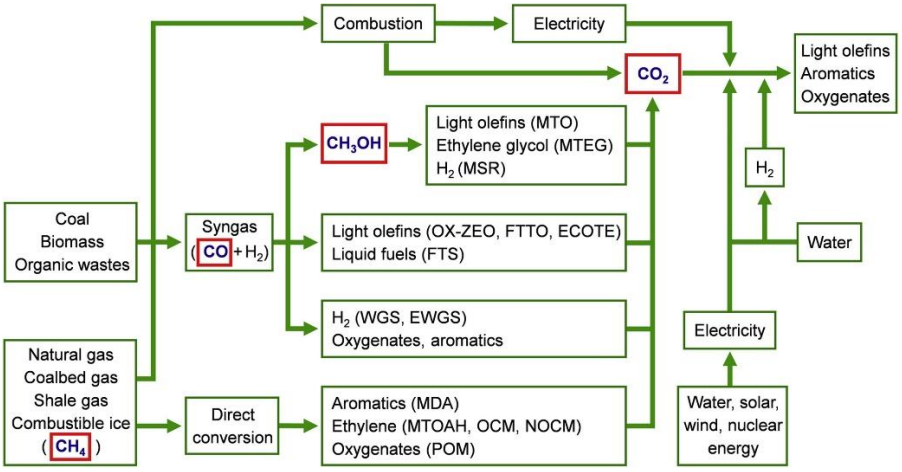

Figure 1.1. The origins and conversion pathways of C_1 molecules. Reprinted with permission from ref. 2. Copyright © 2020 Elsevier B.V.

1.2. Methane Conversion in Heterogeneous Catalysts

1.2.1 C–H activation of methane

Dissociation of sp^3 hybridized C–H bonds in alkane transitions is mainly discussed to understand the mechanism of methane activation. Two mechanisms are proposed in Figure 1.2.[26] One mechanism is the formation of radical intermediate ($\cdot CH_3$) due to electrophilic oxygen atoms through hydrogen atom transfer. Solid catalysts with M–O sites—e.g., zeolites or metal oxides,[27] and high-valent oxo metal complexes that provide radicals through charge transfer excitation (*i.e.*, ·OH, ·O–R)[28]—can become active sites for catalysts. In a typical electro-/photoactivated reaction process, electric or photonic energy often promotes the formation of reactive oxygen-containing species over electro-/photocatalysts to activate the C–H bond of methane through electrophilic processes. The other mechanism is the formation of M–C σ-bond as an intermediate of the unsaturated metal atoms on solid

catalysts in heterogeneous systems.[29,30] The oxidative addition mechanism, C–H bond dissociation presents the back-donation of the M(d_π) electrons into the C–H (σ*) state.[31] The main difference from radical intermediate formation is that the C–H bond is broken directly by two successive reactions, the electrophilic and the nucleophilic stage.[32]

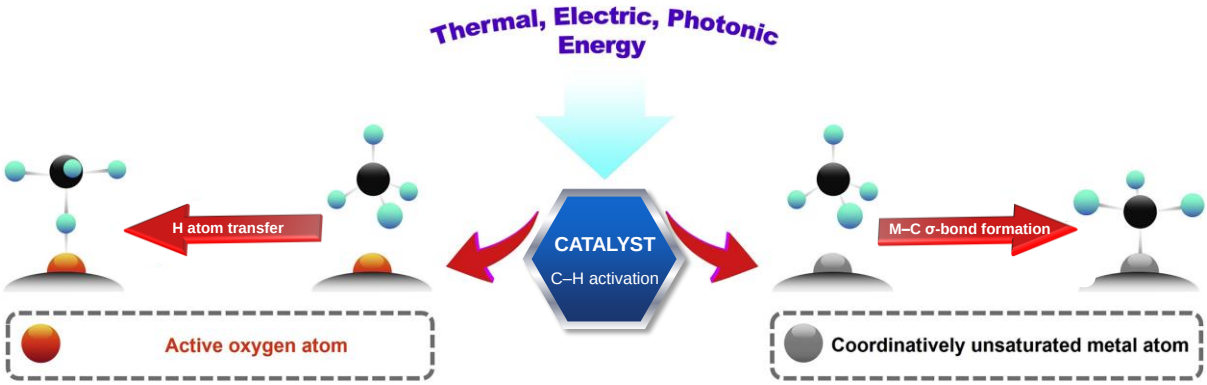

Figure 1.2. The mechanism of C–H bond dissociation of methane by thermal, electric, and photonic energy. Reprinted with permission from ref. 26. Copyright © 2019 Elsevier Inc.

Major two issues of selective oxidation of saturated hydrocarbons are suggested: finding ways to initiate C–H bond activation with the lowest energy and selective conversion to desired products to avoid sequential overreaction of full combustion to CO_2 and H_2O.[33] The alkanes with larger hydrocarbon chains are more accessible to convert because of the ability of the physisorption on the catalysts; hence the "stickiness" of the alkane molecule.[34] The trend is correlated with the dissociation energies of the C–H bonds depending on the bond types of alkyl groups, so the highest energy required for the methane (105 kcal mol^{-1}) compared to the H–CR_3 (93–95 kcal mol^{-1}).[35] Indeed, the C–H bond activation is considered the rate-determining step of the reactions.[36] The operation requires energy-intensive conditions with high temperature and pressure. These conditions could disturb the selectivity of the products because the desired products are usually more reactive than the alkane. The consequence of harsh reaction conditions, rigid oxide catalysts with redox properties could be the solution to oxidize the alkane. Nevertheless, the elucidation of the mechanism through *in situ* characterizations is difficult due to their harsh conditions.

1.2.2 Oxidative methane conversion

Direct routes for methane oxidation to oxygenates—e.g., methanol, formaldehyde and formic acid for C_1 products; and ethane, benzene, and acetic acid for C_{2+} products—are mainly discussed in this chapter. The oxygenates are practically produced through syngas conversion and the direct conversion is more energy-efficient, cost-efficient and straightforward. However, the selective oxidation of methane is made challenging by its requirement of high temperature and subsequent catalyst deactivation through the sintering, coking and leaching problems, and the full oxidation of

oxygenates to the CO_2 and H_2O due to their higher reactivity. One solution would be reducing the catalyst temperature. However, low-temperature catalysis easily results in poor methane conversion. Therefore, highly thermostable catalysts are essential for oxidative methane conversion in heterogeneous systems.

Direct conversion into methanol is mainly studied to obtain C_1 oxygenates. Under ambient conditions the methane monooxygenase (MMO) enzymes can participate in the methane conversion by activation of oxygen adsorbed on the catalyst surface into methoxy species.[37–39] Iron-[40] and copper-exchanged[41,42] zeolites can initiate C–H activation at relatively low temperatures (<473 K) by mimicking the structure of MMOs with di/tricoper[43] or di-iron active clusters. The direct oxidation of methane to methanol using oxygen or water via copper-exchanged zeolites under mild conditions of 210 °C was first reported by Narsimhan *et al.*[9] Hutchings *et al.*[40] reported a Fe-Cu-ZSM-5 catalyst from methane to methanol using hydrogen peroxide and achieved high methane conversion. In particular, high selectivity of 90% was shown with a 10% methane conversion of 323 K. Bokhoven *et al.*[41] reported a selectivity of 97% for methanol production using a Cu-MOR catalyst using water as an oxidant (Figure 1.3).

The process of methane is cyclic. An activated catalyst reacts with methoxide bound-methane and then extracts methanol with water through re-oxidation of the active site. Density functional theory (DFT) simulation suggests that the proposed mechanisms mainly focus on mono (μ-oxo) dicopper active cores. It reacts with methane and bonds CH_3 with the Cu atom. Brønsted sites are generated via proton abstraction by the zeolite framework shown in state III, which reduces Cu atoms to form methoxy species. Secondly, the addition of water relaxes the high-energy Cu^{+}–Cu^{+} species to produce Cu^{I}–OH_2–Cu^{I}, anddesorption of methanol (state VII) and hydrogen formation eventually resets the active site to the initial state of the copper core. The authors evaluate whether the copper center operates in both the oxidation of methane and the desorption of methanol.

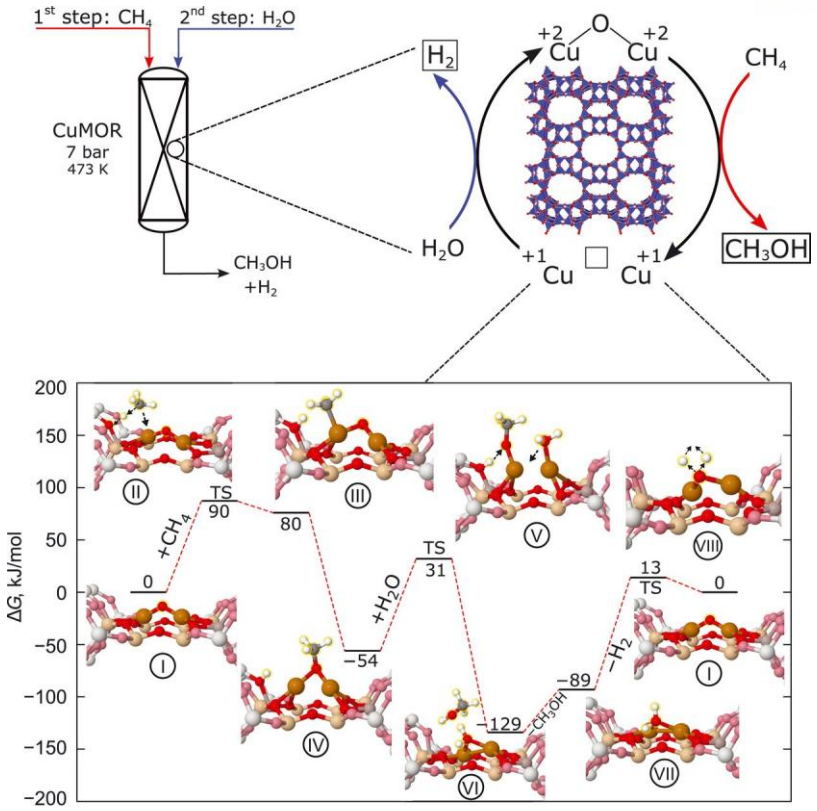

Figure 1.3. The mechanism of partial oxidation with water oxidant. (Top) Schematic representation of the reaction of methane to methanol on the reduction of the mono(μ-oxo)dicopper active core and provide the oxygen atoms into methane to produce methanol. The reduction of water regenerates the active sites to initial active species. (Bottom) The proposed mechanism of methane oxidation by DFT calculation. Reprinted with permission from ref. 41. Copyright © 2017 American Association for the Advancement of Science.

Formaldehyde is an essential raw material used in various industries. Using resins made by polymerizing various organic substances such as phenol and urea as raw materials, adhesives of various viscosities are made and used for engineering wood production. It is the raw material of pentaerythritol, a versatile building block with durability, low cost, heat and chemical resistance. It is mainly used as a finishing material for vehicles. Due to its antiseptic and antibacterial properties, formaldehyde is widely used in medical applications, such as drug encapsulation in hard gel form.

From the industrial point of view, formaldehyde is produced in two ways. One is the catalytic oxidation of methanol, called the Formox process ($2CH_3OH + O_2 \rightarrow 2CH_2O + 2H_2O$) in the presence of Fe–Mo–V metal oxide catalyst at 250–400 °C.[44,45] The other is the dehydrogenation of methanol ($CH_3OH \rightarrow CH_2O + H_2$) using polycrystalline silver catalyst at 600–700 °C.[46] The catalytic methane conversion of formaldehyde is thus accompanied by the successive reactions with methanol production. The period of methane conversion to formaldehyde requires a longer period of residence time but it is quite short in the gas flow system.[47] Therefore, the conversions to formaldehyde with the single run are

reported less than 5% at a high temperature of 600 °C.[48,49] Acidic oxides such as V_2O_5, MoO_3, and B_2O_3 are suitable for the direct conversion of methane to formaldehyde with the addition of an oxygen atom into CH_{4x}.[50] In the cases of V_2O_5 and MoO_3, the active centers of V^{5+}=O and Mo^{6+}=O are proposed by electron paramagnetic resonance (EPR) spectroscopy, which has high reducibility to the radical centers of V^{5+}–O– and Mo^{6+}–O– species. The catalysis proceeds as follows:[51] ([ ]$^-$: oxygen vacancy)

$$V^{5+}–O^- + CH_4 \rightarrow V^{5+}–OH + CH_3^{\cdot},$$

$$V^{5+}–O_2^{2-} + CH_3^{\cdot} \rightarrow V^{4+}–OCH_3^-,$$

$$V^{4+}–OCH_3^- + V^{5+}–O_2^{2-} \rightarrow V^{4+}OH^- + V^{4+}[\,]^- + CH_2O.$$

Whether the mechanism is accurate or not is still controversial, but when it comes to formaldehyde production it is more selective than nonselective oxidation ($8V^{5+} + 4O^{2-} + CH_4 \rightarrow 8V^{4+} + 2H_2O + CO_2$), resulting in the correct direction in the overall context. Rellán-Piñeiro *et al.*[52] reported the DFT calculation of molybdenum-based oxides in the methanol oxidation to formaldehyde. The unique character of the Mo^{VI}–Mo^{IV} pair that Mo^{VI} is the active site and Mo^{IV} provides the oxygen vacancy.

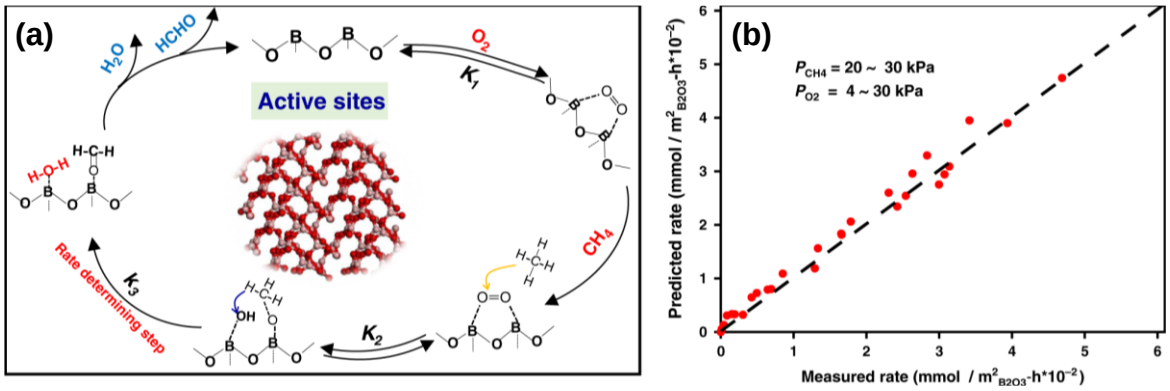

Figure 1.4. The direct methane oxidation to formaldehyde on B_2O_3-based catalysts. (a) The proposed mechanism and (b) Parity plots derived from the methane conversion rates which are calculated by pseudo-steady-state approximation depending on the measured O-exchange between oxygen molecules in the presence of CH_4. Reprinted with permission from ref. 11. Copyright © 2020 Springer Nature.

Tian *et al.*[11] reported the direct methane to formaldehyde and carbon monoxide on B_2O_3-based catalysts supported on the various oxides (Al_2O_3, TiO_2, ZnO, ZrO_2, and SiO_2) and ZSM-5 zeolite structure. The reaction results clearly showed the high selectivity of 94% with equimolar mixture of HCHO and CO with 6% conversion of methane at 550 °C, regardless of the oxide support. The authors propose a methane oxidation mechanism based on kinetics and isotopic assessment of oxygen activation in Figure 1.4a.

First, the oxygen atom is adsorbed on the electron-deficient B center, forming an intermediate in

a 5-membered ring. The CH_4 molecule attacks the oxygen adsorbed on the B–O–B center. A hydroxyl group and a methoxy species are formed and bound to each B site. The H atoms extracted from the methoxy species are converted to formaldehyde and water, which is evaluated as a rate-determining step, and the active site at the BO_3 center leads to a product called a desorption process. The methane conversion rates are estimated through the catalytic turnover in Figure 1.4b and agree precisely with the experiments of wide pressure ranges of reactant gases up to 30 kPa. In conclusion, the possibility of selective methane conversion to formaldehyde by oxygen bonds provided by acidic oxides was confirmed.

C–C coupling reaction of CH_4 enables C–C chain extension for the production of valuable chemicals such as ethylene and propylene in the petrochemical industry. Various attempts have been reported to produce C_{2+} hydrocarbons through the dehydrogenation (also called decomposition) of methane itself. In the case of dehydrogenation, the possibility of side reactions is low, which would predict high selectivity. Nonoxidative coupling of methane (NOCM, $2CH_4 \rightarrow C_2H_4 + 2H_2$) occurs as the C–H bonds in methane are activated to form CH_x and hydrogen, followed by oligomerization of CH_x. Belgued *et al.*[53] was the first to discover a Pt/SiO_2 catalyst with 95% C_{2+} selectivity at 250 °C despite low methane conversion. Xiao *et al.*[54] reported that the bimetallic Pt–Bi catalyst supported on ZSM-5 zeolite has a high selectivity of over 90% for the C_2 species of ethane and ethylene. The authors conclude that the Pt metal site is considered the active site for methane activation, and that the Bi promoter is responsible for the selectivity and stability of the catalyst. The methane dehydroaromatization (MDA, $6CH_4 \rightarrow C_6H_6 + 9H_2$) is another nonoxidative reaction that converts methane to liquid aromatics such as benzene, toluene, and xylene. Wang *et al.*[55] and co-workers reported that they were reactive in Mo-based zeolite catalysts in the 1990s. MDA catalysts require metal sites (Mo, Fe) for non-oxidative CH_4 activation and an acidic zeolite support chain function capable of bonding carbon bonds to aromatic rings.[56–59] Bao *et al.*[17] reported the $Fe@SiO_2$ with a single Fe atomic site embedded in the SiO_2 that can withstand high temperatures. It showed a methane conversion of 48.1% at 1,363K with a hydrocarbon selectivity of over 99%. To boost the forward reaction of MDA, hydrogen removal techniques are also have been developed. Kumar *et al.*[60] reported the scavenging hydrogen by Zr metal particles on the MoC_x/H-ZSM-5 catalyst. The saturated hydrogen produced zirconium hydride (ZrH_x) and the desorption of hydrogen process could regenerate the catalyst. Morejudo *et al.*[16] reported the $BaZrO_3$-based membrane reactor which could remove the hydrogen with their electrochemical control.

Oxidative coupling of methane (OCM) with O_2 has been extensively studied going back to Keller and Bhasin in the 1980s.[61] The primary products of the OCM reactions are ethylene and ethane. They generate in the following equations:

$$4CH_4 + O_2 \rightarrow 2C_2H_6 + 2H_2O \ (\Delta G°_{298K} = -321 \text{ kJ mol}^{-1})$$

$$2C_2H_6 + O_2 \rightarrow 2C_2H_4 + 2H_2O \ (\Delta G°_{298K} = -255 \text{ kJ mol}^{-1})$$

The mechanism of the OCM inevitably goes through the methane activation to methyl radicals on the catalyst surface and the coupling reaction of two methyl radicals produces the ethane. Further oxidative dehydrogenation to ethylene could be the best way to produce the desired C_2 product.[62] However, the reactions are not only highly exothermic, but they occur at high temperatures over 750 °C in heterogeneous catalysis.[63–66] In addition, the presence of oxidants can cause hotspots in some localized areas of the reactor due to its high endothermic nature, which can be up to 150 °C higher than the reactor temperature.[67] The higher temperature accelerates the overoxidation to form H_2O and CO_2 and worsens the catalyst stability. Thermally stable catalysts and heat management in the reactors are thus required to prevent uneven high temperatures.

Metal oxide catalysts are widely studied because of their high thermal stability. Kiani *et al.*[68] investigated OCM using $Mn/Na_2WO_4/SiO_2$ catalysts according to crystallinity, synthesis method, calcination temperature and reaction conditions. They explained that the catalytic reaction is the effect of oxygen on methane oxidation by the Mars-van-Krevelen mechanism. The mechanism undergoes dissociative adsorption of oxygen at the active site to form lattice oxygen, which is then reduced to its initial form through the reaction of lattice oxygen with gaseous methane to form a methyl radical. Despite advances in various *in situ* and *operando* spectroscopy to identify mechanisms, high-temperature catalytic reactions remain challenging to elucidate. Xu *et al.*[69] reported the $La_2B_2O_7$ (B = Ti, Zr, Ce) compounds categorized by complex oxide thin film structures for the OCM reaction. They have different crystalline phases depending on the B-site cations that monoclinic layered perovskite ($La_2Ti_2O_7$), cubic pyrochlore ($La_2Zr_2O_7$) or disordered defective cubic fluorite ($La_2Ce_2O_7$). The catalyst performance consists of methane conversion (550–800 °C) and C_2 selectivity follows the order of $La_2Ce_2O_7 > La_2Zr_2O_7 > La_2Ti_2O_7$. Superoxide O_2^- site on the catalyst surface strongly influences the OCM performance and it is demonstrated by Raman, EPR, *in situ* diffuse reflectance infrared Fourier transform spectroscopy (DRIFTS), X-ray photoelectron spectroscopy (XPS), temperature-programmed desorption with CO_2 (CO_2-TPD) measurements. In their statistical analysis for OCM conversion, Zavyalova *et al.*[70] selected the 18 core elements. The C_2 selectivity enhanced range from 72 to 82% by the selected elements which all have strong basicity such as alkali (Cs, Na) and alkaline-earth (Sr, Ba) metals. In addition, the catalyst activity could be positively affected by the dopants such as Mn, W, and Cl anion which have the C_2 yield range from 16 to 26%.

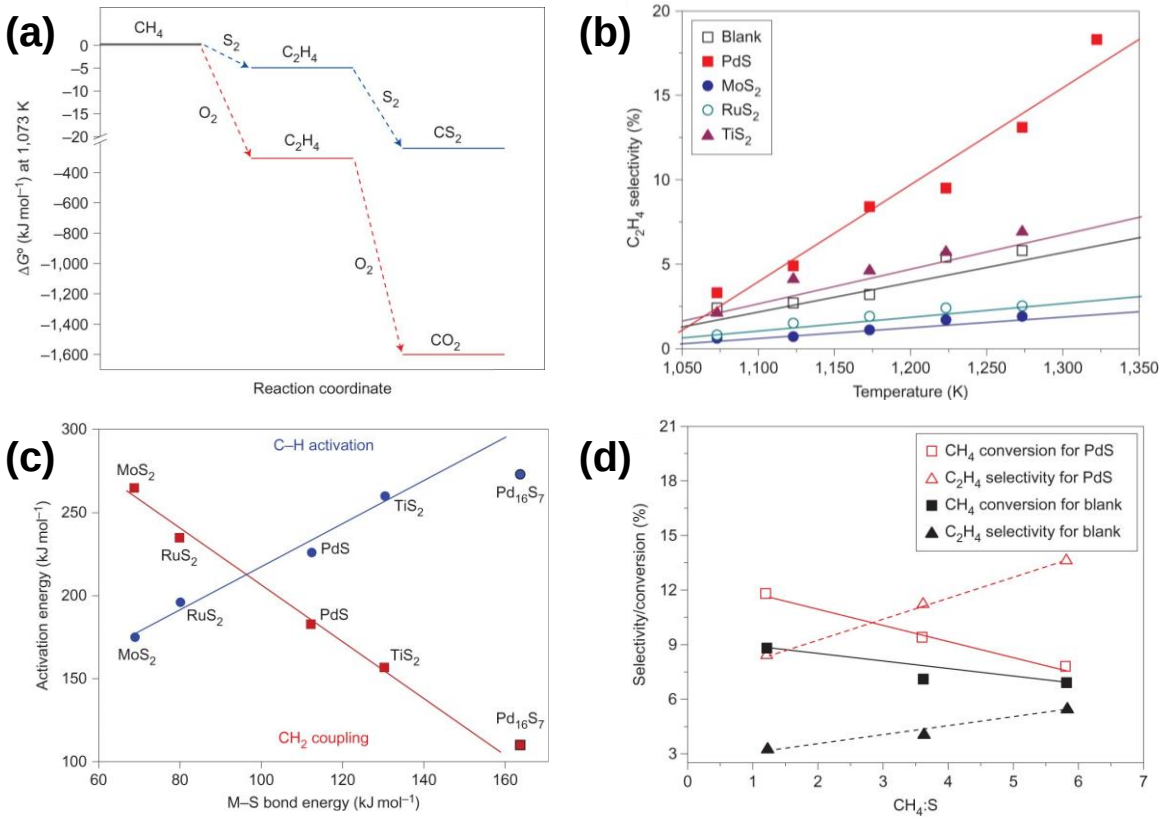

Figure 1.5. (a) Compared the thermodynamic calculations of the methane coupling reaction using O_2 and S_2 as the oxidants. The sulfur mitigates the overoxidation of methane at 1,073 K. (b) The ethylene selectivity of the metal sulfide catalysts. (c) DFT-based calculations of correlations of the CH_2 coupling and C–H activation depending on the M–S bond energy. (d) The effect of CH_4/S feed ratios of PdS catalyst and blank for methane conversion and ethylene selectivity at 1,223 K. Reprinted with permission from ref. 71. Copyright © 2012 Springer Nature.

Using milder oxidants for coupling reactions (e.g., S_2, SO_3, and NO) could enhance the selectivity in place of an O_2. Marks *et al.*[71] suggested using the elemental sulfur as a selective 'soft' oxidant such as MoS_2, RuS_2, TiS_2, PdS to produce ethylene. The oxidation processes with oxygen and sulfur have different thermodynamic properties. The weaker C–S and H–S bonds than C–O, and H–O inspires the expectations of stable intermediates to contribute to the selective catalytic oxidative coupling of methane because of the thermoneutral properties of sulfur. The standard Gibbs-free energy of the reactions at 1,073 K represents the difference in the oxidation tendencies depending on the oxidants.

$$2CH_4 + O_2 \rightarrow C_2H_4 + 2H_2O, (\Delta G° = -307 \text{ kJ mol}^{-1})$$

$$2CH_4 + S_2 \rightarrow C_2H_4 + 2H_2S, (\Delta G° = -4.90 \text{ kJ mol}^{-1})$$

The significant differences of the Gibbs-free energies to overoxidation to CS_2 and CO_2 are calculated 80 times in Figure 1.5a, so the selectivity of ethylene increases. Among the four metal sulfides, PdS showed the highest ethylene selectivity with the 15% conversion at 1,323 K in a CH_4/S ratio of 5.8

(Figure 1.5b). The DFT calculation showed the correlations of the energies of CH_2 coupling and C–H activation. The weak M–S bond enhances the activation of methane through the abstraction of hydrogen atoms while making the coupling reaction harder. To link the coupling, strong M–S bonds are preferred so the compromise energies between the CH_2 coupling and C–H activation of PdS at the borderline could be shown the highest ethylene selectivity (Figure 1.5c). The feed ratio of CH_4/S significantly affects the methane conversion and C_2H_4 selectivity for the PdS catalyst. The larger feed ratio refers to the lack of the amount of oxidant but it brings positive effects for the selectivity of ethylene. It is revealed that the reduction of PdS to $Pd_{16}S_7$ phase exhibited the highest activity in the reaction condition. (Figure 1.5d) In summary, the OCM process prevents coke formation such as partial oxidation, but most intermediates are highly reactive, making them very susceptible to further oxidation of CO_2. Therefore, it is important that the methyl radicals formed on the catalyst surface form a stable intermediate on the catalyst surface. The methyl radicals formed should not react with oxygen and the two methyl groups should react stably on the catalyst surface. Therefore, the proportion of oxidizing agent in the reactant must also be optimized.

Furthermore, direct methane conversions to formic acid,[51,72–74] acetic acid,[18,75–77] methyl acetate[78] and methyl trifluoroacetate[79,80] are reported in a manner similar to that described above. However, not all reactions have yet been developed as commercially viable processes on an industrial scale. Although Siluria has attempted to commercialize the OCM process by 2019, no commercial success has been achieved to date. In heterogeneous catalysts, the methane conversion reaction proceeds under high-temperature reaction conditions. Therefore, it is necessary to ensure the structural stability of the catalyst and to control so that the selectivity is not deteriorated by the high reactivity of the target product. In addition, more advanced facilities are needed to enable various *in situ* characterizations to elucidate the mechanism of the reaction.

1.2.3 Dry reforming of methane

Syngas (H_2/CO) is one of the most important platform chemicals that uses non-petroleum resources to supply energy and chemical feedstocks that can be generated from natural gas, coal, biomass, carbon-containing waste and carbon dioxide. The conversion of methane to syngas has been mainly carried out by SRM or commercial scale autothermal reforming. A reaction that supplies hydrogen, the reforming reaction is emerging as an important field of eco-friendly research. Dry reforming of methane (DRM, $CH_4 + CO_2 \rightarrow 2CO + 2H_2$) is an important reaction that oxidizes methane to carbon dioxide to produce synthesis gas. DRM is one of the carbon capture, use and storage (CCUS) studies that encompass all technologies that can chemically treat CO_2 and is being studied to address climate change challenges and achieve carbon neutrality by 2050.

DRM is highly endothermic (ΔH_{298K} = 247 kJ mol^{-1}) due to the C–H bond cleavage so that the high-temperature conditions (873–1273 K) are indispensable.[81] From a stoichiometric point of view,

the lower pressure is favorable for the forward reaction and the H_2/CO ratio of resulting syngas converges to unity, which could be advantageous for application to FT process over those produced in other reforming reactions.[82,83] The industrial scale of DRM has not been developed, so more research is needed due to its great potential in the future as an alternative way to produce syngas. There have been industrial experiences of reforming reactions using large-scale CO_2-rich gases.[84] To date, two methods are reported and are the CALCOR (Caloric, Germany) and SPARG (Haldor Topsøe, Denmark) processes respectively.[85,86] First introduced in the 1940s, the CALCOR process combines the SRM and DRM (a.k.a. autothermal reforming). Before the reforming reaction proceeds, sulfur removal by desulfurization was required, and the reaction was tested in which H_2O is injected in addition to CH_4 and CO_2. The SPARG process uses the sulfur without discarding the H_2S step for passivation of the catalyst surface, which could have the coke resistance properties developed in the 1980s. To maintain the long-term durability of the catalyst, it is necessary to prevent the production of NiS, a major cause of loss of C–H activation capacity.[87] As reactors grow in size, it is essential to address the pressure drop problem due to the deposition of carbon in solid form, and all catalysts used in large-scale reactions are known as Ni or Ru supported on alumina-magnesia (Ni–Ru/$MgAl_2O_4$). That is, the elements composed of the catalyst is the best to suppress coke formation. It is expected to be important to maintain this composition for the commercialization of the DRM reaction.

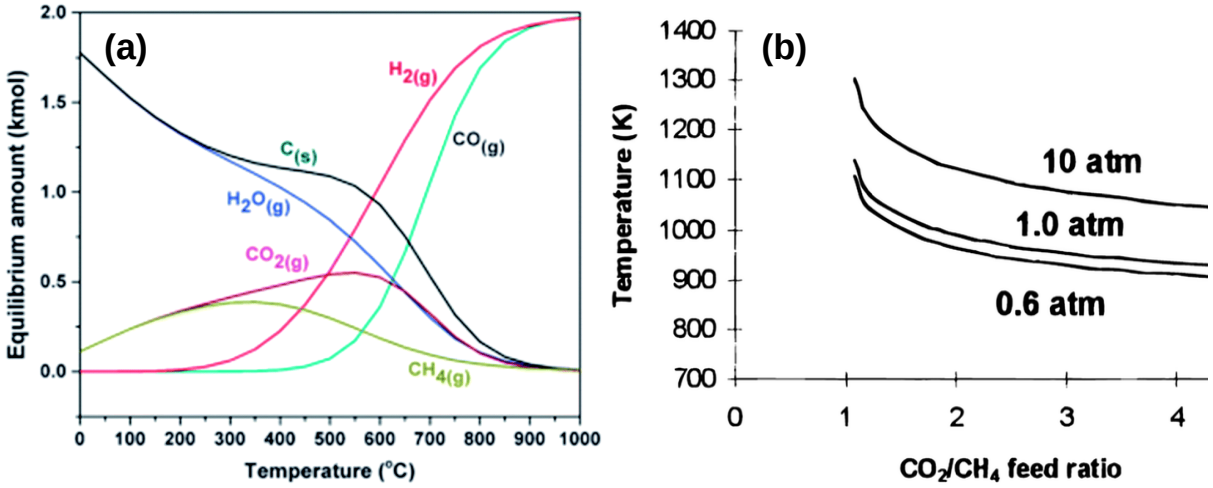

Figure 1.6. Thermodynamic perspectives of DRM. (a) Thermodynamic equilibrium plot during the DRM. (b) Thermodynamic analysis of the baseline for carbon deposition according to pressures, temperatures, and feed ratios. Carbon deposition does not occur in high-temperature conditions. Reprinted with permission from ref. 88. Copyright © Royal Society of Chemistry 2016.

Major problems are catalyst sintering from the very high endothermic reaction and the following deactivation by carbon deposition on the catalyst surface. Carbon deposition is most affected by thermodynamics in Figure 1.6a. The conversion of methane increases with elevated temperature and

reaches full conversion above 800 °C. The carbon dioxide did not participate in the reaction under 600 °C and react actively at higher temperatures. Undesired byproducts of carbon and water could be generated in the range of 300–800 °C. Solid carbon is harmful in the durability of the flow reactors which causes the pressure drop by two side reactions which is called Boudouard reaction and methane decomposition.[88,89]

$$\text{Boudouard reaction: } 2CO \rightarrow C + CO_2, (\Delta H° = -171 \text{ kJ mol}^{-1})$$

$$\text{Methane decomposition: } CH_4 \rightarrow C + 2H_2, (\Delta H° = 75 \text{ kJ mol}^{-1})$$

The Boudouard reaction is exothermic and generally occurs below 700 °C, while the methane decomposition reaction is exothermic and occurs above 560 °C. Therefore, in terms of process development, a method of reducing side reactions by performing the process at a temperature of 700 °C or more may be appropriate. In theory, the production of carbon and water could not be observed at high temperatures above 900 °C. However, the system must be continuously energized for highly endothermic DRM reaction, which is not suitable for commercialization given the current net energy cost. On the other hand, the conversions of methane and carbon dioxide are too low to be commercialized below 600 °C. Therefore, the method of preparing the catalyst surface to prevent carbon deposition is the most difficult, but it is a highly reactive and energy-efficient method that allows the reaction to be carried out in the temperature range of 560 to 700 °C. Carbon deposition is also affected by the pressure differences in the reactor shown in Figure 1.6b. The high pressure of the reactor requires higher temperatures to avoid carbon deposition. In low-pressure conditions, not only forward reactions predominant, but also the tendency to have fewer side reactions to generate carbons. In addition, the higher the CO_2 ratio corresponding to oxidizing agents, the lower the carbon production. Based on the above results, it is necessary to develop catalysts and establish actual process facilities that can maintain high activity and stable H_2/CO ratio to unity while suppressing carbon deposition below 700 °C.

A variety of metal-based catalysts corresponding to groups 8, 9, and 10 (Fe, Co, Ni, Ru, Rh, Pd, Ir, and Pt) have been reported for DRM. Among them, Ni metal catalysts have been reported most often than other metals in terms of CH_4 conversion and price competitiveness. The research mainly focuses on improving the stability of the catalyst. Ni catalysts are highly reactive on most supports, but the Tammann temperature of Ni metal itself is known to be around 600 °C, so it is important to prevent sintering over the temperature.[90] When Ni particles aggregates, the active sites for DRM are reduced and they become a favorable form for carbon deposition. Details of improving stability are described in Chapter 1.3. Active metal sites such as Ni are responsible for the activation of CH_4 in reactions such as DRM and SRM. On the other hand, the support plays various roles, such as improving the activity and stability of the catalyst through high dispersion of the active site, promoting the reaction of the active site by lattice oxygen, preventing sintering, and preventing coke deposition. Diverse supports are tested of single oxides (Al_2O_3, MgO, CeO_2, ZrO_2, SiO_2, La_2O_3, TiO_2), mixed oxides (MgO–Al_2O_3, CeO_2–ZrO_2,

CeO_2–Al_2O_3), and zeolites (zeolite Y, zeolite A, and ZSM-5). Promoters are also widely used to improve the stability, selectivity, and activity of catalysts, mainly alkali and alkaline earth metals or rare earth metals. Alkali and alkaline earth metals with their basic properties can be easily reacted with CO_2 oxidants, which promotes the oxidation of methane. In rare earth metal oxides such as CeO_2 or ZrO_2, oxidation is promoted by the redox properties.

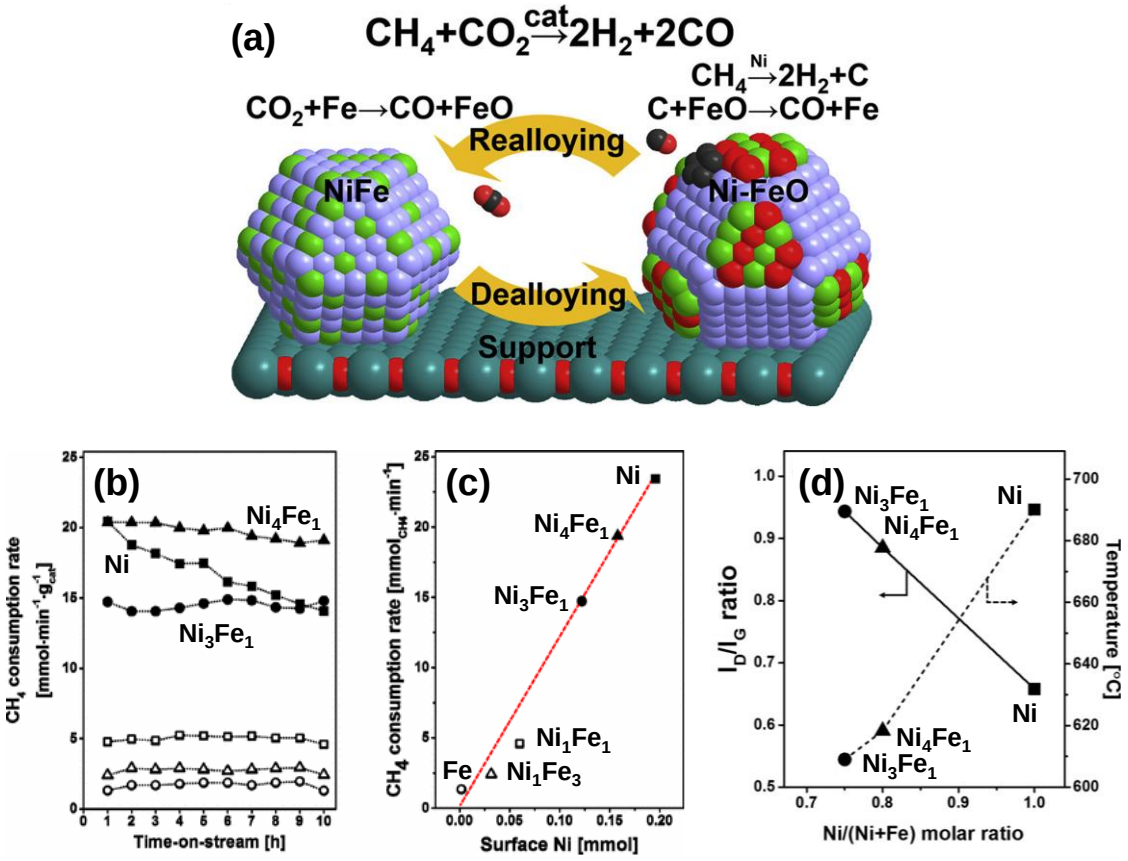

Figure 1.7. (a) Schematic illustration of Ni–Fe bimetallic catalysts for DRM. The methane consumption rate (b) as a function of time on stream and (c) the amount of surface Ni. (d) The ratio of D- and G-band intensities (I_D/I_G) and the temperature for coke elimination of the spent catalysts depending on the Ni and Fe ratios. Reprinted with permission from ref. 91. Copyright © 2017 American Chemical Society.

Ni-based bimetallic catalyst improves the reactivity and stability of the catalyst through a complementary catalytic reaction. Methane activation is mainly generated in Ni metals, and the remaining metals provide oxygen to Ni metals in CO_2 to prevent carbon deposition and prevent catalytic activity. Müller *et al.*[91] investigated the NiFe bimetallic catalysts that were supported on $Mg_xAl_yO_z$ for methane activation and coke evaluation according to Ni and Fe ratios. Ni_4Fe_1 catalyst showed highest activity and stability due to coke resistance (Figure 1.7a–b). Unlike monometallic Ni catalysts, whose reactivity decreases over time, bimetallic catalysts commonly exhibit catalytic reaction stabilities. The methane consumption rate is linearly dependent on the quantity of the surface Ni which is estimated by the hydrogen chemisorption (see Figure 1.7c). Only Ni metal is involved in methane activation. Raman and TGA measurements were performed to determine the degree of defects in the coke produced on the

spent catalysts. As shown in Figure 1.7d, the higher the I_D/I_G value, the lower the crystallinity of the deposited carbon. The lower I_D/I_G indicates the easier regeneration of carbon on the catalyst surface, which means that it is difficult to deposit carbon on the surface. Therefore, high temperature (690 °C) is required for coke removal of Ni catalyst due to its high crystallinity. The dealloyed FeO on the metal surface could regenerate Fe in alloy form through reduction by hydrogen and removal of deposited coke on the active sites. Marin *et al.*[92] reported the NiFe bimetallic catalyst mainly focused on the role of Fe. They also concluded the highest activity and stability were confirmed even in a catalyst containing a relatively small amount of Fe compared to Ni which follows a Mars-van Krevelen mechanism. Chin *et al.*[93] reported the DFT calculations of activity of NiCo(111) surface and the counterpart of Ni(111) and Co(111) to elucidate the C–H bond activation pathway during DRM. The RWGS occurs concomitantly in the DRM reaction, and it is confirmed that the RWGS eventually reached a chemical equilibrium at three different NiCo surfaces (see Figure 1.8d–f). Pressure ratios of CO_2-to-CO and H_2O-to-H_2 has thermodynamic relationship as follows:

$$\frac{P_{CO_2}}{P_{CO}} = \frac{1}{K_{RWGS}} \frac{P_{H_2O}}{P_{H_2}}$$

where K_{RWGS} is the equilibrium constant for the RWGS reaction. The pathways of initial C–H bond activation on Ni, Co and Ni–Co are different. For Ni clusters, the first-order rate coefficients for DRM are independent of both CO_2/CO and H_2O/H_2 ratios in Figure 1.8a. The C–H bond activation on Ni(111) occurs via oxidative addition of a Ni-atom into the three-center $(H_3C\cdots{}^{*}\cdots H)^{‡}$ transition state. The rate is only proportional to the methane pressure, and adjacent Ni atoms are far (2.05 Å) from hydrogen atoms in methane, making it difficult to remove. For Co clusters, the rate coefficients are strongly dependent on CO_2/CO and H_2O/H_2 ratios (see Figure 1.8b). In addition, the rate is much smaller than the Ni clusters and it is affected by the oxygen coverage on Co clusters during the steady-state reaction due to its high oxophilic nature. The activation on Co(111) occurs into the four-center $(H_3C\cdots{}^{*}\cdots H\cdots O^{*})^{‡}$ transition state. The hydrogen atom is stabilized by O* on a vicinal Co^{II} site of a shorter distance (1.17 Å) than the elongated C–H bond. (1.44 Å) For Ni–Co clusters, the rate coefficients are dependent in the same manner as Co clusters. The first-order rate coefficients display a volcano-shaped which has the highest values close to 0.8 among the three clusters (see Figure 1.8c). At the transition state, the elongation of the C–H bond from 1.10 to 1.47 Å could indicates the bond weakening, and the go through the four-center $(H_3C\cdots{}^{*}\cdots H\cdots O^{*})^{‡}$ transition state. In addition, the metal insertion in the transition state into C–H bonding stabilizes both the leaving atom (1.85 Å for H–Co^{I} bond distance) and CH_3 fragment (2.28 Å for C–Co^{I} bond distance). Thus, the activation energy keeps decreasing on the Ni–Co clusters by reactive oxygen in the kinetically relevant step, which leads not only enhances the CH_4 turnover but accomplishes the elimination of coke deposition on the metal surface.

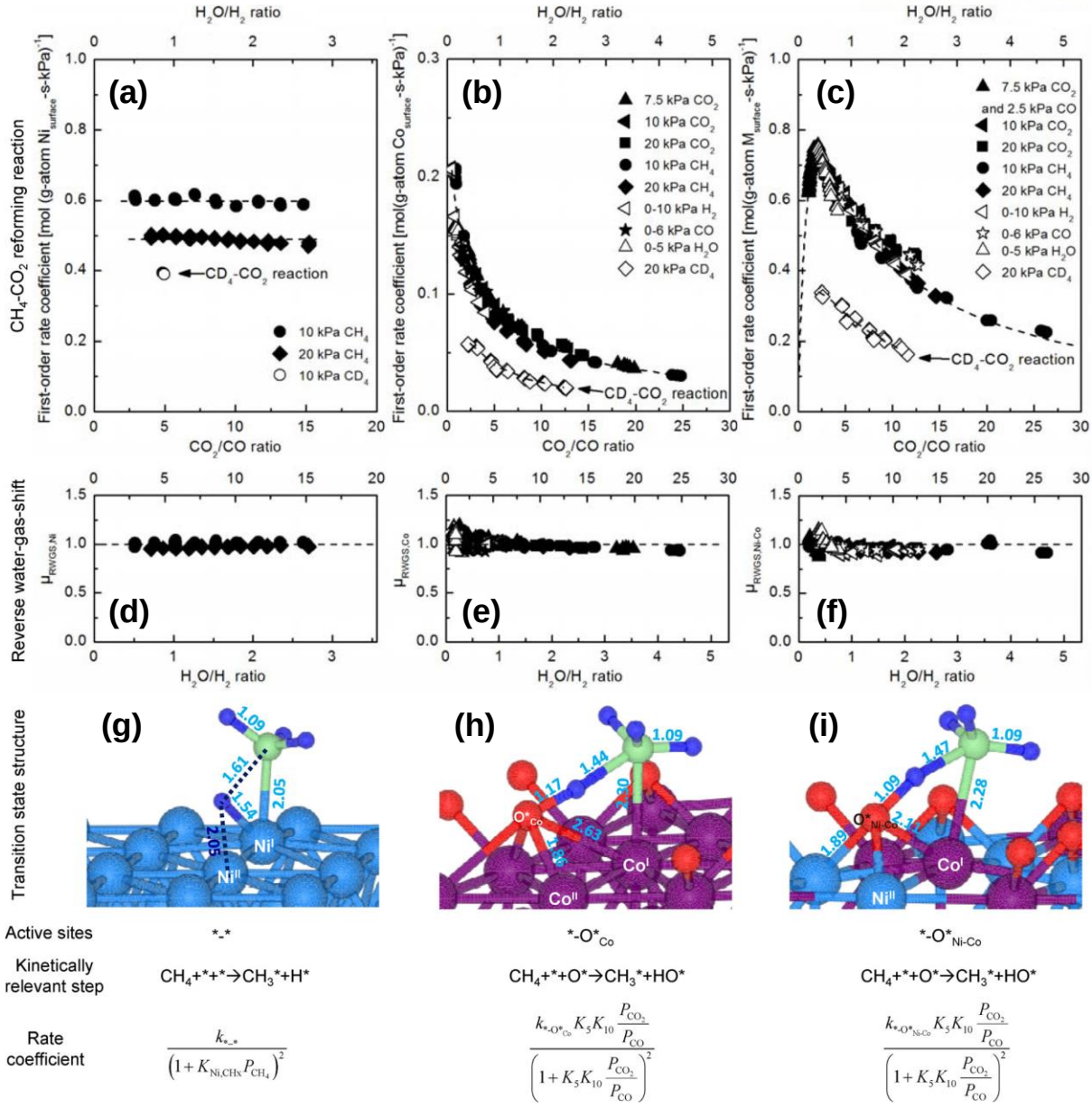

Figure 1.8. (a–c) First-order rate coefficients ($k^{1st}_{M,f}$) of methane forward conversion of CO_2 to CO ratio predicted values from regression of rate data with evaluated rate coefficient. (d–f) The approach-to-equilibrium values ($\mu_{RWGS,\,M}$) for RWGS of H_2O to H_2 ratio as single-valued functions during DRM at 600 °C. (M = Ni, Co, or Ni–Co) structure and bond structure (unit in Å) of the transition state for the initial C–H bond dissociation in CH_4 catalyzed by a *-* site-pair on Ni(111) surface (g), a *-O*$_{Co}$ site-pair on O*/Co(111) surface (h), and a *-O*$_{Ni–Co}$ site-pair on O*/Ni-Co(111) surface (i). The equilibrium constants of K_5 and K_{10} are defined for the steps of CO_2 dissociation to CO and CO desorption respectively. Reprinted with permission from ref. 93. Copyright © 2017 American Chemical Society.

SMSI has been proposed based on the occupancy of oxygen vacancy by metal atoms which could be modified the electronic or chemical properties.[94–97] Rodriguez and Senanayake *et al.* announced the DRM on a Ni-Co/CeO_2 catalysts by monolayer (ML) deposition focused on the C–H bond activation

by the SMSI at temperatures below 500 °C.[98–100] Small amounts (i.e., < 0.3 ML) of metals (Co, Ni, or Cu) are supported on the CeO_2 (111) surface by vapor deposition and analyzed by ambient pressure X-ray photoelectron spectroscopy (AP-XPS).[98] Figure 1.9a represents the C 1s XPS spectra observed on pristine CeO_2(111) and 0.2 ML deposited Co/CeO_2(111) surfaces exposed to the 1 torr of CH_4 at 300 K. The peaks of CH_x and CO_x are found on the Co/CeO_2 surface near 285 eV and 290 eV respectively, which was not found on the pristine CeO_2 surface. The highest peak of the CH_x species is observed when the Co coverage is between 0.15 and 0.2 ML, indicating that the small cluster Co deposition is suitable for methane activation. The oxygen vacancies of metal oxides are important to activate the CO_2 for catalytic activation of DRM through oxygen mobility and adsorption to CH_4. The XPS measurement could investigate the reduction of CeO_2 to compare the concentration of Ce^{3+} species. In Figure 1.9b, the Ce^{3+} concentration follows the order of Co/CeO_2 > Ni/CeO_2 > Cu/CeO_2 at the temperatures between 500 to 700 °C with the CH_4 exposure. The Co/CeO_2 surface is the most easily reduced by methane, and the formation of CH_x is promoted in the process. The catalytic performance was conducted by equimolar CH_4 and CO_2 streams to produce syngas (DRM) and C_2 molecules (ethane and ethylene) according to the Co coverage on the CeO_2(111) surface (see Figure 1.9c). Pristine CeO_2(111) did not show any conversions. The highest syngas production and C_2 molecules were identified at Co coverage of 0.15 and 0.10 ML, respectively. This explains the importance of the SMSI effect of Co clusters on CeO_2 for a critical role in DRM. Nevertheless, the low-temperature reaction accompanied the carbon deposition confirmed by the peak increase at the C 1s spectra. The authors attempted to investigate Co–CeO_2 catalysts to the flow system. Figure 1.9d presents the results of a temperature-programmed surface reaction (TPSR) of DRM of Co–CeO_2 catalyst. In temperature-programmed reduction with methane (CH_4-TPR), the Co_3O_4 is reduced to CoO and finally Co^0 phase at 200 and 280 °C, respectively. In comparison, the DRM-TPSR results confirm CoO and Co metallic phase coexistence up to 500 °C because of the consumption of CO_2 and CH_4. The AP-XPS profiles could confirm it in Figure 1.9e. The pre-reduced Co–CeO_2 catalysts dominate the Co^0 and Ce^{3+} phases in the blue line. The phases of the catalyst coincide with oxidation states Co^0, Co^{2+}, Ce^{3+} and Ce^{4+} during the DRM process. Therefore, the DRM significantly affects the oxygen vacancies of both Co and CeO_2, which could provide oxygen to CH_4, and heals the oxygen vacancies from the cobalt interface.

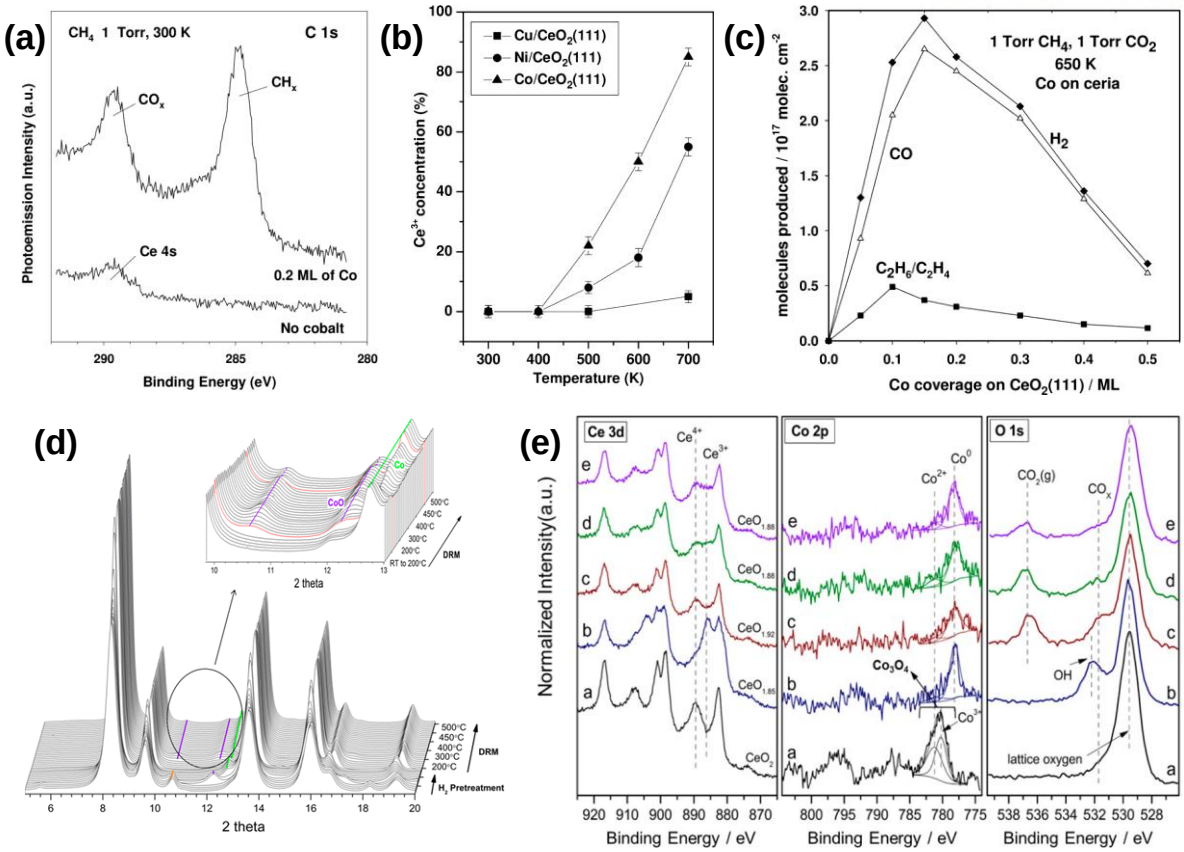

Figure 1.9. (a) C 1s AP-XPS spectra before and after 0.2 ML of Co deposition on CeO_2 (111) film under 1 Torr flow of CH_4 at 300 K for 5 min. (b) Ce^{3+} concentration measured by XPS as a function of temperature in the presence of CH_4 in 0.2 ML of metal (Co, Ni, and Cu) catalysts deposited on CeO_2. (c) Catalytic performance for DRM and ethane production on Co/CeO_2 catalysts as a function of Co coverage. Amounts of CO/H_2 and ethane/ethylene formed after exposing the Co/CeO_2 surfaces to 1 Torr of CO_2 at 650 K for 5 min. (d) *In situ* XRD profiles were collected during the DRM on a 10 wt% Co–CeO_2 catalyst before the reduction in H_2 at 550 °C. (e) AP-XPS spectra in the Ce 3d, Co 2p, and O 1s regions of 10 wt% Co–CeO_2 catalyst. It corresponds to as prepared at 25 °C (black), cooled to 25 °C after 1 h of H_2 pretreatment at 550 °C (blue), and during the DRM with isometric pressures of CO_2 and CH_4 (75 mTorr) at 25 °C (brown), 400 °C (green), and 500 °C (purple). Reprinted with permission from refs. 98 and 99, respectively. Copyright © 2017 Wiley-VCH Verlag GmbH & Co. KGaA, Weinheim. Copyright © 2018 American Chemical Society.

1.3. Thermally Stable Nanocatalysts

1.3.1 Nanocatalysts

Due to their small size and morphologies, nanomaterials are highly dispersible and have diverse properties of interest to the field of catalysis.[101,102] Uniform nanoparticles can be deposited on a support or grown on the catalyst surface through a bottom-up process. The nanocatalyst may have excellent

catalytic performance in both the activity, selectivity, durability and reusability of the intermediates of homogeneous catalysts and heterologous catalysts.[103,104] Much research has been done to understand the roles of catalysts, including the size,[105] shape[106] and composition[107] of metal nanoparticles (Figure 1.10a). In addition, catalytic activity and stability according to the surface morphology[108] and the confinement effect[109,110] in the pore system of the support are also studied. Small nanoparticles have a higher surface-to-volume ratio and increase with surface defects such as terraces, edges and corners. Specific defects can effectively improve catalytic reactions due to the difference in surface energy of various surface defects (Figure 1.10b).[111,112] Uniformly constructed nanostructures have shown excellent performance in photocatalysts and electrocatalysts.[113–118] There have been many advances in single-atom catalysts (SACs) that maximize atomic efficiency by reducing the size of nanoparticles. However, the nanoparticles could not maintain their structure due to the melting point depression and are unsuitable for adaptation to heterogeneous reactions at high temperatures.[119,120] Diverse approaches have been reported to improve thermal stability, including stable intermetallic structures[121], conversion of nanoparticles to SACs[122], anchoring by covalent bonds[123] and support reconstruction[124] based on the metal-support interaction. The following considerations should be considered to design the nanocatalysts (see Figure 1.11).[125] The strategies of compromise nanostructures by the functionalized building blocks and allocation of active sites on support should be considered. In addition, the control of the spacing and dispersion of active sites and tuning accessibility to exposure active site properly discussed.

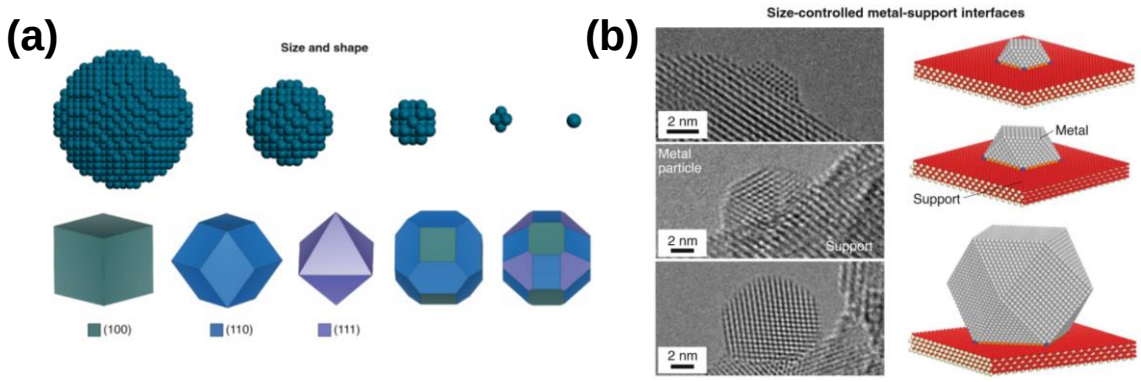

Figure 1.10. (a) Schematic illustration showing the control of particle size or morphology. The exposed facets are color-coded, highlighting the variation with particle shape. (b) Controllable metal-support interface by tuning the size of metal nanoparticles. Reprinted with permission from ref. 119. Copyright © 2021 Springer Nature Limited.

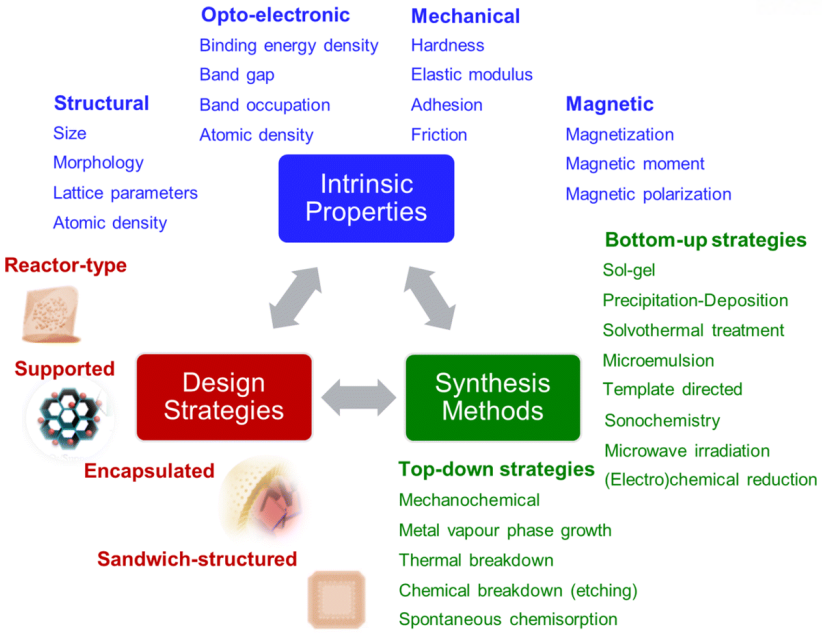

Figure 1.11. Schematic illustration of the interplay between the intrinsic properties, design strategy, and synthesis methods in the rational design of nanocatalysts. Reprinted with permission from ref. 125. Copyright © The Royal Society of Chemistry 2019.

Porous nanomaterials from crystalline zeolite structure, mesoporous materials and metal-organic framework (MOF) have been extensively studied to use in diverse ways—from gas separation, energy storage and ion exchange to heterogeneous catalysis and green chemistry.[126] They are classified into three categories depending on pore diameters: microporous (< 2 nm), mesoporous (2–50 nm) and macroporous (> 50 nm). There are two ways to create pores using a soft or hard template. Mesoporous silicas (*m*-SiO_2) are one of the representative materials synthesized by soft-templating methods such as MCM-41[127] and SBA-15.[128,129] After the invention of the stöber method,[130] the classic method to synthesize silica nanospheres through the polymerization of a silica source, *m*-SiO_2 are mainly synthesized in a mixed environment of alcohol and water by reaction of tetraalkyl silicates.[131,132] The soft templating uses surfactants such as micelles, liquid crystals and vesicles as the structure-directing agents, assembled molecular aggregates. Diverse architectures of *m*-SiO_2 could be synthesized by the shapes of assembled micelles, which are determined by the critical micelle concentration (CMC). When the concentration of micelle exceeds the CMC, hexagonal, cubic, and lamellar micelle structures can self-assemble, becoming soft templates to construct a variety of mesoporous materials such as 0D to 3D types, mesoporous core@shell and asymmetric nanoparticles.[133,134] The block copolymers also have been widely adapted with diverse synthetic strategies including solvent evaporation-induced self-assembly (EISA) (Figure 1.12).[135] The packing of aggregates of copolymer induces as the concentration of the copolymer increases with the slow drying of solvent and uses it as a template to create structures of various ordered morphologies. Mesoporous metal oxides and carbon are firstly introduced in 1998 by Yang *et al.*[136], and in 2004 Dai *et al.*[137] by Pluronic P123 and polystyrene-b-poly(4-vinylpryidine) as

the self-assemblies of block copolymers, respectively. In addition, Yamauchi *et al.*[138] reported platinum framework constructed by connecting nanoparticles using polystyrene-*b*-poly(ethylene oxide) in 2008. Nanoparticles and porous materials synthesized by nanotechnology can thus be used as a more advanced catalyst that exhibits improved activity, selectivity, stability and durability.

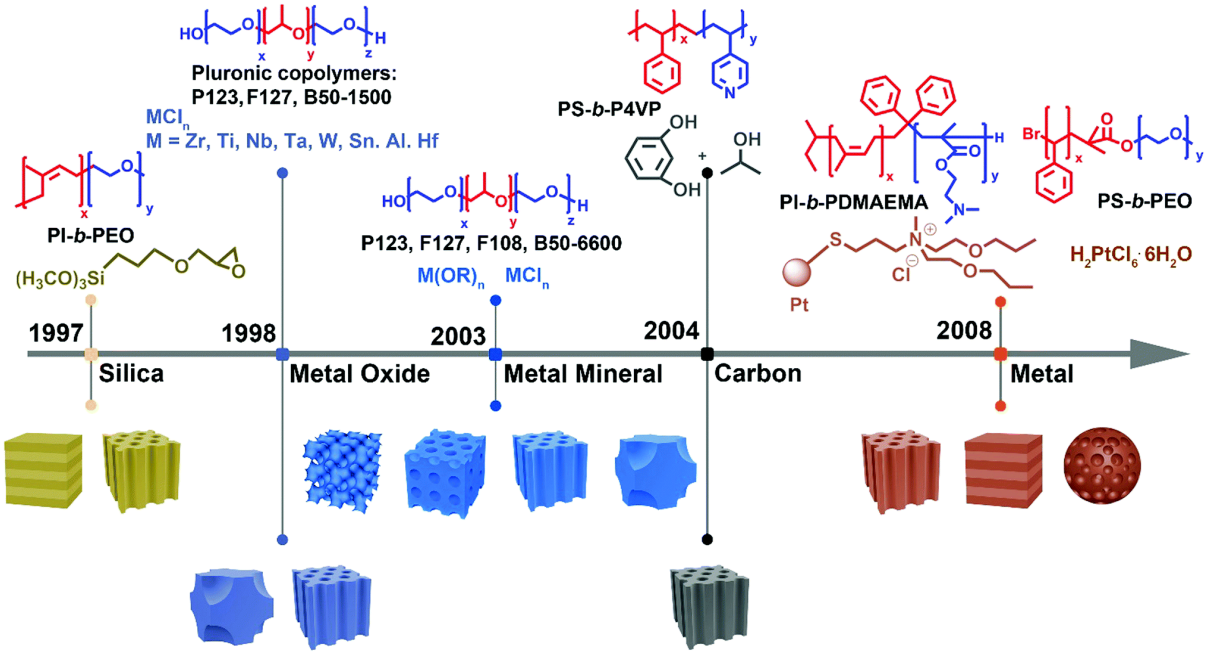

Figure 1.12. Schematic illustration of the single-micelle-directed fabrication of ordered mesoporous materials with multilevel architectures and their typical properties and applications. Reprinted with permission from ref. 135. Copyright © The Royal Society of Chemistry 2020.

1.3.2 Synthetic strategies for stable catalysts

Activity and selectivity are criteria for evaluating catalytic performance, but in methane conversion reactions, stability must be secured to maintain the characteristics of long-term catalyst under high-temperature conditions. The stability and durability of the catalyst are of importance in the actual process and the reactions of methane conversion. Study universal ways to prevent inactivation while maintaining catalytic activity and selectivity to ensure cost savings, stable catalytic reactivity, and increase catalytic replacement cycles.[139] Catalyst deactivation can be caused by different phenomena such as chemical, physical, and thermal mechanisms.[140] Sintering is a major reason for deactivation due to the migration of nanoparticle aggregation by sufficient thermal energy at high temperatures. The detrimental effects of sintering include reduction of active sites in terms of surface area and undercoordinated atoms at edges and corners. In addition, different electronic properties provide different adsorption energy depending on the size of nanoparticles.

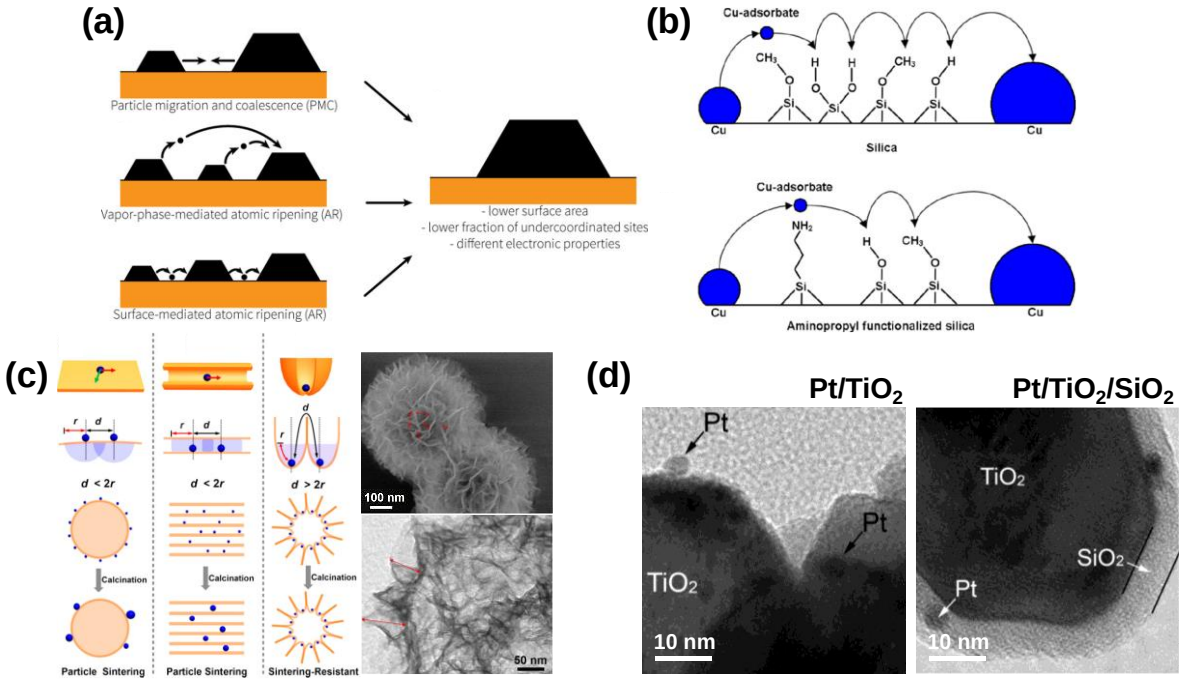

Figure 1.13. (a) The major sintering mechanisms of the active sites of the catalyst. The growth of active sites caused by migration of particle or vapor-phase and surface-mediated ripening are mainly discussed. (b) The proposed strategy of stability enhancement through the aminopropyl functionalization on silica to increasing diffusion distance. (c) The nanoparticle sintering depending on the surface geometries. Unlike flat and cylindrical structures, nanobowl-shaped surfaces effectively mitigate the aggregation which has limited spaces for migration. (d) TEM images of before and after SiO_2 deposition on a Pt/TiO_2 catalyst through wet chemical methods. Reprinted with permission from refs. 141–144, respectively. Copyright © 2017 American Chemical Society. Copyright © 2015 American Chemical Society. Copyright © 2017 Creative Commons License. Copyright © 2013 American Chemical Society.

Figure 1.13a represents the potential sintering mechanisms of the active sites of the catalyst.[141] Particle migration and coalescence (PMC) and atomic ripening (AR) are mainly discussed as the sintering processes. PMC arises from the coordinating motion on the support by a selective motion of small nanoparticles that can move freely at relatively low temperatures due to excessive thermal energy at high temperatures. AR refers to the movement of an atom itself such as a vapor phase, and a support as a medium is not essential for migration. It is a phenomenon known as Ostwald ripening in which small particles dissolve and redeposit onto larger particles. It can effectively inhibit sintering by diverse strategies to interfere with the migration of nanoparticles. In Figure 1.13b, de Jong *et al.*, reported the support functionalization of Cu/SiO_2 catalysts retard the Ostwald ripening of metal sites in methanol synthesis.[142] The aminopropyl functionalized support increases the travel distance of Cu nanoparticles (NPs), leading to a higher transition state for AR and thereby mitigating the sintering. Abe *et al.* published the sinter-resistant nanoparticles depending on the structural differences of the support (see Figure 1.13c).[143] The nanobowl-shaped wide-mouthed compartments prepared by self-assembled silica

with a hierarchical structure enhance Pt nanoparticles' sintering. They classified the support structures according to the relationship between distance and radius. The sintering-resistant NPs without protection address diverse combinations of oxide supports. The deposition of oxides as a sintering barrier has been extensively studied to protect active sites while maintaining catalytic activity. Xia *et al.* reported the sinter-resistant to affect up to 700 °C through SiO_2 deposition on Pt/TiO_2 catalysts (Figure 1.13d).[144] The catalytic performance has been investigated depending on the thicknesses of SiO_2 of 1.5, 2.3, 2.8, 4.1, and 5.6 nm. The high activity could be observed up to 2.8 nm of the reduction of p-nitrophenol, but thicker catalysts fully enclosed the catalyst surface loses the activity despite higher sinter-resistant ability even at 750 °C.

Encapsulated structures of nanomaterials are classified depending on the morphology which is core@shell, yolk@shell/hollow structures and sandwiched multi-core-shell structures, as shown in Figure 1.14a. Unique and diverse nanostructures are often named more complex than conventional catalysts. For core@shell structures with core or multi-core components can consist of metal, carbon, metal oxide, etc. Most core@shell nanostructures used as catalysts must consist of porous shells to diffuse to the active site to avoid loss of reactivity. Advantages of core@shell architecture include high distribution and stability due to space constraints of the active sites by the shell and SMSIs that occur at interfaces between cores and shells. In the case of the yolk@shell or yolk@hollow structures, nanoparticles are embedded in the mesoporous oxide shells as a support, and a hollow cavity may be more advantageous in terms of diffusion of reactants. The cavity is mainly produced by the removal of soft[145] or hard[146,147] templates such as organic polymers or silica, which are mainly calcined or etched by strong acids, respectively. Sandwiched multi-core-shell structures have single or multiple active core sites embedded between the two layers composed of the same or different materials.[148,149] The system is structurally designed to maintain catalytic activity and improve stability, often through the synergies of each component. The properties and advantages of core@shell structures in thermocatalysis are illustrated in Figure 1.14b. Protective shells encapsulate the active cores against the sintering with their high thermal stability and porosity.[150,151] Selective reactions can be induced by the structure and size of pores in finely constructed microporous shells, which can be expected to serve as molecular sieves that can selectively filter the molecules.[152,153] Active interfaces can also be created between two substances, which also improves the stability of catalysts. Depending on the structure combinations, different reactions can also occur continuously in each part, which is called tandem or multifunctional catalyst.

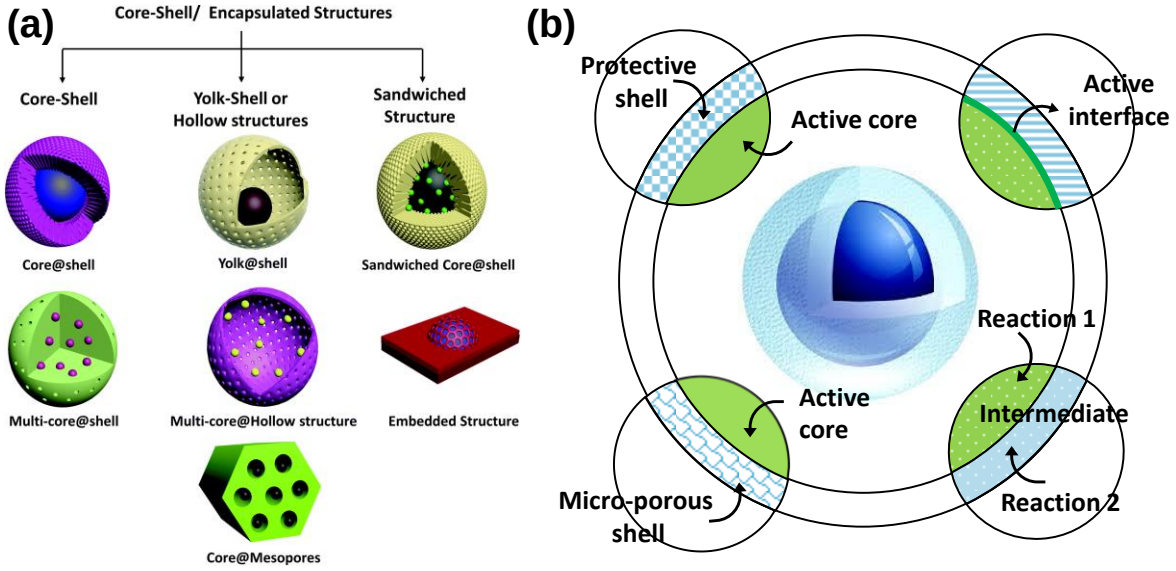

Figure 1.14. (a) Schematic categorization of encapsulated structures depending on the morphology. (b) Properties and advantages of core@shell structures in thermocatalysis. Reprinted with permission from ref. 149. Copyright © The Royal Society of Chemistry 2020.

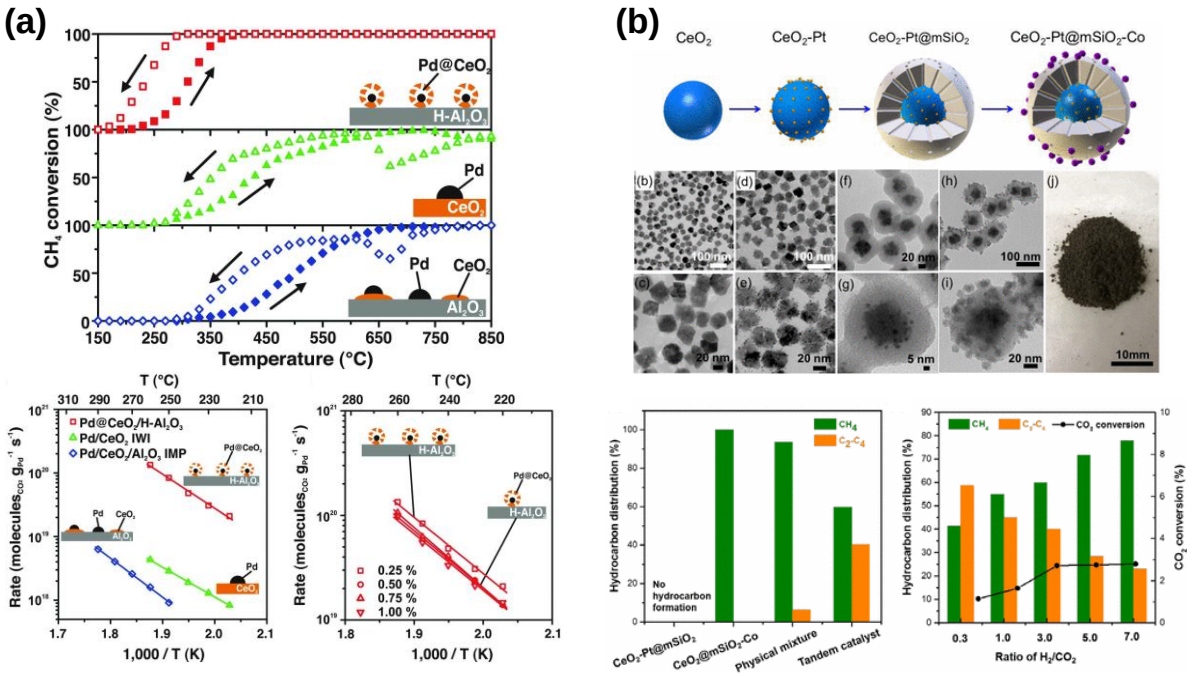

Figure 1.15. (a) The light-off curves, kinetic rates of methane combustion according to the temperature. Pd@CeO_2 has exceptionally high activity with full combustion below 400 °C and the structural advantage is expected through the calculation of normalized kinetic rates, which are independent by metal loadings. (b) Schematic illustration of synthetic processes and TEM images of CeO_2–Pt@*m*SiO_2–Co nanostructure to the CO_2 hydrogenation tandem catalysis. Reprinted with permission from refs. 154 and 155, respectively. Copyright © 2012 The American Association for the Advancement of Science. Copyright © 2017 American Chemical Society.

Core@shell catalysts are widely applied to thermocatalysis due to the confinement effects of active sites with high dispersion and stability as a sintering barrier. Cargnello *et al.* reported the Pd@CeO_2 subunit core@shell nanostructure on the hydrophobically functionalized Al_2O_3 for the methane combustion reaction.[154] Compared to the Pd/CeO_2 and Pd/CeO_2/Al_2O_3 catalysts, the Pd@CeO_2/Al_2O_3 catalysts showed much higher catalytic activity, recording complete combustion below 400 °C. Also, the catalyst structure could be maintained against sintering up to 800 °C (Figure 1.15a). Calculation of the kinetic rate reveals the high intrinsic activity of the Pd@CeO_2 catalyst, which is 40-fold and 200-fold higher than Pd/CeO_2 and Pd/CeO_2/Al_2O_3, respectively. The activation energies are compared according to Pd loading of 0.25 to 1.00 wt%, which showed similar reaction rates when normalized by the amount of metal, indicating that the superior activity induced from the core@shell structure of the catalyst. Yang *et al.* reported the CeO_2–Pt@*m*SiO_2–Co nanostructure as tandem catalysis for CO_2 hydrogenation to C_2–C_4 hydrocarbons.[155] Nanocatalysts are prepared in a total of four stages: synthesis of uniform size CeO_2 nanoparticles, deposition of as-prepared 3 nm-sized Pt nanoparticles on CeO_2, overcoating of *m*-SiO_2 with the soft template of cetyltrimethylammonium bromide, and deposition of uniform Co nanoparticle (Figure 1.15b). CeO_2–Pt@*m*SiO_2 nanoparticles without Co particles on the surface showed no activity of the reaction. Co particles are the active site of the methanation reaction, suggesting that the intermediate product CO generated C_{2+} hydrocarbons on the CeO_2-Pt surface inside the mesopores. The hierarchical structure suggested that the C_{2+} selectivity by the tandem reaction was significantly higher than physically mixed catalysts and that a low H_2/CO_2 ratio was important, which could lead to a high CO/CO_2 ratio to maximize C_{2+} selectivity.

Diverse strategies for encapsulation of catalysts to resist sintering are widely studied to improve catalyst stability.[25,156] Deposition methods, SMSI, and Stöber sol-gel methods have been extensively studied to construct shells on the catalyst as a barrier.[157–159] Chemical vapor deposition (CVD) is a vacuum deposition technique to produce thin films on the substrate by chemical reaction or decomposition of volatile precursors in the reaction chamber. Although the effectiveness of overlayer coating, the thick and nonuniform layers cannot exert effects of stability enhancement while high catalytic activity. The ALD is an advanced technique of CVD with the ability of conformal coating due to its self-limiting system.[160] Precursors to deposit each atom, highly reactive while inert, is injected into the chamber to react on the substrate by alternating pulses. This allows thin film deposition of various types of materials including metals and metal oxides.

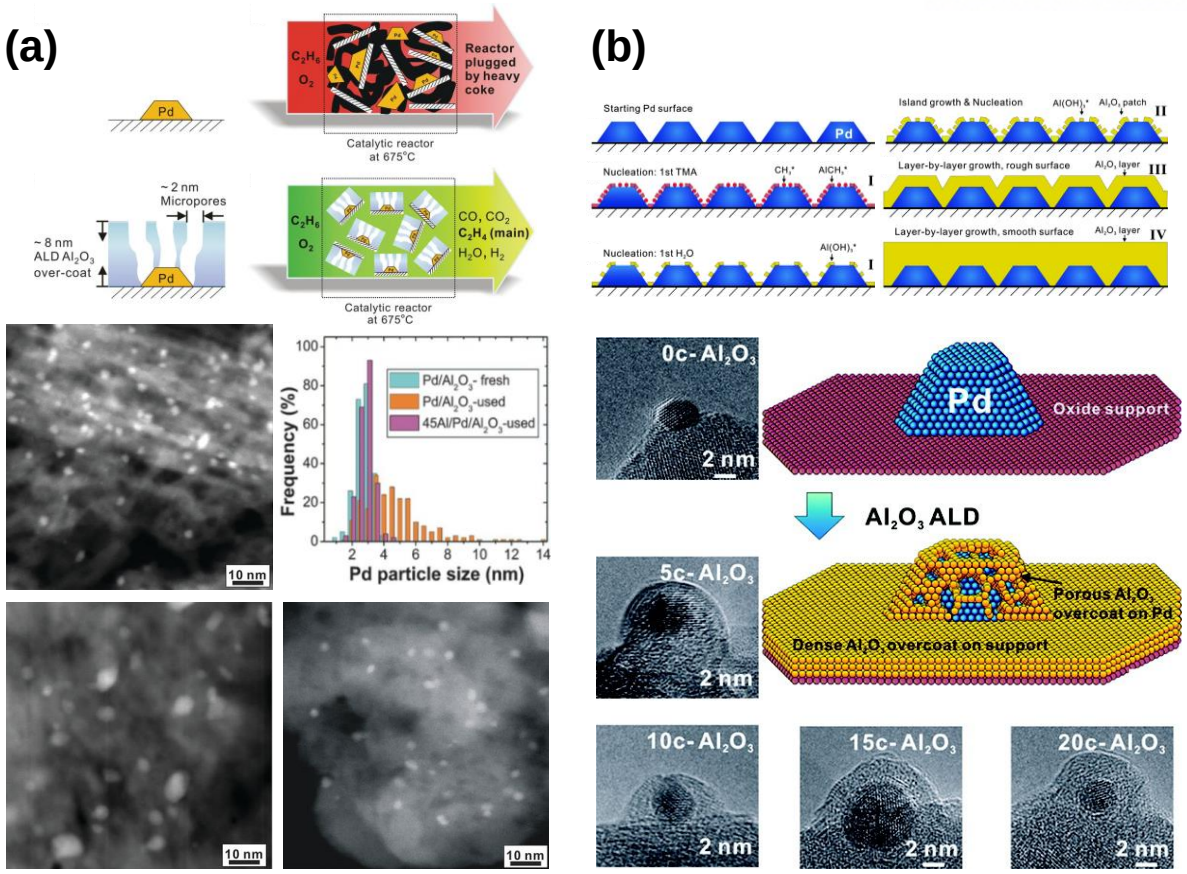

Figure 1.16. (a) The schematic illustration of Pd/Al_2O_3 and $45Al/Pd/Al_2O_3$ depending on the Al_2O_3 deposition by ALD, and fresh/spent images of the catalysts to compare the degree of Pd nanoparticle growth. The microporous Al_2O_3 shell on the surface endow with the durability of catalyst and enhances the ethane conversion without Pd nanoparticle sintering. (b) The ALD process of Al_2O_3 formation on Pd nanoparticles depending on the number of ALD cycles. Reprinted with permission from refs. 161 and 162, respectively. Copyright © 2012 The American Association for the Advancement of Science. Copyright © 2012 American Chemical Society.

Stair *et al.* published the coke- and sinter-resistant Al_2O_3 overcoated by ALD on Pd/Al_2O_3 catalyst for oxidative dehydrogenation of ethane (ODHE) (Figure 1.16a).[161] The 8 nm thickness of Al_2O_3 shells is overcoated by 45 cycles of ALD processes denoted as 45Al/Pd/Al2O3, and the channels of micropores that went inside the active site are confirmed BET measurements and CO chemisorption. The activity of the Pd/Al_2O_3 catalyst was lost in a short time due to sintering and accompanied severe coking. Unlike Pd/Al_2O_3, $45Al/Pd/Al_2O_3$ showed the ethane conversion increased more than 10 times and the sintering and coking were significantly reduced according to the durability of the time. The investigation of the Pd particle size of the spent catalyst was not increased by agglomeration. Elam *et al.* investigated the porous structures of Al_2O_3 depending on the number of ALD cycles on Pd nanoparticles (Figure 1.16b).[162] Al_2O_3 generated in the initial ALD cycle was found to form incomplete thin films, which was interpreted as a trend of increasing mass per cycle by *in situ* quartz crystal

microbalance (QCM) measurements. Amorphous Al_2O_3 is formed preferentially on edges, corners, etc., where the surface energy is relatively high, and the gradually widening area eventually forms the official form of Al_2O_3 on the surface. Micropores can be regenerated at high temperatures due to incomplete metal oxides produced by ALD.

1.4. Outline of This Dissertation

This dissertation includes the rational synthetic strategies of nanotechnology-based catalysts for the chemical conversions of methane. Because methane is a tiny molecule with tetrahedral symmetry, it is not easy to convert. The chemical conversion of methane occurs under high-temperature conditions in heterogeneous catalysis. There is a problem of changing the structure of the catalyst by causing phenomena such as sintering, leaching, and coke deposition by high thermal energy. It is essential to prepare a catalyst with high thermal stability because the activity is reduced or deactivated with structural change. First of all, a study was conducted on the partial oxidation of methane to formaldehyde, one of the direct conversion reactions. Formaldehyde is a high value-added basic raw material produced through oxidation or dehydrogenation of methanol, and the study of direct oxidation from methane has high industrial value. Catalysts reported to be suitable for carrying out the reaction of methane with formaldehyde include vanadium-based and molybdenum-based catalysts. A highly reactive intermediate is basically produced in the reaction pathway in an oxidation reaction. The substance containing oxygen is highly reactive and is readily oxidized to produce carbon dioxide. In order to minimize this, it is advantageous to increase the selectivity to carry out the reaction at a low temperature. It has been reported that vanadium-based catalysts exhibit significant methane conversions between 1–10% under relatively low temperature conditions (600 °C) than molybdenum-based catalysts. Therefore, based on this, the above reaction was performed using a vanadium-based catalyst.

Chapter 2 introduces the highly dispersed VO_x/*m*-SiO_2 catalysts depending on the amount of content, synthesis method, and support type to elucidate the active sites for partial oxidation of methane to formaldehyde. There are three surface vanadium species in vanadium-based supported catalysts: isolated, polymeric, and bulk structures, respectively. The dispersion of active site depends on the vanadium content and the impregnation method. The V=O active center of the isolated species was reported as the predominant active site in the reaction of methane to formaldehyde. By preparing a highly dispersed catalyst, improving the activity by increasing the active site is possible. It can also form SMSI with support that enhance the stability of the active site. Once this soft template is stabilized, silica grows in the region opposite to the template by the sol-gel process of tetraethyl orthosilicate. The resulting composite is calcined to produce mesoporous silica. Two representative types of mesoporous silica, MCF-17 and SBA-15, were prepared and used as supports. Also, differences in impregnation methods can have a significant impact on dispersion. In wet impregnation, the catalyst is prepared by

dissolving the precursor in a solvent, mixing it with a support, drying and calcination. On the other hand, dry impregnation is prepared by mixing the precursor and support in a solid state, pyrolysis them under nitrogen conditions, and then calcination. Here, various VO_x/*m*-SiO_2 catalysts were prepared with 1, 3 and 5% vanadium loadings on two types of mesoporous silica using two impregnation methods to compare their activity.

Chapter 3 presents the exceptionally high activity and stability of SiO_2@V_2O_5@Al_2O_3 nanocatalysts for partial oxidation of methane to formaldehyde. Studies have been conducted to improve the activity by preparing nanostructured catalysts with previously studied vanadium-based silica combinations. The nanospheres were fabricated by a sol-gel process called the Stöber method, and the excess vanadium precursor was supported via a hydrothermal process to prepare a core@shell SiO_2@V_2O_5 catalyst. As a result of performing the reaction methane to formaldehyde under the same conditions as in Chapter 2, the initial activity was excellent at 20%, but there was a problem of deactivation within 1 h. Another strategy for improving catalyst stability is the encapsulation method. Various beneficial effects can be expected when a material with high thermal stability is covered on the catalyst surface and used as a heterogeneous catalyst. It can prevent sintering, coking and leaching of the active core and create a new active interface between them as a protective shell. In addition, selective reactions are possible depending on the pore size of the shell. It can also be developed for tandem catalysis, where the catalyst is performed continuously in the core and shell. Encapsulation is mainly reported to cover the core fabricated by the colloidal method with mesoporous silica. This method has limitations in manufacturing shells of various materials, and it is difficult to control the thickness of the shell. It was also burdensome to redissolve the SiO_2@V_2O_5 catalyst in the solvent. Here, we developed a technique for depositing metal oxide shells such as Al_2O_3 and TiO_2 to the desired thickness through an ALD process. ALD has been a good surface technique to create atomic-scale thin films by controlling the thickness according to the number of depositions, but it has been mainly used for 2D plate materials. Developed in the form of a rotating porous cylinder for application in 3D materials, it can deposit Al_2O_3 with high thermal stability on all surfaces of nanoparticles with high reproducibility. This development is a technology that can be applied to most materials, including a variety of catalysts used in the past, making it highly industrially scalable. The SiO_2@V_2O_5@Al_2O_3 nanocatalysts thus prepared showed high thermal stability, and no further sintering occurred. In addition, as a result of comparing the reactivity by depositing Al_2O_3 with different thicknesses on the nanocatalyst, the methane conversion rate at a specific thickness was 22.2%, setting the highest record at 600 °C. This is a SiO_2@V_2O_5@Al_2O_3-(*50*) catalyst, in which 10 nm thick Al_2O_3 was deposited through *50* ALD cycles. The reaction remained active for 35 h, and a high formaldehyde selectivity of 57.8% was also recorded.

Chapter 4 presents the coke-resistant Ni/CeO_2/Al_2O_3 nanocatalysts for DRM suppressed by Al_2O_3 oxide through the ALD process. To date, the only commercial conversion of methane is SRM, which reacts with water. In this way, synthesis gas, an essential industrial platform material, is obtained

and used to produce various chemicals. It is also making the biggest contribution to hydrogen energy production, which is in the spotlight as an energy transition. DRM has high research value in terms of energy and environment because it produces syngas by reacting carbon dioxide and methane. However, due to the common presence of carbon atoms in both reactants, side reactions in which carbon is deposited on the catalyst surface easily occur. Although it is reasonable to use a Ni-based catalyst to activate the methane, carbon is prone to deposition due to the direct bonding mechanism between the Ni metal and the carbon atoms in the methane. When the O atom in carbon dioxide participates in the reaction, it helps to prevent precipitation. Hydrophilic metal oxide such as CeO_2 with high oxygen vacancies as support can prevent deposition and increase activity. Therefore, Ni/CeO_2 nanocatalysts were prepared by mixing the prepared Ni and CeO_2 rod nanoparticles. Although high activity was shown in the DRM, there was a problem in that coke deposition occurred. To solve this problem, an Al_2O_3 shell was introduced on the nanocatalyst surface in the same way as in Chapter 3. As a result of DRM of Ni/CeO_2/Al2O_3 catalysts deposited via ALD process of 1, 2, and 10 cycles, no carbon deposition occurred in all catalysts. Therefore, by depositing the thinnest atomic-level oxide on the catalyst surface, a catalyst with high stability can be prepared without changing the basic properties of the catalyst itself.

1.5. References

1. S. Chu and A. Majumdar, Opportunities and challenges for a sustainable energy future. *Nature* **2012**, *488*, 294.
2. Y. Liu, D. Deng and X. Bao, Catalysis for Selected C_1 Chemistry. *Chem* **2020**, *6*, 2497.
3. M. Han, D. N. Assanis and S. V. Bohac, Sources of hydrocarbon emissions from low-temperature premixed compression ignition combustion from a common rail direct injection diesel engine. *Combust. Sci. Technol.* **2009**, *181*, 496.
4. W. Zhou, K. Cheng, J. Kang, C. Zhou, V. Subramanian, Q. Zhang and Y. Wang, New horizon in C_1 chemistry: breaking the selectivity limitation in transformation of syngas and hydrogenation of CO_2 into hydrocarbon chemicals and fuels. *Chem. Soc. Rev.* **2019**, *48*, 3193.
5. I. Yarulina, A. D. Chowdhury, F. Meirer, B. M. Weckhuysen and J. Gascon, Recent trends and fundamental insights in the methanol-to-hydrocarbons process. *Nat. Catal.* **2018**, *1*, 398.
6. F. Valentini, V. Kozell, C. Petrucci, A. Marrocchi, Y. Gu, D. Gelman and L. Vaccaro, Formic acid, a biomass-derived source of energy and hydrogen for biomass upgrading. *Energy Environ. Sci.* **2019**, *12*, 2646.
7. J. Bao, G. Yang, Y. Yoneyama and N. Tsubaki, Significant advances in C_1 catalysis: highly efficient catalysts and catalytic reactions. *ACS Catal.* **2019**, *9*, 3026.
8. P. Summa, B. Samojeden and M. Motak, Dry and steam reforming of methane. Comparison and analysis of recently investigated catalytic materials. A short review. *Pol. J. Chem. Technol.* **2019**, *21*, 31.
9. K. Narsimhan, K. Iyoki, K. Dinh and Y. Román-Leshkov, Catalytic oxidation of methane into methanol over copper-exchanged zeolites with oxygen at low temperature. *ACS Cent. Sci.* **2016**, *2*, 424.

10. K. T. Dinh, M. M. Sullivan, K. Narsimhan, P. Serna, R. J. Meyer, M. Dincă and Y. Román-Leshkov, Continuous partial oxidation of methane to methanol catalyzed by diffusion-paired copper dimers in copper-exchanged zeolites. *J. Am. Chem. Soc.* **2019**, *141*, 11641.

11. J. Tian, J. Tan, Z. Zhang, P. Han, M. Yin, S. Wan, J. Lin, S. Wang and Y. Wang, Direct conversion of methane to formaldehyde and CO on B_2O_3 catalysts. *Nat. comm.* **2020**, *11*, 5693.

12. E. Yang, J. G. Lee, D. H. Kim, Y. S. Jung, J. H. Kwak, E. D. Park and K. An, SiO_2@V_2O_5@Al_2O_3 core–shell catalysts with high activity and stability for methane oxidation to formaldehyde. *J. Catal.* **2018**, *368*, 134.

13. P. Schwach, N. Hamilton, M. Eichelbaum, L. Thum, T. Lunkenbein, R. Schlögl and A. Trunschke, Structure sensitivity of the oxidative activation of methane over MgO model catalysts: II. Nature of active sites and reaction mechanism. *J. Catal.* **2015**, *329*, 574.

14. V. Fleischer, R. Steuer, S. Parishan and R. Schomäcker, Investigation of the surface reaction network of the oxidative coupling of methane over Na_2WO_4/Mn/SiO_2 catalyst by temperature programmed and dynamic experiments. *J. Catal.* **2016**, *341*, 91.

15. N. Kosinov, F. J. Coumans, E. A. Uslamin, A. S. Wijpkema, B. Mezari and E. J. Hensen, Methane dehydroaromatization by Mo/HZSM-5: mono-or bifunctional catalysis? *ACS Catal.* **2017**, *7*, 520.

16. S. H. Morejudo, R. Zanón, S. Escolástico, I. Yuste-Tirados, H. Malerød-Fjeld, P. K. Vestre, W. G. Coors, A. Martínez, T. Norby and J. M. Serra, Direct conversion of methane to aromatics in a catalytic co-ionic membrane reactor. *Science* **2016**, *353*, 563.

17. Y. Tang, Y. Li, V. Fung, D.-e. Jiang, W. Huang, S. Zhang, Y. Iwasawa, T. Sakata, L. Nguyen and X. Zhang, Single rhodium atoms anchored in micropores for efficient transformation of methane under mild conditions. *Nat. comm.* **2018**, *9*, 1231.

18. J. Shan, M. Li, L. F. Allard, S. Lee and M. Flytzani-Stephanopoulos, Mild oxidation of methane to methanol or acetic acid on supported isolated rhodium catalysts. *Nature* **2017**, *551*, 605.

19. P. Forzatti and L. Lietti, Catalyst deactivation. *Catal. Today* **1999**, *52*, 165.

20. A. Safaei, M. A. Shandiz, S. Sanjabi and Z. Barber, Modeling the melting temperature of nanoparticles by an analytical approach. *J. Phys. Chem. C* **2008**, *112*, 99.

21. T. W. van Deelen, C. H. Mejía and K. P. de Jong, Control of metal-support interactions in heterogeneous catalysts to enhance activity and selectivity. *Nat. Catal.* **2019**, *2*, 955.

22. S. Masuda, Y. Shimoji, K. Mori, Y. Kuwahara and H. Yamashita, Interconversion of formate/bicarbonate for hydrogen storage/release: Improved activity following sacrificial surface modification of a Ag@ Pd/TiO_2 catalyst with a TiO_x shell. *ACS Appl. Energy Mater.* **2020**, *3*, 5819.

23. A. E. Settle, N. S. Cleveland, C. A. Farberow, D. R. Conklin, X. Huo, A. A. Dameron, R. W. Tracy, R. Sarkar, E. J. Kautz and A. Devaraj, Enhanced catalyst durability for bio-based adipic acid production by atomic layer deposition. *Joule* **2019**, *3*, 2219.

24. E. Sarnello, Z. Lu, S. Seifert, R. E. Winans and T. Li, Design and characterization of ALD-based overcoats for supported metal nanoparticle catalysts. *ACS Catal.* **2021**, *11*, 2605.

25. H. O. Otor, J. B. Steiner, C. García-Sancho and A. C. Alba-Rubio, Encapsulation methods for control of catalyst deactivation: A review. *ACS Catal.* **2020**, *10*, 7630.

26. X. Meng, X. Cui, N. P. Rajan, L. Yu, D. Deng and X. Bao, Direct methane conversion under mild condition by thermo-, electro-, or photocatalysis. *Chem* **2019**, *5*, 2296.

27. A. A. Latimer, A. R. Kulkarni, H. Aljama, J. H. Montoya, J. S. Yoo, C. Tsai, F. Abild-Pedersen,

F. Studt and J. K. Nørskov, Understanding trends in C–H bond activation in heterogeneous catalysis. *Nat. Mater.* **2017**, *16*, 225.

28. A. Hu, J.-J. Guo, H. Pan and Z. Zuo, Selective functionalization of methane, ethane, and higher alkanes by cerium photocatalysis. *Science* **2018**, *361*, 668.

29. Z. Liang, T. Li, M. Kim, A. Asthagiri and J. F. Weaver, Low-temperature activation of methane on the IrO_2(110) surface. *Science* **2017**, *356*, 299.

30. Y.-Q. Su, J.-X. Liu, I. A. Filot, L. Zhang and E. J. Hensen, Highly active and stable CH_4 oxidation by substitution of Ce^{4+} by two Pd^{2+} ions in CeO_2(111). *ACS Catal.* **2018**, *8*, 6552.

31. T. R. Cundari, Calculation of a methane carbon-hydrogen oxidative addition trajectory: comparison to experiment and methane activation by high-valent complexes. *J. Am. Chem. Soc.* **1994**, *116*, 340.

32. A. E. Shilov and G. B. Shul'pin, Activation of C−H bonds by metal complexes. *Chem. Rev.* **1997**, *97*, 2879.

33. M. Sun, J. Zhang, P. Putaj, V. Caps, F. d. r. Lefebvre, J. Pelletier and J.-M. Basset, Catalytic oxidation of light alkanes (C_1–C_4) by heteropoly compounds. *Chem. Rev.* **2014**, *114*, 981.

34. R. Burch, D. Crittle and M. Hayes, C–H bond activation in hydrocarbon oxidation on heterogeneous catalysts. *Catal. Today* **1999**, *47*, 229.

35. J. A. Labinger, Selective alkane oxidation: hot and cold approaches to a hot problem. *J. Mol. Catal. A Chem.* **2004**, *220*, 27.

36. C. Jones, D. Taube, V. R. Ziatdinov, R. A. Periana, R. J. Nielsen, J. Oxgaard and W. A. Goddard III, Selective oxidation of methane to methanol catalyzed, with C–H activation, by homogeneous, cationic gold. *Angew. Chem.* **2004**, *116*, 4726.

37. R. L. Lieberman and A. C. Rosenzweig, Crystal structure of a membrane-bound metalloenzyme that catalyses the biological oxidation of methane. *Nature* **2005**, *434*, 177.

38. R. Balasubramanian, S. M. Smith, S. Rawat, L. A. Yatsunyk, T. L. Stemmler and A. C. Rosenzweig, Oxidation of methane by a biological dicopper centre. *Nature* **2010**, *465*, 115.

39. M.-H. Baik, M. Newcomb, R. A. Friesner and S. J. Lippard, Mechanistic studies on the hydroxylation of methane by methane monooxygenase. *Chem. Rev.* **2003**, *103*, 2385.

40. C. Hammond, M. M. Forde, M. H. Ab Rahim, A. Thetford, Q. He, R. L. Jenkins, N. Dimitratos, J. A. Lopez-Sanchez, N. F. Dummer and D. M. Murphy, Direct catalytic conversion of methane to methanol in an aqueous medium by using copper-promoted Fe-ZSM-5. *Angew. Chem.* **2012**, *124*, 5219.

41. V. L. Sushkevich, D. Palagin, M. Ranocchiari and J. A. van Bokhoven, Selective anaerobic oxidation of methane enables direct synthesis of methanol. *Science* **2017**, *356*, 523.

42. V. L. Sushkevich and J. A. van Bokhoven, Methane-to-Methanol: Activity descriptors in copper-exchanged zeolites for the rational design of materials. *ACS Catal.* **2019**, *9*, 6293.

43. P. J. Smeets, M. H. Groothaert and R. A. Schoonheydt, Cu based zeolites: A UV–vis study of the active site in the selective methane oxidation at low temperatures. *Catal. Today* **2005**, *110*, 303.

44. A. W. Franz, H. Kronemayer, D. Pfeiffer, R. D. Pilz, G. Reuss, W. Disteldorf, A. O. Gamer and A. Hilt, Formaldehyde. *Ullmann's Encyclopedia of Industrial Chemistry* **2016**, 1.

45. C. Brookes, P. Wells, G. Cibin, N. Dimitratos, W. Jones, D. J. Morgan and M. Bowker, Molybdenum oxide on Fe_2O_3 core–shell catalysts: probing the nature of the structural motifs

responsible for methanol oxidation catalysis. *ACS Catal.* **2014**, *4*, 243.

46. G. J. Millar and M. Collins, Industrial production of formaldehyde using polycrystalline silver catalyst. *Ind. Eng. Chem. Res.* **2017**, *56*, 9247.

47. A. De Vekki and S. Marakaev, Catalytic partial oxidation of methane to formaldehyde. *Russ. J. Appl. Chem.* **2009**, *82*, 521.

48. F. Arena and A. Parmaliana, Scientific basis for process and catalyst design in the selective oxidation of methane to formaldehyde. *Acc. Chem. Res.* **2003**, *36*, 867.

49. L. Nguyen, S. Loridant, H. Launay, A. Pigamo, J. Dubois and J. Millet, Study of new catalysts based on vanadium oxide supported on mesoporous silica for the partial oxidation of methane to formaldehyde: Catalytic properties and reaction mechanism. *J. Catal.* **2006**, *237*, 38.

50. M. Smith and U. Ozkan, The partial oxidation of methane to formaldehyde: role of different crystal planes of MoO_3. *J. Catal.* **1993**, *141*, 124.

51. V. Arutyunov and O. Krylov, *Oxidative conversion of methane.* Nauka, Moscow, **1998**.

52. M. Rellán-Piñeiro and N. López, The active molybdenum oxide phase in the methanol oxidation to formaldehyde (Formox process): A DFT study. *ChemSusChem* **2015**, *8*, 2231.

53. M. Belgued, P. Pareja, A. Amariglio and H. Amariglio, Conversion of methane into higher hydrocarbons on platinum. *Nature* **1991**, *352*, 789.

54. Y. Xiao and A. Varma, Highly selective nonoxidative coupling of methane over Pt-Bi bimetallic catalysts. *ACS Catal.* **2018**, *8*, 2735.

55. L. Wang, L. Tao, M. Xie, G. Xu, J. Huang and Y. Xu, Dehydrogenation and aromatization of methane under non-oxidizing conditions. *Catal. Lett.* **1993**, *21*, 35.

56. S. Liu, L. Wang, R. Ohnishi and M. Ichikawa, Bifunctional catalysis of Mo/HZSM-5 in the dehydroaromatization of methane to benzene and naphthalene XAFS/TG/DTA/MASS/FTIR characterization and supporting effects. *J. Catal.* **1999**, *181*, 175.

57. H. Zheng, D. Ma, X. Bao, J. Z. Hu, J. H. Kwak, Y. Wang and C. H. Peden, Direct observation of the active center for methane dehydroaromatization using an ultrahigh field ^{95}Mo-NMR spectroscopy. *J. Am. Chem. Soc.* **2008**, *130*, 3722.

58. G. Li, I. Vollmer, C. Liu, J. Gascon and E. A. Pidko, Structure and reactivity of the Mo/ZSM-5 dehydroaromatization catalyst: an operando computational study. *ACS Catal.* **2019**, *9*, 8731.

59. N. Kosinov, E. A. Uslamin, L. Meng, A. Parastaev, Y. Liu and E. J. Hensen, Reversible nature of coke formation on Mo/ZSM-5 methane dehydroaromatization catalysts. *Angew. Chem. Int. Ed.* **2019**, *58*, 7068.

60. A. Kumar, K. Song, L. Liu, Y. Han and A. Bhan, Absorptive hydrogen scavenging for enhanced aromatics yield during non-oxidative methane dehydroaromatization on Mo/H-ZSM-5 catalysts. *Angew. Chem. Int. Ed.* **2018**, *57*, 15577.

61. G. Keller and M. Bhasin, Synthesis of ethylene via oxidative coupling of methane: I. Determination of active catalysts. *J. Catal.* **1982**, *73*, 9.

62. Y. Gao, L. Neal, D. Ding, W. Wu, C. Baroi, A. M. Gaffney and F. Li, Recent advances in intensified ethylene production—a review. *ACS Catal.* **2019**, *9*, 8592.

63. B. L. Farrell and S. Linic, Oxidative coupling of methane over mixed oxide catalysts designed for solid oxide membrane reactors. *Catal. Sci. Technol.* **2016**, *6*, 4370.

64. P. Schwach, M. G. Willinger, A. Trunschke and R. Schlögl, Methane coupling over magnesium

oxide: how doping can work. *Angew. Chem. Int. Ed.* **2013**, *52*, 11381.

65. B. L. Farrell, V. O. Igenegbai and S. Linic, A viewpoint on direct methane conversion to ethane and ethylene using oxidative coupling on solid catalysts, *ACS Catal.* **2016**, *6*, 4340.

66. Y.-H. Hou, W.-C. Han, W.-S. Xia and H.-L. Wan, Structure sensitivity of $La_2O_2CO_3$ catalysts in the oxidative coupling of methane. *ACS Catal.* **2015**, *5*, 1663.

67. J. Bremer and K. Sundmacher, Operation range extension via hot-spot control for catalytic CO_2 methanation reactors. *React. Chem. Eng.* **2019**, *4*, 1019.

68. D. Kiani, S. Sourav, J. Baltrusaitis and I. E. Wachs, Oxidative coupling of methane (OCM) by SiO_2-supported tungsten oxide catalysts promoted with Mn and Na. *ACS Catal.* **2019**, *9*, 5912.

69. J. Xu, Y. Zhang, X. Xu, X. Fang, R. Xi, Y. Liu, R. Zheng and X. Wang, Constructing $La_2B_2O_7$ (B= Ti, Zr, Ce) compounds with three typical crystalline phases for the oxidative coupling of methane: The effect of phase structures, superoxide anions, and alkalinity on the reactivity. *ACS Catal.* **2019**, *9*, 4030.

70. U. Zavyalova, M. Holena, R. Schlögl and M. Baerns, Statistical analysis of past catalytic data on oxidative methane coupling for new insights into the composition of high-performance catalysts. *ChemCatChem* **2011**, *3*, 1935.

71. Q. Zhu, S. L. Wegener, C. Xie, O. Uche, M. Neurock and T. J. Marks, Sulfur as a selective 'soft'oxidant for catalytic methane conversion probed by experiment and theory. *Nat. Chem.* **2013**, *5*, 104.

72. J.-S. Min, H. Ishige, M. Misono and N. Mizuno, Low-temperature selective oxidation of methane into formic acid with H_2–O_2 gas mixture catalyzed by bifunctional catalyst of palladium–heteropoly compound. *J. Catal.* **2001**, *198*, 116.

73. X. Yu, B. Wu, M. Huang, Z. Lu, J. Li, L. Zhong and Y. Sun, IrFe/ZSM-5 synergistic catalyst for selective oxidation of methane to formic acid. *Energy & Fuels* **2021**, *35*, 4418.

74. A. Rahbari, M. Ramdin, L. J. Van Den Broeke and T. J. Vlugt, Combined steam reforming of methane and formic acid to produce syngas with an adjustable H_2:CO ratio. *Ind. Eng. Chem. Res.* **2018**, *57*, 10663.

75. K. Narsimhan, V. K. Michaelis, G. Mathies, W. R. Gunther, R. G. Griffin and Y. Roman-Leshkov, Methane to acetic acid over Cu-exchanged zeolites: mechanistic insights from a site-specific carbonylation reaction. *J. Am. Chem. Soc.* **2015**, *137*, 1825.

76. M. Lin and A. Sen, Direct catalytic conversion of methane to acetic acid in an aqueous medium. *Nature* **1994**, *368*, 613.

77. W. Panjan, J. Sirijaraensre, C. Warakulwit, P. Pantu and J. Limtrakul, The conversion of CO_2 and CH_4 to acetic acid over the Au-exchanged ZSM-5 catalyst: a density functional theory study. *Phys. Chem. Chem. Phys.* **2012**, *14*, 16588.

78. Q. Yuan, Q. Zhang and Y. Wang, Direct conversion of methane to methyl acetate with nitrous oxide and carbon monoxide over heterogeneous catalysts containing both rhodium and iron phosphate. *J. Catal.* **2005**, *233*, 221.

79. M. Vargaftik, I. Stolarov and I. Moiseev, Highly selective partial oxidation of methane to methyl trifluoroacetate. *J. Chem. Soc. Chem. Comm.* **1990**, 1049.

80. Y. Zhang, M. Zhang, Z. Han, S. Huang, D. Yuan and W. Su, Atmosphere-pressure methane oxidation to methyl trifluoroacetate enabled by a porous organic polymer-supported single-site palladium catalyst. *ACS Catal.* **2021**, *11*, 1008.

81. S. Wang, G. Lu and G. J. Millar, Carbon dioxide reforming of methane to produce synthesis gas over metal-supported catalysts: state of the art. *Energy & fuels* **1996**, *10*, 896.

82. M. K. Nikoo and N. Amin, Thermodynamic analysis of carbon dioxide reforming of methane in view of solid carbon formation. *Fuel Process. Technol.* **2011**, *92*, 678.

83. W. L. Luyben, Design and control of the dry methane reforming process. *Ind. Eng. Chem. Res.* **2014**, *53*, 14423.

84. P. M. Mortensen and I. Dybkjær, Industrial scale experience on steam reforming of CO_2-rich gas. *Appl. Catal. A* **2015**, *495*, 141.

85. T. ST C, P. Neumann and F. Von Linde, The calcor standard and calcor economy processes. *Oil Gas European Magazine* **2001**, 45.

86. P. Ferreira-Aparicio, M. Benito and J. Sanz, New trends in reforming technologies: from hydrogen industrial plants to multifuel microreformers. *Catal. Rev.* **2005**, *47*, 491.

87. J. Rostrup-Nielsen, 40 years in catalysis. *Catal. Today* **2006**, *111*, 4.

88. S. Arora and R. Prasad, An overview on dry reforming of methane: strategies to reduce carbonaceous deactivation of catalysts. *RSC Adv.* **2016**, *6*, 108668.

89. A. Shamsi and C. D. Johnson, Effect of pressure on the carbon deposition route in CO_2 reforming of $^{13}CH_4$. *Catal. Today* **2003**, *84*, 17.

90. W. Shen, J. Dumesic and C. Hill Jr, Criteria for stable Ni particle size under methanation reaction conditions: Nickel transport and particle size growth via nickel carbonyl. *J. Catal.* **1981**, *68*, 152.

91. S. M. Kim, P. M. Abdala, T. Margossian, D. Hosseini, L. Foppa, A. Armutlulu, W. van Beek, A. Comas-Vives, C. Copéret and C. Müller, Cooperativity and dynamics increase the performance of NiFe dry reforming catalysts. *J. Am. Chem. Soc.* **2017**, *139*, 1937.

92. S. A. Theofanidis, V. V. Galvita, H. Poelman and G. B. Marin, Enhanced carbon-resistant dry reforming Fe-Ni catalyst: Role of Fe. *ACS Catal.* **2015**, *5*, 3028.

93. W. Tu, M. Ghoussoub, C. V. Singh and Y.-H. C. Chin, Consequences of surface oxophilicity of Ni, Ni-Co, and Co clusters on methane activation. *J. Am. Chem. Soc.* **2017**, *139*, 6928.

94. M. Sanchez and J. Gazquez, Oxygen vacancy model in strong metal-support interaction. *J. Catal.* **1987**, *104*, 120.

95. A. Bruix, J. A. Rodriguez, P. J. Ramírez, S. D. Senanayake, J. Evans, J. B. Park, D. Stacchiola, P. Liu, J. Hrbek and F. Illas, A new type of strong metal–support interaction and the production of H_2 through the transformation of water on $Pt/CeO_2(111)$ and $Pt/CeO_x/TiO_2(110)$ catalysts. *J. Am. Chem. Soc.* **2012**, *134*, 8968.

96. T. Lunkenbein, J. Schumann, M. Behrens, R. Schlögl and M. G. Willinger, Formation of a ZnO overlayer in industrial $Cu/ZnO/Al_2O_3$ catalysts induced by strong metal–support interactions. *Angew. Chem.* **2015**, *127*, 4627.

97. J. Schumann, M. Eichelbaum, T. Lunkenbein, N. Thomas, M. C. Alvarez Galvan, R. Schlögl and M. Behrens, Promoting strong metal support interaction: Doping ZnO for enhanced activity of Cu/ZnO: M (M= Al, Ga, Mg) catalysts. *ACS Catal.* **2015**, *5*, 3260.

98. Z. Liu, P. Lustemberg, R. A. Gutiérrez, J. J. Carey, R. M. Palomino, M. Vorokhta, D. C. Grinter, P. J. Ramírez, V. Matolín and M. Nolan, *In situ* investigation of methane dry reforming on metal/ceria (111) surfaces: metal–support interactions and C−H bond activation at low temperature. *Angew. Chem. Int. Ed.* **2017**, *56*, 13041.

99. F. Zhang, Z. Liu, S. Zhang, N. Akter, R. M. Palomino, D. Vovchok, I. Orozco, D. Salazar, J. A. Rodriguez and J. Llorca, In situ elucidation of the active state of Co–CeO_x catalysts in the dry reforming of methane: The important role of the reducible oxide support and interactions with cobalt. *ACS Catal.* **2018**, *8*, 3550.

100. Z. Liu, D. C. Grinter, P. G. Lustemberg, T. D. Nguyen-Phan, Y. Zhou, S. Luo, I. Waluyo, E. J. Crumlin, D. J. Stacchiola and J. Zhou, Dry reforming of methane on a highly-active Ni-CeO_2 catalyst: Effects of metal-support interactions on C−H bond breaking. *Angew. Chem.* **2016**, *128*, 7581.

101. M.-C. Daniel and D. Astruc, Gold nanoparticles: assembly, supramolecular chemistry, quantum-size-related properties, and applications toward biology, catalysis, and nanotechnology. *Chem. Rev.* **2004**, *104*, 293.

102. M. B. Gawande, V. D. Bonifácio, R. S. Varma, I. D. Nogueira, N. Bundaleski, C. A. A. Ghumman, O. M. Teodoro and P. S. Branco, Magnetically recyclable magnetite–ceria (Nanocat-Fe-Ce) nanocatalyst–applications in multicomponent reactions under benign conditions. *Green Chem.* **2013**, *15*, 1226.

103. C. S. Diercks, Y. Liu, K. E. Cordova and O. M. Yaghi, The role of reticular chemistry in the design of CO_2 reduction catalysts. *Nat. Mater.* **2018**, *17*, 301.

104. K. Yamamoto, T. Imaoka, W.-J. Chun, O. Enoki, H. Katoh, M. Takenaga and A. Sonoi, Size-specific catalytic activity of platinum clusters enhances oxygen reduction reactions. *Nat. Chem.* **2009**, *1*, 397.

105. L. Liu and A. Corma, Metal catalysts for heterogeneous catalysis: from single atoms to nanoclusters and nanoparticles. *Chem. Rev.* **2018**, *118*, 4981.

106. B. Roldan Cuenya, Metal nanoparticle catalysts beginning to shape-up. *Acc. Chem. Res.* **2013**, *46*, 1682.

107. L. Piccolo, Z. Li, I. Demiroglu, F. Moyon, Z. Konuspayeva, G. Berhault, P. Afanasiev, W. Lefebvre, J. Yuan and R. L. Johnston, Understanding and controlling the structure and segregation behaviour of AuRh nanocatalysts. *Sci. Rep.* **2016**, *6*, 1.

108. H. Ha, S. Yoon, K. An and H. Y. Kim, Catalytic CO oxidation over Au nanoparticles supported on CeO_2 nanocrystals: effect of the Au–CeO_2 interface. *ACS Catal.* **2018**, *8*, 11491.

109. Y. Liu, Y. Ning, L. Yu, Z. Zhou, Q. Liu, Y. Zhang, H. Chen, J. Xiao, P. Liu and F. Yang, Structure and electronic properties of interface-confined oxide nanostructures. *ACS Nano* **2017**, *11*, 11449.

110. X. Pan, Z. Fan, W. Chen, Y. Ding, H. Luo and X. Bao, Enhanced ethanol production inside carbon-nanotube reactors containing catalytic particles. *Nat. Mater.* **2007**, *6*, 507.

111. M. Cargnello, V. V. Doan-Nguyen, T. R. Gordon, R. E. Diaz, E. A. Stach, R. J. Gorte, P. Fornasiero and C. B. Murray, Control of metal nanocrystal size reveals metal-support interface role for ceria catalysts. *Science* **2013**, *341*, 771.

112. D. Jiang, W. Wang, L. Zhang, Y. Zheng and Z. Wang, Insights into the surface-defect dependence of photoreactivity over CeO_2 nanocrystals with well-defined crystal facets. *ACS Catal.* **2015**, *5*, 4851.

113. C. Chen, Y. Kang, Z. Huo, Z. Zhu, W. Huang, H. L. Xin, J. D. Snyder, D. Li, J. A. Herron and M. Mavrikakis, Highly crystalline multimetallic nanoframes with three-dimensional electrocatalytic surfaces. *Science* **2014**, *343*, 1339.

114. D. Wang, H. L. Xin, R. Hovden, H. Wang, Y. Yu, D. A. Muller, F. J. DiSalvo and H. D. Abruña, Structurally ordered intermetallic platinum–cobalt core–shell nanoparticles with enhanced

activity and stability as oxygen reduction electrocatalysts. *Nat. Mater.* **2013**, *12*, 81.

115. L. Zhang, L. T. Roling, X. Wang, M. Vara, M. Chi, J. Liu, S.-I. Choi, J. Park, J. A. Herron and Z. Xie, Platinum-based nanocages with subnanometer-thick walls and well-defined, controllable facets. *Science* **2015**, *349*, 412.

116. Z. Niu, N. Becknell, Y. Yu, D. Kim, C. Chen, N. Kornienko, G. A. Somorjai and P. Yang, Anisotropic phase segregation and migration of Pt in nanocrystals en route to nanoframe catalysts. *Nat. Mater.* **2016**, *15*, 1188.

117. J. H. Koh, D. H. Won, T. Eom, N.-K. Kim, K. D. Jung, H. Kim, Y. J. Hwang and B. K. Min, Facile CO_2 electro-reduction to formate via oxygen bidentate intermediate stabilized by high-index planes of Bi dendrite catalyst. *ACS Catal.* **2017**, *7*, 5071.

118. Y. Lei, S. Lee, K.-B. Low, C. L. Marshall and J. W. Elam, Combining electronic and geometric effects of ZnO-promoted Pt nanocatalysts for aqueous phase reforming of 1-propanol. *ACS Catal.* **2016**, *6*, 3457.

119. S. Mitchell, R. Qin, N. Zheng and J. Pérez-Ramírez, Nanoscale engineering of catalytic materials for sustainable technologies. *Nat. Nanotechnol.* **2020**, *16*, 129.

120. J. Lee, J. Lee, T. Tanaka and H. Mori, *In situ* atomic-scale observation of melting point suppression in nanometer-sized gold particles. *Nanotechnology* **2009**, *20*, 475706.

121. Y. Nakaya, J. Hirayama, S. Yamazoe, K.-i. Shimizu and S. Furukawa, Single-atom Pt in intermetallics as an ultrastable and selective catalyst for propane dehydrogenation. *Nat. comm.* **2020**, *11*, 2838.

122. S. Wei, A. Li, J.-C. Liu, Z. Li, W. Chen, Y. Gong, Q. Zhang, W.-C. Cheong, Y. Wang and L. Zheng, Direct observation of noble metal nanoparticles transforming to thermally stable single atoms. *Nat. Nanotechnol.* **2018**, *13*, 856.

123. R. Lang, W. Xi, J.-C. Liu, Y.-T. Cui, T. Li, A. F. Lee, F. Chen, Y. Chen, L. Li and L. Li, Non defect-stabilized thermally stable single-atom catalyst. *Nat. Comm.* **2019**, *10*, 234.

124. D. Yan, J. Chen and H. Jia, Temperature-induced structure reconstruction to prepare a thermally stable single-atom platinum catalyst. *Angew. Chem. Int. Ed.* **2020**, *59*, 13562.

125. P. Prinsen and R. Luque, Introduction to nanocatalysts, *Nanoparticle Design and Characterization for Catalytic Applications in Sustainable Chemistry*, **2019**.

126. T. D. Bennett, F.-X. Coudert, S. L. James and A. I. Cooper, The changing state of porous materials. *Nat. Mater.* **2021**. DOI: 10.1038/s41563-021-00957-w

127. C.-Y. Chen, H.-X. Li and M. E. Davis, Studies on mesoporous materials: I. Synthesis and characterization of MCM-41. *Micropor. Mater.* **1993**, *2*, 17.

128. M. Kruk, M. Jaroniec, C. H. Ko and R. Ryoo, Characterization of the porous structure of SBA-15. *Chem. Mater.* **2000**, *12*, 1961.

129. D. Zhao, J. Sun, Q. Li and G. D. Stucky, Morphological control of highly ordered mesoporous silica SBA-15. *Chem. Mater.* **2000**, *12*, 275.

130. W. Stöber, A. Fink and E. Bohn, Controlled growth of monodisperse silica spheres in the micron size range. *J. Colloid Interface Sci.* **1968**, *26*, 62.

131. J. Liu, S. Z. Qiao, H. Liu, J. Chen, A. Orpe, D. Zhao and G. Q. Lu, Extension of the Stöber method to the preparation of monodisperse resorcinol–formaldehyde resin polymer and carbon spheres. *Angew. Chem.* **2011**, *123*, 6069.

132. J. Choma, D. Jamioła, K. Augustynek, M. Marszewski, M. Gao and M. Jaroniec, New opportunities in Stöber synthesis: preparation of microporous and mesoporous carbon spheres. *J. Mater. Chem.* **2012**, *22*, 12636.

133. T. Zhao, A. Elzatahry, X. Li and D. Zhao, Single-micelle-directed synthesis of mesoporous materials. *Nat. Rev. Mater.* **2019**, *4*, 775.

134. J. S. Beck, J. C. Vartuli, W. J. Roth, M. E. Leonowicz, C. T. Kresge, K. D. Schmitt, C. T. W. Chu, D. H. Olson, E. W. Sheppard, S. B. McCullen, J. B. Higgins and J. L. Schlenker, A new family of mesoporous molecular sieves prepared with liquid crystal templates. *J. Am. Chem. Soc.* **1992**, *114*, 10834.

135. C. Li, Q. Li, Y. V. Kaneti, D. Hou, Y. Yamauchi and Y. Mai, Self-assembly of block copolymers towards mesoporous materials for energy storage and conversion systems. *Chem. Soc. Rev.* **2020**, *49*, 4681.

136. P. Yang, D. Zhao, D. I. Margolese, B. F. Chmelka and G. D. Stucky, Generalized syntheses of large-pore mesoporous metal oxides with semicrystalline frameworks. *Nature* **1998**, *396*, 152.

137. C. Liang, K. Hong, G. A. Guiochon, J. W. Mays and S. Dai, Synthesis of a large-scale highly ordered porous carbon film by self-assembly of block copolymers. *Angew. Chem. Int. Ed.* **2004**, *43*, 5785.

138. Y. Yamauchi, A. Sugiyama, R. Morimoto, A. Takai and K. Kuroda, Mesoporous platinum with giant mesocages templated from lyotropic liquid crystals consisting of diblock copolymers. *Angew. Chem. Int. Ed.* **2008**, *47*, 5371.

139. J. Tollefson, Worth its weight in platinum. *Nature News* **2007**, *450*, 334.

140. J. G. de Vries, *Handbook of homogeneous hydrogenation, Weinheim: Wiley-VCH*, **2007**.

141. E. D. Goodman, J. A. Schwalbe and M. Cargnello, Mechanistic understanding and the rational design of sinter-resistant heterogeneous catalysts. *ACS Catal.* **2017**, *7*, 7156.

142. R. Van den Berg, T. E. Parmentier, C. F. Elkjær, C. J. Gommes, J. Sehested, S. Helveg, P. E. de Jongh and K. P. de Jong, Support functionalization to retard Ostwald ripening in copper methanol synthesis catalysts. *ACS Catal.* **2015**, *5*, 4439.

143. J. Liu, Q. Ji, T. Imai, K. Ariga and H. Abe, Sintering-resistant nanoparticles in wide-mouthed compartments for sustained catalytic performance. *Sci. Rep.* **2017**, *7*, 41773.

144. P. Lu, C. T. Campbell and Y. Xia, A sinter-resistant catalytic system fabricated by maneuvering the selectivity of SiO_2 deposition onto the TiO_2 surface versus the Pt nanoparticle surface. *Nano Lett.* **2013**, *13*, 4957.

145. X. Du, C. Zhao, Y. Luan, C. Zhang, M. Jaroniec, H. Huang, X. Zhang and S.-Z. Qiao, Dendritic porous yolk@ordered mesoporous shell structured heterogeneous nanocatalysts with enhanced stability. *J. Mater. Chem. A* **2017**, *5*, 21560.

146. Z.-Y. Lim, C. Wu, W. G. Wang, K.-L. Choy and H. Yin, Porosity effect on ZrO_2 hollow shells and hydrothermal stability for catalytic steam reforming of methane. *J. Mater. Chem. A* **2016**, *4*, 153.

147. H. Zhao, S. Yao, M. Zhang, F. Huang, Q. Fan, S. Zhang, H. Liu, D. Ma and C. Gao, Ultra-small platinum nanoparticles encapsulated in sub-50 nm hollow titania nanospheres for low-temperature water–gas shift reaction. *ACS Appl. Mater. Interfaces* **2018**, *10*, 36954.

148. S. Das, J. Ashok, Z. Bian, N. Dewangan, M. Wai, Y. Du, A. Borgna, K. Hidajat and S. Kawi, Silica–Ceria sandwiched Ni core–shell catalyst for low temperature dry reforming of biogas:

Coke resistance and mechanistic insights. *Appl. Catal. B* **2018**, *230*, 220.

149. S. Das, J. P.-Ramírez, J. Gong, N. Dewangan, K. Hidajat, B. C. Gates, and S. Kawi, Core-shell structured catalysts for thermocatalytic, photocatalytic, and electrocatalytic conversion of CO_2, *Chem. Soc. Rev.* **2020**, *49*, 2997.

150. F. Wang, B. Han, L. Zhang, L. Xu, H. Yu and W. Shi, CO_2 reforming with methane over small-sized Ni@SiO_2 catalysts with unique features of sintering-free and low carbon. *Appl. Catal. B* **2018**, *235*, 26.

151. J. Zhang and F. Li, Coke-resistant Ni@SiO_2 catalyst for dry reforming of methane. *Appl. Catal. B* **2015**, *176*, 513.

152. S. Li, A. Tuel, D. Laprune, F. d. r. Meunier and D. Farrusseng, Transition-metal nanoparticles in hollow zeolite single crystals as bifunctional and size-selective hydrogenation catalysts. *Chem. Mater.* **2015**, *27*, 276.

153. F. Goodarzi, L. Kang, F. R. Wang, F. Joensen, S. Kegnæs and J. Mielby, Methanation of carbon dioxide over zeolite-encapsulated nickel nanoparticles. *ChemCatChem* **2018**, *10*, 1566.

154. M. Cargnello, J. D. Jaén, J. H. Garrido, K. Bakhmutsky, T. Montini, J. C. Gámez, R. Gorte and P. Fornasiero, Exceptional activity for methane combustion over modular Pd@CeO_2 subunits on functionalized Al_2O_3. *Science* **2012**, *337*, 713.

155. C. Xie, C. Chen, Y. Yu, J. Su, Y. Li, G. A. Somorjai and P. Yang, Tandem catalysis for CO_2 hydrogenation to C_2–C_4 Hydrocarbons. *Nano Lett.* **2017**, *17*, 3798.

156. B. J. O'Neill, D. H. Jackson, J. Lee, C. Canlas, P. C. Stair, C. L. Marshall, J. W. Elam, T. F. Kuech, J. A. Dumesic and G. W. Huber, Catalyst design with atomic layer deposition. *ACS Catal.* **2015**, *5*, 1804.

157. S. Liu, W. Xu, Y. Niu, B. Zhang, L. Zheng, W. Liu, L. Li and J. Wang, Ultrastable Au nanoparticles on titania through an encapsulation strategy under oxidative atmosphere. *Nature Comm.* **2019**, *10*, 5790.

158. P. Hester, S. Xu, W. Liang, N. Al-Janabi, R. Vakili, P. Hill, C. A. Muryn, X. Chen, P. A. Martin and X. Fan, On thermal stability and catalytic reactivity of Zr-based metal–organic framework (UiO-67) encapsulated Pt catalysts. *J. Catal.* **2016**, *340*, 85.

159. J. C. Matsubu, S. Zhang, L. DeRita, N. S. Marinkovic, J. G. Chen, G. W. Graham, X. Pan and P. Christopher, Adsorbate-mediated strong metal–support interactions in oxide-supported Rh catalysts. *Nat. Chem.* **2017**, *9*, 120.

160. J. Lu, J. W. Elam and P. C. Stair, Atomic layer deposition—Sequential self-limiting surface reactions for advanced catalyst "bottom-up" synthesis. *Surf. Sci. Rep.* **2016**, *71*, 410.

161. J. Lu, B. Fu, M. C. Kung, G. Xiao, J. W. Elam, H. H. Kung and P. C. Stair, Coking-and sintering-resistant palladium catalysts achieved through atomic layer deposition. *Science* **2012**, *335*, 1205.

162. J. Lu, B. Liu, J. P. Greeley, Z. Feng, J. A. Libera, Y. Lei, M. J. Bedzyk, P. C. Stair and J. W. Elam, Porous alumina protective coatings on palladium nanoparticles by self-poisoned atomic layer deposition. *Chem. Mater.* **2012**, *24*, 2047.

Chapter 2

Methane Oxidation to Formaldehyde over Vanadium Oxide Supported on Various Mesoporous Silicas

This chapter includes the published contents:
E. Yang, J. G. Lee, E. D. Park and K. An, *Korean J. Chem. Eng.* **2021**. DOI: 10.1007/s11814-021-0758-8. Reproduced with permission. Copyright © Springer Nature.

2.1. Introduction

Direct oxidation of methane to formaldehyde in a single step is a very important process in upgrading natural gas to more valuable chemicals. Essentially, the indirect methane catalytic process that converts methane to formaldehyde proceeds via three steps: SRM to produce syngas, conversion of syngas to methanol, and partial oxidation of methanol to formaldehyde.[1–4] However, the four symmetrical sigma C−H bonds of methane (ΔH_{C-H} = 438.8 kJ mol^{-1}) are kinetically inert, and therefore, difficult to engage in catalytic oxidation reactions; hence, high temperatures over 500 °C are generally required for methane activation.[5–6] For direct oxidation of methane to formaldehyde, highly dispersed MoO_x and VO_x supported on SiO_2 exhibit higher activity at elevated temperatures (550−600 °C). However, the maximum single pass yield of MoO_x and VO_x catalysts supported on SiO_2 is generally reported to be around 2−10%.[7–10] In addition, the metastable formaldehyde may be further oxidized, producing CO_2 and H_2O as undesirable products during the oxidation process at high temperatures. Herman *et al.* compared V_2O_5 and MoO_3 catalysts supported on SiO_2 prepared by the wet impregnation (WI) method, in the partial oxidation of methanol to formaldehyde. The reported activity of V_2O_5/SiO_2 and MoO_3/SiO_2 catalysts was 9.52% and 0.08% with a formaldehyde selectivity of 15.7% and 100 % at 630 °C, respectively.[11] Parmaliana *et al.* reported that VO_x supported on *m*-SiO_2 prepared by the WI method exhibited two orders of magnitude higher reaction rate than that of MoO_3 catalysts, at 600 °C.[12] Due to these harsh conditions and low conversion rates, there are few studies on the direct oxidation of methane to formaldehyde. According to the previous results using V_2O_5/SiO_2 catalysts, it was found that most of the methane to formaldehyde conversion reactions at about 600 °C showed a low conversion of less than 10%. In particular, *m*-SiO_2 with a large surface area has been used as good support, but more systematic research is needed. Fundamental research aimed at the development and understanding of

catalysts with high efficiency should be carried out in consideration of the abundance and future value of methane resources.

Mesoporous materials have been widely used as excellent supports for incorporating active metals or oxides with high dispersion, owing to their high surface area, large pore volume, and well-ordered pore structure.[13–16] Among them, *m*-SiO_2 is preferentially selected because it is produced by simple sol-gel chemistry with high reproducibility. Depending on the micellar structure determined by the concentration and type of surfactants, including alkylammonium salts and block copolymers, a versatile *m*-SiO_2 structure can be formed with controlled pore structures. The resulting high surface area and well-organized internal pores serve to anchor active oxide species, which is advantageous because the degree of dispersion of vanadium oxides is known to be influenced by the surface structure of the support. Depending on the loading of the vanadium precursors and the resulting dispersion, three types of states are formed in the supported vanadium oxide catalysts: an isolated species, a thin polymeric overlayer, and crystalline V_2O_5.[17] The preparation method also influences the surface structure of the supported vanadium oxide catalysts. It was reported that the molecular structure was strongly affected by the pH of the vanadium precursor solution used during WI synthesis, which is the most popular and general method for the preparation of supported catalysts. The highly dispersed monomeric structure of the vanadium oxide changed to the polymerized form, and finally to the V_2O_5 bulk structure, as the pH decreased: $[VO_4]^{3-} \rightarrow [V_2O_7]^{2-} \rightarrow [V_4O_{12}]^{4+} \rightarrow [V_{10}O_{27}(OH)]^{5-} \rightarrow V_2O_5$ bulk.[18] When the solvent-free dry impregnation (DI) method was used, more distorted surface species such as $[VO_4]^{3+}$ can be obtained.[19]

To determine the best VO_x/*m*-SiO_2 catalyst with the highest catalytic performance in methane oxidation to formaldehyde, we prepared a series of VO_x/*m*-SiO_2 catalysts by changing the type of *m*-SiO_2, vanadium loading, and preparation method. Using these catalysts, we investigated how the loading of V on *m*-SiO_2 with different surface areas and pore structure influences the configuration of the VO_x active species and the corresponding catalytic reaction. We prepared the VO_x/*m*-SiO_2 catalysts with three different vanadium loadings (1, 3, and 5%) by the WI and DI methods. Two types of *m*-SiO_2, SBA-15, and MCF-17 were used to investigate the role of VO_x/*m*-SiO_2 catalysts. Transmission electron microscopy (TEM), Brunauer-Emmett-Teller (BET) measurements, X-ray diffraction (XRD), H_2-TPR, ultraviolet-visible (UV-Vis) spectroscopy, and Raman spectroscopy were used to determine the major species of vanadium oxides depending on the type of *m*-SiO_2, vanadium loading, and preparation method. The activity and selectivity of the methane oxidation to HCHO were also correlated with the vanadium species.

2.2. Experimental Methods

2.2.1 Preparation of m-SiO_2 (SBA-15 and MCF-17)

Two different *m*-SiO_2, SBA-15, and MCF-17 were synthesized by the reported methods with slight modification.[20,21] For the preparation of SBA-15, 37 g of Pluronic P123 ($EO_{20}PO_{70}EO_{20}$; EO = ethylene oxide, PO = propylene oxide, Sigma-Aldrich, average M_w = 5,800) as a structure-directing agent were dissolved in 185 mL of concentrated hydrochloric acid (HCl, 35.0–37.0 %) and 1.16 L of water in a sealed polypropylene bottle under vigorous stirring at 35 °C for 5 h. Subsequently, 84 mL of tetraethyl orthosilicate (Sigma-Aldrich, 98%) in a separating funnel was added to the solution mixture and kept at 35 °C overnight without stirring. Hydrothermal treatment was carried out by storing the bottle in an oven at 80 °C for 24 h. The resulting white slurry was filtered by a vacuum filter and washed with deionized water and ethanol. After calcination in air at 550 °C for 6 h, SBA-15 in the form of white powder was collected. MCF-17 was synthesized by a similar procedure as that adopted for SBA-15.[22] In brief, 40 g of Pluronic P123 and 40 g of 1,3,5-trimethylbenzene (Sigma-Aldrich, 98%) were dissolved in 100 mL of concentrated HCl and 650 mL of water under vigorous stirring at 35 °C for 5 h. Then, 92 mL of tetraethyl orthosilicate were added in the same manner and kept at 35 °C overnight. Before the hydrothermal process at 80 °C, 0.46 g of ammonium fluoride (Sigma-Aldrich, 98%) was added as a mineralizer to the solution. Filtration, washing, and calcination were performed by the same procedure as the SBA-15 synthesis, to obtain powdered MCF-17.

2.2.2 Fabrication of VO_x/m-SiO_2 catalysts

Two different preparation methods were used for VO_x/*m*-SiO_2 catalysts: WI and DI. For the WI, ammonium metavanadate (NH_4VO_3, Alfa Aesar, 99%), vanadyl acetylacetone ($VO(acac)_2$, Sigma-Aldrich, 97%), and oxalic acid ($H_2C_2O_4$, Acros, 99+%) were used. A certain amount of NH_4VO_3 calculated according to the metal loading was dissolved in water, and then, $H_2C_2O_4$ was added to the solution. The solution was stirred vigorously until the color changed to blue. After the addition of as-synthesized *m*-SiO_2, the mixed slurry was dried overnight at 100 °C and calcined at 400 °C for 3 h. The resulting catalyst was pelletized and sieved to 150–250 μm particulate size before use in the catalytic reaction. For the DI, $VO(acac)_2$ and *m*-SiO_2 were mixed according to the metal loading in a mortar. After physical mixing in a mortar, the powder was loaded in a crucible inside a tubular furnace. Thermal treatment in N_2 atmosphere at 240 °C for 3 h and calcination with O_2 was carried out at 500 °C for 17 h for complete oxidation. The obtained catalysts were pelletized and sieved in the same manner as the WI method.

2.2.3 Characterization

Nitrogen adsorption isotherms were obtained using a Microtrac BELsorp-max analyzer after outgassing the sample at 150 °C for 12 h. The pore size distribution was determined by the Barrett–Joyner–Halenda (BJH) method. Powder XRD was carried out in the 2θ range of 10–80° (Cu Kα radiation, λ= 1.5418 Å) using a PANalytical X'Pert Pro. TEM measurement was performed using a JEOL JEM-2100F instrument operated at 200 kV. H_2-TPR was carried out in a Micromeritics AutoChem II 2920 instrument. In short, a catalyst sample (50 mg) was prepared into a U-shaped quartz tube and outgassed under pure He flow (50 NmL min^{-1}) for 30 min to remove moisture and impurities. After cooling to 50 °C, 10 vol% H_2/He stream (50 NmL min^{-1}) was introduced and the temperature was raised to 800 °C at a 10 °C min^{-1} heating rate. The amount of consumed H_2 was recorded by gas chromatography (GC) using a Delsi Nermag thermal conductivity detector (TCD). UV-Vis diffuse reflectance spectra were obtained by an Agilent Cary 5000 UV-Vis-NIR spectrophotometer measured from 200–2200 nm, and a halon white reflectance standard was used as the standard. Raman analysis was carried out on a WITec alpha300R spectrometer equipped with 532 nm laser excitation. The spectra were collected using a charge-coupled device detector with a 10 s exposure and 10-fold accumulation.

2.2.4 Methane oxidation

Catalytic methane oxidation was carried out under atmospheric pressure and at a constant temperature of 600 °C in a laboratory-scale fixed bed reactor. VO_x/*m*-SiO_2 catalyst (100 mg) was loaded into a quartz tube (inner diameter = 1 cm) together with 1 g of purified quartz sand. A gas mixture of CH_4 and O_2 was fed through the catalyst bed using a mass flow controller (total flow of 40 mL min^{-1}, 24,000 mL g_{cat}^{-1} h^{-1}, 1:1 molar ratio). The reaction temperature was detected by a K-type thermocouple closely attached to the inside of the catalyst bed covered by the furnace. The product composition was analyzed using an online GC (YL6500) equipped with Porapak-N and molecular sieve columns using Ar as a carrier gas. The separated gases, including H_2, CO_2, CO, and CH_4, were detected by the GC, which connected to both TCD and flame ionization detector (FID) with a methanizer. No methane conversion was detected when the reaction was measured in an empty quartz reactor or when only *m*-SiO_2 without vanadium loading was tested. Before entering GC, HCHO was trapped in a cold trap containing 10.5 g of Na_2SO_3 and 1.63 g of H_2SO_4 dissolved in 100 mL of an aqueous solution. The concentration of HCHO was quantitatively determined by titration between the produced NaOH and the contained H_2SO_4 residue.[7,23,24]

2.3. Results and Discussion

2.3.1 Structural characterizations of VO_x/m-SiO_2 catalysts

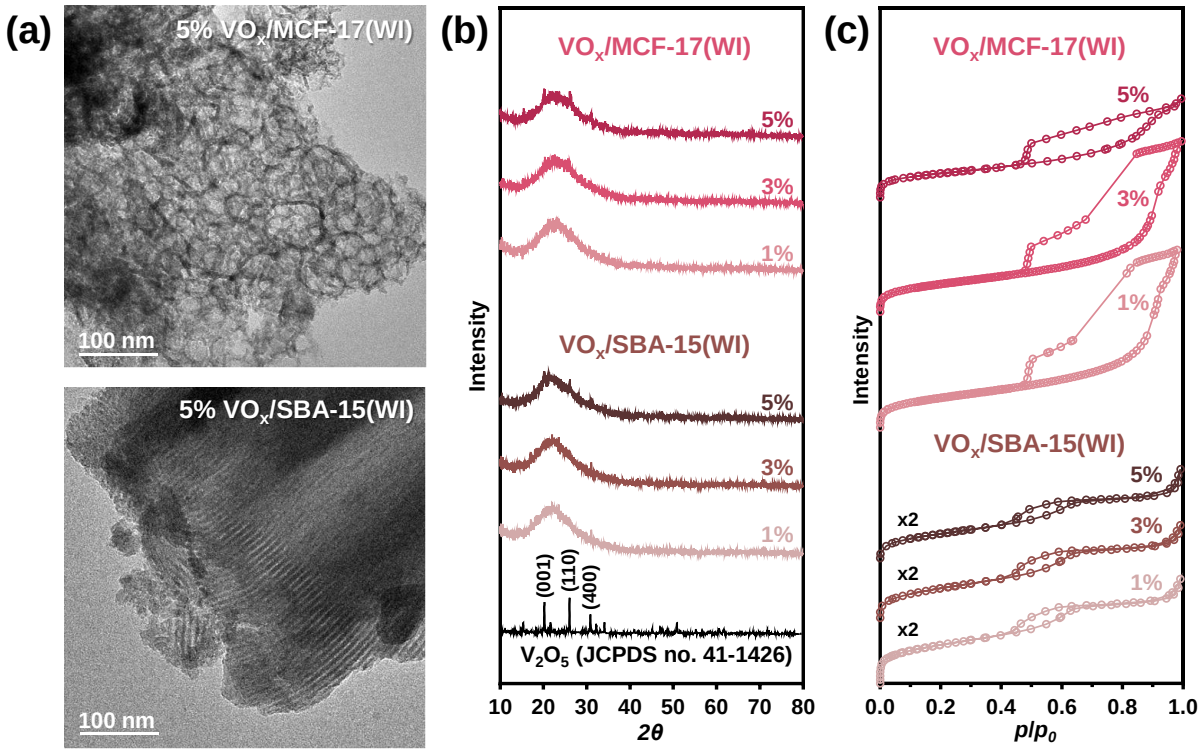

Figure 2.1. VO_x/*m*-SiO_2 catalysts prepared by the wet impregnation (WI) method: (a) TEM images of 5% VO_x/MCF-17 and VO_x/SBA-15, (b) XRD patterns, and (c) N_2 adsorption-desorption isotherms of VO_x/*m*-SiO_2 catalysts with the different vanadium loadings.

Two different *m*-SiO_2, MCF-17, and SBA-15 were used to load vanadium with a weight percent of 1, 3, and 5. Each VO_x/*m*-SiO_2 catalyst was prepared by either the WI or DI method. Figure 2.1 shows TEM images, XRD patterns, and N_2 adsorption/desorption isotherms of 1, 3, and 5% VO_x/MCF-17 and VO_x/SBA-15 catalysts through the WI method. The TEM images shown in Figure 2.1 reveal that the pore size of MCF-17 (30–50 nm) is greater than that of SBA-15 (≤ 10 nm diameter). Unlike MCF-17 with mesocellular pore structures generated by a pore-swelling agent, 1,3,5-trimethylbenzene, SBA-15 has well-ordered hexagonal channels with a *p6mm* symmetry. However, the vanadium species are hardly distinguishable from the *m*-SiO_2 in the TEM images due to the high dispersion and small size of the VO_x. Figure 2.1b shows the XRD patterns measured in the range of 10–80°. The broad reflection at 23° originated from the amorphous *m*-SiO_2. The characteristic reflections of V_2O_5 at 20° and 26° which are assigned to the (001) and (110) phases appear slightly as the vanadium loading increases. Figure 2.1c shows the N_2 adsorption-desorption isotherms of the VO_x/MCF-17 and VO_x/SBA-15 catalysts. Surface areas determined by BET measurements and pore diameters calculated by the BJH method are summarized in Table 2.1. The type IV isotherm trends are shown in Figure 2.1c demonstrate the characteristics of mesoporous structures of all VO_x/*m*-SiO_2 catalysts. The catalyst supported on MCF-

17 has a larger hysteresis curve area than that of SBA-15, while the surface area of VO_x/MCF-17 (570–700 m^2 g^{-1}) is also greater than that of VO_x/SBA-15 (300–360 m^2 g^{-1}). Figure 2.1c indicates that the surface area of the catalysts decreases gradually as the vanadium content increases.

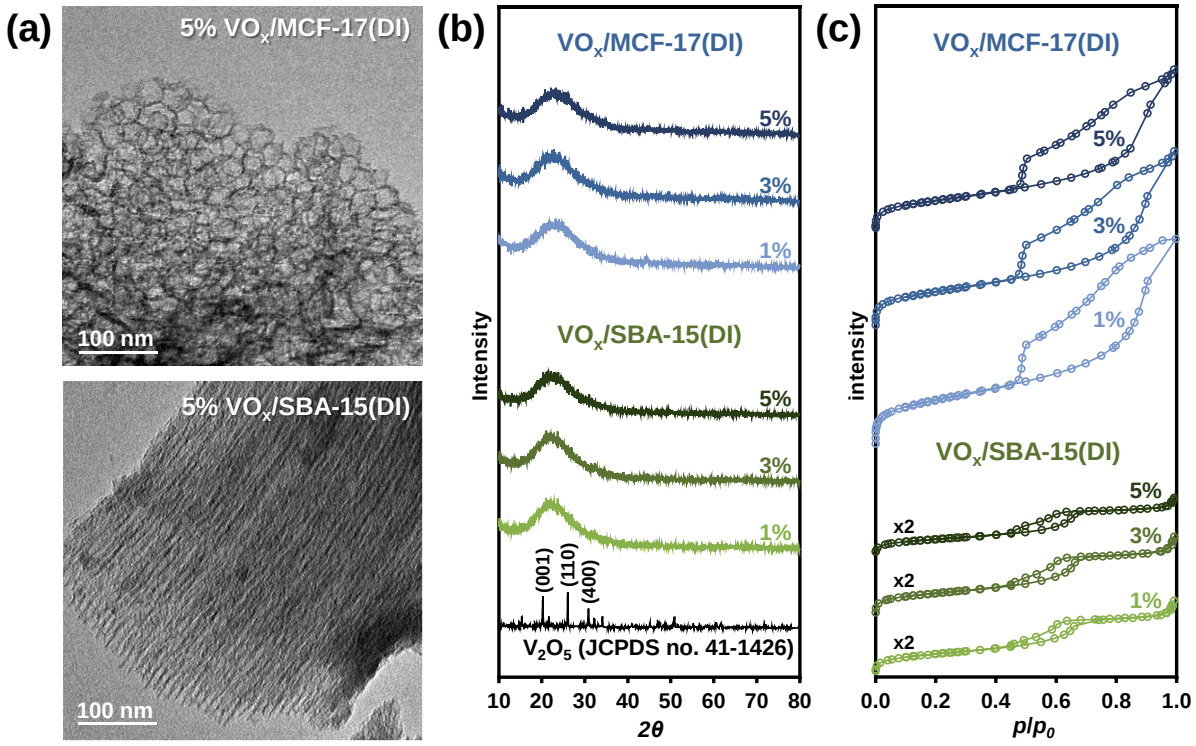

Figure 2.2. VO_x/*m*-SiO_2 catalysts prepared by the dry impregnation (DI) method: (a) TEM images of 5% VO_x/MCF-17 and VO_x/SBA-15, (b) XRD patterns, and (c) N_2 adsorption-desorption isotherms of VO_x/*m*-SiO_2 catalysts with the different vanadium loadings.

Figure 2.2 shows characterization results of VO_x/MCF-17 and VO_x/SBA-15 catalysts prepared by the DI method. Again, the TEM images do not identify the VO_x species on the silica support. Similarly, the XRD patterns in Figure 2.2b show that the VO_x species is hardly detectable due to the high dispersion and small size of the VO_x species. XRD measurements of surface vanadium species are only suitable for bulk structures for nanoparticles of at least 4 nm or larger.[25] For this reason, the crystal structure of the VO_x cannot be identified clearly by the current characterization tools. Surface areas and pore diameters of VO_x/MCF-17 and VO_x/SBA-15 catalysts prepared by the DI method have similar results to those of the WI method (Figure 2.2c and Table 2.1). The surface areas of MCF-17 catalysts are evaluated to be about twice higher than that of SBA-15 catalysts due to the structural difference of the *m*-SiO_2. The structure of MCF-17 has the larger pore with the undulations of mesopores by the addition of trimethylbenzene, whereas SBA-15 has narrow size distribution (Figure 2.3). HAADF-STEM and EDS mapping images of 5% VO_x/SBA-15(WI) and 5% VO_x/MCF-17(DI) showed the high dispersion of vanadium on both *m*-SiO_2 regardless of the preparation methods of catalysts. (Figure 2.4) From these results, it is revealed that both WI and DI methods produced VO_x/*m*-SiO_2 catalysts with a

high dispersion of vanadium species on *m*-SiO_2 supports and the preparation method does not affect the physical properties of the catalyst.

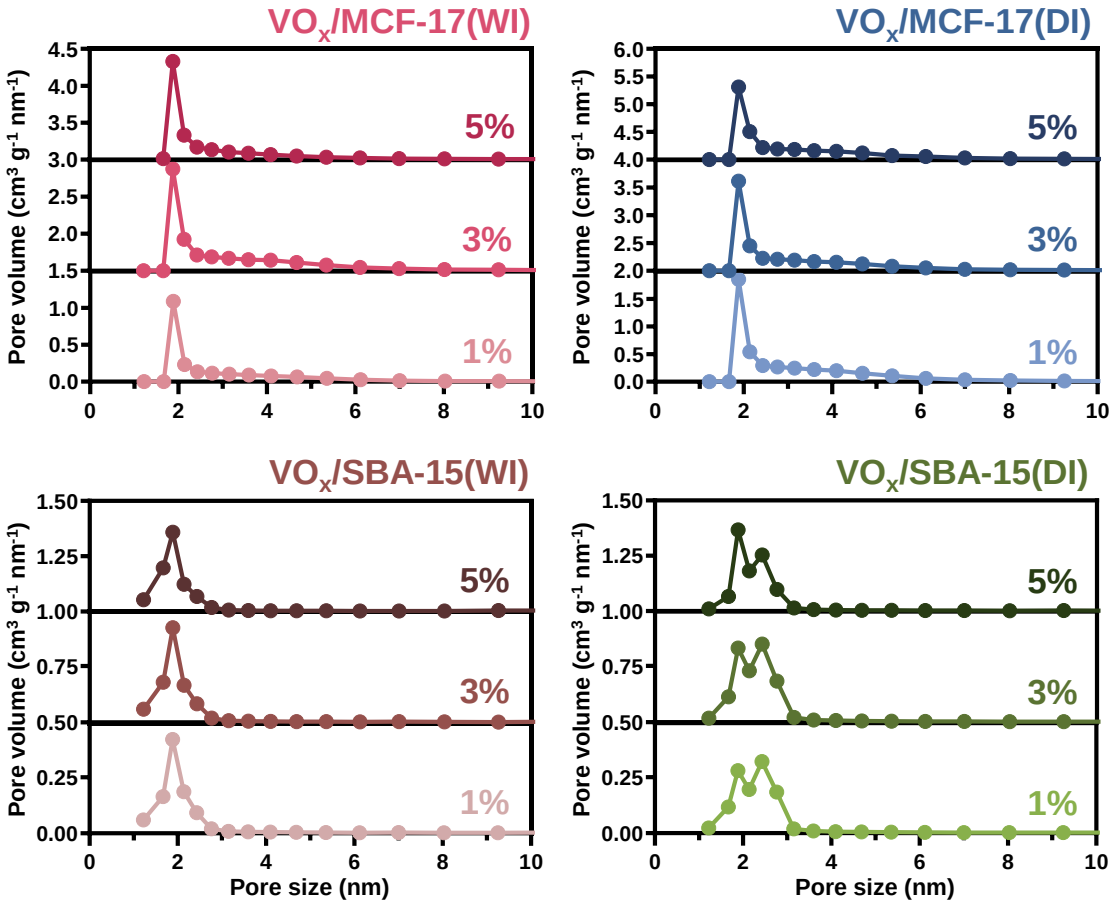

Figure 2.3. Pore size distributions of VO_x/*m*-SiO_2 catalysts according to the BJH method.

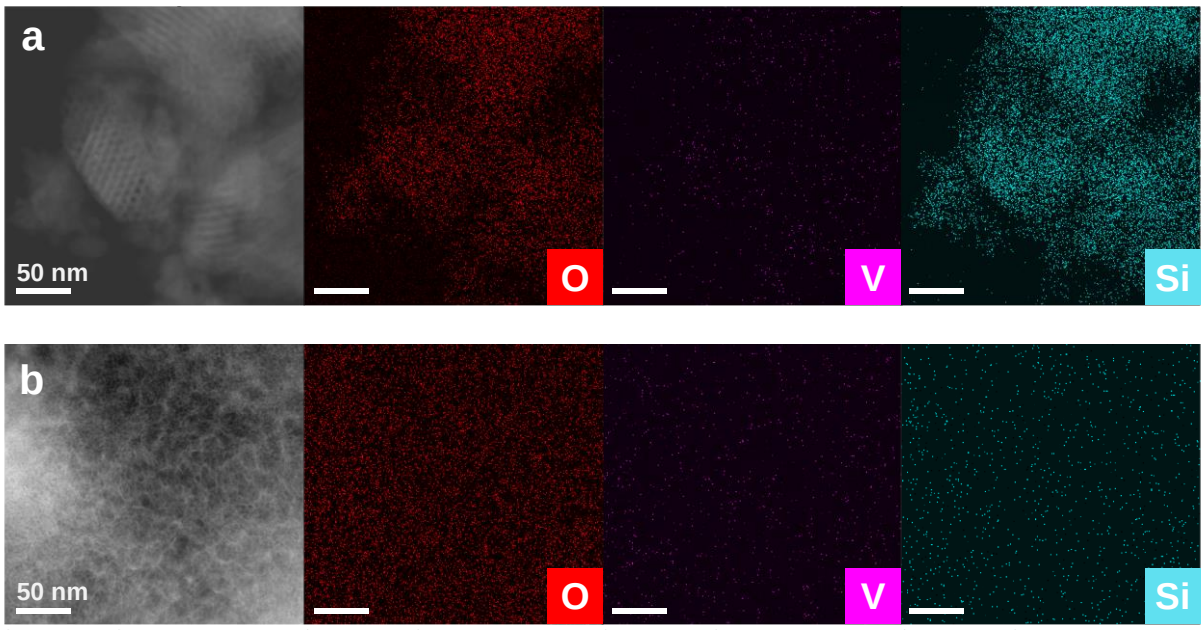

Figure 2.4. HAADF-STEM and EDS mapping images of (a) 5% VO_x/SBA-15(WI) and (b) 5%

VO_x/MCF-17(DI).

Table 2.1. BET surface areas (a_s) and pore diameters (d_{pore}) of VO_x/*m*-SiO_2 catalysts.

Catalyst	Vanadium loading	Surface area	Pore diameter
	(%)	a_s, (m^2 g^{-1})	d_{pore}, (nm)
VO_x/MCF-17 (WI)	1	652	9.00
	3	617	9.12
	5	578	9.24
VO_x/SBA-15 (WI)	1	361	4.61
	3	347	4.58
	5	318	4.80
VO_x/MCF-17 (DI)	1	750	7.13
	3	582	7.86
	5	506	8.36
VO_x/SBA-15 (DI)	1	350	5.46
	3	362	5.50
	5	275	5.44

2.3.2 Active Vanadium Phases of VO_x/m-SiO_2 Catalysts

The concentration of the VO_x species on *m*-SiO_2 supports is highly correlated with the nature of the vanadium active sites, which contain the terminal V=O group as an isolated tetrahedral monovanadate (VO_4) species.[26] The structure of the supported VO_x species can be changed on metal oxides (SiO_2, ZrO_2, Al_2O_3, and TiO_2) with various chemical properties, due to surface interactions at high temperatures.[27] The chemical information of the VO_x active species including reducibility, distribution, and quantity, was identified by H_2-TPR spectra. Figure 2.5 shows TPR profiles of VO_x/*m*-SiO_2 catalysts obtained at 100–800 °C. Below 500 °C, a representative peak is observed of the isolated V^{5+} species in $[VO_4]^{3-}$ on the *m*-SiO_2 support. This represents a vanadium species in the form of a distorted tetrahedral coordination site with one short V=O and three V–O bonds attached to the support.[9,28] Crystalline V_2O_5 species appear at higher reduction temperatures.[2,29] As the vanadium loading increases in the VO_x/*m*-SiO_2 catalysts, the main peak shifts to higher temperatures, and the peak intensity increases. The H_2-TPR spectra of the 3% VO_x/SBA-15 and VO_x/MCF-17 catalysts prepared by the WI method show shoulder peaks at 595 °C, indicating crystalline V_2O_5, while the same catalysts with 5% loading have higher peak intensities at 533–538 °C corresponding to the polymeric and crystalline V_2O_5 phase (Figure 2.5, left). The 5% loaded VO_x/SBA-15 and VO_x/MCF-17 catalysts prepared by the DI method have major peaks at 501 and 514 °C, respectively. They also have minor shoulder peaks at 586 and 604 °C, demonstrating that they still have dominant isolated $[VO_4]^{3-}$ species, compared to the overlapping peaks derived from the isolated and crystalline phase of the 5% VO_x/*m*-

SiO_2 catalysts by the WI method (Figure 2.5, right). It was revealed that the DI method is much more efficient in creating monomeric VO_4 species in VO_x/m-SiO_2 catalysts.

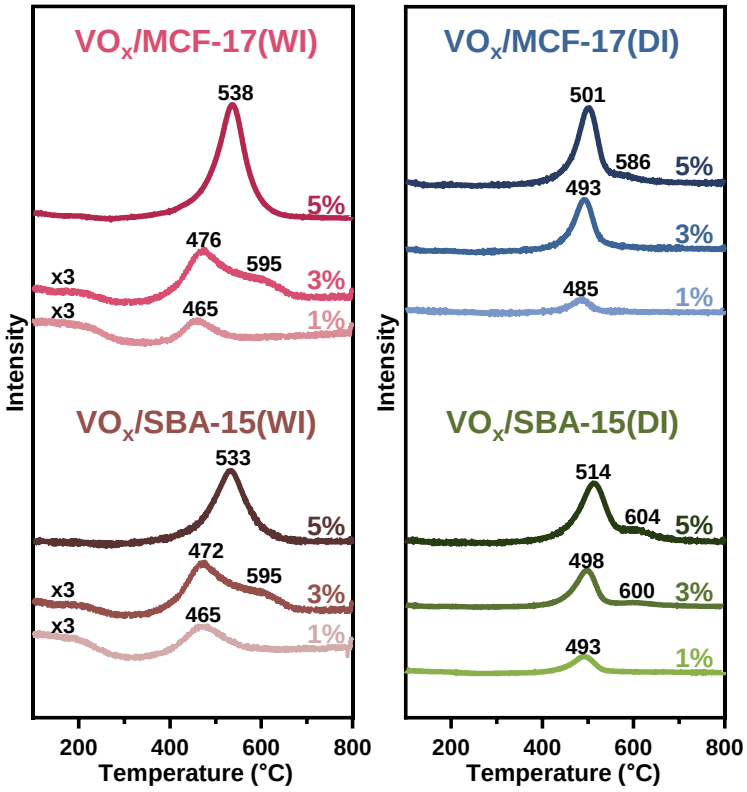

Figure 2.5. H_2-TPR spectra of VO_x/m-SiO_2 catalysts prepared by the WI and DI methods.

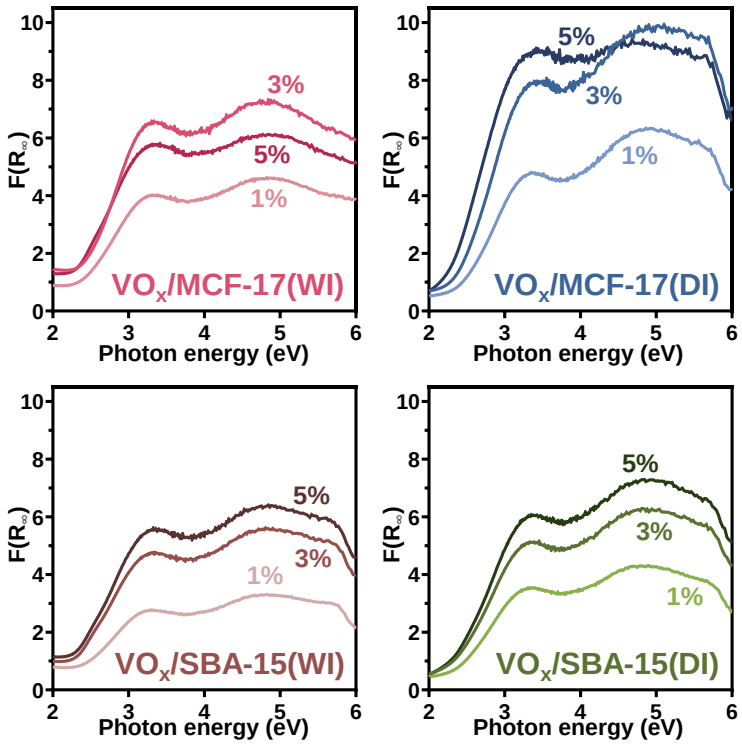

Figure 2.6. UV-Vis diffuse reflectance spectra of VO_x/m-SiO_2 catalysts prepared by the WI and DI

methods.

Diffuse reflectance UV-Vis spectra of $VO_x/m\text{-}SiO_2$ catalysts were obtained in the range of 2–6 eV (620–210 nm). The square root of the Kubelka–Munk function multiplied by the photon energy $(F(R_\infty)hv)^{1/2}$ versus the photon energy (hv) was plotted to determine the dispersion and local structure of VO_x on the support.[30–32] (Figure 2.6) The value of the absorption energy band (ε_0) was calculated by extrapolation of the Kubelka–Munk function from the linear fit of the x-intercept at the low-energy side. The ε_0 value of more than 3 eV is assigned to the presence of VO_x species with T_d coordination, whereas the value lower than 3 eV is ascribed to polymeric or further bulk V_2O_5. There is no obvious change in the ε_0 values (2.11–2.35 eV) of the $V_2O_5/m\text{-}SiO_2$ catalysts as a function of vanadium loading, indicating that they possess a dominant V_2O_5 phase. However, V_2O_5/MCF-17(DI) catalysts with 1, 3, and 5% of vanadium loading have 2.35, 2.32, and 2.11 eV of ε_0 values, respectively. In particular, 1% VO_x/MCF-17(DI) showed the highest ε_0 value (2.35 eV), demonstrating the highest amount of monomeric VO_x species on $m\text{-}SiO_2$. These results demonstrated that $V_2O_5/m\text{-}SiO_2$ catalysts prepared by the DI method show higher ε_0 values due to more numerous monomeric T_d species than those of catalysts by the WI method.

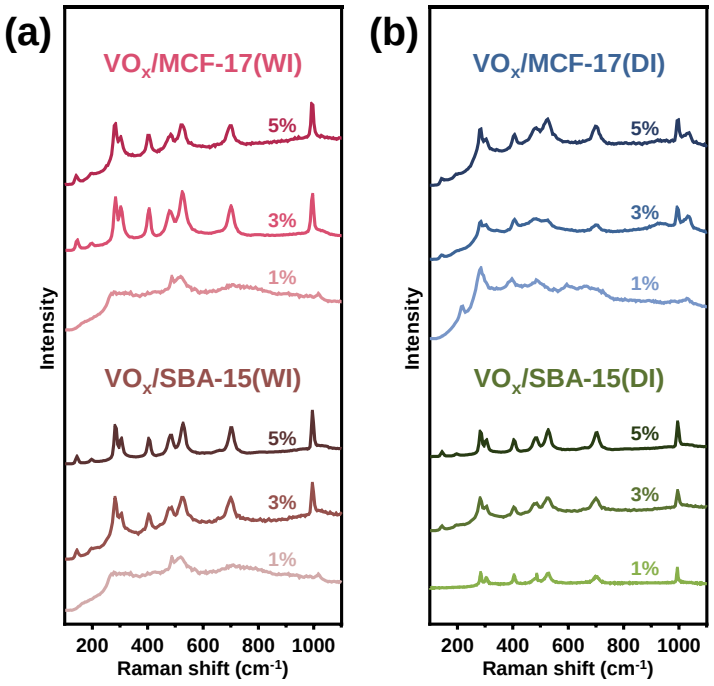

Figure 2.7. (a) Raman spectra of $VO_x/m\text{-}SiO_2$ catalysts prepared by (a) WI and (b) DI methods.

Raman spectroscopy was also used to identify an active vanadium site, including monomeric and polymeric vanadyl species.[33–35] Figure 2.7 shows the Raman spectra of $VO_x/m\text{-}SiO_2$ catalysts depending on the synthesis method and vanadium loading. The peak at 1040 cm^{-1} indicates the V=O stretching from monomeric VO_4 species, and the peaks at 140, 285, 305, 406, 521, 703, and 995 cm^{-1} correspond to the presence of crystalline V_2O_5 phase originated from a second V=O Raman stretching.[36] In Figure 2.7a, the monomeric VO_4 phase is dominant in 1% $V_2O_5/m\text{-}SiO_2$ catalysts prepared by the WI method.

As the vanadium content increases to 3 and 5%, the monomeric phase disappears and a distinct V_2O_5 peak appears at 995 cm^{-1} (Figure 2.7a). VO_x/SBA-15(DI) catalysts have a similar peak at 995 cm^{-1} (Figure 2.7b), because of the crystalline V_2O_5 phase. However, VO_x/MCF-17(DI) catalysts with a higher surface area show distinct peaks at 1040 cm^{-1}, revealing the presence of VO_4 species regardless of the vanadium content. The overall Raman peaks are sharper for the VO_x/*m*-SiO_2(WI) due to the higher content of the crystalline V_2O_5 than for VO_x/*m*-SiO_2(DI). Although VO_x/MCF-17(DI) catalysts also have the crystalline V_2O_5 phase, they contain the monomeric VO_4 phase as well. Depending on the synthesis method, the distributions of the surface vanadium species are different in VO_x/*m*-SiO_2 catalysts.

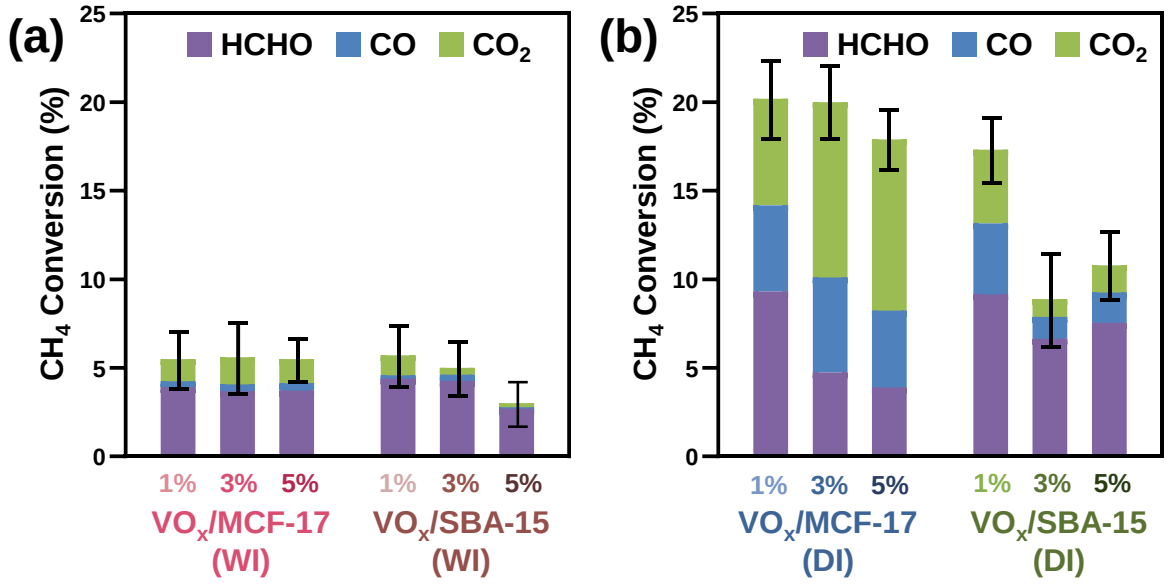

Figure 2.8. (a) Catalyst results of methane oxidation to formaldehyde over VO_x/*m*-SiO_2 catalysts prepared by (a) WI and (b) DI methods. Reaction conditions: CH_4/O_2 volume ratio of 1:1, 600 °C, 1 bar, W_{cat} = 100 mg, GHSV = 24,000 mL g_{cat}^{-1} h^{-1}.

2.3.3 Methane oxidation to formaldehyde

Catalytic methane oxidation was carried out in a fixed bed reactor at 600 °C in the presence of various VO_x/*m*-SiO_2 catalysts. Figure 2.8 and Table 2.2 summarize the catalytic results, including the methane conversion and the HCHO selectivity. Methane conversion is determined from the results of three repeated reactions and the deviations are indicated by error bars. While all VO_x/*m*-SiO_2(WI) catalysts show low methane conversion, less than 6% (Figure 2.8a), VO_x/*m*-SiO_2(DI) of the catalysts exhibit much higher conversion than VO_x/*m*-SiO_2(WI). In particular, VO*x* supported on MCF-17 show higher conversion percentages than those of SBA-15 prepared by DI, demonstrating that MCF-17 with its higher surface area and distinct mesocellular pore structure is a better support than SBA-15. As the vanadium content decreases to 1%, the methane conversion increases, demonstrating that a high

dispersion of VO_x is crucial for methane oxidation to formaldehyde. Among the catalysts, 1%

Table 2.2. Catalyst performance of VO_x/m-SiO_2 catalysts. (Reaction conditions: CH_4/O_2 volume ratio 1:1, 600 °C, 1 bar, W_{cat} = 100 mg, GHSV = 24,000 mL g_{cat}^{-1} h^{-1})

Catalyst	Vanadium loading	Conversion	Selectivity (%)		
	(%)	(%)	HCHO	CO	CO_2
VO_x/MCF-17 (WI)	1	5.5	71.2	6.1	22.7
	3	5.6	65.6	7.0	27.4
	5	5.5	67.4	7.5	25.1
VO_x/SBA-15 (WI)	1	5.7	77.0	3.4	19.6
	3	5.0	85.1	7.1	7.9
	5	3.0	89.4	3.4	7.2
VO_x/MCF-17 (DI)	1	20.2	46.1	24.1	29.8
	3	20.0	23.7	26.8	49.5
	5	17.9	21.7	24.3	54.0
VO_x/SBA-15 (DI)	1	17.3	52.9	23.1	24.1
	3	8.9	74.7	13.9	11.3
	5	10.8	69.8	15.9	14.2

VO_x/MCF-17(DI) shows the highest conversion (20.2%) because of the distinct monomeric VO_4 phase (Figure 2.8a). As the CH_4 conversion increases, a general trend of decrease in HCHO selectivity due to deep oxidation was observed. The high methane conversion of VO_x/MCF-17(DI) catalysts also yields greater selectivity for CO_2. However, the calculated production of net formaldehyde was much higher in VO_x/MCF-17(DI) catalysts with the high methane conversion. The Raman spectroscopy in Figure 2.7 shows a clear V=O bond stretch from the isolated species in all VO_x/MCF-17(DI) catalysts that recorded high CH_4 conversion regardless of the vanadium loading. In addition, the results of H_2-TPR showed a small change in peak maxima with vanadium loading, indicating a consistent monomeric VO_4 species in MCF-17. Also, the smallest ε_0 value of 1% VO_x/MCF-17(DI) represents the monomeric VO_4 species. Therefore, the vanadium content of VO_x/m-SiO_2 catalysts correlated with methane conversion demonstrates that the dispersions of vanadium and the monomeric VO_x phase are the most important factors for methane oxidation to formaldehyde. The DI method was also shown to be a better synthesis method than the WI for the high distribution of isolated tetrahedral species on m-SiO_2. In general, it is easy to think that using a solvent will make it more homogeneous, but it seems to be limited to a macroscopic point of view. When impregnation is carried out using a solvent (WI), the uniformity is often poor during the drying process.[37] A rotary evaporator is used to make the catalyst as uniform as possible for preparation. However, the WI causes a wide distribution of active species as the dissolved vanadium precursor solution forms water droplets on the catalyst surface during drying. As the solvent evaporates, the concentration imbalance is tilted towards the edge of the droplet rather than the center.[38]

This leads to a mixture of monomeric VO_4 species and bulk structure despite the low vanadium loading in the calcination process, and most of the vanadium load can be agglomerated. On the other hand, in the DI method, heat treatment proceeds immediately after solid mixing. Except for molecular transport through the calcination process, the aggregation of vanadium has limitations. Therefore, high dispersion catalysts can be synthesized by DI method rather than WI.

Table 2.2. Catalyst performance of $VO_x/m\text{-}SiO_2$ catalysts in the reaction conditions of CH_4/O_2 volume ratio 1:1, 600 °C, 1 bar, W_{cat} = 100 mg, GHSV = 24,000 mL g_{cat}^{-1} h^{-1}.

Catalyst	Vanadium loading	Conversion	Selectivity (%)		
	(%)	(%)	HCHO	CO	CO_2
VO_x/MCF-17 (WI)	1	5.5	71.2	6.1	22.7
	3	5.6	65.6	7.0	27.4
	5	5.5	67.4	7.5	25.1
VO_x/SBA-15 (WI)	1	5.7	77.0	3.4	19.6
	3	5.0	85.1	7.1	7.9
	5	3.0	89.4	3.4	7.2
VO_x/MCF-17 (DI)	1	20.2	46.1	24.1	29.8
	3	20.0	23.7	26.8	49.5
	5	17.9	21.7	24.3	54.0
VO_x/SBA-15 (DI)	1	17.3	52.9	23.1	24.1
	3	8.9	74.7	13.9	11.3
	5	10.8	69.8	15.9	14.2

2.4. Conclusion

The isolated monomeric VO_4 species proved to be a key active species for methane oxidation to formaldehyde. This is evidenced based on the reaction results and properties of the catalyst prepared by three factors. The role of $VO_x/m\text{-}SiO_2$ catalysts was investigated by varying the type of $m\text{-}SiO_2$ (SBA-15 and MCF-17), vanadium loading (1%, 3%, and 5%), and preparation method (WI and DI). Because the surface area and pore size of MCF-17 were greater than that of SBA-15, the VO_x/MCF-17 catalysts resulted in higher dispersion of the vanadium species. H_2-TPR and Raman results showed that DI was the better method for obtaining the isolated tetrahedral monovanadate species in $VO_x/m\text{-}SiO_2$ catalysts. Methane oxidation over various $VO_x/m\text{-}SiO_2$ catalysts at 600 °C showed that $VO_x/m\text{-}SiO_2$(DI) catalysts led to much higher conversion rates than $VO_x/m\text{-}SiO_2$(WI). As the vanadium content was decreased to 1%, the methane conversion increased, because of the high dispersion of monomeric VO_4 in the catalysts with low vanadium loading. Owing to the high surface area and distinct mesocellular pore structure of MCF-17, 1% VO_x/MCF-17(DI) showed the highest conversion (20.2%). As the methane conversion increased, the selectivity toward formaldehyde decreased; however, the net production of

formaldehyde was much higher when using VO_x/MCF-17(DI) than when using the VO_x/SBA-15(DI) and VO_x/SBA-15(WI) catalysts. In particular, VO_x/*m*-SiO_2 prepared by using MCF-17 via the DI method was proven to be the best catalyst for the direct conversion of methane oxidation to formaldehyde.

2.5. References

1. N. Ohler and A. T. Bell, Selective oxidation of methane over MoO_x/SiO_2: isolation of the kinetics of reactions occurring in the gas phase and on the surfaces of SiO_2 and MoO_x. *J. Catal.*, **2005**, *231*, 115.
2. F. Arena, N. Giordano and A. Parmaliana, Working Mechanism of Oxide Catalysts in the Partial Oxidation of Methane to Formaldehyde. II. Redox Properties and Reactivity of SiO_2, MoO_3/SiO_2, V_2O_5/SiO_2, TiO_2, and V_2O_5/TiO_2 Systems. *J. Catal.*, **1997**, *167*, 66.
3. N. Ohler and A. T. Bell, Study of the elementary processes involved in the selective oxidation of methane over MoO_x/SiO_2. *J. Phys. Chem. B*, **2006**, *110*, 2700.
4. J. H. Lunsford, Catalytic conversion of methane to more useful chemicals and fuels: a challenge for the 21st century. *Catal. Today*, **2000**, *63*, 165.
5. C. Hammond, S. Conrad and I. Hermans, Oxidative methane upgrading. *ChemSusChem* **2012**, *5*, 1668.
6. M. Monai, T. Montini, R. J. Gorte and P. Fornasiero, Catalytic oxidation of methane: Pd and beyond. *Eur. J. Inorg. Chem.*, **2018**, *25*, 2884.
7. L. Nguyen, S. Loridant, H. Launay, A. Pigamo, J. Dubois and J. Millet, Study of new catalysts based on vanadium oxide supported on mesoporous silica for the partial oxidation of methane to formaldehyde: Catalytic properties and reaction mechanism. *J. Catal.*, **2006**, *237*, 38.
8. F. Arena and A. Parmaliana, Scientific basis for process and catalyst design in the selective oxidation of methane to formaldehyde. *Acc. Chem. Res.*, **2003**, *36*, 867.
9. G. Du, S. Lim, Y. Yang, C. Wang, L. Pfefferle and G. L. Haller, Catalytic performance of vanadium incorporated MCM-41 catalysts for the partial oxidation of methane to formaldehyde. *Appl. Catal. A*, **2006**, *302*, 48.
10. G. J. Hutchings, M. S. Scurrell and J. R. Woodhouse, Oxidative Coupling of Methane Using Oxide Catalysts. *Chem. Soc. Rev.*, **1989**, *18*, 251.
11. R. G. Herman, Q. Sun, C. Shi, K. Klier, C.-B. Wang, H. Hu, I. E. Wachs and M. M. Bhasin, Development of active oxide catalysts for the direct oxidation of methane to formaldehyde. *Catal. Today*, **1997**, *37*, 1.
12. A. Parmaliana, V. Sokolovskii, D. Miceli, F. Arena and N. Giordano, Silica-Supported MoO_3 and V_2O_5 Catalysts in Partial Oxidation of Methane to Formaldehyde, *ACS Symp. Ser., Am. Chem. Soc., Washington, DC*, **1993**, 43.
13. X. H. Sun, Y. F. Shi, P. Zhang, C. M. Zheng, X. Y. Zheng, F. Zhang, Y. C. Zhang, N. J. Guan, D. Y. Zhao and G. D. Stucky, Container Effect in Nanocasting Synthesis of Mesoporous Metal Oxides. *J. Am. Chem. Soc.*, **2011**, *133*, 14542.
14. C. Perego and R. Millini, Porous materials in catalysis: challenges for mesoporous materials. *Chem. Soc. Rev.*, **2013**, *42*, 3956.
15. D. Gu and F. Schuth, Synthesis of non-siliceous mesoporous oxides. *Chem. Soc. Rev.*, **2014**, *43*, 313.

16. P. Wallis, S. Wohlrab, V. N. Kalevaru, M. Frank and A. Martin, Impact of support pore structure and morphology on catalyst performance of VO_x/SBA-15 for selective methane oxidation. *Catal. Today*, **2016**, *278*, 120.

17. K. Inumaru, M. Misono and T. Okuhara, Structure and catalysis of vanadium oxide overlayers on oxide supports. *Appl. Catal. A*, **1997**, *149*, 133.

18. I. E. Wachs, Catalysis science of supported vanadium oxide catalysts. *Dalton Trans.*, **2013**, *42*, 11762.

19. J. A. Schwarz, C. Contescu and A. Contescu, Methods for Preparation of Catalytic Materials. *Chem. Rev.*, **1995**, *95*, 477.

20. D. Zhao, J. Sun, Q. Li and G. D. Stucky, Morphological control of highly ordered mesoporous silica SBA-15. *Chem. Mater.*, **2000**, *12*, 275.

21. T. Klimova, A. Esquivel, J. Reyes, M. Rubio, X. Bokhimi and J. Aracil, Factorial design for the evaluation of the influence of synthesis parameters upon the textural and structural properties of SBA-15 ordered materials. *Micropor. Mesopor. Mat.*, **2006**, *93*, 331.

22. C.-K. Tsung, J. N. Kuhn, W. Huang, C. Aliaga, L.-I. Hung, G. A. Somorjai and P. Yang, Sub-10 nm platinum nanocrystals with size and shape control: catalytic study for ethylene and pyrrole hydrogenation. *J. Am. Chem. Soc.*, **2009**, *131*, 5816.

23. S. Siggia and W. Maxcy, Improved procedure for determination of aldehydes. *Anal. Chem.*, **1947**, *19*, 1023.

24. T. Sugino, A. Kido, N. Azuma, A. Ueno, Y and Udagawa, Partial oxidation of methane on silica-supported silicomolybdic acid catalysts in an excess amount of water vapor. *J. Catal.*, **2000**, *190*, 118.

25. C. A. Carrero, R. Schloegl, I. E. Wachs and R. Schomaecker, Critical Literature Review of the Kinetics for the Oxidative Dehydrogenation of Propane over Well-Defined Supported Vanadium Oxide Catalysts, *ACS Catal.*, **2014**, *4*, 3357.

26. G. Du, S. Lim, M. Pinault, C. Wang, F. Fang, L. Pfefferle and G. L. Haller, Synthesis, characterization, and catalytic performance of highly dispersed vanadium grafted SBA-15 catalyst. *J. Catal.*, **2008**, *253*, 74.

27. B. Olthof, A. Khodakov, A. T. Bell and E. Iglesia, Effects of support composition and pretreatment conditions on the structure of vanadia dispersed on SiO_2, Al_2O_3, TiO_2, ZrO_2, and HfO_2. *J. Phys. Chem. B*, **2000**, *104*, 1516.

28. D. Wei, H. Wang, X. Feng, W.-T. Chueh, P. Ravikovitch, M. Lyubovsky, C. Li, T. Takeguchi and G. L. Haller, Synthesis and characterization of vanadium-substituted mesoporous molecular sieves. *J. Phys. Chem. B*, **1999**, *103*, 2113.

29. V. Sokolovskii, F. Arena, S. Coluccia and A. Parmaliana, Coordination Symmetry and Reduction Features of V Ions in V_2O_5/SiO_2 Catalysts: Relevance to the Partial Oxidation of Light Alkanes. *J. Catal.*, **1998**, *173*, 238.

30. X. Gao and I. E. Wachs, Investigation of surface structures of supported vanadium oxide catalysts by UV–vis–NIR diffuse reflectance spectroscopy. *J. Phys. Chem. B*, **2000**, *104*, 1261.

31. L. J. Burcham, G. Deo, X. Gao and I. E. Wachs, *In situ* IR, Raman, and UV-Vis DRS spectroscopy of supported vanadium oxide catalysts during methanol oxidation. *Top. Catal.*, **2000**, *11*, 85.

32. X. Gao, S. R. Bare, B. M. Weckhuysen and I. E. Wachs, *In situ* spectroscopic investigation of molecular structures of highly dispersed vanadium oxide on silica under various conditions. *J. Phys. Chem. B*, **1998**, *102*, 10842.

33. H. Launay, S. Loridant, A. Pigamo, J. Dubois and J. Millet, Vanadium species in new catalysts for the selective oxidation of methane to formaldehyde: Specificity and molecular structure

dynamics with water. *J. Catal.*, **2007**, *246*, 390.

34. D. E. Keller, T. Visser, F. Soulimani, D. C. Koningsberger and B. M. Weckhuysen, Hydration effects on the molecular structure of silica-supported vanadium oxide catalysts: A combined IR, Raman, UV–vis and EXAFS study. *Vib. Spectrosc.*, **2007**, *43*, 140.

35. B. M. Weckhuysen and D. E. Keller, Chemistry, spectroscopy and the role of supported vanadium oxides in heterogeneous catalysis. *Catal. Today*, **2003**, *78*, 25.

36. A. G. Anshits, E. V. Kondratenko, E. N. Voskresenskaya, L. I. Kurteeva and N. I. Pavlenko, The influence of O_2 on oxidative coupling of methane over oxide catalysts using N_2O as oxidant. *Catal. Today*, **1998**, *46*, 211.

37. R. D. Deegan, O. Bakajin, T.F. Dupont, G. Huber, S.R. Nagel and T.A. Witten, Capillary flow as the cause of ring stains from dried liquid drops, *Nature*, **1997**, *389*, 827.

38. S. Kumar, J. S. Katz and C. M. Schroeder, Heterogeneous drying and nonmonotonic contact angle dynamics in concentrated film-forming latex drops, *Phys. Rev. Fluids*, **2017**, *2*, 114304.

Chapter 3

SiO_2@V_2O_5@Al_2O_3 Core–Shell Catalysts with High Activity and Stability for Methane Oxidation to Formaldehyde

This chapter includes the published contents:
E. Yang, J. G. Lee, D. H. Kim, Y. S. Jung, J. H. Kwak, E. D. Park and K. An. *J. Catal.* **2018**, *368*, 134. DOI: 10.1016/j.jcat.2018.09.027.

3.1. Introduction

Methane, the main component of natural gas, is mainly used for heating and electricity generation.[1–3] Recent progress in shale gas collection technology based on hydraulic fracturing presents a further stimulus for converting abundant methane to more valuable chemical feedstocks and thus reducing dependence on petroleum resources.[1] Nevertheless, the four strong C–H bonds of methane (bond energy = 413 kJ mol^{-1}) present a serious obstacle to its chemical conversion. At elevated temperatures, methane can be catalytically converted to syngas, which can be used as a feedstock for the catalytic production of added-value hydrocarbons or alcohols. Although several indirect processes for the oxidative conversion of methane to formaldehyde (HCHO), methanol (CH_3OH), and ethylene (C_2H_4) have been developed and applied industrially,[4–8] direct conversion of methane by partial oxidation is still challenging in view of the abovementioned high C–H bond energy and the need to avoid the production of carbon dioxide as a GHG.[9] Previous studies on methane oxidation to HCHO demonstrated that temperatures above 600 °C are required to break the strong C–H bonds and identified supported V_2O_5 and MoO_3 as the best partial oxidation catalysts for producing HCHO or CH_3OH.[10–12] However, HCHO easily undergoes further oxidation to CO and H_2O, which requires the development of efficient partial oxidation catalysts, for example, by modifying the above catalysts while preserving their high-temperature active sites. Notably, the use of noble metals such as Pt or Pd for C–H bond activation results in the complete oxidation of methane to CO, CO_2, and H_2O.[13–16] For these reasons, the partial oxidation of methane to HCHO is still regarded as a challenging reaction, and the best methane-to-HCHO conversion achieved so far at 600 °C is less than 10%. Parmaliana *et al.* reported that conversions of 1–3% obtained at 600 °C for V_2O_5/SiO_2 catalysts prepared by impregnation further increased to 25% at 700 °C, although the HCHO selectivity was less than 30%.[10] Nguyen *et al.* used *m*-

SiO_2 to prepare several impregnated V_2O_5/SiO_2 catalysts,[11] since silica was identified as the best support for V_2O_5-based catalysts for methane partial oxidation,[10–13,17–20] achieving methane-to-HCHO conversion and selectivity of 6.3 and 58%, respectively, at 600 °C.[11]

The thermal stability of catalytically active surface species can be increased by protection/encapsulation with robust oxide(s). In well-designed core@shell-type catalysts, highly disperse active species in the core can be protected against deactivation caused by sintering or coking during high-temperature reactions.[21–31] ALD is considered an attractive thin film growth technique for homogeneous encapsulation of active species, allowing the surfaces of core species to be uniformly coated with layers of controlled thickness at an atomic scale.[32–35] In view of the fact that overly thick ALD coatings reduce the activity of core catalysts, the abovementioned control of coating layer thickness is critical for the maximization of catalyst activity/stability and for the preservation of active species under severe reaction conditions.

Here, we designed highly disperse V_2O_5 nanocatalysts supported on SiO_2 spheres for the direct oxidation of methane to HCHO, utilizing a hydrothermal reaction to attach V_2O_5 nanoparticles uniformly to the surfaces of SiO_2 spheres. The original structure of V_2O_5 nanoparticles collapsed at temperatures above 300 °C, which was mitigated by further coating SiO_2@V_2O_5 core@shell structures via the alumina ALD with trimethylaluminum (TMA) as an alumina source.[36] Multicycle ALD coating afforded controlled-layer-thickness SiO_2@V_2O_5@-Al_2O_3 core@shell nanostructures, which were used for the catalytic oxidation of methane to HCHO in a plug-flow fixed-bed reactor at 600 °C. Whereas negligible conversion was observed for SiO_2@V_2O_5 catalysts without alumina shells because of V_2O_5 nanoparticle sintering, SiO_2@V_2O_5@Al_2O_3 core@shell nanostructures exhibited increased thermal stability at 600 °C which depended on the thickness of their alumina coatings. TEM, scanning electron microscopy (SEM), scanning transmission electron microscopy (STEM), energy dispersive X-ray spectroscopy (EDS), *in situ* XRD, Raman spectroscopy, H_2-TPR, and diffuse reflectance UV-vis spectroscopy analyses were used to determine the mechanism of core vanadium species preservation at high temperature and the type of core@shell structures achieving maximal methane-to-HCHO conversion without undergoing deactivation. Compared with conventional V_2O_5 supported on *m*-SiO_2 catalysts prepared by impregnation, SiO_2@V_2O_5@Al_2O_3 core@shell nanostructures achieved exceptionally high methane conversion and featured increased stability, which was ascribed to the presence of alumina shells over V_2O_5 nanoparticles.

3.2. Experiential Methods

3.2.1 Preparation of SiO_2@V_2O_5 nanostructures

Silica spheres were synthesized by the Stöber method.[37] Briefly, NH_4OH (7.5 mL) and H_2O (24 mL) were dispersed in ethanol (294 mL) under vigorous stirring at room temperature. Tetraethyl orthosilicate (TEOS; Aldrich, 98%, 15 mL) was added dropwise to the obtained solution, and the reaction mixture was stirred for 24 h further. The resulting opaque solution was filtered, and the filter cake was washed with ethanol and dried at 70 °C to obtain silica spheres. To synthesize SiO_2@V_2O_5 core@shell nanostructures, as-prepared silica spheres (0.3 g) were mixed with vanadyl acetylacetonate ($VO(acac)_2$; Sigma-Aldrich, 97%, 0.83 g) in dimethylformamide (40 mL) under 3 h sonication.[38] The obtained dispersion was placed in a 50 mL Teflon-lined autoclave reactor and heated at 220 °C for 24 h. The dark precipitate was separated by centrifugation, washed with ethanol, dried at 70 °C, and calcined at 400 °C for 3 h to obtain SiO_2@V_2O_5 core@shell nanostructures.

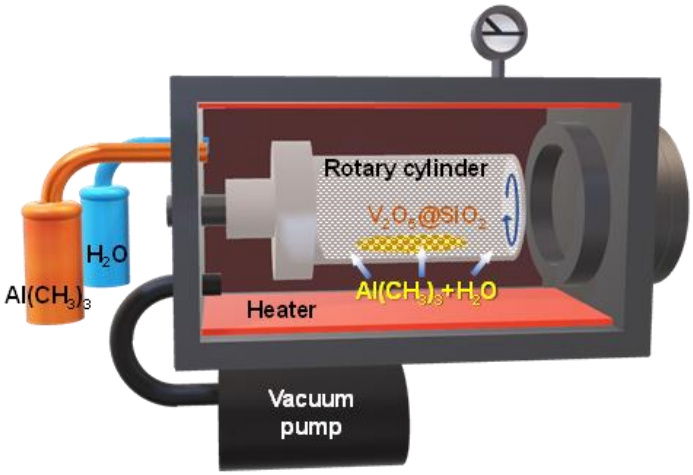

Figure 3.1. A schematic illustration of ALD for the preparation of SiO_2@V_2O_5@Al_2O_3 core@shell nanostructures.

3.2.2 Preparation of SiO_2@V_2O_5@Al_2O_3-(x) (x = 10, 30, 40, 50, 70, and 100) core@shell nanostructures

Al_2O_3 shells were grown on SiO_2@V_2O_5 core@shell structures in a rotary ALD reactor using a TMA (Sigma-Aldrich, 97%; alumina precursor)–Ar–H_2O–Ar sequence.[36] An overview of the ALD equipment is provided in Figure 3.1. First, SiO_2@V_2O_5 powders were loaded into a porous stainless-steel cylinder that was rotated at 140 rpm inside the reaction chamber. For a single cycle of the ALD sequence, TMA introduced at a pressure of 2 Torr was deposited onto V_2O_5 surfaces at 180 °C, and the chamber was subsequently evacuated to remove CH_4 generated as a byproduct and unreacted TMA. The chamber was filled with Ar to a pressure of 20 Torr and evacuated after several minutes. Then H_2O

(2 Torr) was introduced to replace the methyl groups of the attached TMA with OH groups, and the chamber was evacuated to remove the produced CH_4 and excess H_2O and purged with Ar (20 Torr). For the second cycle, the above steps were repeated. The number of cycles was denoted as (x) and was found to be proportional to the thickness of Al_2O_3 shells. SiO_2@V_2O_5@Al_2O_3-(x) core@shell nanostructures with controlled Al_2O_3 shell thickness were prepared using different numbers of ALD cycles (x = *10*, *30*, *40*, *50*, *70*, and *100*).

3.2.3 Preparation of mesoporous silica-supported V_2O_5 catalysts

Conventional V_2O_5/*m*-SiO_2 catalysts were prepared by incipient wetness impregnation. *m*-SiO_2 with a mesocellular structure (MCF-17) prepared by a previously described method was used as a support.[39] Briefly, 1,3,5-trimethylbenzene (Sigma-Aldrich, 98%; 4 g) was dissolved in 75 mL of an aqueous solution containing 4 g of Pluronic P123 triblock copolymer (Aldrich, average $M_w \approx 5800$ Da) and 10 mL of concentrated HCl. The reaction mixture was stirred for 2 h at 40 °C and then treated with TEOS (9.2 mL) and maintained for 5 min. The resulting solution was kept at 40 °C for 20 h without stirring, treated with NH_4F (Sigma-Aldrich, 98%; 46 mg), and further aged in a closed bottle at 100 °C for another 24 h. The obtained white precipitate was filtered, washed with water and ethanol, and calcined in air at 600 °C for 6 h to obtain MCF-17. V_2O_5/*m*-SiO_2 catalysts were prepared by exposing MCF-17 (1 g) overnight to a solution of ammonium vanadium oxide (NH_4VO_3, Alfa Aesar, 99%) in the presence of oxalic acid dihydrate ($C_2H_2O_4 \cdot 2H_2O$, Acros Organics, 99%). Centrifugation followed by drying afforded solid V_2O_5/*m*-SiO_2 catalysts with vanadium precursor loadings of 1, 3, and 5 wt% after calcination at 350 °C for 4 h. Conventional V_2O_5/Al_2O_3 catalysts were also prepared by the same impregnation method in the presence of commercial Al_2O_3 (Puralox SBa200, Sasol) for comparison. In detail, 1 g of Al_2O_3 was mixed with oxalic acid dihydrate in an ethanol solution of NH_4VO_3. After drying at 60 °C and calcination at 350 °C 4 h, 3 and 5 wt% of V_2O_5/Al_2O_3 catalysts were obtained.

3.2.4 Characterization

Powder and *in situ* XRD patterns were acquired in a 2θ range of 20–80° (Cu K_α radiation, λ = 1.5418 Å) using PANalytical X'Pert Pro and Rigaku SmartLab X-ray diffractometers, respectively. Prior to measurements, samples were loaded onto a holder and preheated at 150 °C for 30 min under Ar. *In situ* spectra were recorded for catalysts exposed to a heated gas mixture of 4% CH_4, 4% O_2, and balance Ar in steps of 50 °C from 100 to 800 °C using a specially constructed cell. BET surface areas were determined from N_2 adsorption/desorption isotherms recorded on a microtrac BELsorp-Max analyzer. Pore size distributions were determined by the Barrett–Joyner–Halenda method. SEM imaging was performed using a Hitachi S-4800 microscope, and TEM imaging was performed using a JEOL JEM-2100F instrument operated at 200 kV. An EDS analyzer was used for elemental analysis

(Oxford Instruments, X-Max 80 T). TPR was carried out on the abovementioned Micromeritics AutoChem II 2920 instrument. Typically, a catalyst sample (100 mg) was loaded into a U-shaped quartz tube and outgassed under He flow at 150 °C for 30 min. Subsequently, the temperature was increased to 800 °C at a rate of 10 °C min^{-1} in a flow of 10% H_2 in He (50 mL min^{-1}). The amount of H_2 consumed was determined by GC using a Delsi Nermag TCD. Diffuse reflectance UV–vis spectra were recorded with a scan step of 1 nm on an Agilent Cary 5000 UV–vis spectrophotometer operated in the region 200–2200 nm. A halon white (PTFE) reflectance standard was used as a reference background. Raman spectra were collected utilizing a WITec alpha300 R spectrometer equipped with a 532 nm diode laser. The laser power was set to 0.1 mW. To obtain sufficient signal-to-noise ratios, spectra were obtained using charge coupled device (CCD) with 10-s exposure and 10-fold accumulation.

3.2.5 Methane oxidation

Catalytic methane oxidation was conducted in a laboratory-scale flow reactor at atmospheric pressure and a constant temperature of 600 °C. As-synthesized vanadium-based catalysts were pelletized and sieved to a particle size of 150–250 μm. A 100 mg catalyst sample was loaded into a quartz tube (inner diameter 1 cm) together with 1 g of purified sand. CH_4 (99.95%) and O_2 (99.995%) in a 1:1 v/v ratio were fed from the top to the bottom of the catalyst bed at a rate of 40 sccm using mass flow controllers, and the gas hourly space velocity (GHSV) was maintained at 24,000 mL g_{cat}^{-1} h^{-1}. The reactor was heated to 600 °C in a furnace and equipped with an inserted thermocouple to monitor temperature. Products were monitored using an online GC (YL6500) equipped with Porapak-N and molecular sieve columns connected to both TCD and FID with a methanizer (Ar was flowed in as a reference). No methane conversion was detected when empty quartz or bare SiO_2 spheres without V_2O_5 were tested. HCHO, CO, CO_2, and H_2 were identified as the main reaction products. Before the converted gases entered the GC, HCHO was trapped in 10.5 g of Na_2SO_3 and 1.63 g of H_2SO_4 cooled in an ice bath, and the amount of trapped HCHO was determined by titrating the produced NaOH with H_2SO_4.[11,40,41] Methane conversion was calculated as the ratio of consumed and original methane amounts using GC data for points in stabilized areas with maximum activity values. Selectivity was calculated as the ratio of product amount and total converted methane amount. The conversion of SiO_2@V_2O_5@Al_2O_3-(*x*) core@shell nanostructures (*x* = *0*, *10*, *30*, *40*, *50*, *70*, and *100*) was determined by the average value of methane conversions, in which each reaction was conducted more than three times for reproducibility. We calculated turnover frequency (TOF_{HCHO}) by the number of CH_4 molecules reacted to HCHO on each available vanadium site per time. By assuming that an isolated vanadium species on the outermost surface of the V_2O_5 nanoparticles was contacted with the alumina shell, the total surface area of the core@shell catalyst was determined by the size and mass of the structure. SiO_2 spheres with an average diameter of 150 nm were wrapped in V_2O_5 with a thickness of ca. 35 nm. The mass of a single nanostructure was obtained by multiplying the volume and density that were

calculated from the BET measurement. The number of core@shell nanostructures was estimated by the mass of a single nanoparticle; thus the total surface area and the isolated surface vanadium sites (7.3×10^{18}) were finally determined for the TOFs.

3.3. Results and Discussion

3.3.1 Preparation of SiO_2@V_2O_5@Al_2O_3 core@shell catalysts

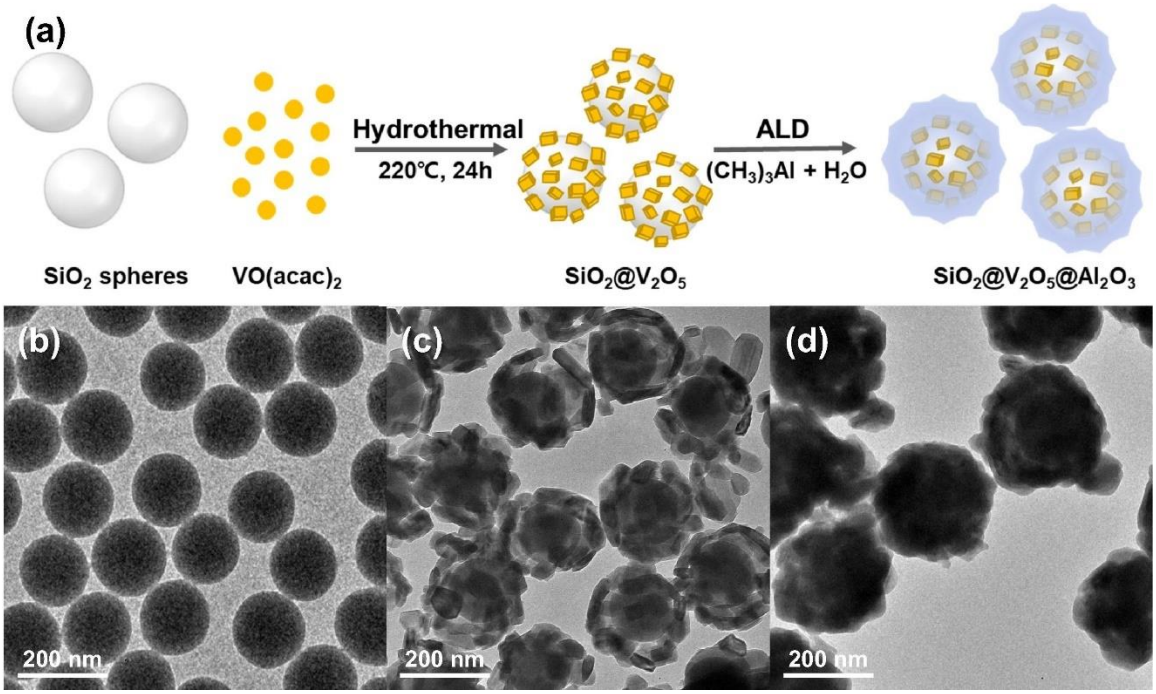

Figure 3.2. (a) Schematic preparation of SiO_2@V_2O_5@Al_2O_3 core@shell nanostructures. TEM images of (b) SiO_2 spheres, (c) SiO_2@V_2O_5, and (d) SiO_2@V_2O_5@Al_2O_3-(*50*) core@shell nanostructures.

As mentioned above, SiO_2@V_2O_5@Al_2O_3 core@shell nanostructures were prepared by hydrothermal synthesis followed by ALD (Figure 3.2a), and SiO_2 spheres with an average size of 150 nm were synthesized using the well-known Stöber method (Figure 3.2b).[37] Discrete V_2O_5 nanoparticles with an average size of 35 nm were deposited on the surfaces of SiO_2 spheres by a hydrothermal reaction in the presence of $VO(acac)_2$ (Figure 3.2c). During the reaction, small vanadium clusters were first formed by nucleation, and then the vanadium species were mostly attached to SiO_2 spheres, because of the hydrophilic nature of the SiO_2 surface. By subsequent ALD with various numbers of repeating cycles, thin Al_2O_3 layers were deposited over SiO_2@V_2O_5 core@shells with a controlled thickness. Figure 3.2d shows a TEM image of representative SiO_2@V_2O_5@Al_2O_3-(*50*) core@shell nanostructures, unambiguously demonstrating the presence of Al_2O_3 layers coating the core structures.

The surface morphology of SiO_2@V_2O_5@Al_2O_3-(*50*) core@shell nanostructures was investigated by SEM, STEM, and EDS. Figure 3.3a clearly demonstrates that outer Al_2O_3 layers were

homogeneously deposited on the entire surface of SiO_2@V_2O_5 nanostructures. STEM imaging and the corresponding elemental mappings with EDS line scanning (Figure 3.3b) showed that O and V (derived from V_2O_5) were uniformly dispersed in the shell, while Si (derived from silica spheres) was mainly located in the core. Moreover, the distribution of alumina over the whole core@shell nanostructures demonstrated that they were coated by thin Al_2O_3 shell layers. SiO_2@V_2O_5@Al_2O_3-(*x*) core@shell nanostructures were also characterized by high-resolution TEM (Figure 3.4), which revealed that 100 ALD cycles were sufficient to obtain full coverage by 20-nm-thick Al_2O_3 layers, while *10* cycles did not suffice for an effective coating.

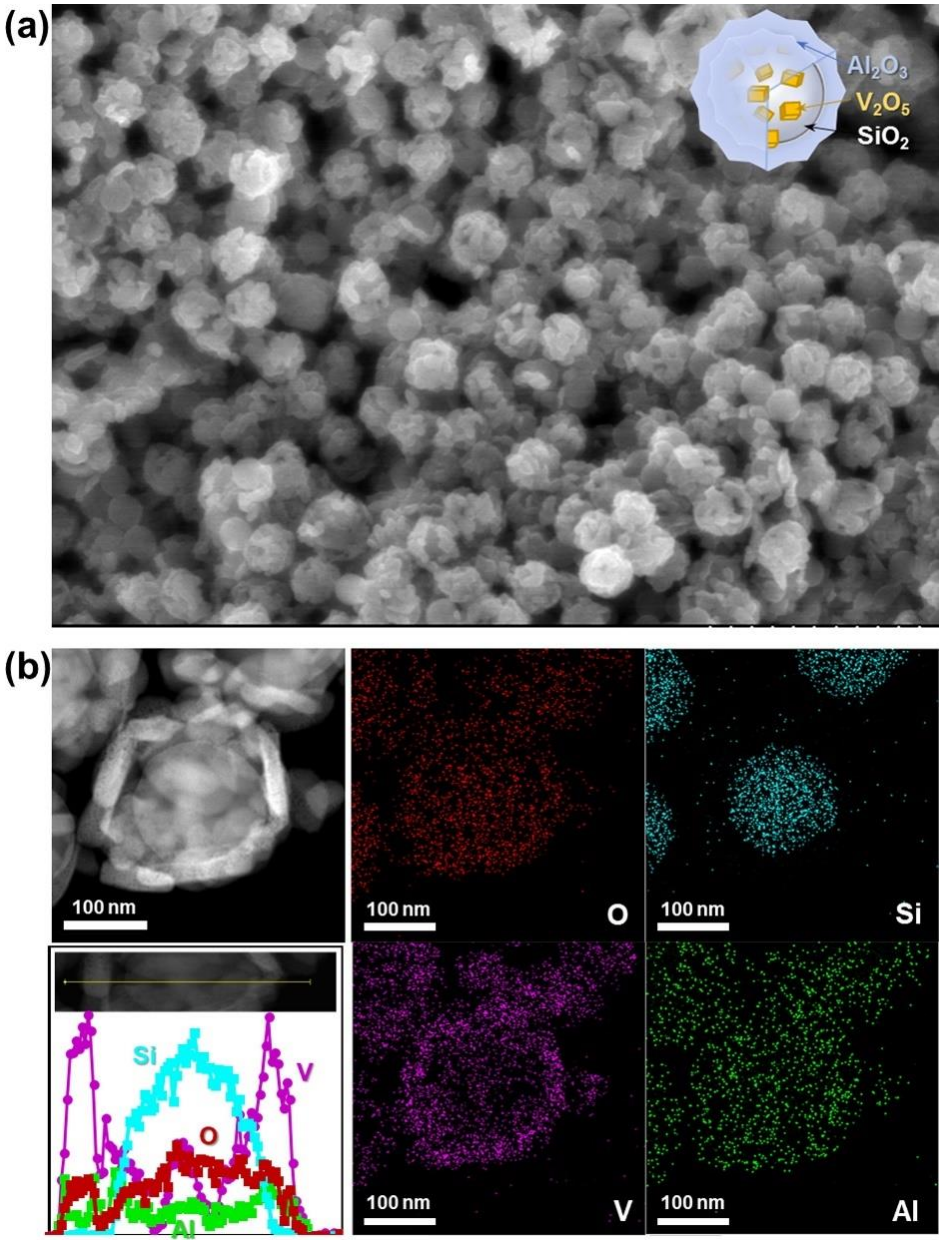

Figure 3.3. Structural characterization of SiO_2@V_2O_5@Al_2O_3-(*50*) core@shell nanostructures: (a) SEM image, (b) STEM images with a line-scan EDS spectrum.

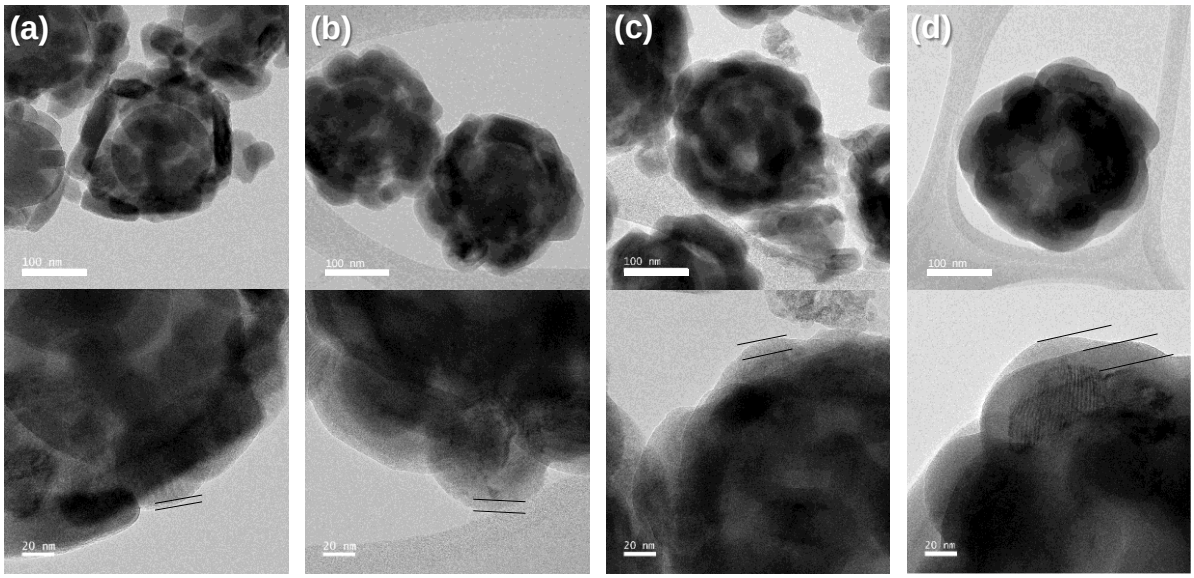

Figure 3.4. TEM and high-resolution TEM images of (a) SiO_2@V_2O_5@Al_2O_3-(*10*), (b) SiO_2@V_2O_5@Al_2O_3-(*30*), (c) SiO_2@V_2O_5@Al_2O_3-(*50*), and (d) SiO_2@V_2O_5@Al_2O_3-(*100*) core@shell nanostructures prepared by different ALD cycles.

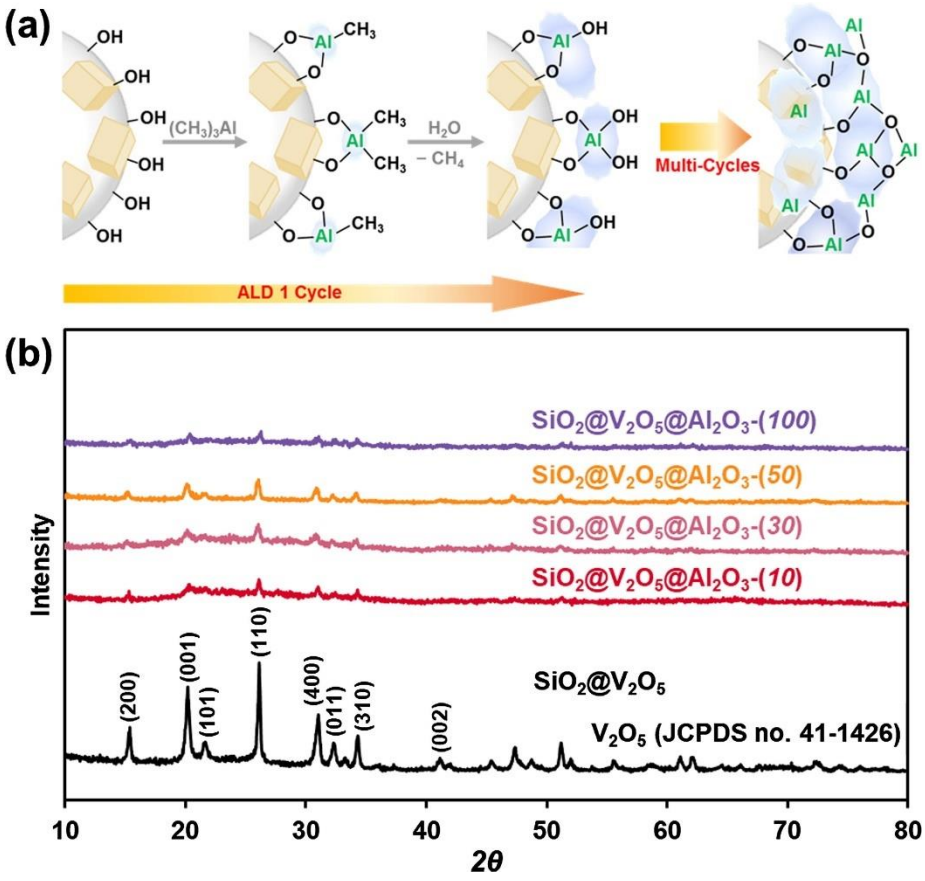

Figure 3.5. (a) Schematic illustration of the ALD process used for multicycle coating of Al_2O_3 shells on SiO_2@V_2O_5 nanostructures. (b) XRD patterns of SiO_2@V_2O_5@Al_2O_3-(*x*) nanostructures. (*x = 0, 10, 30, 50, 100*)

The shell thickness of SiO_2@V_2O_5@Al_2O_3 core@shell nanostructures increased with the number of ALD cycles (Figure 3.5a). The introduced TMA precursor was adsorbed onto V_2O_5 surfaces to create Al–O bonds, and $Al(OH)_4$ units (together with methane) were finally produced upon the addition of water vapor. Subsequent ALD cycles resulted in the deposition of additional alumina layers over SiO_2@V_2O_5. The XRD patterns of SiO_2@V_2O_5 core@shell catalysts (Figure 3.5b) revealed the presence of characteristic peaks of V_2O_5 (*Pmmn*, $a = 1.1516$, $b = 0.3566$, $c = 0.4372$ nm). Application of the Scherrer equation to the (110) peak allowed the crystallite size of SiO_2@V_2O_5 core@shell structures to be estimated as 40.1 nm, which agreed with values obtained by TEM and SEM. However, much weaker XRD peaks were observed for SiO_2@V_2O_5@Al_2O_3 core@shell nanostructures (Figure 3.5b), since the Al_2O_3 shell was not crystalline. XRD analysis of SiO_2@V_2O_5@Al_2O_3-(x), (*x = 10, 30, 50, and 100*) nanostructures revealed that as the number of ALD cycles increased from *10* to *100*, the crystallite size (calculated as mentioned above) increased from 31.3 to 34.6 nm. Two explanations were proposed for this result, namely (a) as-prepared V_2O_5 nanoparticles diffused to Al_2O_3 surfaces with decreased sizes of V_2O_5 and (b) diffraction from the V_2O_5 core was hindered by thick Al_2O_3 shells obtained after an increased number of ALD cycles.

3.3.2 Thermal stability of V_2O_5 species in core@shell nanostructures

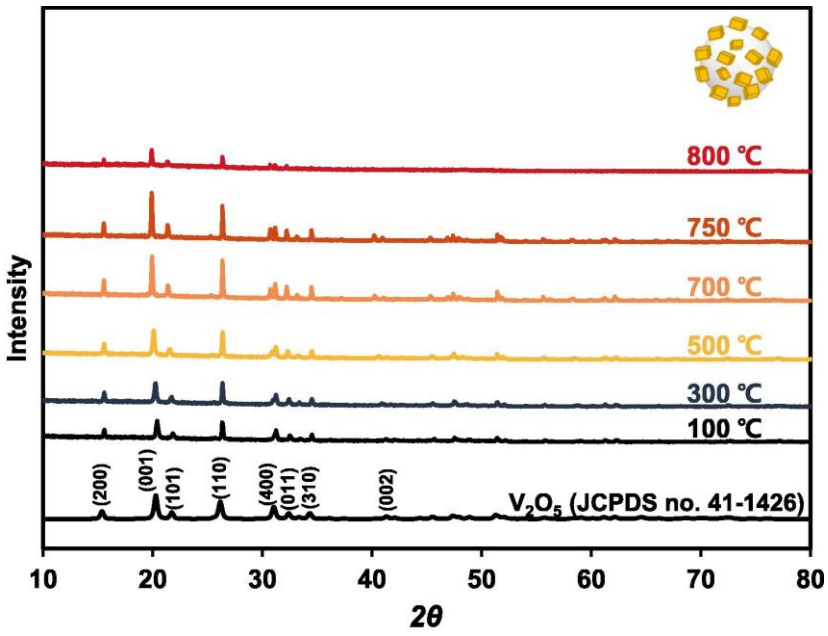

Figure 3.6. *In situ* XRD patterns of SiO_2@V_2O_5 nanostructures.

The thermal stability of SiO_2@V_2O_5 core@shell catalysts before and after Al_2O_3 deposition was probed by *in situ* XRD analysis at 100–800 °C under 4% CH_4, 4% O_2, and balance Ar. Figure 3.6 shows that the characteristic XRD peaks of V_2O_5 were preserved in SiO_2@V_2O_5 core@shells, while the peak intensity increased with increasing temperature up to 750 °C. The crystallite size calculated by the

Scherrer equation for V_2O_5 nanoparticles increased from 50.8 nm at 100 °C to 77.9 nm at 750 °C. At a high temperature, the outer V_2O_5 nanoparticles gradually collapsed. Above 800 °C, structural dissociation decreased XRD peak resolution, and only the main peaks were observed. Conversely, SiO_2@V_2O_5@Al_2O_3-(*50*) core@shell nanostructures maintained their XRD peak intensities up to 800 °C, which demonstrated that the presence of Al_2O_3 shells prevented the aggregation of core V_2O_5 nanoparticles at a high temperature (Figure 3.7). Detailed information on the particle size of core V_2O_5 in SiO_2@V_2O_5@Al_2O_3 core@shell nanostructures determined by *in situ* XRD analysis is provided in Table 3.1.

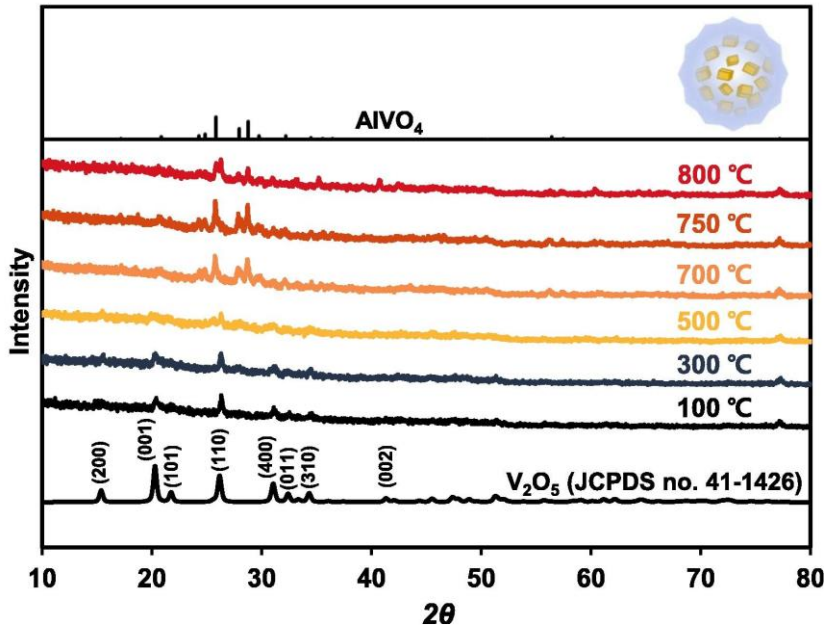

Figure 3.7. *In situ* XRD patterns of SiO_2@V_2O_5@Al_2O_3-(*50*) nanostructures.

Table 3.1. The calculated particle sizes of SiO_2@V_2O_5 and SiO_2@V_2O_5@Al_2O_3-(*50*) core@shell nanostructures derived from *in situ* XRD along the (110) peaks.

Temperature (°C)	SiO_2@V_2O_5	SiO_2@V_2O_5@Al_2O_3-(50)
100	50.81	35.55
300	54.89	26.37
500	56.75	39.92
700	72.64	34.32
750	77.89	28.49
800	71.36	21.20

Interestingly, new peaks are recognized in SiO_2@V_2O_5@Al_2O_3 core@shell nanostructures beyond 700 °C in Figure 3.7. When we examined the possibility of any other crystalline structure of either alumina or vanadium oxide, these were matched neither to crystalline aluminas such as alpha,

gamma, and theta, nor to vanadium oxides including V_2O_3, V_4O_7, and VO_2. The high-resolution TEM images in Figure 3.4. show that the thin Al_2O_3 shell did not show any crystallinity. Previous studies reported that the $AlVO_4$ phase formed from a solid-state reaction between V_2O_5 and Al_2O_3 beyond 570 °C[42–44] and the additional XRD peaks in the range 26–30° (Figure 3.7) corresponded to the characteristic peaks of $AlVO_4$. Based on these results, as the temperature increased, thin alumina shells were not crystallized but generated new $AlVO_4$ species resulting from a solid-state reaction between V_2O_5 and Al_2O_3 above 700 °C.

3.3.3 Catalytic oxidation of methane to formaldehyde

Methane oxidation over $SiO_2@V_2O_5@Al_2O_3$ core@shell nanostructures with controlled Al_2O_3 shell thickness was carried out in a laboratory-scale flow reactor operated at 600 °C at a CH_4/O_2 ratio of 1:1 (v/v). Figure 3.8 shows methane conversion as a function of time on stream over $SiO_2@V_2O_5@Al_2O_3$-(*50*) nanostructures at 600 °C.

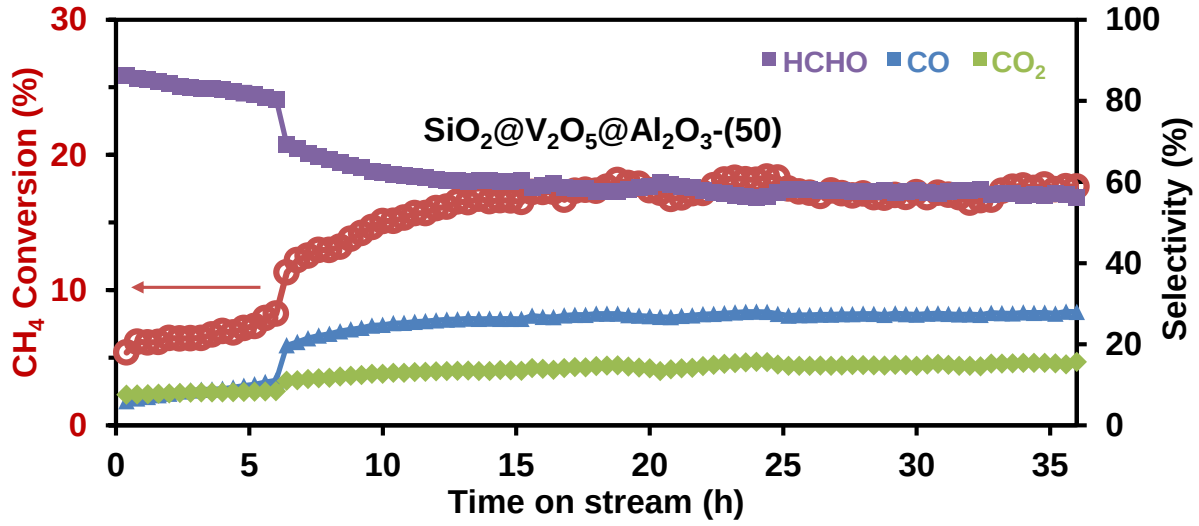

Figure 3.8. Methane conversion and selectivity obtained for $SiO_2@V_2O_5@Al_2O_3$-(*50*) nanostructures at 600 °C as a function of time on stream.

The initially observed gradual increase of conversion with time on stream was followed by an abrupt change at 6 h (at which point the product selectivity changed as well) and subsequent saturation to the maximum. Abrupt changes were also found in other $SiO_2@V_2O_5@Al_2O_3$ nanostructures with a different thickness of the Al_2O_3 shell (Figure 3.9). This behavior was ascribed to a structural rearrangement of the catalyst, but more detailed information is required for a sound conclusion. Methane conversion of the $SiO_2@V_2O_5@Al_2O_3$-(*50*) nanostructures reached 22.2%, and the corresponding HCHO, CO, and CO_2 selectivities equaled 57.8, 27.4, and 14.8%, respectively (Table 3.2). Beyond 35 h, the overall conversion and selectivity stayed constant, demonstrating that the $SiO_2@V_2O_5@Al_2O_3$-(*50*) nanostructures were thermally stable by having long-term stability in the high

temperature methane oxidation. Additionally, we conducted methane oxidation over SiO_2@V_2O_5@Al_2O_3-(*x*) nanostructures having different shell thicknesses (Figure 3.10a). Notably, whereas the maximum conversion of methane observed for SiO_2@V_2O_5@Al_2O_3-(*50*) equaled 22.2%, negligible conversion was observed for *x* = *0–30*. Thus, the original SiO_2@V_2O_5 core@shell structures did not show substantial methane oxidation activity because of the instability of V_2O_5 nanoparticles at 600 °C.

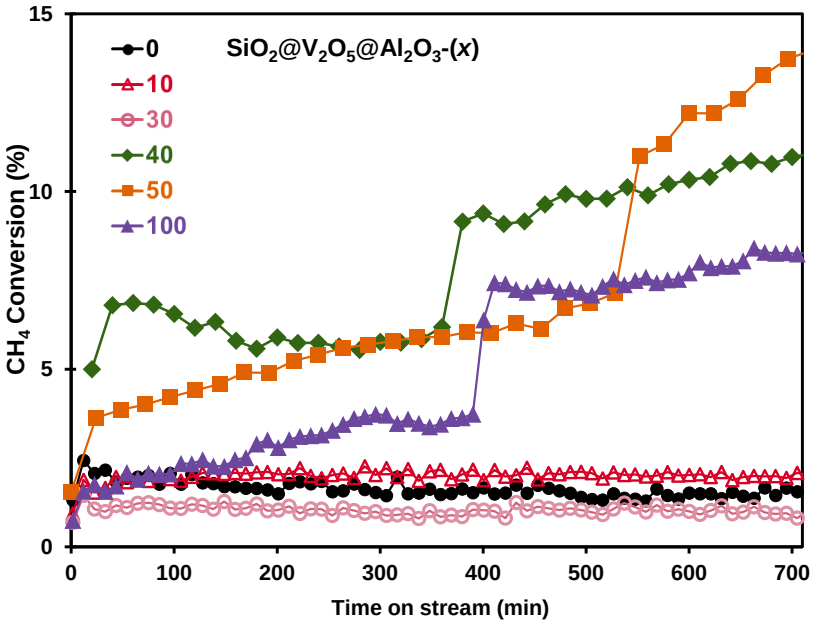

Figure 3.9. Methane conversion of SiO_2@V_2O_5@Al_2O_3-(*x*) core@shell nanostructures (*x = 0, 10, 30, 40, 50, and 100*) at 600 °C.

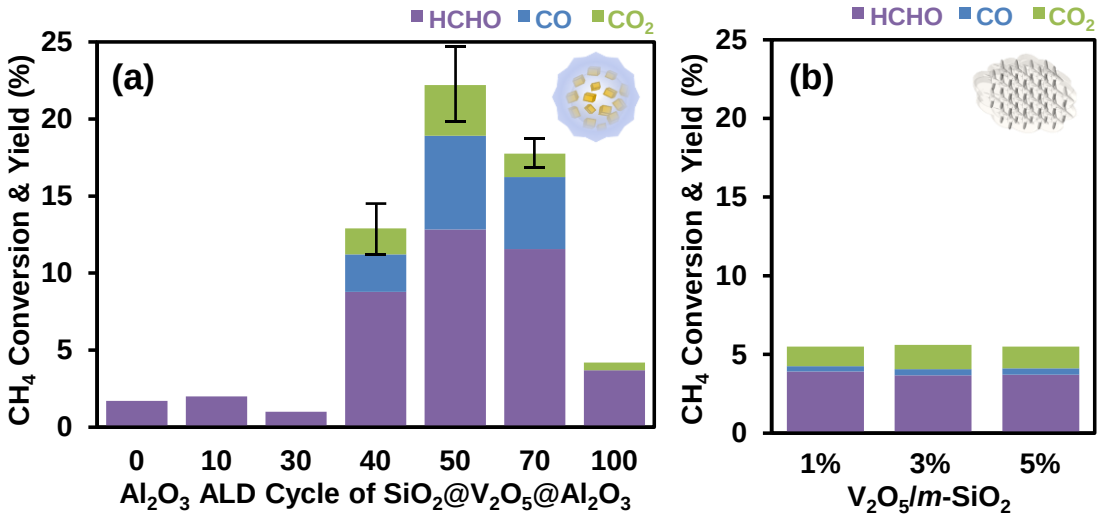

Figure 3.10. Methane oxidation of various SiO_2@V_2O_5@Al_2O_3 core@shell nanostructures and supported V_2O_5/*m*-SiO_2 catalysts. (a) Comparison of SiO_2@V_2O_5@Al_2O_3-(*x*) core@shell nanostructures in terms of achieved methane conversion and product yield. (b) Methane oxidation performance of V_2O_5/*m*-SiO_2 catalysts with vanadium loadings of 1, 3, and 5 wt%. Reaction conditions: 40 sccm of 1:1 (v/v) CH_4/O_2, 600 °C, atmospheric pressure, 0.1 g catalyst.

Table 3.2. Methane oxidation performance of selected vanadium-based catalysts obtained at a CH_4/O_2 ratio of 1:1 (v/v) and a reaction temperature of 600 °C (*n.d.* = not detected).[a]

Catalyst	ALD cycle no.	Conversion (%)	TOF (s^{-1})	Selectivity (%)		
				HCHO	CO	CO_2
$SiO_2@V_2O_5$	0	1.7	0.02	*n.d.*	0	0
$SiO_2@V_2O_5@Al_2O_3$-(*10*)	10	2.0	0.02	*n.d.*	0	0
$SiO_2@V_2O_5@Al_2O_3$-(*30*)	30	1.0	0.01	*n.d.*	0	0
$SiO_2@V_2O_5@Al_2O_3$-(*40*)	40	12.9	0.10	68	19	13
$SiO_2@V_2O_5@Al_2O_3$-(*50*)	50	22.2	0.14	58	27	15
$SiO_2@V_2O_5@Al_2O_3$-(*70*)	70	18.7	0.13	62	25	13
$SiO_2@V_2O_5@Al_2O_3$-(*100*)	100	3.7	0.04	100	0	0
V_2O_5/*m*-SiO_2 1 wt%		5.5	0.03	71	6	23
V_2O_5/*m*-SiO_2 3 wt%		5.6	0.03	66	7	27
V_2O_5/*m*-SiO_2 5 wt%		5.5	0.03	67	8	25

[a] Each reaction was conducted more than three times for reproducibility. The conversion and TOF are mean values and the deviation is within 15%.

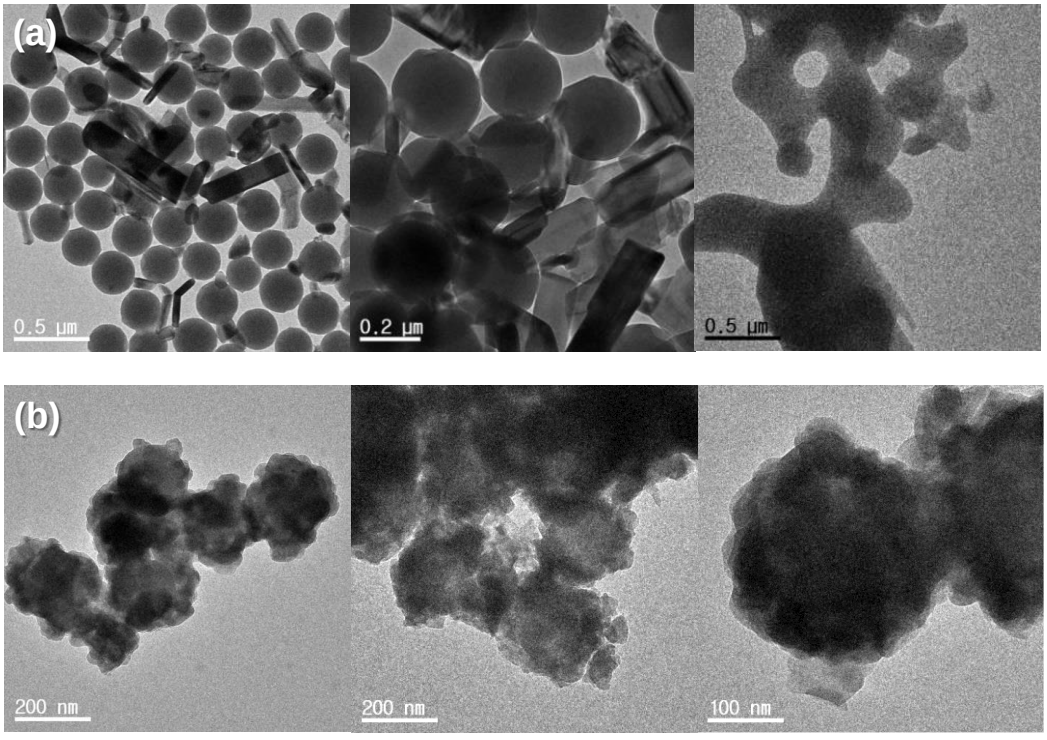

Figure 3.11. TEM images of the spent catalysts after methane oxidation at 600 ºC: (a) $SiO_2@V_2O_5$ and (b) $SiO_2@V_2O_5@Al_2O_3$-(*50*).

TEM imaging of spent catalysts confirmed the agglomeration of vanadium species after the reaction (Figure 3.11). When the number of ALD cycles was increased to $x = 40$, stabilization of core

vanadium species resulted in a maximum methane conversion of 12.9%. The protective effect of the Al_2O_3 shell was maximized in SiO_2@V_2O_5@Al_2O_3-(*50*), which featured strongly enlaced Al_2O_3 shells that still provided enough space for constant exchange of reactants and products, with further shell thickness increases resulting in deteriorated performance; for example, a conversion of only 3.7% was observed for SiO_2@V_2O_5@Al_2O_3-(*100*) (Table 3.2 and Figure 3.4d). Figure 3.10a compares the methane conversions and selectivity yields obtained from various SiO_2@V_2O_5@Al_2O_3-(*x*) core@shell nanostructures (*x* = *0*, *10*, *30*, *40*, *50*, *70*, and *100*).

Nguyen *et al.* showed that HCHO could be produced with 57.5% selectivity by oxidation of methane (total methane conversion = 6.3%) over V_2O_5/SiO_2 catalysts at a GHSV of 185,000 mL g_{cat}^{-1} h^{-1} and 600 °C.[11] For comparison, we also prepared MCF-17-supported V_2O_5 catalysts with different vanadium loadings. Figure 3.10b shows the methane oxidation performance of V_2O_5/*m*-SiO_2 catalysts with vanadium loadings of 1, 3, and 5 wt%, revealing that methane conversion (5.5–5.6%) and HCHO selectivity (65.7–71.2%) obtained at 600 °C were in good agreement with those reported by Nguyen *et al*.[11] Table 3.2 summarizes the methane oxidation performance of core@shell nanostructures with controlled Al_2O_3 shell thicknesses and that of supported V_2O_5/*m*-SiO_2 catalysts, demonstrating that the best methane conversion achieved for SiO_2@V_2O_5@Al_2O_3-(*50*) has never been achieved before for any vanadium-based catalyst at 600 °C.[45–50] Recent research on methane oxidation to formaldehyde shows advanced methane conversion and selectivity toward HCHO over modified vanadium-supported catalysts.[45–49] Loricera *et al*. reported vanadium oxide-supported silica catalysts prepared by the sol–gel method.[45] They reported 2.3% CH_4 conversion and 33% HCHO selectivity (reaction conditions: 600 °C, GHSV = 2830 mL min^{-1} g_{cat}^{-1}, CH_4:O_2 = 9). Wallis *et al*. studied the role of the support pore structure and morphology of VO_x/SBA-15 catalysts.[46] They exhibited 1% CH_4 conversion and 40% HCHO selectivity (reaction conditions: 540–650 °C, GHSV = 360,000 mL g_{cat}^{-1} h^{-1}, CH_4:O_2 = 9). The same group also discovered that vanadium (2.5 wt%) supported on 0.2 wt% Ti-doped SBA-15 showed higher selectivity to HCHO (46%) with 1.2% CH_4 conversion, compared with VO_x/SBA-15 at 600 °C.[47] Very recently, Dang *et al*. reported on VO_x/MCM-41 catalysts to study the influence of vanadium sources.[48] They found that vanadyl acetyl acetonate facilitated the highest VO_x density, exhibiting 5% CH_4 conversion and 32% HCHO selectivity (reaction conditions: 600 °C, GHSV = 360,830 mL g_{cat}^{-1} h^{-1}, CH_4:O_2 = 9). A comparison of the performance of vanadium supported catalysts is summarized in Table 3.3. Based on the existing results, 2.2% VO_x/SiO_2, developed by Nguyen *et al*., showed the best CH_4 conversion of 6.3% with 58% HCHO selectivity (reaction conditions: 600 °C, GHSV = 185,000 mL g_{cat}^{-1} h^{-1}, CH_4:O_2 = 38:13).[11] When GHSV was 8000 mL g_{cat}^{-1} h^{-1}, the conversion increased further to 7.7%, while the selectivity toward HCHO decreased to 49%. However, these effects were caused by additional water to the stream. Later, they reported that the water created hydroxylated monomeric species, which influenced the positive effect by enhancing methane oxidation to formaldehyde.[49] Although the reaction conditions, including gas composition, the feed rate

(GHSV), and temperature, varied from study to study, SiO_2@V_2O_5@Al_2O_3-(*50*) nanostructures in our study still exhibit the best catalytic activity, with 22.2% of CH_4 conversion and 57.8% HCHO selectivity at 600 °C under 24,000 mL g_{cat}^{-1} h^{-1}, surpassing all previously known vanadium-based catalysts at 600 °C.

Table 3.3. Comparison of the performance of vanadium supported catalysts for methane oxidation to formaldehyde reported in the literature.

Catalyst	Feed composition (%) $CH_4/O_2/H_2O$	GHSV (mL g_{cat}^{-1} h^{-1})	Temper-atrue (°C)	CH_4 conversion	Selec-tivity in HCHO (%)	Refer-ence
SiO_2@V_2O_5@Al_2O_3-(*50*)	50/50/0	24,000	600	22.2	58	This work
2.2% V/SiO_2	38/13/9	185,000	600	6.3	58	11
2.2% V/SiO_2	38/13/9	8,000	585	7.7	49	11
2.8% V/SiO_2 (MCM-A)	54/10/0	180,000	595	3.1	28	11
3.9% V/SiO_2	80/10/0	166,000	600	1.8	37	11
2.0% V/SiO_2	90/10/0	2,830	600	2.3	33	45
2.6% V/SiO_2 (SBA-15)	90/10/0	360,000	600	1.0	40	46
2.5% V/Ti-SiO_2	90/10/0	360,000	600	1.2	46	47
2.8% V/SiO_2 (MCM-A)	90/10/0	360,000	600	5.0	32	48

3.3.4 Characterization of V_2O_5 in SiO_2@V_2O_5@Al_2O_3-(x) core@shell catalysts

The catalytic activity of supported vanadium catalysts is known to depend on the dispersion of vanadium, the nature of vanadium active sites, and the metal-support interaction determined by the selection of suitable oxide supports.[51–56] For many forms of catalytic oxidation, including the partial oxidation of hydrocarbons, oxidative dehydrogenation of alkanes to alkenes, selective catalytic reduction of NO_x, and the oxidation of SO_2,[52,57–59] isolated tetrahedral (T_d) vanadium oxide species containing terminal V=O groups have been proposed as active sites.[56,60–62] To characterize vanadium species in SiO_2@V_2O_5@Al_2O_3 core@shell nanostructures and compare them with those in V_2O_5/*m*-SiO_2 catalysts, the above materials were analyzed by Raman spectroscopy, H_2-TPR, and diffuse reflectance UV-vis spectroscopy.

Raman spectroscopy is a powerful tool for characterizing the dispersion of vanadium oxide species over high-surface-area supports.[60,63–65] Figure 3.12 shows Raman spectra of SiO_2@V_2O_5 and SiO_2@V_2O_5@Al_2O_3-(*50*) core@shell nanostructures at 600 °C, revealing the presence of bands at 995 (V=O), 703, 406, 305, and 285 cm^{-1} in all cases and thus indicating that all catalysts contained

crystalline V_2O_5.[53,66,67] Although the Raman spectra of 3 wt% V_2O_5/*m*-SiO_2 were similar to those of core@shell catalysts prepared from crystalline V_2O_5, a shoulder peak at 1040 cm^{-1} ascribed to the symmetric V=O stretch of isolated VO_4 species was observed in the former case (Figure 3.12).[51] Interestingly, as the vanadium content of V_2O_5/*m*-SiO_2 decreased to 1 wt%, the above shoulder peak became dominant (Figure 3.13), which indicated that the relative content of crystalline V_2O_5 in V_2O_5/*m*-SiO_2 catalysts decreased at low vanadium loadings. After methane oxidation at 600 °C, the major Raman spectra of SiO_2@V_2O_5@Al_2O_3-(*50*) core@shell nanostructures were still observed, demonstrating high thermal stability (Figure 3.12).

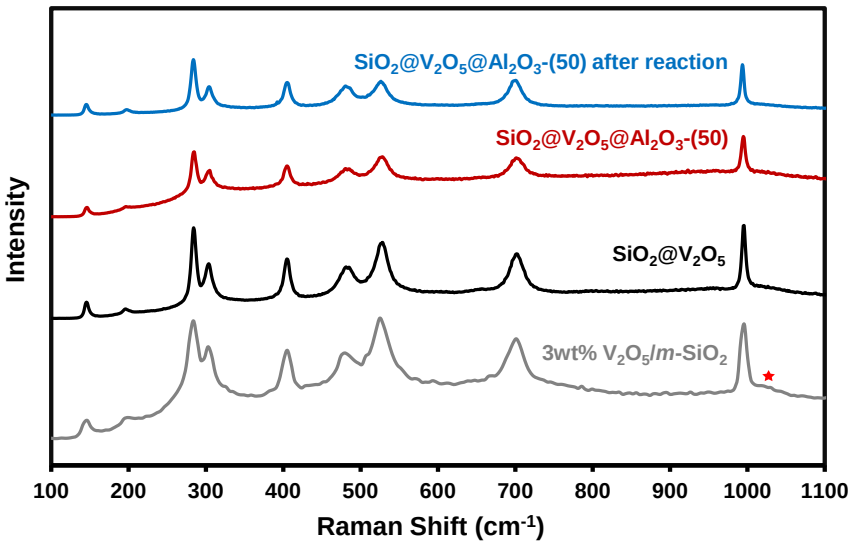

Figure 3.12. Raman spectra of SiO_2@V_2O_5 and SiO_2@V_2O_5@Al_2O_3-(*50*) core@-shell nanostructures, and 3 wt% V_2O_5/*m*-SiO_2.

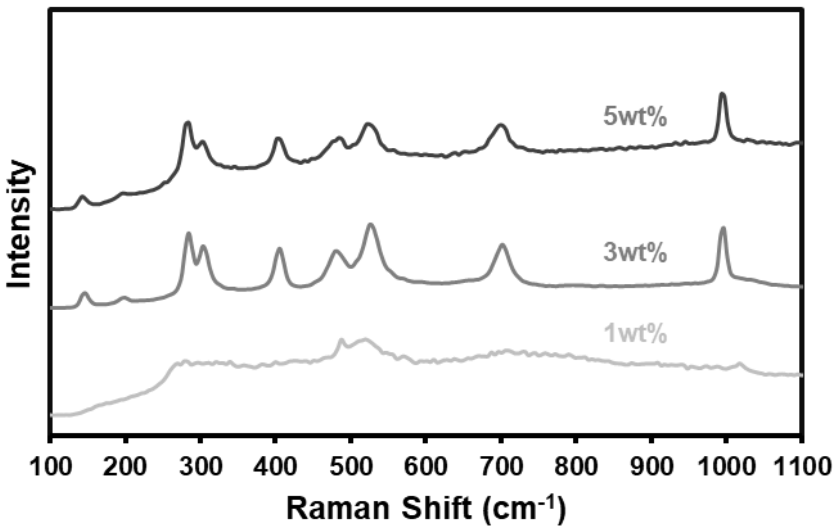

Figure 3.13. Raman spectra of 1, 3, and 5 wt% V_2O_5/*m*-SiO_2 catalysts.

The dispersion and type of active vanadium species were evaluated by H_2-TPR. In previous reports, the low-temperature H_2-TPR reduction peak observed at 460–500 °C was ascribed to the reduction of V^{5+} in highly dispersed monomeric species to V^{3+}.[51,68–70] As the vanadium loading increased, the reduction peaks shifted to higher temperatures as a consequence of reduction kinetics (i.e., because of the effect of the partial pressure of water formed during reduction and the effect of the actual reactant concentration described by the Kissinger equation).[68–72] The high-temperature reduction peak at ~600 °C was assigned to the reduction of vanadium in polymeric and bulklike V_2O_5 species.[50,73]

The TPR profiles in Figure 3.14 show that 3 wt% V_2O_5/*m*-SiO_2 contained highly disperse monomeric species as well as a small amount of V_2O_5 species, in good agreement with the results of Raman spectroscopy analysis. Pristine SiO_2@V_2O_5 contained only bulk V_2O_5 species, which was ascribed to the size of V_2O_5 nanoparticles (35 nm). Conversely, the SiO_2@V_2O_5@Al_2O_3-(*50*) core@shell catalyst contained both V_2O_5 and highly disperse monomeric species, exhibiting two broad TPR bands at 550 and 620 °C. In the case of spent SiO_2@V_2O_5@Al_2O_3-(*50*) after methane oxidation, a dominant high-temperature band at 600 °C was observed, together with a low-temperature band of negligible intensity. (Figure 3.15b).

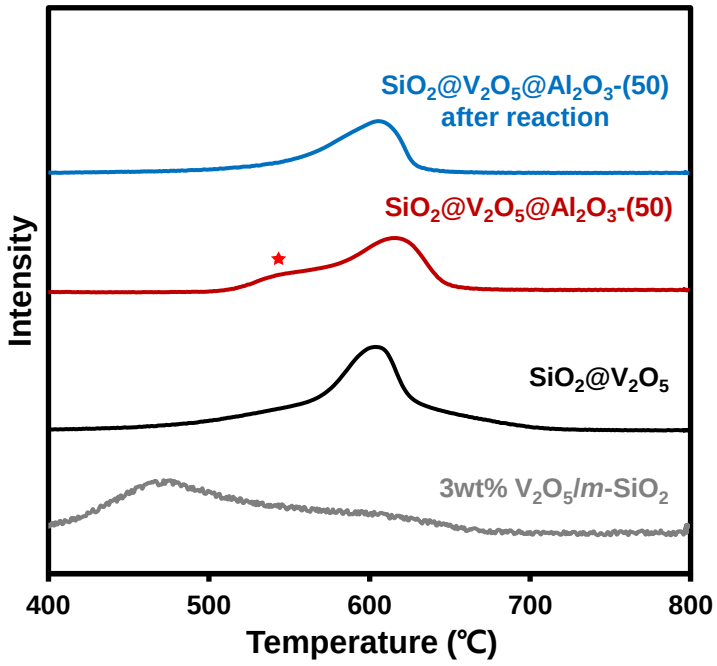

Figure 3.14. H_2-TPR spectra of SiO_2@V_2O_5 and SiO_2@V_2O_5@Al_2O_3-(*50*) core@shell nanostructures, and 3 wt% V_2O_5/*m*-SiO_2.

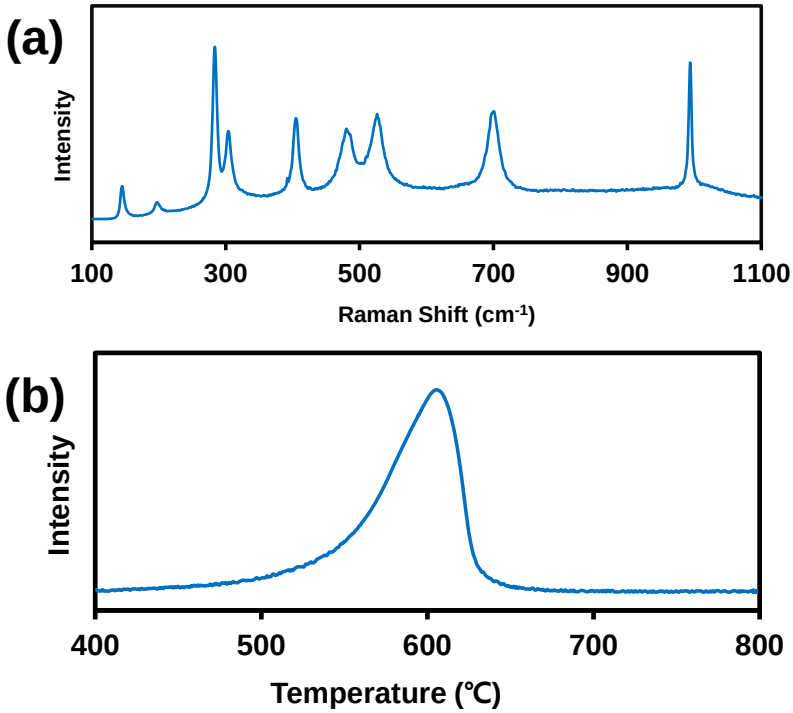

Figure 3.15. (a) Raman spectra and (b) H_2-TPR curves of the spent SiO_2@V_2O_5@Al_2O_3-(*50*) catalysts after methane oxidation at 600 °C.

Finally, diffuse reflectance UV-vis spectroscopy was applied to investigate the dispersion and local structure of supported vanadium catalysts.[74–76] For dispersed V_2O_5 domains, Barton *et al.* plotted the square root of the Kubelka-Munk function multiplied by the photon energy[67] versus the photon energy to estimate the position of the absorption edge by extrapolating the linear part of the rising curve to zero, showing that the obtained values could be used to determine the average domain size of oxide nanoparticles.[75,77] The diffuse reflectance UV-vis spectra of investigated catalysts are shown in Figure 3.16. The absorption band just above 3 eV was ascribed to VO_x species with T_d coordination,[66] while that around 5.5 eV evidenced the presence of monomeric T_d species.[68,78,79] The absorption edge positions of 3 wt% V_2O_5/*m*-SiO_2 (2.6 eV), SiO_2@V_2O_5 and SiO_2@V_2O_5@Al_2O_3-(*50*) (<2.4 eV) indicated that the former catalyst contained homogeneous T_d VO_x species with a smaller domain size than that of the other two catalysts. The low-energy shoulder observed for core@shell catalysts comprising 35 nm V_2O_5 nanoparticles was ascribed to the bimodal size distribution of crystalline V_2O_5 species, which was not observed for V_2O_5/*m*-SiO_2. Notably, no shoulder was observed for other V_2O_5/*m*-SiO_2 catalysts (1 and 5 wt% loading; Figure 3.17). Furthermore, the size distributions deduced from shoulder peaks were different for SiO_2@V_2O_5 and SiO_2@V_2O_5@Al_2O_3-(*50*) core@shell catalysts, demonstrating that the properties of crystalline V_2O_5 species are changed by the deposition of Al_2O_3 shells.

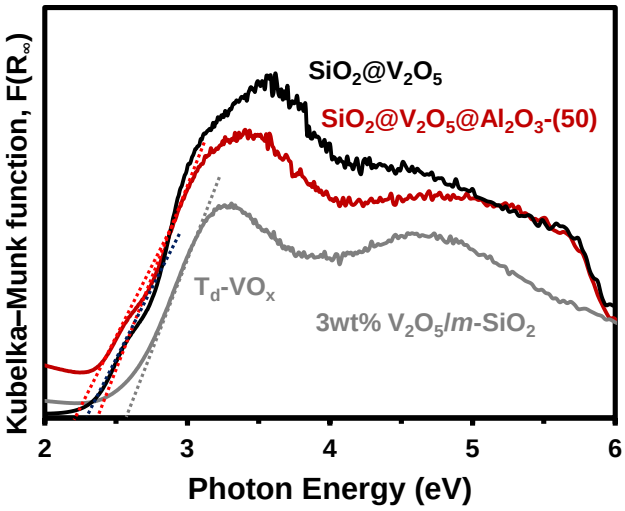

Figure 3.16. UV-vis diffuse reflectance spectra of SiO_2@V_2O_5 and SiO_2@V_2O_5@Al_2O_3-(*50*) core@shell nanostructures, and 3 wt% V_2O_5/*m*-SiO_2.

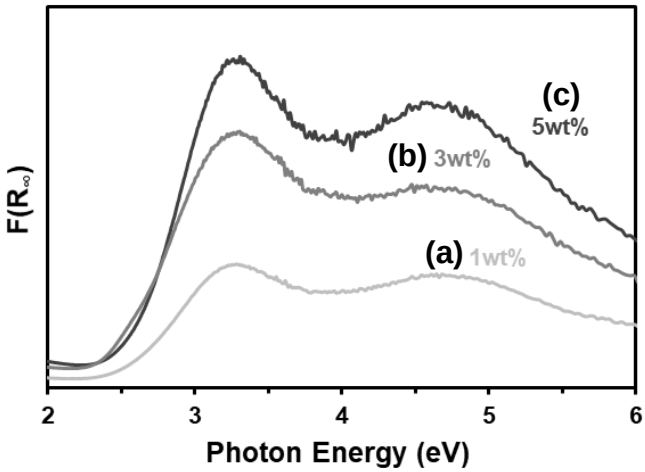

Figure 3.17. UV-vis diffuse reflectance spectra of (a) 1, (b) 3, and (c) 5 wt% V_2O_5/*m*-SiO_2 catalysts.

Since the interaction between V_2O_5 and Al_2O_3 influenced the catalytic performance, we carried out methane oxidation over conventional V_2O_5/Al_2O_3 catalysts. When V_2O_5/Al_2O_3 catalysts were prepared by impregnation with different vanadium loadings of 3 and 5 wt% and the reaction was tested, negligible conversion was obtained (less than 2% methane conversion) for both catalysts. These results were agreement with the previous study conducted by Koranne *et al.*[50] They compared the activity and selectivity of silica- and- alumina-supported vanadium oxide catalysts and found that V_2O_5/Al_2O_3 catalysts showed very low methane conversion, producing no formaldehyde, in contrast to V_2O_5/SiO_2. It was revealed that V_2O_5/Al_2O_3 catalysts were not suitable for methane oxidation to formaldehyde. When we characterized 3 and 5 wt% V_2O_5/Al_2O_3 catalysts prepared by impregnation, we could not find any distinct features in H_2-TPR and UV-vis diffuse reflectance spectra of the two

catalysts (Figure 3.18). Martinez-Huerta *et al.* reported that neither terminal V=O nor bridging V–O–V bonds influenced the chemical properties of the supported VO_x/Al_2O_3 catalysts; instead the bridging V–O–Al bond was the catalytic active site for oxidative dehydrogenation of ethane to ethylene.[42]

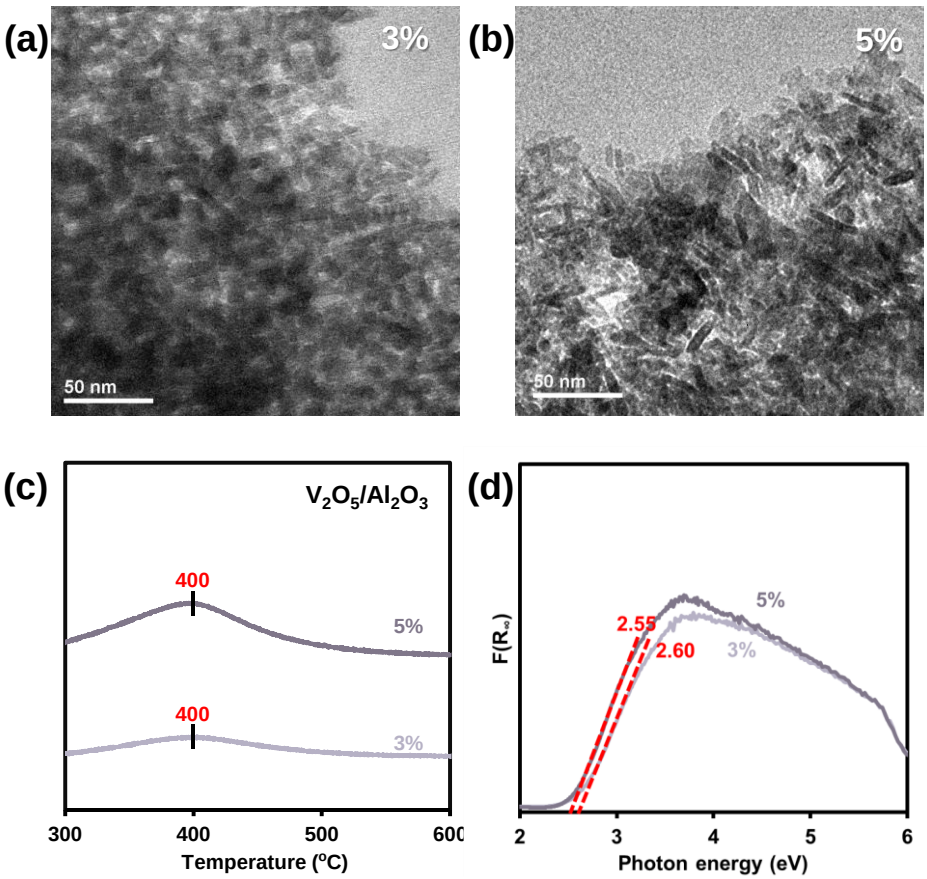

Figure 3.18. TEM images of (a) 3 and (b) 5 wt% V_2O_5/Al_2O_3 catalysts prepared by impregnation. (c) H_2-TPR curves and (d) UV-vis diffuse reflectance spectra of 3 and 5 wt% V_2O_5/Al_2O_3 catalysts.

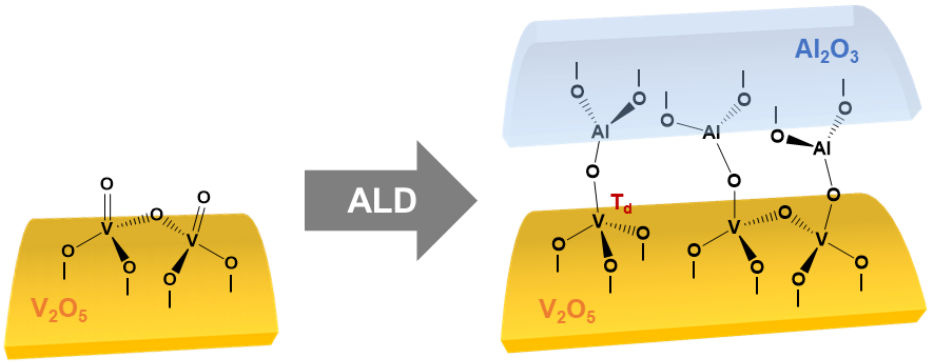

Figure 3.19. Formation of new T_d vanadium species and V–O–Al bonds by a reaction between V_2O_5 and Al_2O_3 in the $SiO_2@V_2O_5@Al_2O_3$ core@shell catalyst.

The combined results indicate that V_2O_5 nanoparticles formed on SiO_2 spheres were identified as crystalline V_2O_5 species, and the additional Al_2O_3 shells of $SiO_2@V_2O_5@Al_2O_3$-(*50*) were proven to provide new surfaces for creating highly dispersed T_d monomeric species by promoting interactions between Al_2O_3 and V_2O_5 nanoparticles during the ALD process (Figure 3.19). Based on fact that the $AlVO_4$ phase was present in the $SiO_2@V_2O_5@Al_2O_3$ core@shell nanostructures at the elevated temperature, the interaction between Al_2O_3 and V_2O_5 nanoparticles generated bridging V–O–Al bonds in the $AlVO_4$. The highly disperse T_d vanadium species with a V–O–Al bond of the $SiO_2@V_2O_5@Al_2O_3$ core@shell nanostructures were not seen in the conventional V_2O_5/Al_2O_3 catalysts. As a result, the newly formed T_d monomeric vanadium species connected to the V–O–Al bond facilitated methane oxidation at 600 °C and achieve high methane conversion. Additionally, the Al_2O_3 shell protected V_2O_5 nanoparticles against sintering.

3.4. Conclusion

Here, we successfully prepared $SiO_2@V_2O_5@Al_2O_3$ core@shell nanostructures by hydrothermal synthesis and subsequent ALD. Methane conversion was carried out over $SiO_2@V_2O_5@Al_2O_3$ core@shell nanostructures and V_2O_5/*m*-SiO_2 catalysts in a flow reactor at a CH_4/O_2 ratio of 1:1 (v/v) and 600 °C, and the major reaction products were identified as HCHO, CO, CO_2, and H_2. $SiO_2@V_2O_5@Al_2O_3$-(*50*) exhibited methane conversion of 22.2% and formaldehyde selectivity of 57.8%, whereas 1, 3, and 5 wt% V_2O_5/*m*-SiO_2 catalysts prepared by impregnation exhibited methane conversions of 5.5–5.6% and HCHO selectivities of 65.7–71.2% under the same conditions. As the catalytic activity of supported vanadium catalysts largely depends on the dispersion of vanadium and the nature of vanadium active sites, $SiO_2@V_2O_5@Al_2O_3$ core@shell catalysts were characterized by Raman spectroscopy, H_2-TPR, and diffuse reflectance UV-vis spectroscopy, which revealed that the highly disperse T_d monomeric species with V–O–Al bonds found in $SiO_2@V_2O_5@Al_2O_3$-(*50*) were not present in $SiO_2@V_2O_5$. Thus, these new T_d monomeric vanadium species and V–O–Al bonds were produced by the interactions between Al_2O_3 and V_2O_5 nanoparticles during the ALD process in the presence of crystalline V_2O_5 species, accounting for the high conversion of methane during oxidation at 600 °C. The developed strategy for the preparation of highly active and stable core@shell nanocatalysts is expected not only to provide robust oxide shells protecting against sintering during high-temperature reactions, but also to anchor the new active species inside shells and thus realize outstanding catalytic performance.

3.5. Reference

1. P. Tang, Q. Zhu, Z. Wu and D. Ma, Methane activation: the past and future, *Energy Environ. Sci.*, **2014**, *7*, 2580.

2. E. McFarland, Unconventional chemistry for unconventional natural gas, *Science*, **2012**, *338*, 340.

3. A. T. Ashcroft, A. K. Cheetham, J. S. Foord, M. L. H. Green, C. P. Grey, A. J. Murrell and P. D. F. Vernon, Selective oxidation of methane to synthesis gas using transition metal catalysts, *Nature*, **1990**, *344*, 319.

4. T. V. Choudhary and V. R. Choudhary, Energy-efficient syngas production through, catalytic oxy-methane reforming reactions, *Angew. Chem. Int. Edit.*, **2008**, *47*, 1828.

5. M. Ravi, M. Ranocchiari and J. A. van Bokhoven, A Critical assessment of the direct catalytic oxidation of methane to methanol, *Angew. Chem. Int. Edit.*, **2017**, *56*, 16464.

6. G. J. Hutchings, M. S. Scurrell and J. R. Woodhouse, Oxidative coupling of methane using oxide catalysts, *Chem. Soc. Rev.*, **1989**, *18*, 251.

7. J. H. Lunsford, The catalytic oxidative coupling of methane, *Angew. Chem. Int. Ed. Engl.*, **1995**, *34*, 970.

8. J. H. Lunsford, Catalytic conversion of methane to more useful chemicals and fuels: a challenge for the 21st century, *Catal. Today*, **2000**, *63*, 165.

9. B. C. Enger, R. Lodeng and A. Holmen, A review of catalytic partial oxidation of methane to synthesis gas with emphasis on reaction mechanisms over transition metal catalysts, *Appl. Catal. A*, **2008**, *346*, 1.

10. A. Parmaliana and F. Arena, Working mechanism of oxide catalysts in the partial oxidation of methane to formaldehyde. I. Catalytic behaviour of SiO_2, MoO_3/SiO_2, V_2O_5/SiO_2, TiO_2, and V_2O_5/TiO_2 systems, *J. Catal.*, **1997**, *167*, 57.

11. L. D. Nguyen, S. Loridant, H. Launay, A. Pigamo, J. L. Dubois and J. M. M. Millet, Study of new catalysts based on vanadium oxide supported on mesoporous silica for the partial oxidation of methane to formaldehyde: Catalytic properties and reaction mechanism, *J. Catal.*, **2006**, *237*, 38.

12. F. Arena and A. Parmaliana, Scientific basis for process and catalyst design in the selective oxidation of methane to formaldehyde, *Acc. Chem. Res.*, **2003**, *36*, 867.

13. R. Pitchai and K. Klier, Partial oxidation of methane, *Catal. Rev. Sci. Eng.*, **1986**, *28*, 13.

14. Y. H. Chin, C. Buda, M. Neurock and E. Iglesia, Consequences of metal-oxide interconversion for C–H bond activation during CH_4 reactions on Pd catalysts, *J. Am. Chem. Soc.*, **2013**, *135*, 15425.

15. J. J. Willis, E. D. Goodman, L. H. Wu, A. R. Riscoe, P. Martins, C. J. Tassone and M. Cargnello, Systematic identification of promoters for methane oxidation catalysts using size- and composition-controlled Pd-based bimetallic nanocrystals, *J. Am. Chem. Soc.*, **2017**, *139*, 11989.

16. Y. Kwon, T. Y. Kim, G. Kwon and J. Yi, H. Lee, Selective activation of methane on single-atom catalyst of rhodium dispersed on zirconia for direct conversion, *J. Am. Chem. Soc.*, **2017**, *139*, 17694.

17. S. Kasztelan and J. B. Moffat, Partial oxidation of methane by oxygen over silica, *J. Chem. Soc., Chem. Commun.*, **1987**, 1663.

18. G. N. Kastanas, G. A. Tsigdinos and J. Schwank, Selective oxidation of methane over vycor glass, quartz glass and various silica, magnesia and alumina surfaces, *Appl. Catal.*, **1988**, *44*, 33.

19. Q. Sun, J. I. Dicosimo, R. G. Herman, K. Klier and M. M. Bhasin, Selective oxidation of methane to formaldehyde and C2 hydrocarbons over double layered Sr/La_2O_3 and MoO_3/SiO_2 catalyst bed, *Catal. Lett.*, **1992**, *15*, 371.

20. A. Parmaliana, F. Frusteri, A. Mezzapica, D. Miceli, M. S. Scurrell and N. Giordano, A basic

approach to evaluate methane partial oxidation catalysts, *J. Catal.*, **1993**, *143*, 262.

21. A. Guerrero-Martínez, J. Pérez-Juste and L. M. Liz-Marzán, Recent progress on silica coating of nanoparticles and related nanomaterials, *Adv. Mater.*, **2010**, *22*, 1182.

22. S. H. Joo, J. Y. Park, C. K. Tsung, Y. Yamada, P. D. Yang and G. A. Somorjai, Thermally stable Pt/mesoporous silica core-shell nanocatalysts for high-temperature reactions, *Nat. Mater.*, **2009**, *8*, 126.

23. Y. Dai, B. Lim, Y. Yang, C. M. Cobley, W. Li, E. C. Cho, B. Grayson, P. T. Fanson, C. T. Campbell and Y. Sun, A sinter-resistant catalytic system based on platinum nanoparticles supported on TiO_2 nanofibers and covered by porous silica, *Angew. Chem.*, **2010**, *122*, 8341.

24. M. Feyen, C. Weidenthaler, R. Güttel, K. Schlichte, U. Holle, A. H. Lu and F. Schüth, High-temperature stable, iron-based core–shell catalysts for ammonia decomposition, *Chem. Eur. J.*, **2011**, *17*, 598.

25. J. Ge, Q. Zhang, T. Zhang and Y. Yin, Core–satellite nanocomposite catalysts protected by a porous silica shell: controllable reactivity, high stability, and magnetic recyclability, *Angew. Chem.*, **2008**, *120*, 9056.

26. Q. Zhang, I. Lee, J. B. Joo, F. Zaera and Y. D. Yin, Core-shell nanostructured catalysts, *Acc. Chem. Res.*, **2013**, *46*, 1816.

27. I. Lee, J. B. Joo, Y. Yin and F. Zaera, A yolk@shell nanoarchitecture for Au/TiO_2 catalysts, *Angew. Chem.*, **2011**, *123*, 10390.

28. P. M. Arnal, M. Comotti and F. Schüth, High-temperature-stable catalysts by hollow sphere encapsulation, *Angew. Chem.*, **2006**, *118*, 8404.

29. M. Cargnello, J. D. Jaén, J. H. Garrido, K. Bakhmutsky, T. Montini, J. C. Gámez, R. Gorte and P. Fornasiero, Exceptional activity for methane combustion over modular Pd@CeO_2 subunits on functionalized Al_2O_3, *Science*, **2012**, *337*, 713.

30. X. Huang, C. Guo, J. Zuo, N. Zheng and G. D. Stucky, An assembly route to inorganic catalytic nanoreactors containing sub-10-nm gold nanoparticles with anti-aggregation properties, *Small*, **2009**, *5*, 361.

31. S. Ikeda, S. Ishino, T. Harada, N. Okamoto, T. Sakata, H. Mori, S. Kuwabata, T. Torimoto and M. Matsumura, Ligand-free platinum nanoparticles encapsulated in a hollow porous carbon shell as a highly active heterogeneous hydrogenation catalyst, *Angew. Chem.*, **2006**, *118*, 7221.

32. J. Lu, B. Fu, M. C. Kung, G. Xiao, J. W. Elam, H. H. Kung and P. C. Stair, Coking-and sintering-resistant palladium catalysts achieved through atomic layer deposition, *Science*, **2012**, *335*, 1205.

33. B. J. O'Neill, D. H. K. Jackson, J. Lee, C. Canlas, P. C. Stair, C. L. Marshall, J. W. Elam, T. F. Kuech, J. A. Dumesic and G. W. Huber, Catalyst design with atomic layer deposition, *ACS Catal.*, **2015**, *5*, 1804.

34. S. T. Christensen, H. Feng, J. L. Libera, N. Guo, J. T. Miller, P. C. Stair and J. W. Elam, Supported Ru-Pt bimetallic nanoparticle catalysts prepared by atomic layer deposition, *Nano Lett.*, **2010**, *10*, 3047.

35. T. M. Onn, S. Y. Zhang, L. Arroyo-Ramirez, Y. C. Chung, G. W. Graham, X. Q. Pan and R. J. Gorte, Improved thermal stability and methane-oxidation activity of Pd/Al_2O_3 catalysts by atomic layer deposition of ZrO_2, *ACS Catal.*, **2015**, *5*, 5696.

36. Y. S. Jung, A. S. Cavanagh, A. C. Dillon, M. D. Groner, S. M. George and S. H. Lee, Enhanced stability of $LiCoO_2$ cathodes in lithium-ion batteries using surface modification by atomic layer deposition, *J. Electrochem. Soc.*, **2010**, *157*, A75.

37. W. Stober, A. Fink and E. Bohn, Controlled growth of monodisperse silica spheres in micron size range, *J. Colloid Interface Sci.*, **1968**, *26*, 62.

38. J. Liu, Y. C. Zhou, J. B. Wang, Y. Pan and D. F. Xue, Template-free solvothermal synthesis of yolk-shell V_2O_5 microspheres as cathode materials for Li-ion batteries, *Chem. Commun.*, **2011**, *47*, 10380.

39. Y. Han, S. S. Lee and J. Y. Ying, Spherical siliceous mesocellular foam particles for high-speed size exclusion chromatography, *Chem. Mater.*, **2007**, *19*, 2292.

40. T. Sugino, A. Kido, N. Azuma, A. Ueno and Y. Udagawa, Partial oxidation of methane on silica-supported silicomolybdic acid catalysts in an excess amount of water vapor, *J. Catal.* **2000**, *190*, 118.

41. S. Siggia and W. Maxcy, Improved procedure for determination of aldehydes, *Anal. Chem.*, **1947**, *19*, 1023.

42. M. V. Martinez-Huerta, X. Gao, H. Tian, I. E. Wachs, J. L. G. Fierro and M. A. Banares, Oxidative dehydrogenation of ethane to ethylene over alumina-supported vanadium oxide catalysts: Relationship between molecular structures and chemical reactivity, *Catal. Today*, **2006**, *118*, 279.

43. J. M. Kanervo, M. E. Harlin, A. O. I. Krause and M. A. Banares, Characterisation of alumina-supported vanadium oxide catalysts by kinetic analysis of H_2-TPR data, *Catal. Today*, **2003**, *78*, 171.

44. E. Arisi, S. A. P. Sanchez, F. Leccabue, B. E. Watts, G. Bocelli, F. Calderon, G. Calestani and L. Righi, Preparation and characterization of $AlVO_4$ compound, *J. Mater. Sci.*, **2004**, *39*, 2107.

45. C. V. Loricera, M. C. Alvarez-Galvan, R. Guil-Lopez, A. A. Ismail, S. A. Al-Sayari and J. L. G. Fierro, Structure and reactivity of sol-gel V/SiO_2 catalysts for the direct conversion of methane to formaldehyde, *Top. Catal.*, **2017**, *60*, 1129.

46. P. Wallis, S. Wohlrab, V. N. Kalevaru, M. Frank and A. Martin, Impact of support pore structure and morphology on catalyst performance of VO_x/SBA-15 for selective methane oxidation, *Catal. Today*, **2016**, *278*, 120.

47. P. Wallis, E. Schonborn, V. N. Kalevaru, A. Martin and S. Wohlrab, Enhanced formaldehyde selectivity in catalytic methane oxidation by vanadia on Ti-doped SBA-15, *RSC Adv.*, **2015**, *5*, 69509.

48. T. T. H. Dang, D. Seeburg, J. Radnik, C. Kreyenschulte, H. Atia, T. T. H. Vu and S. Wohlrab, Influence of V-sources on the catalytic performance of VMCM-41 in the selective oxidation of methane to formaldehyde, *Catal. Commun.*, **2018**, *103*, 56.

49. H. Launay, S. Loridant, A. Pigamo, J. L. Dubois and J. M. M. Millet, Vanadium species in new catalysts for the selective oxidation of methane to formaldehyde: Specificity and molecular structure dynamics with water, *J. Catal.*, **2007**, *246*, 390.

50. M. M. Koranne, J. G. Goodwin and G. Marcelin, Partial oxidation of methane over silica-supported and alumina-supported vanadia catalysts, *J. Catal.*, **1994**, *148*, 388.

51. G. Du, S. Lim, M. Pinault, C. Wang, F. Fang, L. Pfefferle and G. L. Haller, Synthesis, characterization, and catalytic performance of highly dispersed vanadium grafted SBA-15 catalyst, *J. Catal.*, **2008**, *253*, 74.

52. A. Khodakov, B. Olthof, A.T. Bell and E. Iglesia, Structure and catalytic properties of supported vanadium oxides: Support effects on oxidative dehydrogenation reactions, *J. Catal.*, **1999**, *181*, 205.

53. X. T. Gao, S. R. Bare, B. M. Weckhuysen and I. E. Wachs, *In situ* spectroscopic investigation of molecular structures of highly dispersed vanadium oxide on silica under various conditions, *J. Phys. Chem. B*, **1998**, *102*, 10842.

54. G. Busca, G. Centi, L. Marchetti and F. Trifiro, Chemical and spectroscopic study of the nature of a vanadium-oxide monolayer supported on a high-surface-area TiO_2 anatase, *Langmuir*, **1986**,

2, 568.

55. K. Inumaru, M. Misono and T. Okuhara, Structure and catalysis of vanadium oxide overlayers on oxide supports, *Appl. Catal. A*, **1997**, *149*, 133.

56. N. Das, H. Eckert, H. C. Hu, I. E. Wachs, J. F. Walzer and F. J. Feher, Bonding states of surface vanadium(V) oxide phases on silica: Structural characterization by ^{51}V NMR and Raman spectroscopy, *J. Phys. Chem.*, **1993**, *97*, 8240.

57. U. S. Ozkan, T. A. Harris and B. T. Schilf, The partial oxidation of C5 hydrocarbons over vanadia-based catalysts, *Catal. Today*, **1997**, *33*, 57.

58. G. C. Bond and S. F. Tahir, Vanadium-oxide monolayer catalysts - Preparation, characterization and catalytic activity, *Appl. Catal.*, **1991**, *71*, 1

59. G. A. Du, S. Y. Lim, Y. H. Yang, C. Wang, L. Pfefferle and G. L. Haller, Catalytic performance of vanadium incorporated MCM-41 catalysts for the partial oxidation of methane to formaldehyde, *Appl. Catal. A*, **2006**, *302*, 48.

60. I. E. Wachs and B. M. Weckhuysen, Structure and reactivity of surface vanadium oxide species on oxide supports, *Appl. Catal. A*, **1997**, *157*, 67.

61. S. Irusta, L. M. Cornaglia, E. E. Miro and E. A. Lombardo, The role of V=O sites on the oxidation of methane to formaldehyde over V/SiO_2, *J. Catal.*, **1995**, *156*, 167.

62. M. Iwamoto, J. Hirata, K. Matsukami and S. Kagawa, Catalytic-oxidation by oxide radical ions. 1. One-step hydroxylation of benzene to phenol over group 5 and 6 oxides supported on silica gel, *J. Phys. Chem.*, **1983**, *87*, 903.

63. J. H. Kwak, J. E. Herrera, J. Z. Hu, Y. Wang and C. H. F. Peden, A new class of highly dispersed VO_x catalysts on mesoporous silica: Synthesis, characterization, and catalytic activity in the partial oxidation of ethanol, *Appl. Catal. A*, **2006**, *300*, 109.

64. F. Roozeboom, M. C. Mittelmeijerhazeleger, J. A. Moulijn, J. Medema, V. H. J. Debeer and P. J. Gellings, Vanadium-oxide monolayer catalysts. 3. A Raman-spectroscopic and temperature-programmed reduction study of monolayer and crystal-type vanadia on various supports, *J. Phys. Chem.*, **1980**, *84*, 2783.

65. I. E. Wachs, Raman and IR studies of surface metal oxide species on oxide supports: Supported metal oxide catalysts, *Catal. Today*, **1996**, *27*, 437.

66. D. E. Keller, T. Visser, F. Soulimani, D. C. Koningsberger and B. M. Weckhuysen, Hydration effects on the molecular structure of silica-supported vanadium oxide catalysts: A combined IR, Raman, UV-vis and EXAFS study, *Vib. Spectrosc.* **2007**, *43*, 140.

67. X. T. Gao, M. A. Banares, I. E. Wachs, Ethane and *n*-butane oxidation over supported vanadium oxide catalysts: An *in situ* UV-visible diffuse reflectance spectroscopic investigation, *J. Catal.*, **1999**, *188*, 325.

68. R. Bulanek, P. Cicmanec, H. Sheng-Yang, P. Knotek, L. Capek and M. Setnicka, Effect of preparation method on nature and distribution of vanadium species in vanadium-based hexagonal mesoporous silica catalysts: Impact on catalytic behavior in propane ODH, *Appl. Catal. A*, **2012**, *415*, 29.

69. M. D. Soriano, J. A. Cecilia, A. Natoli, J. Jimenez-Jimenez, J. M. L. Nieto and E. Rodriguez-Castellon, Vanadium oxide supported on porous clay heterostructure for the partial oxidation of hydrogen sulphide to sulfur, *Catal. Today*, **2015**, *254*, 36.

70. H. Berndt, A. Martin, A. Bruckner, E. Schreier, D. Muller, H. Kosslick, G. U. Wolf and B. Lucke, Structure and catalytic properties of VO_x/MCM materials for the partial oxidation of methane to formaldehyde, *J. Catal.*, 2000, 191, 384.

71. H. E. Kissinger, Reaction kinetics in differential thermal analysis, *Anal. Chem.*, **1957**, *29*, 1702.

72. H. E. Kissinger, Variation of peak temperature with heating rate in differential thermal analysis, *J. Res. Natl. Bur. Stand.* **1956**, *57*, 217.

73. G. Martra, F. Arena, S. Coluccia, F. Frusteri and A. Parmaliana, Factors controlling the selectivity of V_2O_5 supported catalysts in the oxidative dehydrogenation of propane, *Catal. Today*, **2000**, *63*, 197.

74. J. E. Herrera, J. H. Kwak, J. Z. Hu, Y. Wang, C. H. F. Peden, J. Macht and E. Iglesia, Synthesis, characterization, and catalytic function of novel highly dispersed tungsten oxide catalysts on mesoporous silica, *J. Catal.*, **2006**, *239*, 200.

75. D. G. Barton, M. Shtein, R. D. Wilson, S. L. Soled, E. Iglesia, Structure and electronic properties of solid acids based on tungsten oxide nanostructures, *J. Phys. Chem. B*, **1999**, *103*, 630.

76. A. Khodakov, J. Yang, S. Su, E. Iglesia, A. T. Bell, Structure and properties of vanadium oxide zirconia catalysts for propane oxidative dehydrogenation, *J. Catal.*, **1998**, *177*, 343.

77. R. S. Weber, Effect of local structure on the UV-Visible absorption edges of molybdenum Oxide clusters and supported molybdenum oxides, *J. Catal.*, **1995**, *151*, 470.

78. R. Bulanek, L. Capek, M. Setnicka, P. Cicmanec, DR UV-vis study of the supported vanadium oxide catalysts, *J. Phys. Chem. C*, **2011**, *115*, 12430.

79. G. Catana, R. R. Rao, B. M. Weckhuysen, P. Van Der Voort, E. Vansant and R. A. Schoonheydt, Supported vanadium oxide catalysts: Quantitative spectroscopy, preferential adsorption of $V^{4+/5+}$, and Al_2O_3 coating of zeolite Y, *J. Phys. Chem. B*, **1998**, *102*, 8005.

Chapter 4

Al_2O_3-Coated Ni/CeO_2 Nanoparticles as Coke-Resistant Catalyst for Dry Reforming of Methane

This chapter includes the published contents:
E. Yang, E. Nam, J. Lee, H. Lee, E. D. Park, H. Lim and K. An, *Catal. Sci. Technol.* **2020**, *10*, 8283. DOI: 10.1039/d0cy01615b. Reproduced with permission.

4.1. Introduction

The conversion of carbon dioxide to high value-added chemicals has been intensively studied as a means of addressing the global rise in atmospheric temperatures due to continuous CO_2 emissions.[1–4] Hydrogen is indispensable in the catalytic conversion of CO_2, which is a major cause of global warming, to olefins, gasoline, and diesel. However, in the current industrial structure in which CO_2 is emitted in the process of hydrogen production, the use of technology for producing hydrogen without forming CO_2 is very important. DRM offers the advantage of being able to convert both CH_4 and CO_2, which are commonly found in fossil fuels or biofuels, into more practical syngas.[5–9] The produced syngas is mainly utilized to produce methanol and hydrocarbons through the FT process using a 2:1 ratio of H_2 and CO. Compared to the SRM, which produces H_2 and CO in a 3:1 ratio, the DRM reaction is more attractive for F–T synthesis because the gases produced by DRM can be used directly without expensive procedures for separating CO_2 from the flue gas.[10] Nevertheless, both CH_4 and CO_2 are very stable reactants and require high energy for activation during the endothermic DRM reaction. Many noble metal-based catalysts with high activity have been developed, but the high price and low thermal stability of these catalysts have become major obstacles to their cost-effective commercialization. Due to its excellent catalytic performance and low cost, Ni is the most studied non-noble metal catalyst.[11–14] However, Ni has a low Tammann temperature[15] of 590 °C, at which the Ni solid accumulates sufficient energy to activate mobility and diffusion of the ions, and is thus easily sintered during the high-temperature DRM reaction.[16] In addition, coke deposition occurs due to the undesirable Boudouard reaction ($2CO \leftrightarrow CO_2 + C$) and methane decomposition ($CH_4 \leftrightarrow 2H_2 + C$).[17–19] The accumulation of coke during the reaction causes catalyst deactivation by covering the active sites.[20,21] Various approaches have been proposed to increase the dispersion of Ni by altering steric hindrance with organic surfactants, catalyst structure, catalytic treatment methods, and SMSI to inhibit

the metal sintering of Ni.[22–25] Since Ni-based catalysts easily break C–H bonds and create strong Ni–C bonds, a variety of bimetallic catalysts (NiCo, NiFe and NiCu) or promotors (La, Mg, Ce, Mo and Ga) that can maximize the catalytic properties to adsorb and dissociate CO_2 have been investigated.[26–31] The catalyst support also plays a crucial role in the DRM by maintaining high dispersion of the catalyst and preventing sintering and coke formation at the active sites. Oxides such as MgO, Al_2O_3, CeO_2, ZrO_2, La_2O_3 and SiO_2 are known as suitable supports for the DRM.[32,33] Song *et al.* reported a Ni–Mo/MgO catalyst for the DRM, which exhibited excellent stability and durability at 800 °C.[34] They established that the defect-free MgO support could prevent sintering and coke formation while the active Ni particles migrated to the step edge of MgO(111). Appropriate promoters have also been used to form catalysts with enhanced stability. Alkali or alkaline earth metals (K, Li, Mg, Ca, Ba) and rare earth metals (Ce, Zr, La) were selected as promoters.[35–38] Xu *et al.* reported that in Ni/MgO–Al_2O_3 catalysts, carbon formation on the Ni phase was mitigated by the increased catalyst stability derived from increasing the Mg concentration.[39] One of the most widely studied catalysts for the DRM is Ni-supported CeO_2 catalysts, where the redox property of CeO_2 easily provides oxygen vacancies at the interface, affecting the active site of the metal, resulting in adsorption and reaction of hydrogen with CO_2.[40–43] The versatile oxygen exchange on Ni/CeO_2 promotes steady production of CO and H_2, instead of reducing coke formation. Lustemberg *et al.* reported that Ni/CeO_2 catalysts produced CH_x and CO_x intermediates by the activation of methane in an *in situ* XPS study.[43] Wang *et al.* prepared Ni/CeO_2–Al_2O_3 catalysts with different loadings of CeO_2 as a promoter.[44] The CH_4 conversion rate of the Ni/CeO_2 catalyst was 25.8%, which is higher than that of Ni/Al_2O_3 (14.0%) and Ni/CeO_2–Al_2O_3 catalysts (17.5–18.4%) at 500 °C.

The development of efficient catalysts with high activity is the key for conducting the DRM reaction at low temperature, but it is a very difficult task. Recently, various nanocatalysts, including metal–organic frameworks, have been reported to inhibit carbon deposition in low temperature DRM reactions (400–700 °C), but the low activity has to be overcome further.[45,46] To activate the two reactants and inhibit coke formation, a high reaction temperature is preferred (>800 °C). However, when a high-efficiency catalyst is used at low reaction temperature (below 700 °C) to achieve process efficiency, a large amount of coke is generated because methane decomposition and the Boudouard reaction is relatively dominant in this temperature range.[44,47] In order to overcome coke formation during the DRM reaction at high temperature (~800 °C), core@shell nanostructures with a robust oxide shell as a sintering barrier have been developed.[48–54] The structural properties of core@shell materials not only reduce the sintering of the catalyst, but also provide multiple functionalities for application in tandem reactions.[55,56] Ziwen *et al.* prepared Ni-yolk@Ni@SiO_2 core@shell nanoparticles (NPs) through the sol–gel approach using tetraethylorthosilicate.[57] The yolk–satellite–shell structured Ni-yolk@Ni@SiO_2 catalysts with a porous silica shell showed stable conversion in the DRM reaction for

90 h at 800 °C, with negligible carbon deposition. Zhu *et al.* reported a $Ni/CeO_2/SiO_2$ core@shell catalyst for partial oxidation of methane. The new $Ce_2(Si_2O_7)$ species was formed during reduction at 750 °C by increased SMSI, and Ni was confined between CeO_2 and SiO_2 with high dispersion.[58] SiO_2 is one of most widely studied material to encapsulate core catalyst shell for the preparation of core@shell structure. In particular, *m*-SiO_2 synthesized by sol–gel chemistry in the presence of structure directing organic molecules provides a large surface area and uniform pore structure, allowing reactant molecules to access the core species without destroying the external structure at a high temperature. However, catalytically inert SiO_2 has limitations in providing an additional interfacial effect to the core catalyst. Metal oxide supports such as Al_2O_3, TiO_2, and ZrO_2 with acidic surfaces improve many hydrocarbon conversions such as isomerization, catalytic cracking, alkylation, and transalkylation by synergetic effect with metals. In addition to coating methods including sol–gel, precipitation, and CVD,[59] the ALD technique enables controlled coating of metal oxide layers on the NPs.[60–65] The thickness of the oxide layer is precisely controlled by multiple cycles in the ALD process. In a previous study, controlled Al_2O_3 layers protecting a $SiO_2@V_2O_5$ core yielded 4-fold higher conversion and durability than that of $SiO_2@V_2O_5$ core@shell NPs without the Al_2O_3 layer in the partial oxidation of methane at 600 °C.[66] Using the developed rotary ALD equipment, the Al_2O_3 coating was controlled by multiple ALD cycles with TMA and water. Because a thick coating layer can cover the active core completely, the optimized thickness of the oxide shell should be taken into account for effective encapsulation of the active core species to achieve high activity in high-temperature catalytic reactions without sintering and coking.[67–69] Herein, we prepare Ni/CeO_2 catalysts composed of monodisperse Ni NPs supported on CeO_2 nanorods (NRs) for the DRM reaction. To obtain a coke-resistant catalyst, the thickness of the Al_2O_3 layers coated on the Ni/CeO_2 NPs is controlled by the ALD process with different numbers of cycles. To investigate the catalytic performance of the catalyst in the DRM at 700 and 800 °C, the carbon deposition and conversion of CO_2 and CH_4 are evaluated as a function of the thickness of the Al_2O_3 coating on the Ni/CeO_2 NP catalyst. Compared to the conventional catalysts prepared by wet-impregnation, the NP catalysts are more efficient to observe the sintering behavior of NPs as well as the degree of coking during the DRM at high temperatures.[50] The coke-free characteristics of the $Ni/CeO_2/Al_2O_3$ catalysts are determined by thermogravimetric analysis (TGA), revealing no weight loss for the $Ni/CeO_2/Al_2O_3$ catalysts up to 800 °C, independent of the thickness of the Al_2O_3 layer. It is demonstrated that modification of the catalyst surface using ALD can enhance the inhibition of coking without compromising the catalytic properties.

4.2. Experimental Methods

4.2.1 Preparation of Ni/CeO_2 NP catalysts

Ni NPs were synthesized using a reported method with slight modification.[70] Nickel acetylacetonate (0.77 g; Aldrich, 95%) was dissolved in 12 mL of oleylamine (Aldrich, 70%) in a three-neck round-bottom flask. The mixture was degassed at 100 °C for 15 min and purged under Ar flow. After adding 4 mL of trioctylphosphine (Sigma-Aldrich, 97%), the mixture was heated to 220 °C and held for 2 h. After cooling to room temperature, the black colloid was washed with 5 mL of n-hexane and 50 mL of isopropanol and precipitated by centrifugation. After repeating the washing procedure four times, the precipitate containing Ni NPs was dispersed in *n*-hexane. CeO_2 NRs were synthesized by a hydrothermal method.71 Briefly, 1.74 g of cerium nitrate hexahydrate (Aldrich, 99%) and 19.2 g of sodium hydroxide were dissolved in 40 mL of H_2O. The mixture was transferred to a 50 mL Teflon-lined autoclave reactor and heated at 100 °C for 24 h. The product was collected by centrifugation and washed with water. The precipitate obtained after centrifugation was dried at 60 °C. For preparation of the supported Ni/CeO_2 NP catalysts, 0.5 g of CeO_2 NRs dispersed in 10 mL of 1-octadecene (Aldrich, 90%) and the as-prepared colloid of Ni NPs dispersed in n-hexane were mixed in a flask. *n*-Hexane was removed completely by degassing under vacuum for 1 h, and the solution was heated to 200 °C for 30 min under an inert atmosphere. After washing with 300 mL of acetone and 100 mL of *n*-hexane, the resulting NPs catalysts were obtained by drying at 60 °C.

4.2.2 Preparation of Ni/CeO_2/Al_2O_3-(x) (x = 1, 2, and 10) catalysts

To encapsulate the resulting Ni/CeO_2 NP catalysts, a closed chamber-type rotary ALD reactor was used. The Ni/CeO_2 catalyst powder was loaded into a porous stainless-steel cylinder. Vaporized TMA ($Al(CH_3)_3$, Sigma-Aldrich, 97%) and H_2O at a pressure of 2 Torr were sequentially introduced into the reactor. Between the injection of $Al(CH_3)_3$ and H_2O, Ar was used to buffer each step in the sequence of $Al(CH_3)_3$–Ar–H_2O–Ar. The diffused $Al(CH_3)_3$ was deposited on the NP surface to generate Al_2O_3 shells. The operating temperature, pressure, exposure time, and purge time for $Al(CH_3)_3$ and water were 180 °C, 2 Torr, 2 min, and 30 s, respectively. The number of cycles is represented by (*x*), and is proportional to the thickness of the Al_2O_3 shell. Ni/CeO_2/Al_2O_3-(*x*) catalysts were prepared with different numbers of ALD cycles (*x = 1, 2, and 10*).

4.2.3 Characterization

High-resolution transmission electron microscopy (HRTEM), high-angle annular dark-field scanning transmission electron microscopy (HAADF-STEM), and EDS analyses were performed on a JEOL JEM-2100F instrument operating at 200 kV. H_2-TPR was performed on a MicrotracBEL BELCAT II instrument. For H_2-TPR measurement, the catalyst was loaded into a quartz reactor and

pretreated under an O_2/He flow (20%, 50 mL min^{-1}) at 500 °C for 2 h before measurement. After cooling to 100 °C under He purging for 30 min, the temperature was ramped to 900 °C at a rate of 10 °C min^{-1} under a H_2/He flow (4%, 50 mL min^{-1}). The amount of H_2 consumed was determined by GC using TCD. To quantify the amount of coke deposited on the spent catalysts, TGA was performed using a TGA5500 instrument. The spent catalyst for TEM and TGA measurements was obtained after DRM reaction at 800 °C with gas flows of equimolar mixture of $CH_4/CO_2/N_2$ at a flow rate of 45 mL min^{-1}. XPS was performed with a ThermoFisher K-alpha instrument with an Al-Kα X-ray radiation source. Before the XPS analysis, the catalyst was reduced under a H_2/Ar (4%, 200 mL min^{-1}) flow at 700 °C for 1 h. CO chemisorption was measured on a Micromeritics AutoChem II 2920 instrument. The catalyst was placed on a quartz tube and reduced under 4% H_2/He flow (50 mL min^{-1}) at 700 °C for 1 h. After cooling, a pulse of a loop gas mixture of 10% CO/He was introduced into the catalyst and the peak intensity was monitored by GC until saturation. XRD measurement was carried out on a PANalytical X'Pert Pro X-ray diffractometer in the range of 10–80° (Cu-Kα radiation, λ = 1.5418 Å). *In situ* spectra were acquired with a Rigaku SmartLab X-ray diffractometer while reducing the catalysts prior to heating from 100 to 700 °C in steps of 100 °C in the presence of 4% H_2 and balance Ar (100 mL min^{-1}). After reduction, the gas stream was changed to a mixture of 4% CH_4, 4% CO_2, and balance Ar (100 mL min^{-1}) and the sample was heated at 500–800 °C for investigation of the structural changes under the DRM conditions.

4.2.4 Dry reforming of methane

The catalytic DRM reaction was carried out in a fixed-bed catalytic reactor. The catalyst (20 mg) was loaded into a quartz tube (i.d. = 10 mm) and 1 g of purified sand was charged over the catalyst layer. The catalyst was reduced under a pure flow of H_2 at 50 mL min^{-1} at 700 °C for 1 h before the reaction. The $CH_4/CO_2/N_2$ gas molar ratio was set to equimolar (1:1:1) at a flow rate of 45 mL min^{-1} and the GHSV was 90,000 mL g_{cat}^{-1} h^{-1}. The DRM reaction was carried out at 700 and 800 °C. The gaseous products were monitored by GC (YL6500) equipped with a TCD, with a Carboxen 1000 column. The conversion (X) of CH_4 and CO_2, and the H_2/CO ratio were determined as follows:

$$X_{reactant}(\%) = \frac{F^{in} - F^{out}}{F^{in}} \times 100$$

$$H_2/\mathrm{CO}\ (\%) = \frac{F_{H_2}^{out}}{F_{CO}^{out}} \times 100$$

F^{in} and F^{out} are the flow rate of the reactant (mmol h^{-1}) at the inlet and outlet of the reactor, respectively.

4.3. Results and Discussion

4.3.1 Preparation of $Ni/CeO_2/Al_2O_3$-(x) catalysts

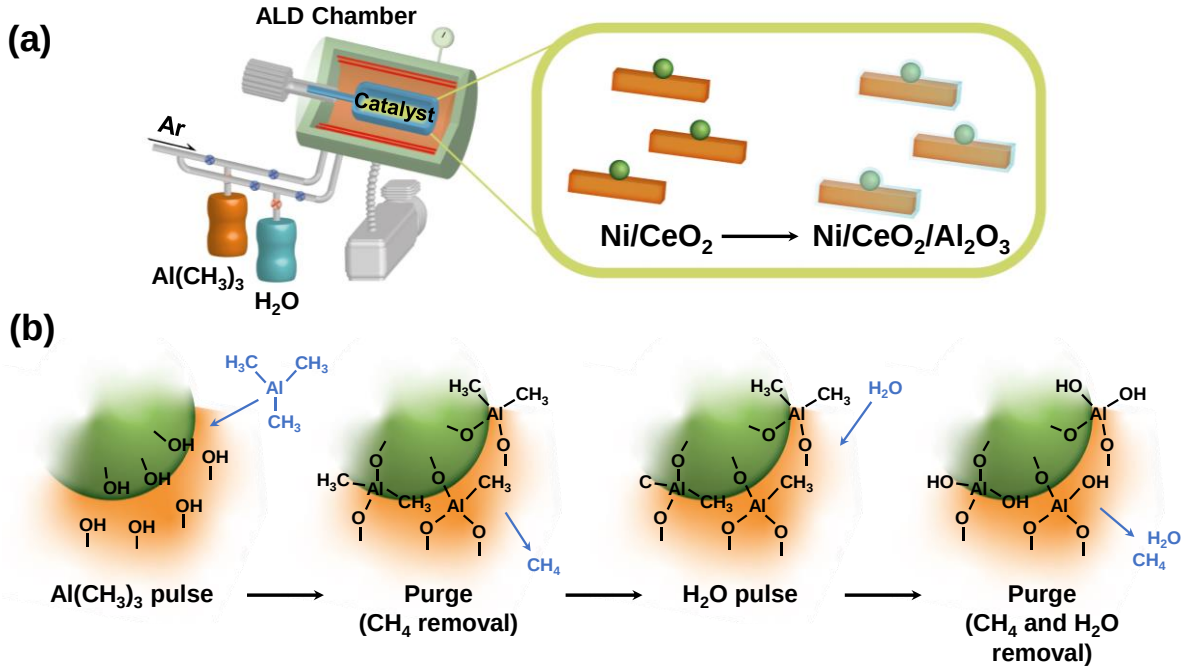

Figure 4.1. Schematic illustration of (a) chamber-type rotary ALD reactor for the preparation of $Ni/CeO_2/Al_2O_3$ catalysts with controlled Al_2O_3 layers and (b) one cycle of the ALD process.

In order to deposit the Al_2O_3 layers for preparation of the coke-resistant catalyst, a chamber-type rotary ALD reactor was used. Figure 4.1 presents a schematic illustration of the ALD reactor used to design the Ni/CeO_2 catalysts with selective coating of the layers of Al_2O_3 by sequential feeding of $Al(CH_3)_3$ and H_2O in a short sequence time (Figure 4.1). One cycle of the ALD process comprised four steps (Figure 4.1b). In the first step, highly reactive $Al(CH_3)_3$ as an alumina source was diffused into a porous stainless steel cylinder containing the Ni/CeO_2 catalysts, while rotating the entire ALD reactor at 140 rpm. The introduced $Al(CH_3)_3$ was deposited onto the NP surfaces at 180 °C in the rotating chamber. In the second step, the chamber was evacuated to remove CH_4 generated as a byproduct with unreacted $Al(CH_3)_3$. After filling with Ar to a pressure of 80 Torr for 2 min, the chamber was evacuated twice. In the third step, H_2O at 2 Torr was added to replace the methyl groups of the attached $Al(CH_3)_3$ with OH groups. Lastly, for removal of the produced CH_4 and excess H_2O, the chamber was evacuated and purged again in the same manner. For multiple cycles, the aforementioned steps were repeated. The number of ALD cycles is denoted as *x* in the catalyst nomenclature, *i.e.*, $Ni/CeO_2/Al_2O_3$-(*x*).

The Ni/CeO_2 catalysts were prepared by incorporating Ni NPs into CeO_2 NRs by the colloidal method. The as-synthesized Ni NPs had a narrow size distribution with an average diameter of 10 nm (Figure 4.2a).[70] The CeO_2 NRs synthesized *via* the hydrothermal method were 6–10 nm thick with a length in the range of 60–140 nm (Figure 4.2b).[71] The TEM image in Figure 4.2c shows that the Ni NPs

were deposited on the CeO_2 NRs after thermal mixing in 1-octadecene, and the original structures of the NPs were maintained. By using the ALD method, Al_2O_3 layers were deposited on the Ni/CeO_2 catalysts (Figure 4.2d). Because the shell thickness is proportional to the number of ALD cycles, the monolayer overcoats deposited with one Al_2O_3 cycle were 0.2 nm-thick.[66] The $Ni/CeO_2/Al_2O_3$-(*x*) catalysts were prepared by using different numbers of ALD cycles (*x = 1, 2, and 10*). Figure 4.2d shows an HR-TEM image of the $Ni/CeO_2/Al_2O_3$-(*10*) catalyst prepared by using 10 ALD cycles. The HR-TEM image also shows the characteristic lattice fringes corresponding to the CeO_2(111) and (002) phases and the overall surface of the Ni/CeO_2 covered by amorphous Al_2O_3 layers. The thickness of the Al_2O_3 layer of $Ni/CeO_2/Al_2O_3$-(*10*) NPs was 2 nm. Fewer ALD cycles for $Ni/CeO_2/Al_2O_3$-(*1*) and $Ni/CeO_2/Al_2O_3$-(*2*) generated thin Al_2O_3 shells that were difficult to distinguish. The HAADF-STEM image and the corresponding EDS mapping image of the $Ni/CeO_2/Al_2O_3$-(*1*) catalyst confirmed the distribution of the Al_2O_3 layers on the Ni/CeO_2 NPs (Figure 4.3). EDS mapping confirmed that the O atoms were distributed throughout the catalyst, while Ni and Ce were localized in their designated areas. Figure 4.3f clearly shows the signals of Al distributed over the entire catalyst surface.

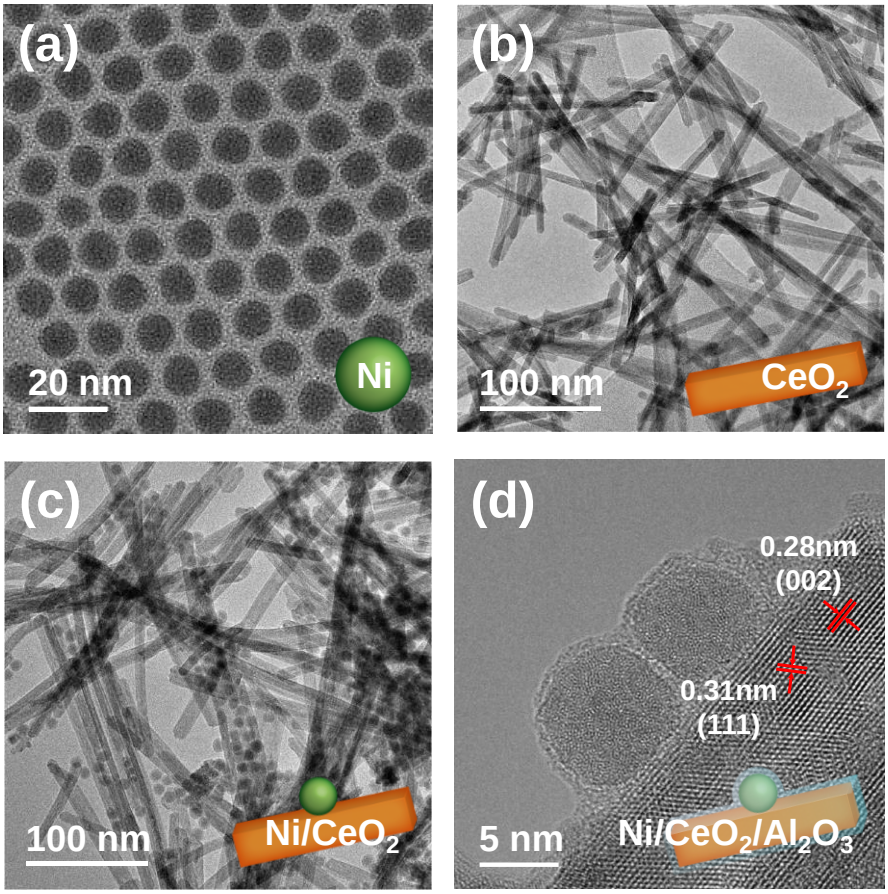

Figure 4.2. TEM images of (a) Ni NPs, (b) CeO_2 NRs, (c) supported Ni/CeO_2 NPs, and (d) $Ni/CeO_2/Al_2O_3$-(*10*) catalyst prepared by ALD process.

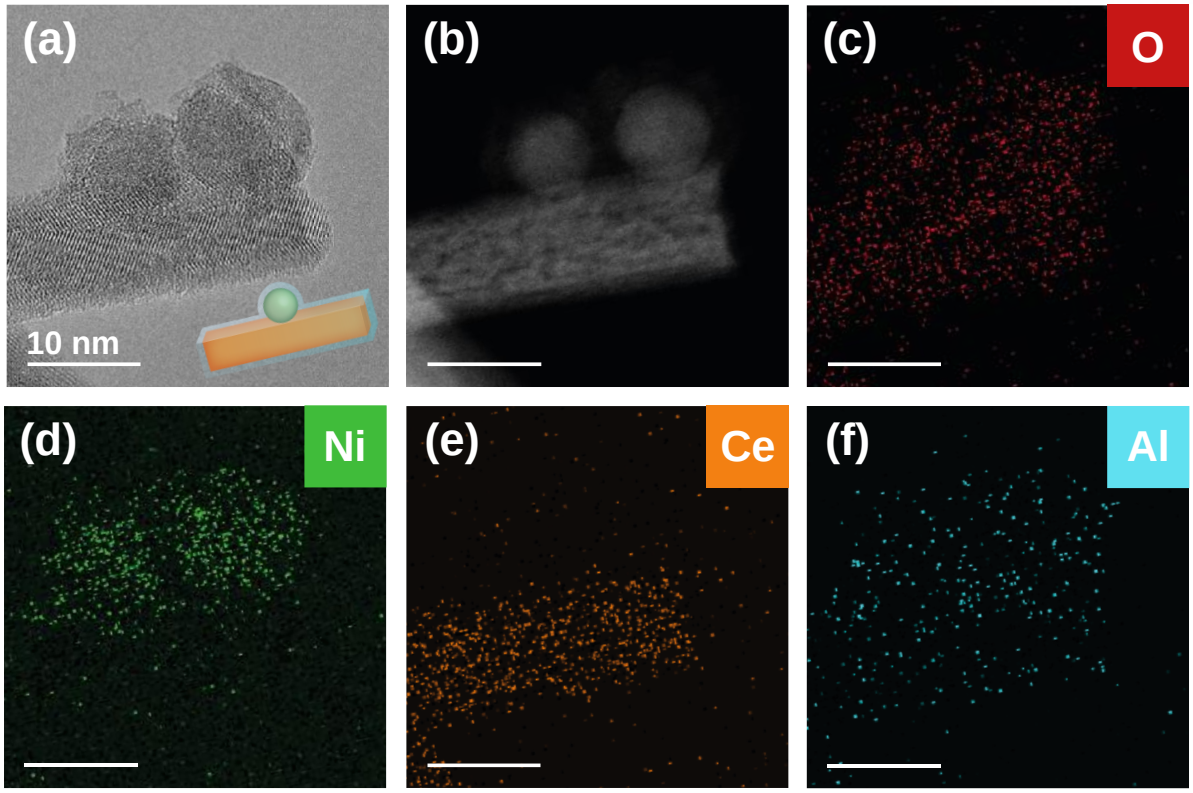

Figure 4.3. (a) HR-TEM, (b) HAADF-STEM, and (c–f) EDS mapping images of Ni/CeO_2/Al_2O_3-(*1*) catalyst. All scale bars represent 10 nm.

4.3.2 Catalytic reaction of Ni/CeO_2/Al_2O_3-(x) catalysts

To investigate the relationship between the catalytic activity and coke formation over the Ni/CeO_2/Al_2O_3-(*x*) (*x = 1, 2, and 10*) catalysts, the DRM reaction was carried out in a fixed-bed reactor. Figure 4.4a and Table 4.1 show the conversion of CH_4 and CO_2 obtained from the reaction at 700 and 800 °C for 12 h with a 1:1:1 volume ratio of CH_4/CO_2/N_2 with a GHSV of 90,000 mL g_{cat}^{-1} h^{-1}. The conversion of CH_4 and CO_2 varied depending on the thickness of the Al_2O_3 shell in the Ni/CeO_2/Al_2O_3 catalyst. The conversions of CH_4 and CO_2 at 700 °C over the Ni/CeO_2/Al_2O_3 catalyst without the Al_2O_3 shell were 62.9 and 68.2%, respectively. The CH_4 and CO_2 conversions at 800 °C over the Ni/CeO_2/Al_2O_3 catalyst further increased to 83.4 and 86.0%, respectively. However, as the number of ALD cycles increased from *1* to *10*, the thickness of the Al_2O_3 shell for Ni/CeO_2/Al_2O_3 increased, whereas the conversion of both CH_4 and CO_2 decreased. The CH_4 conversions over the Ni/CeO_2/Al_2O_3-(*1*) and Ni/CeO_2/Al_2O_3-(*10*) catalysts are 48.6 and 27.9%, which were 23% and 56% lower than those achieved with Ni/CeO_2 catalyst, respectively. The data reveal that the additional Al_2O_3 shell of the Ni/CeO_2/Al_2O_3 catalysts has a negative effect on the DRM reaction because the Al_2O_3 covers the active Ni sites. Figure 4.4b shows the ratio of H_2 to CO as products generated in the DRM reaction at 700 and 800 °C. As the thickness of the Al_2O_3 shell increased, the H_2/CO ratio declined rapidly from 0.82 to 0.69, 0.58, and 0.41 for Ni/CeO_2/Al_2O_3-(*1*),

Ni/CeO_2/Al_2O_3-(*2*), and Ni/CeO_2/Al_2O_3-(*10*) respectively. As the conversion increased, the amount of H_2 produced relative to CO increased further. In general, the lower the activity of the DRM reaction, the lower the H_2/CO activity. The CH_4 activity of the catalyst is lower than that of CO_2, because CH_4 activation is more difficult than CO_2.[43] As the thickness of Al_2O_3 increases, the RWGS reaction dominantly proceeded. Compared to the relatively difficult CH_4 activation on Ni by the Al_2O_3 shell, the RWGS reaction was dominant with increased CO_2 activation on the CeO_2 surface. To evaluate the stability and durability of the Ni/CeO_2/Al_2O_3-(*1*) catalyst, the DRM reaction was performed at 700 °C for 60 h under the same gas condition. The conversion of CH_4 and CO_2 over the first 50% was reduced to 40–50%, but it was confirmed that the reaction proceeded stably while the overall reactivity was maintained steadily (Figure 4.5).

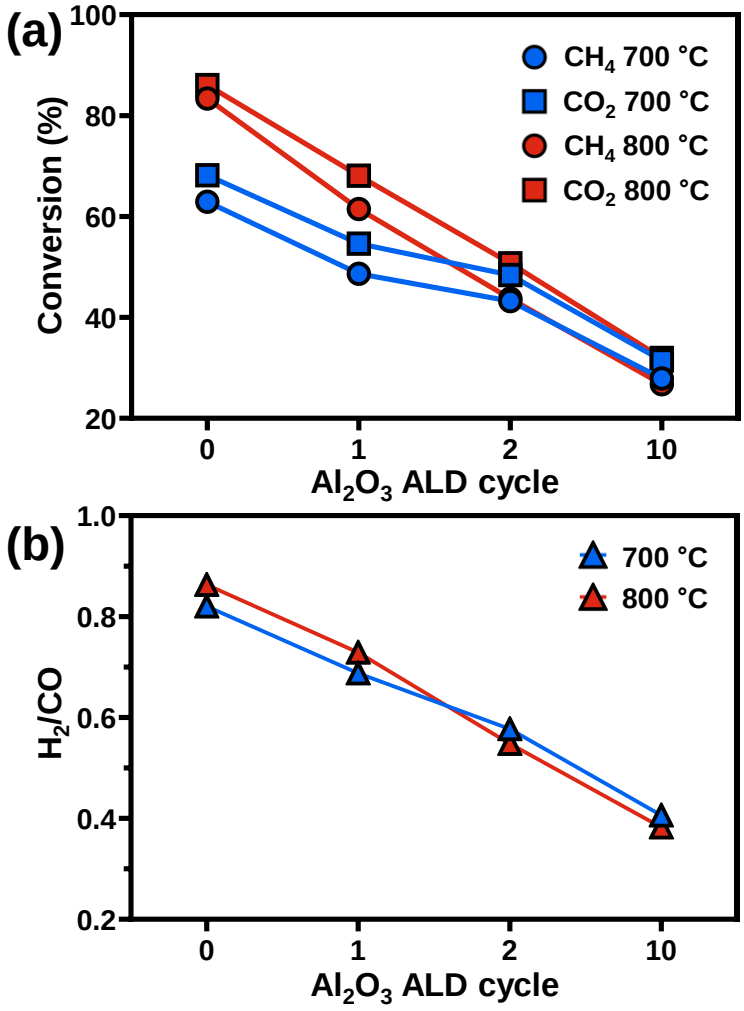

Figure 4.4. Catalyst performance in DRM reaction at 700 °C and 800 °C. (a) Conversion of CH_4 and CO_2, and (b) H_2/CO ratio of product from Ni/CeO_2/Al_2O_3-(*x*) catalyzed reaction as a function of the number of ALD cycles (*x*). Reaction conditions: CH_4/CO_2/N_2 volume ratio of 1:1:1, atmospheric pressure, W_{cat} = 20 mg, GHSV = 90,000 mL g_{cat}^{-1} h^{-1}, and 45 sccm.

Table 4.1. Catalyst performance and H_2/CO ratios of Ni/CeO_2/Al_2O_3-(*x*) catalysts for DRM.

# of ALD cycles (*x*) in Ni/CeO_2/Al_2O_3-(*x*) catalysts	Conversion (%)				H_2/CO	
	700 °C		800 °C		700 °C	800 °C
	CH_4	CO_2	CH_4	CO_2		
0	62.9	68.2	83.4	86.0	0.82	0.86
1	48.6	54.6	61.5	68.1	0.69	0.73
2	43.2	48.4	43.8	50.7	0.58	0.55
10	27.9	31.4	26.8	32.0	0.41	0.38

Reaction conditions: W_{cat} = 20 mg, T = 700–800 °C, P = 1 bar, 45 sccm of 1:1:1 (volume ratio) $CH_4/CO_2/N_2$, atmospheric pressure, GHSV = 90,000 mL g_{cat}^{-1} h^{-1}.

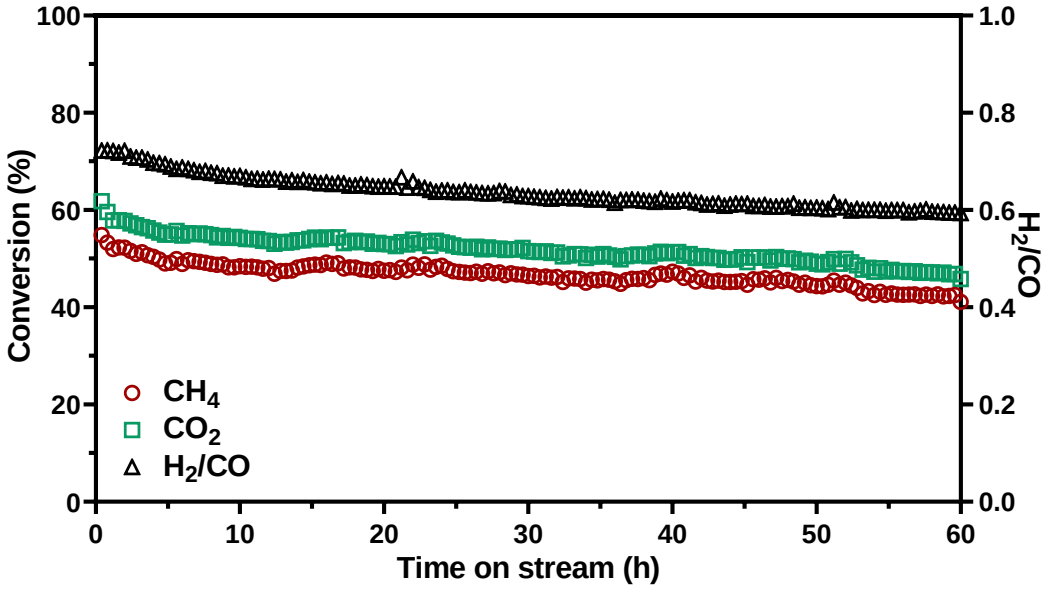

Figure 4.5. Continuous DRM reaction of a Ni/CeO_2/Al_2O_3-(*1*) catalyst showing CH_4 and CO_2 conversions and the H_2/CO ratio. Reaction conditions: $CH_4/CO_2/N_2$ volume ratio of 1:1:1, 700 °C, 60 h, atmospheric pressure, W_{cat} = 20 mg, GHSV = 90,000 mL g_{cat}^{-1} h^{-1}, and 45 sccm.

4.3.3 Coke formation on the catalysts

Most Ni-based catalysts suffer from severe coke deposition at high temperatures, which covers the Ni surface *via* the Boudouard reaction and methane decomposition. In order to prevent undesirable coverage of the Ni surface by carbon and to increase the durability of the catalyst, a strategy for reducing coke formation on the catalyst surface is very important. As a major carbon product formed by coking, carbon nanotubes (CNT) and carbon nanofibers (CNF) were formed in steps: carbon deposition, carbon diffusion, and precipitation at the Ni metal sites.[72] The active Ni sites were encapsulated by carbon (carbon nano-onions, CNO) and the CNO structure could grow until Ni was deactivated by

transformation to the NiO phase. The indiscriminate growth of carbon byproducts causes volume expansion of the catalyst bed. In the present high-temperature DRM reaction, when coking was severe, the quartz reactor expanded, which is a potential danger.

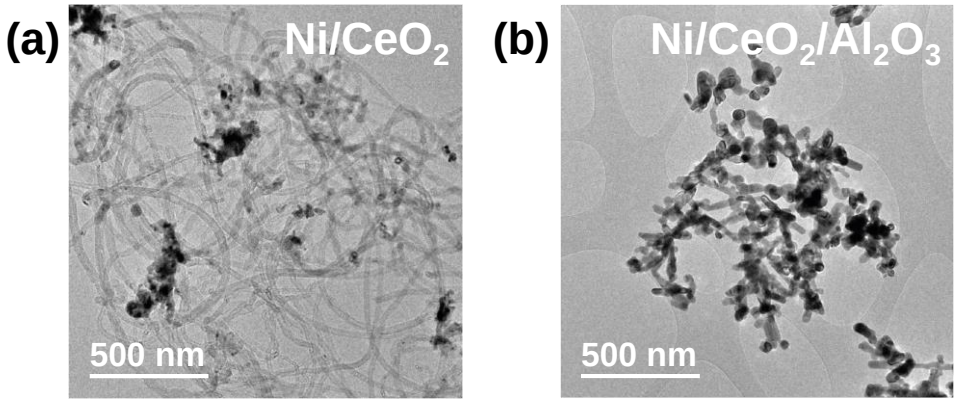

Figure 4.6. TEM images of spent catalysts after DRM: (a) Ni/CeO_2 and (b) $Ni/CeO_2/Al_2O_3$-(*1*) catalysts.

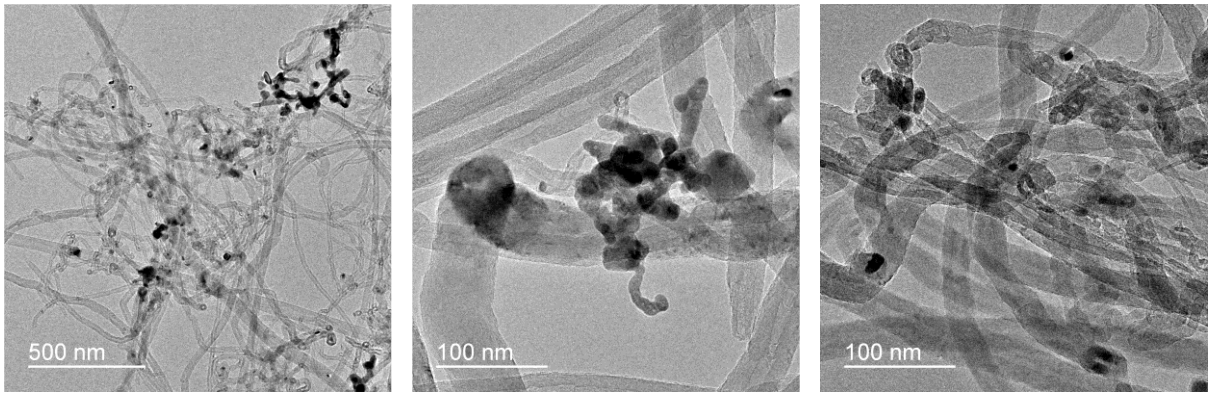

Figure 4.7. TEM images of the spent Ni/CeO_2 catalyst, showing agglomeration of nanoparticles and the carbon growth on Ni.

To alleviate coking metal, it has been reported that core@shell catalysts exhibit improved stability due to protection of the active core metal.[48,73–75] Porous SiO_2 shells are often chosen to improve the catalytic performance and thermal stability, while preventing sintering.[76] Colloidal synthesis is widely used to produce core@shell nanostructures with versatile sol–gel chemistry. However, this method is limited only to some types of oxides during the DRM, it has been reported that core@shell catalysts exhibit improved stability due to protection of the active core such as SiO_2 and TiO_2. In addition, this method is difficult to execute on a large scale, because it involves many sensitive procedures. By using an easy deposition sequence program, a cylindrical ALD reactor loaded with large amounts of catalyst can operate automatically to deposit oxide layers atomically on the catalyst surface. In particular, it is possible to effectively inhibit coke formation on the catalyst with the thinnest atomic layer by using a single ALD cycle in the DRM reaction. The TEM images of the spent catalysts showed a significant difference in the carbon deposition depending on the presence or absence of the Al_2O_3 shell

(Figure 4.6). The spent Ni/CeO_2 catalyst was occluded by massive amounts of coke, accompanied by sintering (Figure 4.7), while no coke was deposited on the $Ni/CeO_2/Al_2O_3$ catalysts, regardless of the thickness of the Al_2O_3 layer. However, the structure of the catalysts collapsed substantially after the DRM reaction at 800 °C. TEM observation of a large area of the spent catalyst showed severe agglomeration *via* sintering due to the lack of thermal stability of both Ni and CeO_2.

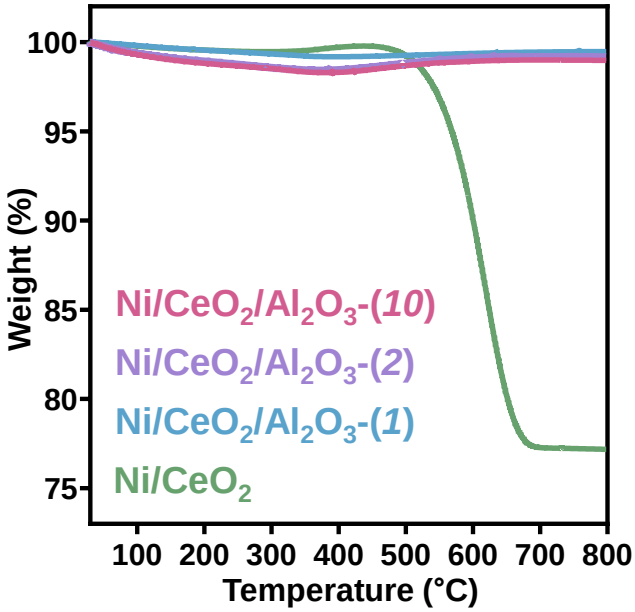

Figure 4.8. Carbon weight loss of Ni/CeO_2 and $Ni/CeO_2/Al_2O_3$-(x) catalysts measured by TGA analysis. All alumina-coated catalysts of $Ni/CeO_2/Al_2O_3$-(x) exhibited coke-resistance, whereas 23% weight loss corresponding to carbon was observed for pristine Ni/CeO_2.

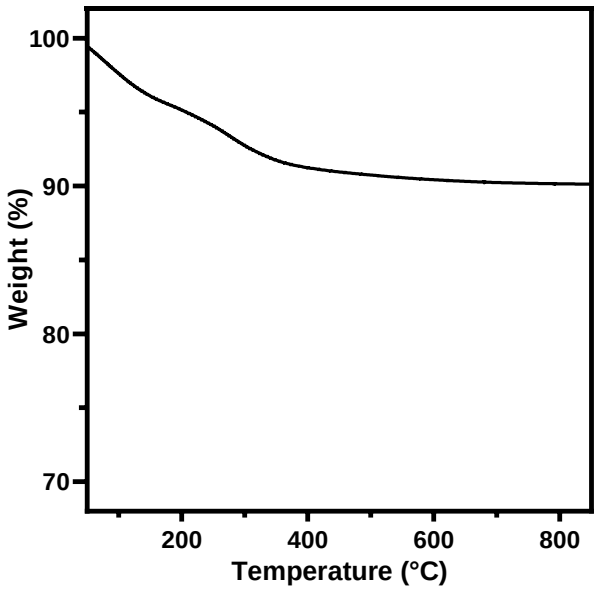

Figure 4.9. TGA measurement of CeO_2 NR.

To understand the coking phenomenon more precisely, TGA was performed on all spent catalysts (Figure 4.8). The Ni/CeO_2 catalyst showed a 23% weight loss, attributed to the oxidation of carbon to release CO_2. However, the $Ni/CeO_2/Al_2O_3$-(*x*) (*x = 1, 2, and 10*) catalysts underwent no weight loss up to 800 °C, demonstrating their coke-free characteristics. A slight increase in the weight of the Ni/CeO_2 catalyst was observed at approximately 450 °C due to the oxidation of Ni to NiO,[57] whereas no significant weight change was observed for the $Ni/CeO_2/Al_2O_3$ catalysts. No significant increase in mass due to the oxidation process of CeO_2 NRs from Ce^{3+} to Ce^{4+} was observed by the TGA analysis (Figure 4.9). Figure 4.10 shows the HAADF-STEM image and EDS mapping data for the spent $Ni/CeO_2/Al_2O_3$-(*1*) catalysts. Although the structure of the catalyst was slightly distorted by the high temperature, sintering was prevented without incorporating Ni into the CeO_2 support (Figure 4.10c and d). The size of the Ni and CeO_2 NPs increased due to aggregation. HAADF-STEM and EDS mapping of the spent catalysts confirm the partial collapse of the original structure (Figure 4.11). The degree of Ni agglomeration was similar regardless of Al_2O_3 deposition. Ni/CeO_2 showed CNT growth, whereas $Ni/CeO_2/Al_2O_3$-(*1*) had well-dispersed Ni NPs without massive agglomeration of Ni or CNT growth due to protection by the Al_2O_3 shell (Figure 4.12). The Al_2O_3 shell plays a significant role in coke resistance and mitigation of Ni sintering. Ni supported on Al_2O_3 catalyst was prepared to investigate the role of Al_2O_3 as a support. High conversions of CH_4 and CO_2 (61 and 73%) were found after DRM reaction with 50 mg of the Ni/Al_2O_3 catalyst at 700 °C (Figure 4.13). Despite the high reactivity of Ni/Al_2O_3, severe Ni sintering and coke deposition were observed (Figure 4.14).

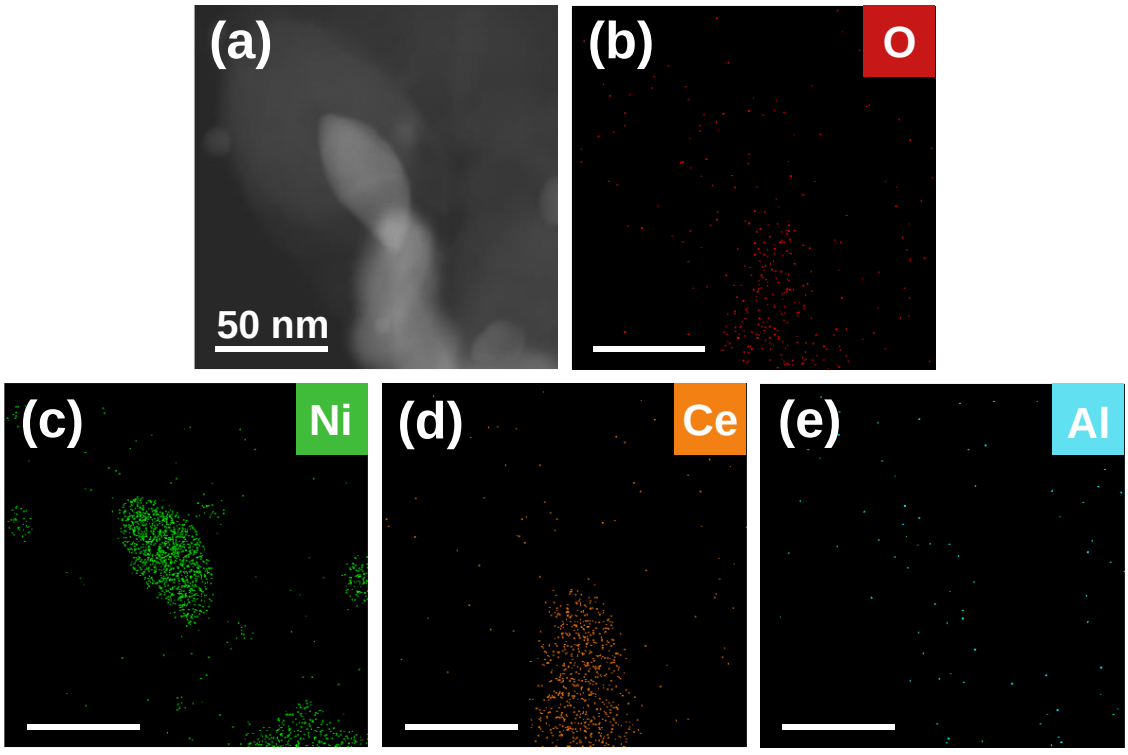

Figure 4.10. (a) HAADF-STEM and (b–e) EDS profile of atoms in spent $Ni/CeO_2/Al_2O_3$-(*1*) catalyst. All scale bars are equal to 50 nm.

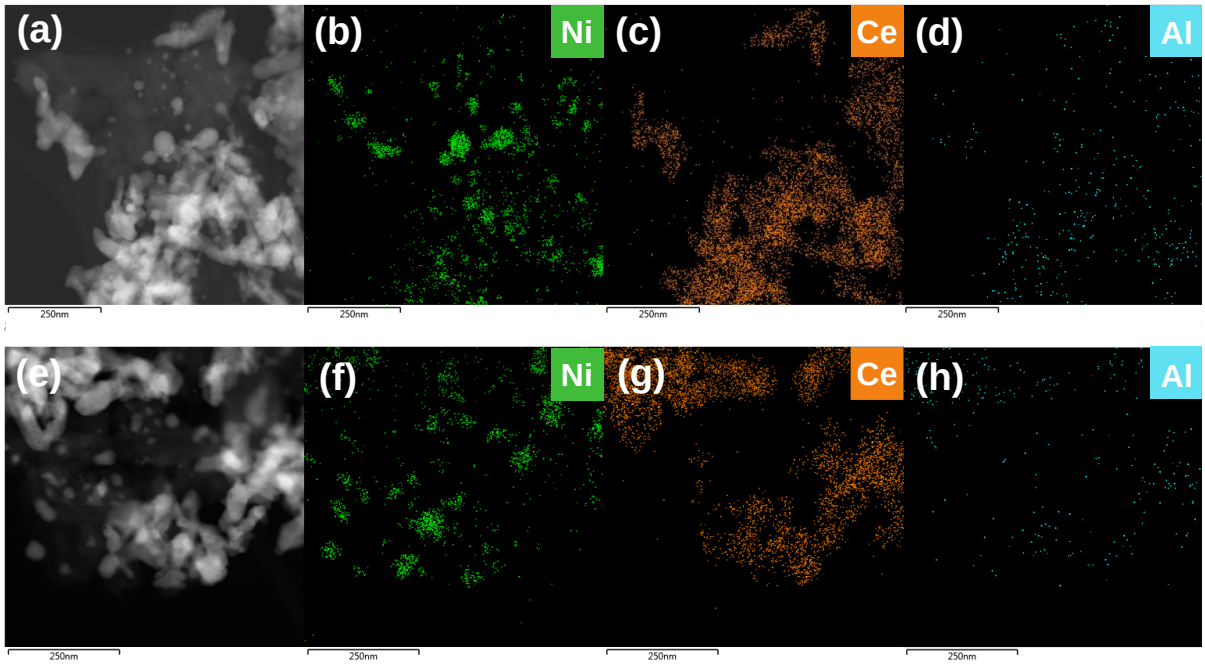

Figure 4.11. HAADF-STEM images (a and e) and following EDS profile (b–d and f–h) of spent Ni/CeO_2/Al_2O_3-(*1*) catalysts.

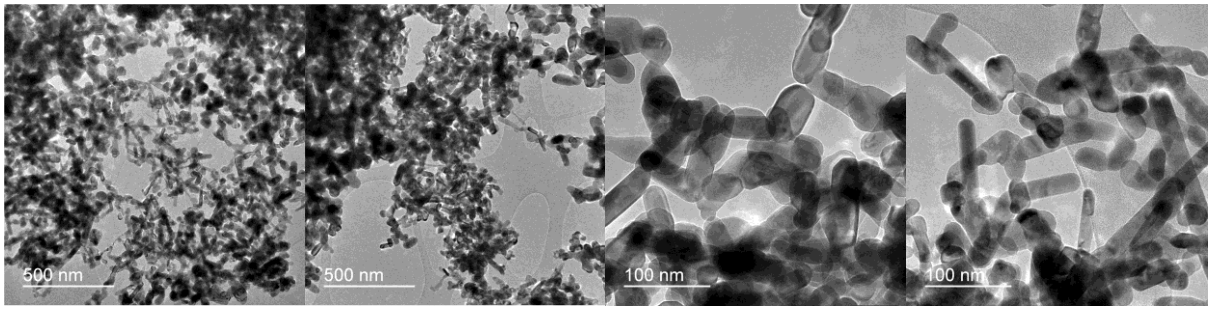

Figure 4.12. TEM images of Ni/CeO_2/Al_2O_3-(*1*) catalysts.

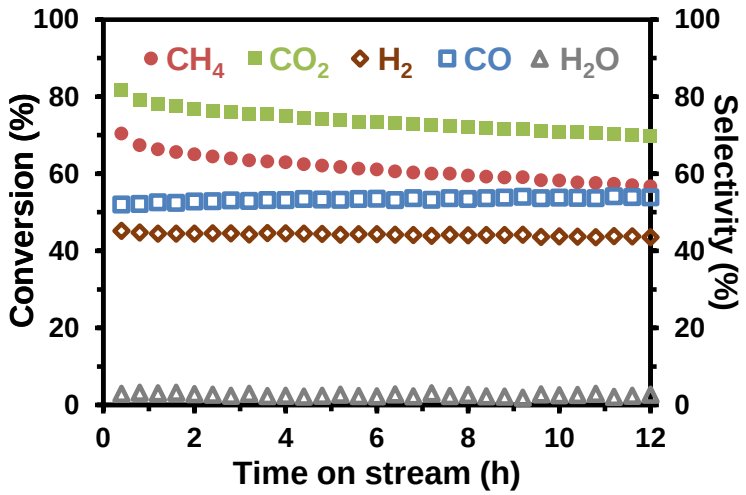

Figure 4.13. The conversions and selectivities obtained for Ni/Al_2O_3 catalysts in DRM reaction at 700 °C as a function of time on stream. Reaction conditions: 50 sccm of CH_4/CO_2/N_2 volume ratio of

1:1:3 (v/v/v), atmospheric pressure, W_{cat} = 50 mg.

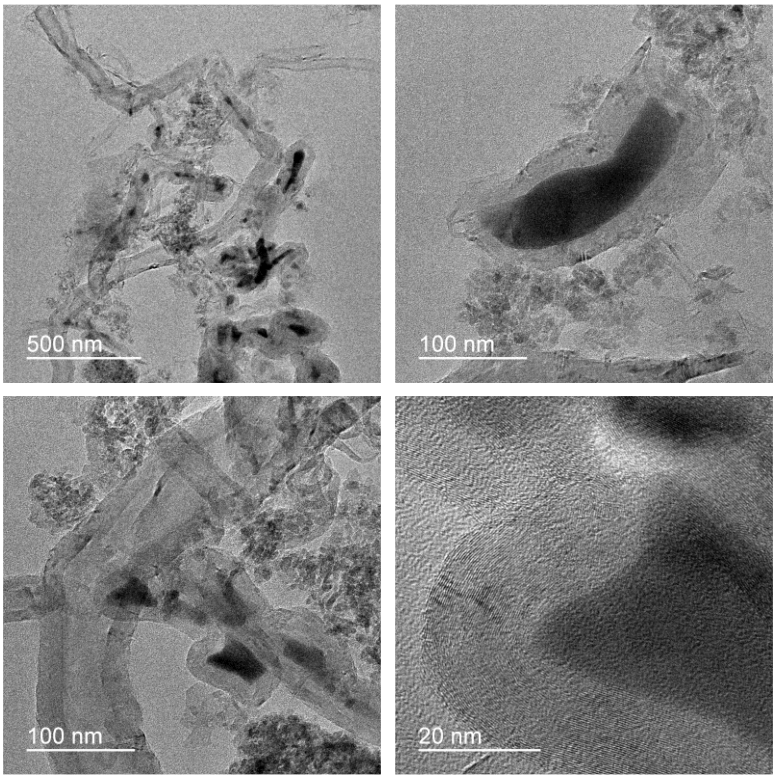

Figure 4.14. TEM images of spent Ni/Al_2O_3 catalysts.

4.3.4 Characterization

The changes in the structure and surface state of the $Ni/CeO_2/Al_2O_3$-(*x*) catalysts were investigated, depending on the thickness of the Al_2O_3 shell. Figure 4.15 shows the XRD patterns of the Ni/CeO_2 NPs in the presence and absence of the Al_2O_3 shell. All samples exhibited the characteristic peaks of CeO_2 with the fluorite structure at 28.7, 33.2, 47.7, and 56.5°, corresponding to the (111), (200), (220), and (311) planes respectively.[41] Compared to the strong XRD peaks of the CeO_2 NRs, the peaks of metallic Ni at 44, 52, and 77° and those of NiO at 37, 43, and 62° were not clearly observed in the XRD pattern because the high dispersion of the Ni small-size NPs resulted in the broadening of the diffraction peaks. Although there was no trace of the XRD peaks corresponding to NiO or Ni_2P, the strongest peak of Ni at 44.4° was not observed. As the thin Al_2O_3 shell was not crystalline, no apparent XRD peaks of Al_2O_3 was observed. Only a slight decrease in the peak intensity of CeO_2 was observed. Interestingly, as the thickness of the Al_2O_3 shell increased, the overall peak intensity decreased. This trend indicates that the amorphous Al_2O_3 shell in $Ni/CeO_2/Al_2O_3$-(*x*) shielded the catalyst surface from exposure, resulting in a decrease in the XRD signal intensity. When XRD study was performed on the spent catalysts of Ni/CeO_2 and $Ni/CeO_2/Al_2O_3$, small peaks of metallic Ni at 44 and 52° were observed due to agglomeration of NPs during the high temperature reaction. (Figure 4.16)

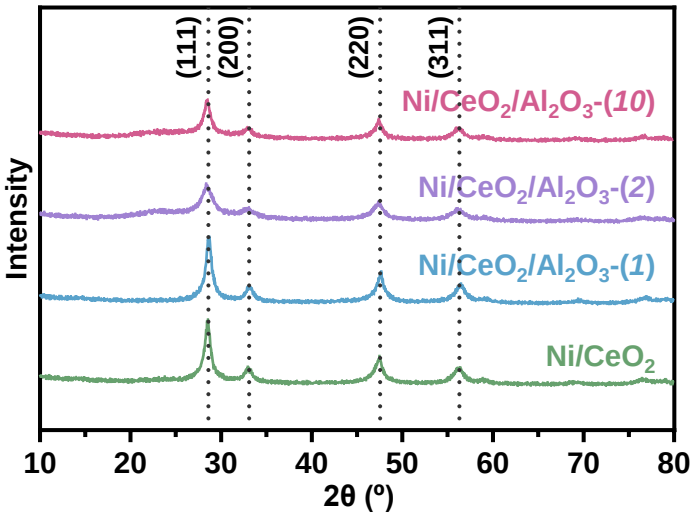

Figure 4.15. XRD spectra of $Ni/CeO_2/Al_2O_3$-(*x*) catalysts.

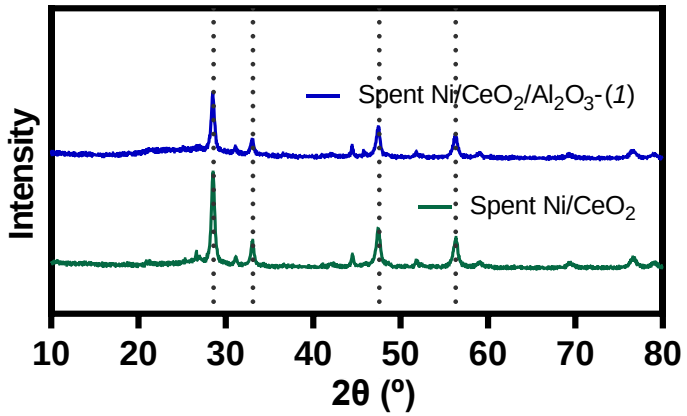

Figure 4.16. XRD patterns of the spent Ni/CeO_2 and $Ni/CeO_2/Al_2O_3$-(*1*) catalysts.

Figure 4.17 shows the H_2-TPR profile of the $Ni/CeO_2/Al_2O_3$-(*x*) catalysts. Two major peaks of the pure CeO_2 (black line) NRs appeared at 525 °C and 813 °C, assigned to the reduced oxygen originating from the surface and bulk CeO_2, respectively.[77] When Ni NPs were supported on the CeO_2 NRs, a distinct peak was observed with a small shoulder at 420 °C, but the original CeO_2 peaks were not identified. Hydrogen dissociation occurs on Ni in a lower temperature region than CeO_2, which results in CeO_2 reduction at lower temperature by hydrogen spillover.[78,79] The shoulder peak at 360 °C was assigned to the reduction of surface oxygen, which interacted weakly with the CeO_2 support.[80] The main peak centered at 420 °C indicates that the complex NiO species interacted strongly with CeO_2.[81] Although there were no significant differences among the $Ni/CeO_2/Al_2O_3$-(*x*) catalysts, the data showed that the Al_2O_3 shell did not affect the structure or interaction between Ni and CeO_2.

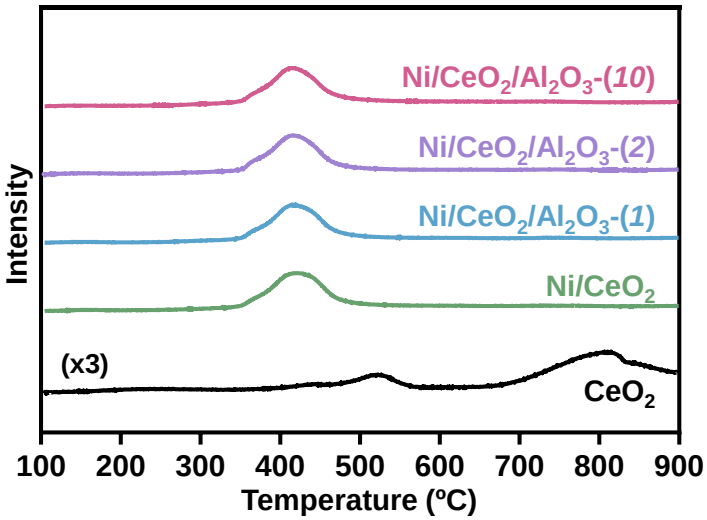

Figure 4.17. H_2-TPR profiles of $Ni/CeO_2/Al_2O_3$-(*x*) catalysts.

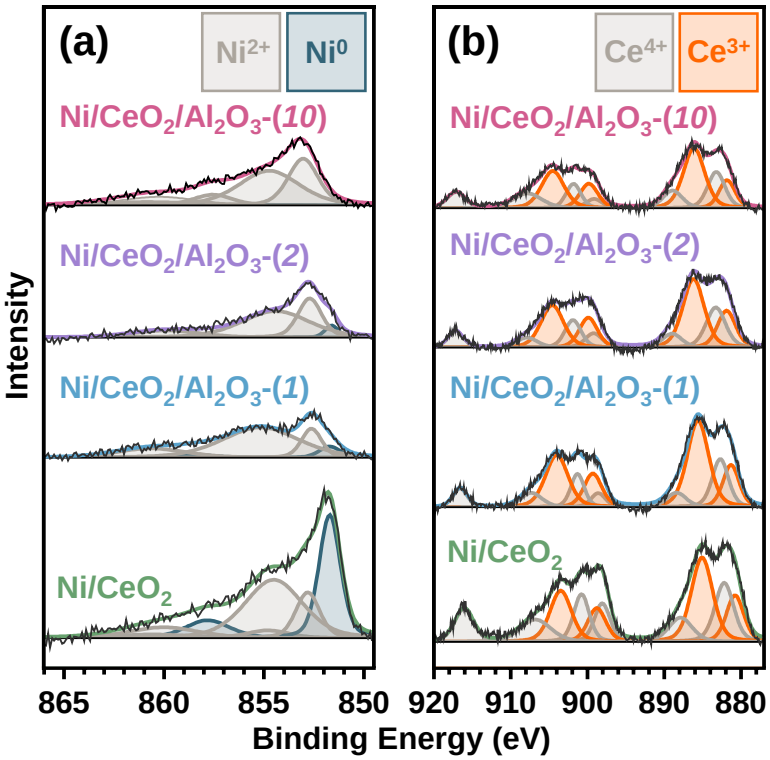

Figure 4.18. Ni 2p and (b) Ce 3d XPS profiles of $Ni/CeO_2/Al_2O_3$-(*x*) catalysts. The catalysts were reduced under a H_2/Ar (4%, 200 mL min^{-1}) flow at 700 °C for 1 h before analysis.

The change in the oxidation state of the $Ni/CeO_2/Al_2O_3$ catalysts was investigated by XPS. Because the catalyst was reduced with H_2 at 700 °C for 1 h before the DRM reaction, XPS measurement was carried out by using the reduced $Ni/CeO_2/Al_2O_3$ catalysts at 700 °C (Figure 4.18). A change in the oxidation state of Ni^{2+} and Ni^0 was identified by deconvolution of the XPS Ni 2p spectra (Figure 4.18a).[82] The XPS profile of as-prepared Ni/CeO_2 showed a distinct signal of the Ni^0 metal phase at 852 eV, indicated in the green region. The relative ratio of Ni^0 to (Ni^0+Ni^{2+}) was 0.37 for Ni/CeO_2 (Table

4.2). As the thickness of the Al_2O_3 layer increased, the amount of the Ni^0 metal phase (indicated by the peak at 852 eV) decreased remarkably. The Ni^0/Ni^{2+} ratio in the $Ni/CeO_2/Al_2O_3$-(*10*) catalyst was 0.01. Although reduction by H_2 was conducted at a high temperature of 700 °C, the surface of the Ni NPs on CeO_2 was only slightly reduced in the presence of the Al_2O_3 shell created by the ALD coating. To compare the dispersion of Ni, CO chemisorption of Ni/CeO_2 and $Ni/CeO_2/Al_2O_3$-(*1*) catalysts was performed. After depositing the Al_2O_3 shell, the Ni dispersion decreased from 2.8% to 1.7%, which was consistent with the decrease in the Ni^0 phase by the XPS and the decrease in catalytic activity (Figure 4.19). The Ce 3d XPS profiles in Figure 4.18b show the redox ability of the CeO_2 NRs.[83] The Ce 3d region was deconvoluted into ten peaks corresponding to oxidation states between Ce^{3+} and Ce^{4+}. The area of the highest binding energy peak at 916 eV indicates the quantity of the Ce^{4+} state. The steep slope in the range of 896–898 eV may be evidence of a large population of Ce^{4+} species, where the multiplets of *v* and *u* correspond to spin–orbit splitting into the $3d_{5/2}$ and $3d_{3/2}$ states. The relative ratio of $Ni^0/(Ni^0+Ni^{2+})$ and $Ce^{3+}/(Ce^{3+}+Ce^{4+})$ in the $Ni/CeO_2/Al_2O_3$ catalysts is summarized in Table 4.2.[84]

Table 4.2. Approximation of degree of reduction of Ni and CeO_2 in $Ni/CeO_2/Al_2O_3$-(*x*) catalysts from XPS results.

# of ALD cycles (*x*) in $Ni/CeO_2/Al_2O_3$-(*x*) catalysts	Relative fraction of oxidation states	
	$[Ni^0]/[Ni^0]+[Ni^{2+}]$	$[Ce^{3+}]/[Ce^{3+}]+[Ce^{4+}]$
0	0.37	0.50
1	0.09	0.65
2	0.06	0.62
10	0.01	0.58

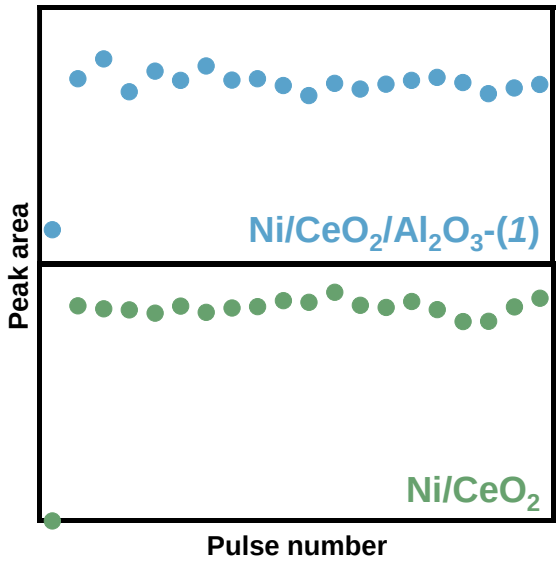

Figure 4.19. CO chemisorption measurement of Ni/CeO_2 and $Ni/CeO_2/Al_2O_3$ catalysts.

Although reduction of the Ni NPs was curtailed by Al_2O_3, the relative fraction of Ce^{3+} in the $Ni/CeO_2/Al_2O_3$-(x) catalysts increased due to the formation of oxygen vacancies in CeO_2. When Al_2O_3 was generated on the Ni/CeO_2 catalyst, the oxophilicity of CeO_2 was enhanced to generate more oxygen vacancies than in the bare Ni/CeO_2 catalyst. It was revealed that the Al_2O_3 layers on the Ni/CeO_2 catalyst not only protected the core catalyst against coking, but also changed the oxidation state of both Ni and CeO_2 during the DRM.[85] Ni can be oxidized during deposition of the Al_2O_3 shell by ALD. The adsorbed TMA on the Ni surface left methyl groups.[86] The methyl groups were removed by oxidation with H_2O, creating voids in the Al_2O_3 layer. The formation of voids decreased with increasing number of ALD cycles, and finally the Al_2O_3 deposition was dense in Ni. The introduced Al_2O_3 layer produced Ni–Al–O bonds on the Ni surface rich in a Ni^{2+} phase. CeO_2 was also reduced by the coated Al_2O_3 layer. Chen *et al.* reported the mechanism of the ALD process of Al_2O_3 on $LiMn_2O_4$. The Al_2O_3 coated $LiMn_2O_4$ had a reduced oxidation state near the surface of Mn ions by doping the Al heteroatom of the TMA into the interstitial sites.[87] XPS studies on SiO_2@V_2O_5@Al_2O_3 core@shell catalysts also showed that the vanadium surface was reduced from V^{5+} to V^{4+} by the oxidized carbons produced by TMA ligands.[88] Thus, the newly formed Al_2O_3 layer helps to decrease the coking substantially, but the weak metallic character of Ni and blocking of the Ni sites by the Al_2O_3 layer are the major factors contributing to decrease in the catalytic conversion.

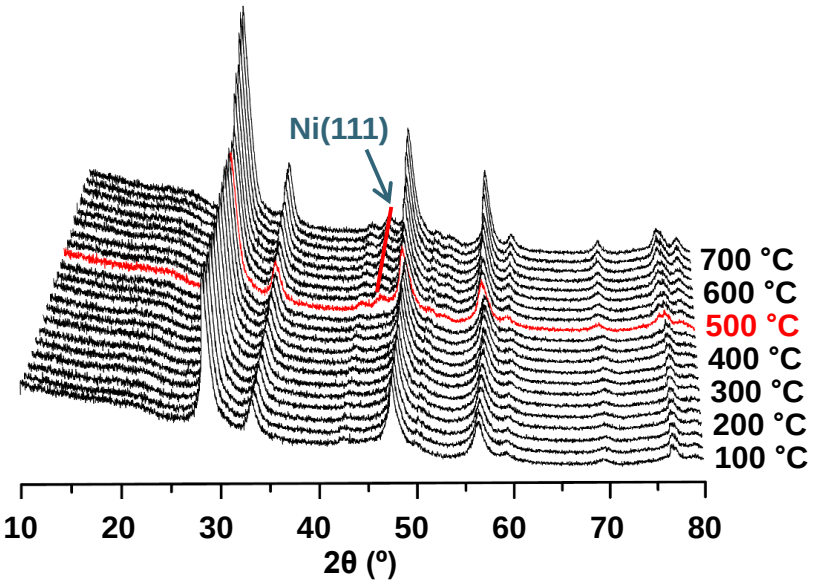

Figure 4.20. *In situ* XRD analyses of $Ni/CeO_2/Al_2O_3$-(*1*) catalyst. Measurement was carried out under a H_2/Ar flow (4%, 100 mL min^{-1}) while ramping the temperature to 700 °C.

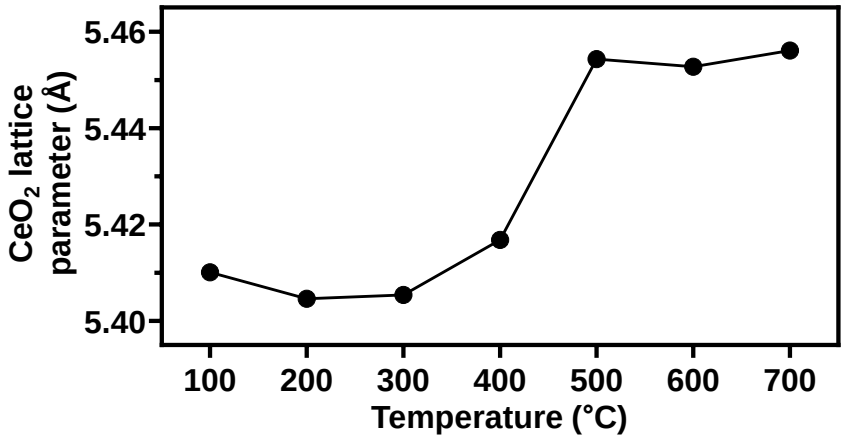

Figure 4.21. CeO_2 lattice parameters of Ni/CeO_2/Al_2O_3-(*1*) catalyst from Rietveld refinement of *in situ* XRD data obtained under H_2 environment.

In order to monitor the catalyst deactivation due to sintering, *in situ* XRD measurements were conducted for the samples subjected to H_2 pretreatment and to the DRM environment. Figure 4.20 shows the *in situ* XRD patterns of the Ni/CeO_2/Al_2O_3-(*1*) catalyst that were treated with flowing H_2 in the temperature range of 100–700 °C. When the temperature reached 500 °C, a small peak of the Ni metallic phase appeared at 44.4°. The temperature-dependent reduction of the Ni active sites was in good agreement with the H_2-TPR results. The change in the lattice parameter of CeO_2 as a function of temperature after Rietveld refinement is shown in Figure 4.21. A steep increase in the lattice parameter of CeO_2 was observed beyond 500 °C due to the thermal expansion of the CeO_2 lattice and redox equilibrium under the reducing environment.[89,90] The structural changes in the Ni/CeO_2/Al_2O_3-(*1*) catalyst subjected to the catalytically relevant reaction conditions of the DRM at 500–800 °C after the reduction pretreatment were investigated by *in situ* XRD. As shown in Figure 4.22, the major peaks corresponding to CeO_2 lost intensity beyond 700 °C, indicating that the structure of the CeO_2 NRs started to collapse after 700 °C. No newly generated peak was identified up to 800 °C.

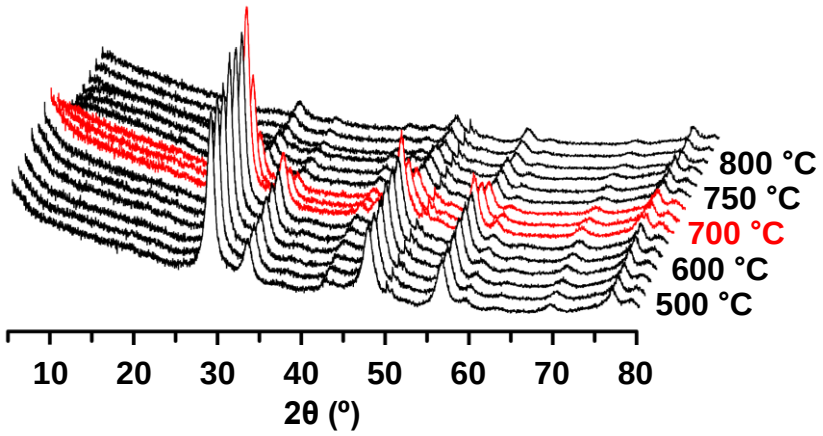

Figure 4.22. *In situ* XRD measurement of Ni/CeO_2/Al_2O_3-(*1*) catalyst under DRM conditions using a mixture gas flow of CH_4:CO_2:Ar = 4:4:92 (100 mL min^{-1}).

4.4. Conclusion

The ALD technique is very efficient for fine tuning the Al_2O_3 shell on Ni/CeO_2 NP catalysts to provide coke-resistance in the DRM reaction. The coke resistance of the $Ni/CeO_2/Al_2O_3$ catalysts up to 800 °C was confirmed by TGA. Increasing the number of ALD cycles from *1* to *10* resulted in decreased conversion of CO_2 and CH_4 at 700 and 800 °C due to coverage of the active Ni sites by the Al_2O_3 layer. TGA, XRD, and XPS characterization showed that the Al_2O_3 layers on the $Ni/CeO_2/Al_2O_3$ catalysts changed the oxidation state of both Ni and CeO_2 during the DRM. Metallic Ni^0 sites and oxygen vacancies on CeO_2 are required for the activation of CH_4 and CO_2, respectively; the atomically grown Al_2O_3 layers generated an oxidized Ni phase and more oxygen vacancies in CeO_2. In the present high-temperature DRM reaction, indiscriminate growth of carbon by-products caused dangerous volume expansion of the catalyst bed. Despite the decrease in the conversion, the newly formed Al_2O_3 layer played a critical role in reducing coke formation to promote sustained DRM reaction at high temperature. ALD can be used to change only the outermost surface to improve the catalyst performance and resistance to coke deposition and sintering. From the present findings, the possibility of surface modification of various catalysts with atomically controlled oxide layers is feasible.

4.5. References

1. S. Kattel, P. Liu and J. G. Chen, Tuning selectivity of CO_2 hydrogenation reactions at the metal/oxide interface, *J. Am. Chem. Soc.*, **2017**, *139*, 9739.
2. O. K. Varghese, M. Paulose, T. J. LaTempa and C. A. Grimes, High-rate solar photocatalytic conversion of CO_2 and water vapor to hydrocarbon fuels, *Nano Lett.*, **2009**, *9*, 731.
3. W.-C. Liu, J. Baek and G. A. Somorjai, The methanol economy: methane and carbon dioxide conversion, *Top. Catal.*, **2018**, *61*, 530.
4. Y. T. Shah and T. H. Gardner, Dry reforming of hydrocarbon feedstocks, *Catal. Rev.*, **2014**, *56*, 476.
5. D. Pakhare, J. Spivey, A review of dry (CO_2) reforming of methane over noble metal catalysts, *Chem. Soc. Rev.*, **2014**, *43*, 7813.
6. M. Bradford and M. Vannice, CO_2 reforming of CH_4, *Catal. Rev.*, **1999**, *41*, 1.
7. S. De, J. Zhang, R. Luque and N. Yan, Ni-based bimetallic heterogeneous catalysts for energy and environmental applications, *Energy Environ. Sci.*, **2016**, *9*, 3314.
8. N. A. K. Aramouni, J. G. Touma, B. Abu Tarboush, J. Zeaiter and M. N. Ahmad, Catalyst design for dry reforming of methane: Analysis review, *Renew. Sustain. Energy Rev.*, **2018**, *82*, 2570.
9. S. Kawi, Y. Kathiraser, J. Ni, U. Oemar, Z. Li and E. T. Saw, Progress in synthesis of highly active and stable nickel-based catalysts for carbon dioxide reforming of methane, *ChemSusChem*, **2015**, *8*, 3556.
10. B. Abdullah, N. A. A. Ghani and D.-V. N. Vo, Recent advances in dry reforming of methane over Ni-based catalysts, *J. Clean. Prod.*, **2017**, *162*, 170.

11. V. M. Gonzalez-Delacruz, R. Pereniguez, F. Ternero, J. P. Holgado and A. Caballero, Modifying the size of nickel metallic particles by H_2/CO treatment in Ni/ZrO_2 methane dry reforming catalysts, *ACS Catal.*, **2011**, *1*, 82.

12. V. Choudhary, A. Rajput and A. Mamman, NiO-alkaline earth oxide catalysts for oxidative methane-to-syngas conversion: Influence of alkaline earth oxide on the surface properties and temperature-programmed reduction/reaction by H_2 and methane, *J. Catal.*, **1998**, *178*, 576.

13. L. Zhou, L. Li, N. Wei, J. Li and J. M. Basset, Effect of $NiAl_2O_4$ formation on Ni/Al_2O_3 stability during dry reforming of methane, *ChemCatChem*, **2015**, *7*, 2508.

14. X. Fang, C. Peng, H. Peng, W. Liu, X. Xu, X. Wang, C. Li and W. Zhou, Methane dry reforming over coke-resistant mesoporous Ni-Al_2O_3 catalysts prepared by evaporation-induced self-assembly method, *ChemCatChem*, **2015**, *7*, 3753.

15. J. A. Moulijn, A. Van Diepen and F. Kapteijn, Catalyst deactivation: is it predictable?: What to do?, *Appl. Catal. A*, **2001**, *212*, 3.

16. A. Sharma, I. Saito, H. Nakagawa and K. Miura, Effect of carbonization temperature on the nickel crystallite size of a Ni/C catalyst for catalytic hydrothermal gasification of organic compounds, *Fuel*, **2007**, *86*, 915.

17. X. Guo, G. Fang, G. Li, H. Ma, H. Fan, L. Yu, C. Ma, X. Wu, D. Deng and M. Wei, Direct, nonoxidative conversion of methane to ethylene, aromatics, and hydrogen, *Science*, **2014**, *344*, 616.

18. Z. Wang, X.-M. Cao, J. Zhu and P. Hu, Activity and coke formation of nickel and nickel carbide in dry reforming: a deactivation scheme from density functional theory, *J. Catal.*, **2014**, *311*, 469.

19. S.-G. Wang, D.-B. Cao, Y.-W. Li, J. Wang and H. Jiao, CO_2 reforming of CH_4 on Ni(111): a density functional theory calculation, *J. Phys. Chem. B*, **2006**, *110*, 9976.

20. L. Li, D. H. Anjum, H. Zhu, Y. Saih, P. V. Laveille, L. D'Souza and J. M. Basset, Synergetic effects leading to coke-resistant NiCo bimetallic catalysts for dry reforming of methane, *ChemCatChem*, **2015**, *7*, 427.

21. C. j. Liu, J. Ye, J. Jiang and Y. Pan, Progresses in the preparation of coke resistant Ni-based catalyst for steam and CO_2 reforming of methane, *ChemCatChem*, **2011**, *3*, 529.

22. X. Gao, H. Liu, K. Hidajat and S. Kawi, Anti-coking Ni/SiO_2 catalyst for dry reforming of methane: Role of oleylamine/oleic acid organic pair, *Chemcatchem*, **2015**, *7*, 4188.

23. Y. Kathiraser, W. Thitsartarn, K. Sutthiumporn and S. Kawi, Inverse $NiAl_2O_4$ on $LaAlO_3$–Al_2O_3: Unique catalytic structure for stable CO_2 reforming of methane, *J. Phys. Chem. C*, **2013**, *117*, 16, 8120.

24. X. Y. Gao, K. Hidajat and S. Kawi, Facile synthesis of Ni/SiO_2 catalyst by sequential hydrogen/air treatment: A superior anti-coking catalyst for dry reforming of methane, *J. CO_2 Util.*, **2016**, *15*, 146.

25. X.Y. Gao, J. Ashok, S. Widjaja, K. Hidajat and S. Kawi, Ni/SiO_2 catalyst prepared via Ni-aliphatic amine complexation for dry reforming of methane: Effect of carbon chain number and amine concentration, *Appl. Catal. A*, **2015**, *503*, 34.

26. X. Gao, Z. Tan, K. Hidajat and S. Kawi, Highly reactive Ni-Co/SiO_2 bimetallic catalyst via complexation with oleylamine/oleic acid organic pair for dry reforming of methane, *Catal. Today*, **2017**, *281*, 250.

27. U. Oemar, Y. Kathiraser, L. Mo, X. K. Ho and S. Kawi, CO_2 reforming of methane over highly active La-promoted Ni supported on SBA-15 catalysts: mechanism and kinetic modelling, *Catal. Sci. Technol.* **2016**, *6*, 1173.

28. J. Ni, J. Zhao, L. Chen, J. Lin and S. Kawi, Lewis acid sites stabilized nickel catalysts for dry (CO_2) reforming of methane, *Chemcatchem*, **2016**, *8*, 3732.

29. L. Mo, K. K. M. Leong and S. Kawi, A highly dispersed and anti-coking Ni–La_2O_3/SiO_2 catalyst for syngas production from dry carbon dioxide reforming of methane, *Catal. Sci. Technol.* **2014**, *4*, 2107.

30. J. Ni, L. Chen, J. Lin, M. K. Schreyer, Z. Wang and S. Kawi, High performance of Mg–La mixed oxides supported Ni catalysts for dry reforming of methane: The effect of crystal structure, *Int. J. Hydrogen Energy*, **2013**, *38*, 13631.

31. K. Sutthiumporn, T. Maneerung, Y. Kathiraser and S. Kawi, CO_2 dry-reforming of methane over $La_{0.8}Sr_{0.2}Ni_{0.8}M_{0.2}O_3$ perovskite (M = Bi, Co, Cr, Cu, Fe): Roles of lattice oxygen on C–H activation and carbon suppression, *Int. J. Hydrogen Energy*, **2012**, *37*, 11195.

32. J.-C. Zhang, B.-H. Ge, T.-F. Liu, Y. Yang, B. Li and W.-Z. Li, Robust ruthenium-saving catalyst for high-temperature carbon dioxide reforming of methane, *ACS Catal.*, **2020**, *10*, 783.

33. L. P. AGH, M. Motak, M. Jaszczur and G. Plus, Use of HTGR process heat with catalysts for dry reforming of methane using CO_2 to syngas for the chemical industry.

34. Y. Song, E. Ozdemir, S. Ramesh, A. Adishev, S. Subramanian, A. Harale, M. Albuali, B. A. Fadhel, A. Jamal and D. Moon, Dry reforming of methane by stable Ni-Mo nanocatalysts on single-crystalline MgO, *Science*, **2020**, *367*, 777.

35. L. C. Buelens, V. V. Galvita, H. Poelman, C. Detavernier and G. B. Marin, Super-dry reforming of methane intensifies CO_2 utilization via Le Chatelier's principle, *Science*, **2016**, *354*, 449.

36. F. Zhang, Z. Liu, X. Chen, N. Rui, L. E. Betancourt, L. Lin, W. Xu, C.-J. Sun, A. M. Abeykoon and J. A. Rodriguez, The effects of Zr-doping into ceria for the dry reforming of methane over Ni/$CeZrO_2$ catalysts: *In-situ* studies with XRD, XAFS and AP-XPS, *ACS Catal.*, **2020**, *10*, 3274.

37. L. Xu, W. Liu, X. Zhang, L. Tao, L. Xia, X. Xu, J. Song, W. Zhou, X. Fang and X. Wang, Ni/La_2O_3 catalysts for dry reforming of methane: Insights into the factors improving the catalytic performance, *ChemCatChem*, **2019**, *11*, 2887.

38. C. Liang, X. Hu, T. Wei, P. Jia, Z. Zhang, D. Dong, S. Zhang, Q. Liu and G. Hu, Methanation of CO_2 over Ni/Al_2O_3 modified with alkaline earth metals: Impacts of oxygen vacancies on catalytic activity, *Int. J. Hydrogen Energy*, **2019**, *44*, 8197.

39. L. Xu, H. Song and L. Chou, Ordered mesoporous MgO-Al_2O_3 composite oxides supported Ni based catalysts for CO_2 reforming of CH_4: Effects of basic modifier and mesopore structure, *Int. J. Hydrogen Energy*, **2013**, *38*, 7307.

40. M. D. Porosoff and J. G. Chen, Trends in the catalytic reduction of CO_2 by hydrogen over supported monometallic and bimetallic catalysts, *J. Catal.*, **2013**, *301*, 30.

41. X. Du, D. Zhang, L. Shi, R. Gao and J. Zhang, Morphology dependence of catalytic properties of Ni/CeO_2 nanostructures for carbon dioxide reforming of methane, *J. Phys. Chem. C*, **2012**, *116*, 10009.

42. D. K. Kim, K. Stöwe, F. Müller and W. F. Maier, Mechanistic study of the unusual catalytic properties of a new NiCe mixed oxide for the CO_2 reforming of methane, *J. Catal.*, **2007**, *247*, 101.

43. Z. Liu, D. C. Grinter, P. G. Lustemberg, T. D. Nguyen-Phan, Y. Zhou, S. Luo, I. Waluyo, E. J. Crumlin, D. J. Stacchiola and J. Zhou, Dry reforming of methane on a highly-active Ni-CeO_2 catalyst: Effects of metal-support interactions on C−H bond breaking, *Angew. Chem. Int. Ed.*, **2016**, *55*, 7455.

44. S. Wang and G. M. Lu, Role of CeO_2 in Ni/CeO_2-Al_2O_3 catalysts for carbon dioxide reforming of methane, *Appl. Catal. B*, **1998**, *19*, 267.

45. A. Jangam, S. Das, N. Dewangan, P. Hongmanorom, W. M. Hui and S. Kawi, Conversion of CO_2 to C1 chemicals: Catalyst design, kinetics and mechanism aspects of the reactions, *Catal. Today*, **2019**, 10.1016/j.cattod.2019.08.049.

46. Z. Bian, S. Das, M. H. Wai, P. Hongmanorom and S. Kawi, A review on bimetallic nickel-based catalysts for CO_2 reforming of methane, *Chemphyschem*, **2017**, *18*, 3117.

47. P. G. Lustemberg, P. J. Ramírez, Z. Liu, R. A. Gutierrez, D. G. Grinter, J. Carrasco, S. D. Senanayake, J. A. Rodriguez and M. V. Ganduglia-Pirovano, Room-temperature activation of methane and dry reforming with CO_2 on Ni-CeO_2 (111) surfaces: effect of Ce^{3+} sites and metal-support interactions on C–H bond cleavage, *ACS Catal.*, **2016**, *6*, 8184.

48. Q. Zhang, I. Lee, J. Ge, F. Zaera and Y. Yin, Surface-protected etching of mesoporous oxide shells for the stabilization of metal nanocatalysts, *Adv. Funct. Mater.*, **2010**, *20*, 2201.

49. J. Ge, Q. Zhang, T. Zhang and Y. Yin, Core-satellite nanocomposite catalysts protected by a porous silica shell: Controllable reactivity, high stability, and magnetic recyclability, *Angew. Chem. Int. Ed.*, **2008**, *47*, 8924.

50. J. W. Han, C. Kim, J. S. Park and H. Lee, Highly coke-resistant Ni nanoparticle catalysts with minimal sintering in dry reforming of methane, *ChemSusChem*, **2014**, *7*, 451.

51. K. Cao, M. Gong, J. Yang, J. Cai, S. Chu, Z. Chen, B. Shan and R. Chen, Nickel catalyst with atomically-thin meshed cobalt coating for improved durability in dry reforming of methane, *J. Catal.*, **2019**, *373*, 351.

52. Q. Fang, S. Xuan, W. Jiang and X. Gong, Yolk-like micro/nanoparticles with superparamagnetic iron oxide cores and hierarchical nickel silicate shells, *Adv. Funct. Mater.*, **2011**, *21*, 1902.

53. X. You, X. Wang, Y. Ma, J. Liu, W. Liu, X. Xu, H. Peng, C. Li, W. Zhou and P. Yuan, Ni-Co/Al_2O_3 bimetallic catalysts for CH_4 steam reforming: elucidating the role of Co for improving coke resistance, *ChemCatChem*, **2014**, *6*, 3377.

54. Z. Li, Z. Wang and S. Kawi, Sintering and coke resistant core/yolk shell catalyst for hydrocarbon reforming, *ChemCatChem*, **2019**, *11*, 202.

55. S. Das, J. P. -Ramírez, J. Gong, N. Dewangan, K. Hidajat, B. C. Gates and S. Kawi, Core–shell structured catalysts for thermocatalytic, photocatalytic, and electrocatalytic conversion of CO_2, *Chem. Soc. Rev.*, **2020**, *49*, 2937.

56. Z. Li, M. Li, Z. Bian, Y. Kathiraser and S. Kawi, Design of highly stable and selective core/yolk–shell nanocatalysts—A review, *Appl. Catal. B*, **2016**, *188*, 324.

57. Z. W. Li, L. Y. Mo, Y. Kathiraser and S. Kawi, Yolk-satellite-shell structured Ni-yolk@Ni@SiO_2 nanocomposite: superb catalyst toward methane CO_2 reforming reaction, *ACS Catal.*, **2014**, *4*, 1526.

58. S. Zhu, X. Lian, T. Fan, Z. Chen, Y. Dong, W. Weng, X. Yi and W. Fang, Thermally stable core–shell Ni/nanorod-CeO_2@SiO_2 catalyst for partial oxidation of methane at high temperatures, *Nanoscale*, **2018**, *10*, 14031.

59. B. J. O'Neill, D. H. K. Jackson, J. Lee, C. Canlas, P. C. Stair, C. L. Marshall, J. W. Elam, T. F. Kuech, J. A. Dumesic and G. W. Huber, Catalyst design with atomic layer deposition, *ACS Catal.*, **2015**, *5*, 1804.

60. J. Lu, B. Fu, M. C. Kung, G. Xiao, J. W. Elam, H. H. Kung and P. C. Stair, Coking- and sintering-resistant palladium catalysts achieved through atomic layer deposition, *Science*, **2012**, *335*, 1205.

61. T. D. Gould, A. Izar, A. W. Weimer, J. L. Falconer and J. W. Medlin, Stabilizing Ni catalysts by molecular layer deposition for harsh, dry reforming conditions, *ACS Catal.*, **2014**, *4*, 2714.

62. H. Ge, B. Zhang, X. Gu, H. Liang, H. Yang, Z. Gao, J. Wang and Y. Qin, A tandem catalyst with multiple metal oxide interfaces produced by atomic layer deposition, *Angew. Chem. Int. Ed.*, **2016**, *55*, 7081.

63. J. Zhang, Z. Yu, Z. Gao, H. Ge, S. Zhao, C. Chen, S. Chen, X. Tong, M. Wang and Z. Zheng, Porous TiO_2 nanotubes with spatially separated platinum and CoO_x cocatalysts produced by atomic layer deposition for photocatalytic hydrogen production, *Angew. Chem. Int. Ed.*, **2017**, *56*, 816.

64. T. M. Onn, S. Zhang, L. Arroyo-Ramirez, Y.-C. Chung, G. W. Graham, X. Pan and R. J. Gorte, Improved thermal stability and methane-oxidation activity of Pd/Al2O3 catalysts by atomic layer deposition of ZrO_2, *ACS Catal.*, **2015**, *5*, 5696.

65. Q. Zhang and J. Guan, Single-atom catalysts for electrocatalytic applications, *Adv. Funct. Mater.*, **2020**, 2000768.

66. E. Yang, J. G. Lee, D. H. Kim, Y. S. Jung, J. H. Kwak, E. D. Park and K. An, SiO_2@V_2O_5@ Al_2O_3 core-shell catalysts with high activity and stability for methane oxidation to formaldehyde, *J. Catal.*, **2018**, *368*, 134.

67. C. Lin, J. B. Jang, L. H. Zhang, E. A. Stach and R. J. Gorte, Improved coking resistance of "Intelligent" Ni catalysts prepared by atomic layer deposition, *ACS Catal.*, **2018**, *8*, 7679.

68. B. J. O'Neill, D. H. K. Jackson, A. J. Crisci, C. A. Farberow, F. Y. Shi, A. C. Alba-Rubio, J. L. Lu, P. J. Dietrich, X. K. Gu, C. L. Marshall, P. C. Stair, J. W. Elam, J. T. Miller, F. H. Ribeiro, P. M. Voyles, J. Greeley, M. Mavrikakis, S. L. Scott, T. F. Kuech and J. A. Dumesic, Stabilization of copper catalysts for liquid-phase reactions by atomic layer deposition, *Angew. Chem. Int. Ed.*, **2013**, *52*, 13808.

69. J. G. Chen, Carbide and nitride overlayers on early transition metal surfaces: Preparation, characterization, and reactivities, *Chem. Rev.*, **1996**, *96*, 1477.

70. S. Carenco, C. H. Wu, A. Shavorskiy, S. Alayoglu, G. A. Somorjai, H. Bluhm and M. Salmeron, Synthesis and structural evolution of nickel-cobalt nanoparticles under H_2 and CO_2, *Small*, **2015**, *11*, 3045.

71. J. Li, Z. Y. Zhang, W. Gao, S. Zhang, Y. Y. Ma and Y. Q. Qu, Pressure regulations on the surface properties of CeO2 nanorods and their catalytic activity for CO oxidation and nitrile hydrolysis reactions, *ACS Appl. Mater. Inter.*, **2016**, *8*, 22988.

72. L. Zhou, L. D. Li, N. N. Wei, J. Li and J. M. Basset, Effect of $NiAl_2O_4$ formation on Ni/Al_2O_3 stability during dry reforming of methane, *ChemCatChem*, **2015**, *7*, 2508.

73. S. Das, J. Ashok, Z. Bian, N. Dewangan, M. H. Wai, Y. Du, A. Borgna, K. Hidajat and S. Kawi, Silica-ceria sandwiched Ni core-shell catalyst for low temperature dry reforming of biogas: Coke resistance and mechanistic insights, *Appl. Catal. B*, **2018**, *230*, 220.

74. Q. Zhang, I. Lee, J. B. Joo, F. Zaera and Y. Yin, Core-shell nanostructured catalysts, *Acc. Chem. Res.*, **2013**, *46*, 1816.

75. K. An, Q. Zhang, S. Alayoglu, N. Musselwhite, J.-Y. Shin and G. A. Somorjai, High-temperature catalytic reforming of n-hexane over supported and core-shell Pt nanoparticle catalysts: Role of oxide-metal interface and thermal stability, *Nano Lett.*, **2016**, *14*, 4907.

76. J. C. Park, J. U. Bang, J. Lee, C. H. Ko and H. Song, Ni@SiO_2 yolk-shell nanoreactor catalysts: High temperature stability and recyclability, *J. Mater. Chem.*, **2010**, *20*, 1239.

77. P. V. R. Rao, V. P. Kumar, G. S. Rao and K. V. R. Chary, Vapor phase selective hydrogenation of acetone to methyl isobutyl ketone (MIBK) over Ni/CeO_2 catalysts, *Catal. Sci. Technol.*, **2012**, *2*, 1665.

78. M. Boaro, M. Vicario, C. Leitenburg, G. Dolcetti and A. Trovarelli, The use of temperature-programmed and dynamic/transient methods in catalysis: characterization of ceria-based, model three-way catalysts, *Catal. Today*, **2003**, *77*, 407.

79. J. Beckers and G. Rothenberg, Redox properties of doped and supported copper-ceria catalysts, *Dalton Trans.*, **2008**, 6573.

80. X. J. Du, D. S. Zhang, L. Y. Shi, R. H. Gao and J. P. Zhang, Morphology dependence of catalytic properties of Ni/CeO_2 nanostructures for carbon dioxide reforming of methane, *J. Phys. Chem. C*, **2012**, *116*, 10009.

81. J. Deng, W. Chu, B. Wang, W. Yang and X. S. Zhao, Mesoporous $Ni/Ce_{1-x}Ni_xO_{2-y}$ heterostructure as an efficient catalyst for converting greenhouse gas to H_2 and syngas, *Catal. Sci. Technol.*, **2016**, *6*, 851.

82. M. C. Biesinger, B. P. Payne, L. W. M. Lau, A. Gerson and R. S. C. Smart, X-ray photoelectron spectroscopic chemical state quantification of mixed nickel metal, oxide and hydroxide systems, *Surf. Interface Anal.*, **2009**, *41*, 324.

83. E. Beche, P. Charvin, D. Perarnau, S. Abanades and G. Flamant, Ce 3d XPS investigation of cerium oxides and mixed cerium oxide ($Ce_xTi_yO_z$), *Surf. Interface Anal.* **2008**, *40*, 264.

84. D. Voychok, C. J. Guild, S. Dissanayake, J. Llorca, E. Stavitski, Z. Y. Liu, R. M. Palomino, I. Waluyo, Y. Y. Li, A. I. Frenkel, J. A. Rodriguez, S. L. Suib and S. D. Senanayake, *In situ* characterization of mesoporous Co/CeO_2 catalysts for the high-temperature water-gas shift, *J. Phys. Chem. C*, **2018**, *122*, 8998.

85. J. Deng, W. Chu, B. Wang, W. Yang and X. S. Zhao, Mesoporous $Ni/Ce_{1-x}Ni_xO_{2-y}$ heterostructure as an efficient catalyst for converting greenhouse gas to H_2 and syngas, *Catal. Sci. Technol.*, **2016**, *6*, 851.

86. F. A. Ospina-Acevedo, S. P. Beltran and P. B. Balbuena, Mechanisms of alumina growth via atomic layer deposition on nickel oxide and metallic nickel surfaces, *Phys. Chem. Chem. Phys.*, **2019**, *21*, 24543.

87. L. Chen, R. E. Warburton, K. -S. Chen, J. A. Libera, C. Johnson, Z. Yang, M. C. Hersam, J. P. Greeley and J. W. Elam, Mechanism for Al_2O_3 atomic layer deposition on $LiMn_2O_4$ from *in situ* measurements and *ab initio* calculations, *Chem*, **2018**, *4*, 2418.

88. K. Knemeyer, M. P. Hermida, P. Ingale, J. Schmidt, J. Kröhnert, R. N. d'Alnoncourt, M. Driess and F. Rosowski, Mechanistic studies of atomic layer deposition on oxidation catalysts – AlO_x and PO_x deposition, *Phys. Chem. Chem. Phys*, **2020**, *22*, 17999.

89. F. Zhang, Z. Y. Liu, S. H. Zhang, N. Akter, R. M. Palomino, D. Voychok, I. Orozco, D. Salazar, J. A. Rodriguez, J. Llorca, J. Lee, D. Kim, W. Q. Xu, A. I. Frenkel, Y. Y. Li, T. Kim and S. D. Senanayake, *In situ* elucidation of the active state of $Co\text{-}CeO_x$ catalysts in the dry reforming of methane: The important role of the reducible oxide support and interactions with cobalt, *ACS Catal.*, **2018**, *8*, 3550.

90. A. L. Marinho, R. C. Rabelo-Neto, F. Epron, N. Bion, F. S. Toniolo and F. B. Noronha, Embedded Ni nanoparticles in $CeZrO_2$ as stable catalyst for dry reforming of methane, *Appl. Catal. B*, **2020**, *268*, 118387.

Chapter 5

Summary and Suggestions for Future Works

5.1. Summary

This paper describes the prerequisites, challenges, overcoming strategies and possibilities for the chemical conversion of methane, and introduces the research carried out with nanotechnology-based catalysts. Methane is a clean resource that is produced from a variety of sources and will not be depleted for long, but research on various ways to harness it is still lacking. Research to produce various chemicals through direct and indirect conversion of methane is one way to address this problem. Heterogeneous catalysts are capable of methane conversion under high temperature reaction conditions that can provide high thermal energy. However, since this causes structural instability of the catalyst, the catalyst composition is limited to materials with high thermal stability. The first strategy to enhance thermal stability is to use mesoporous materials that are stable at high temperatures and have high surface area as supports. Among them, silica is a mesoporous material capable of forming various types of mesopores and has stability at high temperatures. We compared vanadium silica-based catalysts with different vanadium content, impregnation method, and silica type. Of these, for the 1% VO_x/MCF-17 (DI) catalyst, many isolated VO_4 species were stably supported on mesoporous silica with a large surface area, indicating high reactivity in the methane-formaldehyde reaction. There was a difference in thermal stability when comparing the SiO_2@V_2O_5 catalyst with the previous mesoporous catalyst after methane oxidation. Silica spheres with relatively low surface area did not provide sufficient thermal stability towards vanadium oxide compared to VO_x/MCF-17, resulting in phase separation into SiO_2 and V_2O_5 during the reaction. A second way to improve thermal stability is to encapsulate a relatively thermally unstable material with a thermally stable metal oxide and use it as a catalyst. With the invention of 3D rotational ALD, various metal oxides can be deposited on catalyst surfaces, which shows a wide range of potential scalability. Not only can it increase the stability of the catalyst, but it can also have the effect of providing an active interface called $AlVO_4$ that is created during the reaction. The stability of the catalyst was improved while maintaining the basic properties of the catalyst even in the DRM reaction to convert syngas to carbon dioxide. The Al_2O_3 ALD process completely blocked the coke deposition produced by the side reaction of Ni/CeO_2 nanocatalysts in just one cycle. However, the catalytic activity also decreased due to the reductive change of the catalyst. After Al_2O_3 deposition, the reducibility of Ni decreased sharply, and CeO_2 increased. It is suggested that the decrease of the Ni metal phase can decrease the TOF of methane activation, whereas the elevation of the Ce^{3+} phase of

CeO_2 increases the oxophilicity, which can positively affect the prevention of coke deposition.

In the future, various studies may be conducted to improve the stability of the catalytic reaction. The fabrication of refractory metal oxides such as V, Mo, Nb, Ta, W and Re into various forms including core@shell structures will serve as important catalysts for high thermal energy-demanding reactions including methane conversion. It will be a study that can utilize the active sites of catalysts with low thermal stability and high activity for reactions under more diverse conditions. In particular, studies using ALD can fabricate core@shell structures by encapsulating metal oxides regardless of the core material. Therefore, the development potential is limitless, so it is worth studying and commercializing more catalytic reactions.

5.2. Suggestions for Future Works

We propose future work to find suitable strategies to convert methane to produce a variety of chemicals and provide sustainable energy due to sufficient reserves. Currently, the most promising methane utilization method is expected to be hydrogen production through the commercialization of dry reforming. The metallic phase of the Ni particles should be maintained for CH_4 activation, and ensemble catalysts that maximize the dispersion of active sites can enhance the catalytic activity rather than SACs. There is no disagreement that Ni catalysts are the most favorable catalysts for DRM, so the role of support should be further to be studied to prevent sintering and provide oxygen atoms from CO_2. The supports require the properties such as high thermal stability, SMSI formation, and provide oxygen atoms in oxygen vacancies or chemical intermediate phases that react with CO_2. Also, the bimetallic catalysts or promoters with the oxophilic metals can help supply oxygen to the active sites to mitigate coke deposition.

As the energy market trend shifts away from the use of fossil fuels to hydrogen, electricity, and renewable energy, we focus on catalytic decomposition of methane (CDM, $CH_4 \rightarrow 2H_2 + C$) for hydrogen production for energy source and carbon generation to use as the battery additive. CDM features high selectivity for high-purity hydrogen and no carbon dioxide emissions because the reactant is pure methane. However, the disadvantages are low durability over time due to catalyst deactivation due to carbon deposition, low purity of carbon nanomaterials, and higher temperature requirements for methane self-decomposition. McFarland *et al.* reported that a novel heterogeneous system of liquid catalysts of molten Ni–Bi metals produce solid carbon and hydrogen gas products with 95% methane conversion at 1065 °C.[1] The separable system can operate a consistent reaction over a longer period to obtain high-purity hydrogen. Studies focused on the production of monodisperse nanocarbon materials called single-chirality have been conducted using various carbon sources such as ethylene and ethanol.[2] Methane sources are also grown on the catalyst surface in the form of CNTs in the CVD reactors. Potential candidates for CDM catalysts can be listed that capable of forming carbides, such as Fe, Co,

Ni on the support, or refractory metals of W, Mo, Re, V, Nb, Ru, Rh, and Os.[3,4] In addition, research on the direct conversion of raw materials such as natural gas or shale gas will be an important alternative to the utilization of petroleum resources.

5.3. References

1. D. C. Upham, V. Agarwal, A. Khechfe, Z. R. Snodgrass, M. J. Gordon, H. Metiu and E. W. McFarland, Catalytic molten metals for the direct conversion of methane to hydrogen and separable carbon. *Science* **2017**, *358*, 917.
2. J. R. Sanchez-Valencia, T. Dienel, O. Gröning, I. Shorubalko, A. Mueller, M. Jansen, K. Amsharov, P. Ruffieux and R. Fasel, Controlled synthesis of single-chirality carbon nanotubes. *Nature* **2014**, *512*, 61.
3. M. Pudukudy and Z. Yaakob, Methane decomposition over Ni, Co and Fe based monometallic catalysts supported on sol gel derived SiO_2 microflakes. *Chem. Eng. J.* **2015**, *262*, 1009.
4. X. Zhang, B. Graves, M. De Volder, W. Yang, T. Johnson, B. Wen, W. Su, R. Nishida, S. Xie and A. Boies, High-precision solid catalysts for investigation of carbon nanotube synthesis and structure. *Sci. Adv.* **2020**, *6*, eabb6010.

Nomenclature

ALD	Atomic layer deposition
AP-XPS	Ambient pressure X-ray photoelectron spectroscopy
AR	Atomic ripening
BET	Brunauer-Emmett-Teller
BJH	Barrett–Joyner–Halenda
C_1	One-carbon
CCD	Charge coupled device
CCUS	Carbon capture, utilization, and storage
CDM	Catalytic decomposition of methane
CMC	Critical micelle concentration
CNF	Carbon nanofiber
CNO	Carbon nano-onions
CNT	Carbon nanotube
CVD	Chemical vapor deposition
DFT	Density functional theory
DRM	Dry reforming of methane
EDS	Energy-dispersive X-ray spectroscopy
EISA	Evaporation-induced self-assembly
EPR	Electro paramagnetic resonance
FID	Flame ionization detector
FT	Fischer-Tropsch
GC	Gas chromatography
GHG	Greenhouse gas
GHSV	Gas hourly space velocity
HAADF-STEM	High-angle annular dark-field scanning transmission electron microscopy
HRTEM	High-resolution transmission electron microscopy
PEMFC	Proton exchange membrane fuel cell
MDA	Methane dehydroaromatization
ML	Monolayer
MMO	Methane monooxygenase
***m*-SiO_2**	Mesoporous silica
NOCM	Nonoxidative coupling of methane
NPs	Nanoparticles
NRs	Nanorods
OCM	Oxidative coupling of methane
PMC	Particle migration and coalescence
RWGS	Reverse water-gas shift

SACs	Single-atom catalysts
SEM	Temperature-programmed desorption
SMSI	Strong metal-support interaction
SRM	Steam reforming of methane
TCD	Thermal conductivity detector
TEM	Transmission electron microscopy
TMA	Trimethylaluminum
TOF	Turnover frequency
TPD	Temperature-programmed desorption
TPR	Temperature-programmed reduction
TPSR	Temperature-programmed surface reaction
UV-vis	Ultraviolet-visible spectroscopy
VO_4	Isolated tetrahedral monovanadate
WI	Wet impregnation
XPS	X-ray photoelectron spectroscopy
XRD	X-ray Diffraction

Acknowledgements

지난 6년간의 대학원 생활에서 비단 연구뿐만 아니라 세상을 어떻게 살아가야 하는지에 대하여 항상 모범답안으로 앞서 계시는, 늘 본받고 싶은 안광진 지도교수님께 정말 많은 것들을 배울 수 있었음에 진심으로 감사합니다. 이제서야 조금이나마 그 방식을 알 것도 같은데 곁에서 더 많이 배워가지 못해 조금은 아쉽고, 그럼에도 이제는 어디서든 자립할 수 있으리라는 자신감도 얻었습니다. 귀한 시간을 내주셔서 제 학위논문과 디펜스 발표를 심사해 주시고 중요한 코멘트를 주신 주상훈 교수님, 김현유 교수님, 장지욱 교수님, 권영국 교수님께 정말 감사드립니다.

학위 기간 동안 많은 분들의 도움이 있었기에 현재까지 연구와 과제를 수행할 수 있었습니다. 메탄 연구에 가장 큰 도움을 주신 박은덕 교수님, ALD 장비로 제 연구에 큰 기여를 해주신 정윤석 교수님, 촉매 분석에 대한 깊이있는 자문을 해주신 곽자훈 교수님, 초기 연구에 많은 도움을 주신 이만식 박사님, 최근에 집중하고 있는 메탄 열분해 반응에 함께 힘써주시는 이창영 교수님, 메탄 개질반응에 대한 연구에 많은 도움을 주신 고창현 교수님께 감사의 말씀을 전합니다.

제 대학원 생활 동안 같이 고생해 주었던 모든 랩 동기 및 후배들에게 그간 참 고마웠습니다. 대학원에 동기로 함께 입학하여 함께 이제 졸업하여 홀로서기를 시작할 맏형 신명이형, 사실상의 랩실 동기이자 현재 가장 열심히 연구하고 있는 준경이와 지현이, 타지에서도 연구실의 유일한 박사로써 힘써주고 계신 진투 박사님, 그리고 우리 연구실의 실세 호정이까지 모두 긴 시간동안 큰 다툼 한 번 없이 함께해 주어 고맙습니다. 그밖에도 제 연구의 후반에 정말 열심히 함께해준 성실한 계획쟁이이자 문화대장 언우, 항상 신중하게 연구하는 미어캣 지훈, 따뜻한 심장과 강력한 신체를 가진 철인 병관, 침착함과 단호함을 수줍음으로 감추는 실눈캐 대원, 맨날 장난스럽지만 큰 연구를 해나갈 담비 주은이, 우리 연구실 학생인 척 하는 메타몽 광영, 그리고 최근에 합류한 은정이, 윤정이, 창훈이, 신재, 그리고 현건이, 그리고 함께해준 수많은 인턴들도 앞으로의 시간이 그저 행복했으면 좋겠습니다. 항상 선배로서 어렵기만 하고 도움은 많이 되어주지 못했지 않았나 생각합니다. 어려운 점이 있으면 그럼에도 연락했으면 좋겠습니다.

지난 10년간 친구 잘 못만드는 제게도 세월의 위력에 힘입어 참 많은 인연이 생겼습니다. 대학원 생활을 함께한 이제는 잉여가 될 수 없는 성문, 승택, 수환, 혁준이형, 현욱, 진현, 동진이와 사회 선배님들인 창호, 석윤이, 아직도 실없는 얘기를 나누는 20조 용성, 현식, 영수, 재현, 재기, 은나, 주영, 유라, 주람, 도현, 승우, 지금도 함께 잘 살 수 있을 것 같은 현겸, 현명, 경룡, 문기, 그밖에도 동찬, 명조, 성민, 지오, 영호, 그리고 문복이에게도 항상 큰 힘이 되어주어 고마웠음을 전합니다.

끝으로 항상 저를 믿어주신 부모님과 어느새 스스로 훌륭해진 종섭이까지 정말 고맙습니다.

Euiseob Yang

Curriculum Vitae

Education

2016–2021 M.S.-Ph.D. Combined Program in Chemical Engineering, Ulsan National Institute of Science and Technology (UNIST) (Advisor: Prof. Kwangjin An)

2011–2016 B.S. Degree in Chemical Engineering, UNIST, February 2016.

Research Interests

Synthesis of nanoparticles

- Size and shape-controlled nanoparticles: Noble metals and base metals
- Diverse nanoparticles: Bimetallic, core@shell, metal oxides, ferrites, and perovskites oxides
- Processing the homemade atomic layer deposition (ALD) for catalyst enhancement

Diverse catalytic heterogeneous reactions focused on methane

- Partial oxidation to formaldehyde, dry reforming, and catalytic decomposition

Utilize in situ/operando characterizations (TEM, XRD, XAFS, DRIFTS, and XPS)

Publication [†: Equal contribution]

[9] **Euiseob Yang**, Eonu Nam, Jihyeon Lee, Hojeong Lee, Eun Duck Park*, Hankwon Lim*, and Kwangjin An*
"Al_2O_3-Coated Ni/CeO_2 nanoparticles as coke-resistant catalyst for dry reforming of methane"
Catal. Sci. Technol. *10*, 8283–8294 (2020).

[8] **Euiseob Yang**, Jun Gyeong Lee, Dong Hyeon Kim, Yoon Seok Jung, Ja Hun Kwak, Eun Duck Park*, and Kwangjin An*
"SiO_2@V_2O_5@Al_2O_3 core–shell catalysts with high activity and stability for methane oxidation to formaldehyde"
J. Catal. *368*, 134–144 (2018).

[7] **Euiseob Yang**†, Eun Jeong Jang†, Jun Gyeong Lee, Sinmyung Yoon, Jaekyoung Lee, Nathan Musselwhite, Gabor A. Somorjai, Ja Hun Kwak*, and Kwangjin An*
"Acidic effect of porous alumina as supports for Pt nanoparticle catalysts in *n*-hexane reforming"
Catal. Sci. Technol. *8*, 3295–3303 (2018).

[6] **Euiseob Yang**, Jun Gyeong Lee, Eun Duck Park*, and Kwangjin An*
"Methane oxidation to formaldehyde over vanadium oxide supported on various mesoporous silicas"
Korean J. Chem. Eng. *38,* 1224–1230 (2021). DOI: 10.1007/s11814-021-0758-8

[5] Jun Gyeong Lee, Sinmyung Yoon, **Euiseob Yang**, Jae Hwa Lee, Kyung Song, Hoi Ri Moon*, and Kwangjin An*
"Structural evolution of ZIF-67-derived catalysts for furfural hydrogenation"

J. Catal. *392*, 302–312 (2020).

[4] Jihyeon Lee, Ji Hui Seo, Chinh Nguyen-Huy, **Euiseob Yang**, Jun Gyeong Lee, Hojeong Lee, Eun Jeong Jang, Ja Hun Kwak, Jun Hee Lee*, Hosik Lee*, and Kwangjin An*
"Cu_2O(110) surface as an active site for catalytic furfural hydrogenation"
Appl. Catal. B *282*, 119576 (2020).

[3] Hojeong Lee, Chinh Nguyen-Huy, Eun Jeong Jang, Jihyeon Lee, **Euiseob Yang**, Man Sig Lee, Ja Hun Kwak*, and Kwangjin An*
"Interfacial effect of Pd supported on mesoporous oxide for catalytic furfural hydrogenation"
Catal. Today *365*, 291–300 (2021).

[2] Chinh Nguyen-Huy, Jihyeon Lee, Ji Hui Seo, **Euiseob Yang**, Jaekyoung Lee, Keunsu Choi, Hosik Lee, Jae Hyung Kim, Man Sig Lee, Sang Hoon Joo, Ja Hun Kwak, Jun Hee Lee*, and Kwangjin An*
"Structure-dependent catalytic properties of mesoporous cobalt oxides in furfural hydrogenation"
Appl. Catal. A *583*, 117125 (2019).

[1] Chinh Nguyen-Huy, Ji Sun Kim, Sinmyung Yoon, **Euiseob Yang**, Ja Hun Kwak, Man Sig Lee*, and Kwangjin An*
"Supported Pd nanoparticle catalysts with high activities and selectivities in liquid-phase furfural hydrogenation"
Fuel *226*, 607–617 (2018).

Patents

[1] Kwangjin An, Eun Duck Park, and **Euiseob Yang**
"코어-쉘 구조를 갖는 메탄 산화용 촉매, 이의 제조방법 및 이를 이용한 메탄의 산화 방법"
"Catalyst for methane oxidation having a core-shell structure, a process for producing the same, and a process for the oxidation of methane using the same"
Korea Patent Appl. 10-2018-0118267 (Oct. 4, 2018).